Lithium-ion and beyond: safer alternatives

Zur Erlangung des akademischen Grades eines

DOKTORS DER NATURWISSENSCHAFTEN

(Dr. rer. nat.)

der KIT-Fakultät für Chemie und Biowissenschaften

des Karlsruher Instituts für Technologie (KIT)

genehmigte

DISSERTATION

von

Mr. Ulderico Ulissi

aus

San Benedetto del Tronto

KIT-Dekan: Prof. Dr. Reinhard Fischer

Referent: Prof. Dr. Stefano Passerini

Korreferent: Prof. Dr. Helmut Ehrenberg

Tag der mündlichen Prüfung: 13 Dezember 2017

English abstract

High-energy, light lithium-ion batteries are nowadays the power source of choice for several classes of portable electronic devices and the most appealing candidates for application in electric vehicles (EVs). However, commercial lithium-ion batteries, employing graphitic carbon anodes, carbonate-based organic electrolytes, and lithiated transition metal oxide cathodes, require optimization to meet the market demands in terms of enhanced energy and safety. In this thesis work new, safer lithium and lithium-ion configurations are proposed. The first approach is to replace the conventional graphite anode with a nanostructured composite Sn-C alloy anode. The organic-based electrolyte components are replaced with safer ionic liquid-based electrolytes. The materials are tested in lithium-ion cell configurations with an olivine-structured, $LiFePO_4$ cathode material, which ensures added safety, and layered $LiNi_{1/3}Co_{1/3}Mn_{1/3}O_2$, to demonstrate that ionic liquid-based electrolytes can be successfully employed also for higher energy systems. The second approach is to propose alternative cathode chemistries for higher energy, beyond conventional lithium-ion batteries, namely lithium oxygen and lithium sulfur. For Li-O_2, the use of a safe ionic liquid-based electrolyte improves the reversibility of the lithium-oxygen conversion reaction. The system is further optimized by coupling it with the Sn-C alloy anode or the carbon-coated $Zn_{0.9}Fe_{0.1}O$ alloy-conversion anode and optimized cathode configurations to realize high performance, safe, lithium-oxygen and lithium-ion-oxygen cells. The use of safe, all-solid-state electrolytes is studied for application in Li-S batteries, showing a positive effect on the reversibility of the electrochemical process. Novel cathode architectures are investigated, employing low cost, environmentally friendly materials, such as FeS_2 and elemental sulfur. The results show that all the cell chemistries using conventional cathode materials are well suited for application in the new generations of electric and electronic devices. Alternative electrolyte formulations can also efficiently mitigate the issues of beyond lithium-ion technologies, improving the performance and the safety content of the energy storage systems.

Zusammenfassung

Leichte und hochenergetische Lithium-Ionen-Batterien sind heutzutage die Energiequelle der Wahl für tragbare elektronische Geräte und die attraktivsten Kandidaten für die Anwendung in Elektrofahrzeugen. In kommerziellen Lithium-Ionen-Batterien werden Graphitanoden, organische Carbonat-basierte Elektrolyte und lithiumhaltige Übergangsmetalloxidkathoden eingesetzt. Dieser Zellaufbau bedarf jedoch einer Optimierung, um den Anforderungen des Marktes in Bezug auf höhere Energiedichten und Sicherheit gerecht zu werden. In dieser Arbeit werden neue, sicherere Lithium-Metall und Lithium-Ionen Konfigurationen untersucht.

Der erste Ansatz besteht darin, die herkömmliche Graphitanode durch eine nanostrukturierte Sn-C Komposit-Legierungsanode zu ersetzen. Zudem wird der konventionelle organische Elektrolyt durch sicherere Elektrolyte, basierend auf ionischen Flüssigkeiten, ersetzt. Diese Materialien werden in Lithium-Ionen-Zellen in Kombination mit $LiFePO_4$ als Kathodenmaterial, welches zusätzliche Sicherheit gewährleistet, untersucht. Zudem wird das Schichtoxid $LiNi_{1/3}Co_{1/3}Mn_{1/3}O_2$ untersucht, um nachzuweisen, dass die ionischen Flüssigkeiten als Elektrolyte auch für Systeme mit höheren Energiedichten erfolgreich eingesetzt werden können.

Der zweite Ansatz besteht darin, alternative Kathodenmaterialien für Systeme wie Lithium-Sauerstoff und Lithium-Schwefel zu untersuchen, da diese Systeme höhere Energiedichten als die herkömmlichen Lithium-Ionen-Batterien ermöglichen. Die Verwendung von ionische Flüssigkeiten in Elektrolyten verbessert die Reversibilität der Lithium-Sauerstoff-Umwandlungsreaktion in Li-O_2 Zellen. Das System kann durch den Einsatz einer Sn-C Komposit-Legierungsanode oder einer mit Kohlenstoff beschichteten $Zn_{0.9}Fe_{0.1}O$ Konversions-Legierungsanode, kombiniert mit einer optimierten Kathodenkonfiguration, weiter verbessert werden und ermöglicht sichere und leistungsstarke Lithium-Sauerstoff- und Lithium-Ionen-Sauerstoffzellen.

Die Verwendung sicherer Festkörperelektrolyte für den Einsatz in Li-S-Batterien zeigt positive Auswirkungen auf die Reversibilität des elektrochemischen Prozesses. Unter Verwendung von kostengünstigen, umweltfreundlichen Materialien wie FeS_2 und elementarem Schwefel werden neuartige Kathodenarchitekturen untersucht.

Die Ergebnisse zeigen, dass alle Zellkonfigurationen, die herkömmliche Kathodenmaterialien verwenden, gut für den Einsatz in zukünftigen elektrischen und elektronischen Geräten geeignet sind. Alternative Elektrolytzusammensetzungen können zudem die Probleme der Lithium-Ionen-Technologie wirksam entschärfen und die Leistung und das Sicherheitsniveau der Energiespeichersysteme verbessern.

Table of contents

List of acronyms

AM	Active Material
ASSB	All-Solid-State Battery
CF	C:Fes_2 40:60 (wt.%)
CFS(5:5)	C:FeS_2:Sulfur 40:30:30 (wt.%)
CFS(8:2)	C:FeS_2:Sulfur 40:50:10 (wt.%)
DEMETFSI	N-N-Diethyl-N-Methyl-N-(2-Methoxyethyl)Ammonium Bis(Trifluoromethanesulfonyl)Imide
DMC	Dimethyl Carbonate
DME	Dimethoxyethane
DMSO	Dimethyl Sulfoxide
EC	Ethylene Carbonate
EIS	Electrochemical Impedance Spectroscopy
ESS	Energy Storage System
EUCAR	European Council for Automotive Research And Development
EV	Electric Vehicle
FEC	Fluoroethylene Carbonate
GDL	Gas Diffusion Layer
GHG	Greenhouse Gas
IL	Ionic Liquid
IUPAC	International Union of Pure and Applied Chemistry
LFP	$LiFePO_4$
LIB	Lithium-Ion Battery
LISICON	LIthium Super Ionic CONductor
LiTf	Trifluoromethanesulfonate
LiTFSI	Lithium bis(Trifluoromethanesulfonyl)Imide
LMO	$LiMn_2O_4$
LPSI	LiI-Li_3PS_4
LTO	$Li_4Ti_5O_{12}$
MSR	Mechanically Induced Self-Propagating Reactions

NCA	$LiNi_{0.8}Co_{0.15}Al_{0.05}O_2$
NLLSQ	Nonlinear Least Square
NMC	$LiCo_{1/3}Ni_{1/3}Mn_{1/3}O_2$
NMP	N-Methyl-2-Pyrrolidinione
OCV	Open Circuit Voltage
OER	Oxygen Evolution Reaction
ORR	Oxygen Reduction Reaction
PC	Propylene Carbonate
PTFE	Polytetrafluoroethylene
PVDF	Polyvinylidene Fluoride
Pyr_{12O1}TFSI	N-Methoxy-Ethyl-N-Methylpyrrolidinium bis(Trifluoromethanesulfonyl)Imide
Pyr_{14}FSI	*N*-Butyl-N-Methyl-Pyrrolidinium bis(Fluorosulfonyl)Imide
Pyr_{14}TFSI	N-Butyl-N-Methylpyrrolidinium bis(Trifluoromethanesulfonyl)Imide
RT	Room Temperature
RTIL	Room Temperature Ionic Liquid
SDE	Spray Deposited Electrode
SEI	Solid Electrolyte Interphase
SEM	Scanning Electron Microscopy
SHE	Standard Hydrogen Electrode
SSE	Self-Standing Electrode
TGA	Thermo-Gravimetric Analysis
THF	Tetrahydrofuran
TMO-C	$Zn_{0.9}fe_{0.1}o_2$-C
VC	Vinylene Carbonate
VTF/VFT	Vogel-Tammann-Fulcher
XRD	X-Ray Diffraction

Chapter 1: Introduction

Since the industrial revolution, world population has grown by one order of magnitude [1]. One of the direct consequences is a dramatic increase of greenhouse gases (GHGs) emission and other pollutants [2], which pose serious risks for our planet. Our climate is changing, as demonstrated by unexpected heavy rainfalls, floods, and encroaching seas. These, however, are just some of the early consequences of this process [2], and future risks are still difficult to foresee. By using the precautionary principle, great efforts are being made to reduce pollutant emissions and reduce the adverse effects of population growth on our planet [2]. It is believed that to achieve this goal, we, as humanity, will need a new industrial revolution that mostly uses affordable, sustainable and accessible energy sources, such as solar and wind energies [1,3]. These renewable energy sources, however, are intermittent by nature and need to be integrated into a smart electricity distribution grid, coupled with safe, cheap, and reliable stationary energy storage systems (ESS, figure 1.1), such as batteries [3].

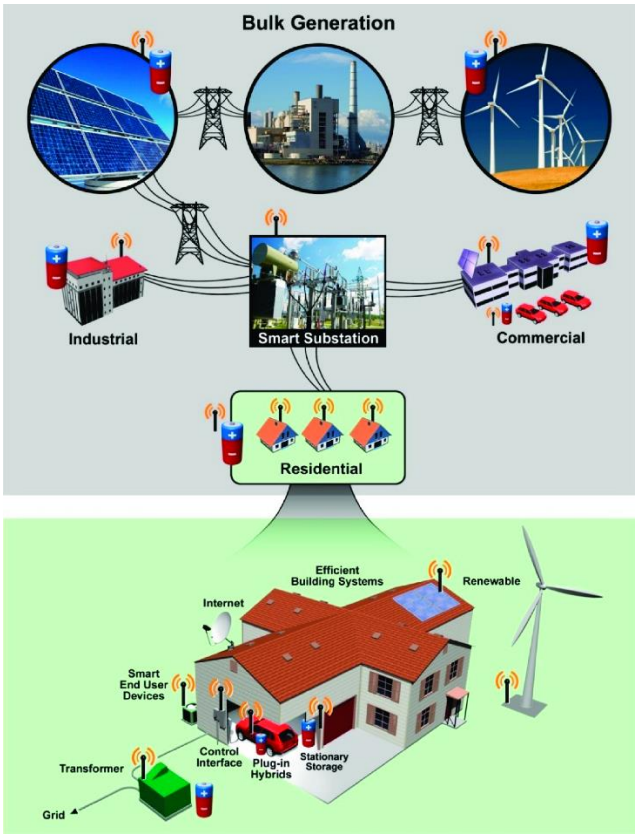

Figure 1.1 Energy storage system integrated into a smart grid with intermittent renewable energy sources [3].

Among the several stationary ESS proposed (Figure 1.2), lithium-ion batteries (LIBs) hold much promise being characterized by high energy/power densities and high coulombic efficiency [3]. The current generation of LIBs, however, is not considered cost-effective for stationary energy storage. A new generation of cheaper and reliable batteries, including new LIBs, could, therefore, be a breakthrough for a smart and green grid [3].

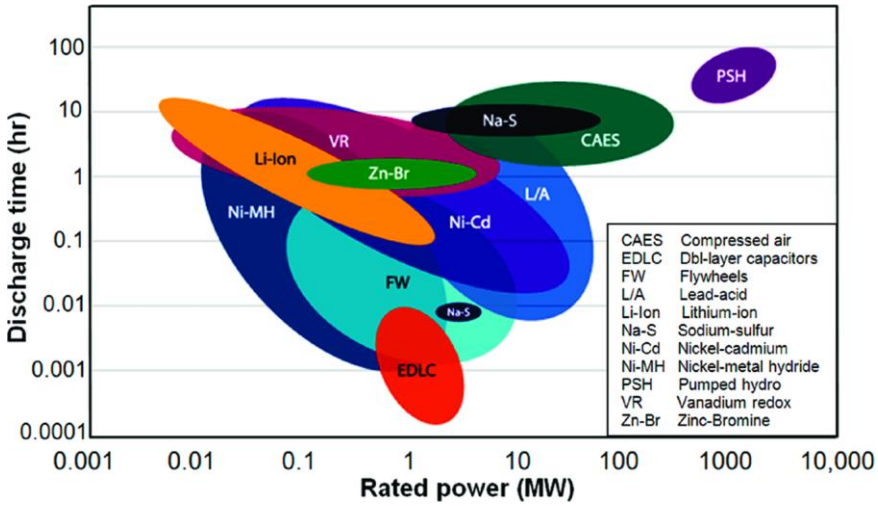

Figure 1.2 Power rating and discharge time (energy rating) of several technologies proposed for stationary energy storage [3]

Storage systems would also play an essential role in distributing renewable energy to electric vehicles (EVs), which will need to be integrated into the smart grid to reduce GHG emission. Nowadays, energy sources for transportation mostly consist of petroleum-derived liquid fuels, a severe threat in terms of GHG emission [4]. EVs, which are considered zero-emission systems [4], represent a viable solution [5] to mitigate this issue. The current generation of EVs is mainly powered by LIBs [4,5]. EVs, however, are not yet widespread mainly due to limited miles range [5]. This limitation is determined by the present generation of batteries, including LIBs, which require additional development to fully meet the market demands in terms of safety, cost, energy, and power densities [5–7]. For all these reasons, during the last decades, there has been a growing interest in developing this technology, which plays a crucial role in the achievement of a sustainable energy system for a greener tomorrow.

1.1 Lithium-ion batteries - Fundamentals

By definition, an electrochemical cell consists of two electrodes separated by the electrolyte [8]. The difference in potential between these two electrodes is the cell potential, measured in volt (V), which is directly correlated to the electrical energy that can be delivered to an external circuit [8,9]. The cell is characterized by two independent half-reactions, one for each electrode [8]. In basic electrochemistry, one commonly refers to only one of the two half-reactions occurring at one electrode, usually called working electrode. The other electrode is conventionally called counter electrode [8]. To measure the potential associated with only one half-reaction, a third electrode, composed by phases having a constant composition (thus a constant potential), can be introduced in the system. This is conventionally called reference electrode [8]. Historically, half-reaction potentials are given with respect to the Standard Hydrogen Electrode (SHE), which is used as reference for zero potential at $a(H^+) = 1$, $a(H_2) = 1$, and T = 25°C. The half-reaction occurring at this electrode is: $2H^+ + 2e^- \rightleftharpoons H_2$. When studying systems involving lithium, it is common to use as reference the lithium redox couple: $Li^+ + e^- \rightleftharpoons Li$, which is characterized by a potential of -3.04 V vs. SHE. Such an electrode can only be considered as a "quasi-reference" electrode [8]. The activity of the Li^+ ions in solution strongly depends on the electrolyte solvent(s) used and the activity of the lithium metal may be affected by the reaction products of the metal electrode and the electrolyte. Nonetheless, and unless specified, all potential values in this thesis work refer to the lithium redox couple, i.e., Li/Li^+. A lithium-ion battery is a galvanic secondary cell, meaning that the electrodes reactions occur spontaneously when the two electrodes are connected by an electron conductor. It means that chemical energy is converted into electric energy [9,10]. Galvanic cells can be either primary (non-rechargeable) or secondary (rechargeable) [8]. Although the IUPAC nomenclature for electrochemistry does not define the term "battery" [11], it is integrated in other IUPAC guidelines [12] and is conventionally used, even in this thesis work, to define the final device assembled from galvanic cells (including a single cell) [13]. It should be noted, however, that by strict definition, a battery is usually the overall assembly of one or more strings. A string (a term which is rarely used in electrochemistry) is defined as a grouping of interconnected galvanic cells with the same nominal voltage as the direct current system (physically, two or more cells connected in series) [14]. To

charge a galvanic secondary cell, energy must be supplied to the system, as the reactions implied in the charge process are not spontaneous. Electric energy is converted in chemical energy, and this is usually done by applying a potential greater than the cell open circuit potential [13,15]. In electrochemistry the anode is defined as the electrode where oxidation takes place, while the cathode is the electrode were reduction takes place, i.e., the cathode is the positive electrode during discharge and the negative electrode during charge [13]. In this thesis, the term cathode is always used to indicate the positive electrode like in most works on lithium-ion batteries. This means that when talking about negative electrode, it will be referred to the anode and, generally, to anode materials for Li-ion batteries. When describing positive electrodes, it will be referred to the cathode and, generally, to cathode materials for Li-ion batteries. The nomenclature will always be referred to a Li-ion battery during discharge. While the evolution of Li-ion batteries will be described more in detail in the next few chapters (chapters 1.2.1, 1.3.1, 1.4.1), some key concepts regarding this system will be discussed here. A lithium-ion cell is composed of two electrodes, negative and positive, and the electrolyte. Each electrode in modern lithium-ion batteries consist of a (thin) layer casted on a metal current collector (Cu, Al, …). Such a layer is usually casted from slurries including the active material (either the cathodic or anodic material), at least one polymeric binder (used to maintain the electrode integrity), and a conductive agent (generally a carbon) to ensure e^- conduction. The anodic material composing the negative electrode is typically graphitic carbon, which is characterized by an electrochemical activity with lithium at relatively low potential, i.e., close to that of metallic lithium. The cathodic material composing the positive electrode can be a transition metal oxide, characterized by a reaction with lithium at rather high potentials. The electrolyte is conventionally composed by at least one organic solvent with a high dielectric constant [16], in which a lithium salt is dissolved granting the ionic charge (Li^+) shuttle mechanism between the anode and the cathode [17]. Conventionally, the electrolyte is soaked in a polymeric separator to prevent the contact of the electrodes [18]. Alternatively, the electrolyte can be embedded in a gel matrix [8,9,13]. In this kind of cells, Li^+ ions are the species shuttling between the anode and the cathode, hence the name "Li-ion battery" or, as first introduced by Armand [19] and realized by Scrosati et al. [20], "rocking-chair battery" (Figure 1.1.1)

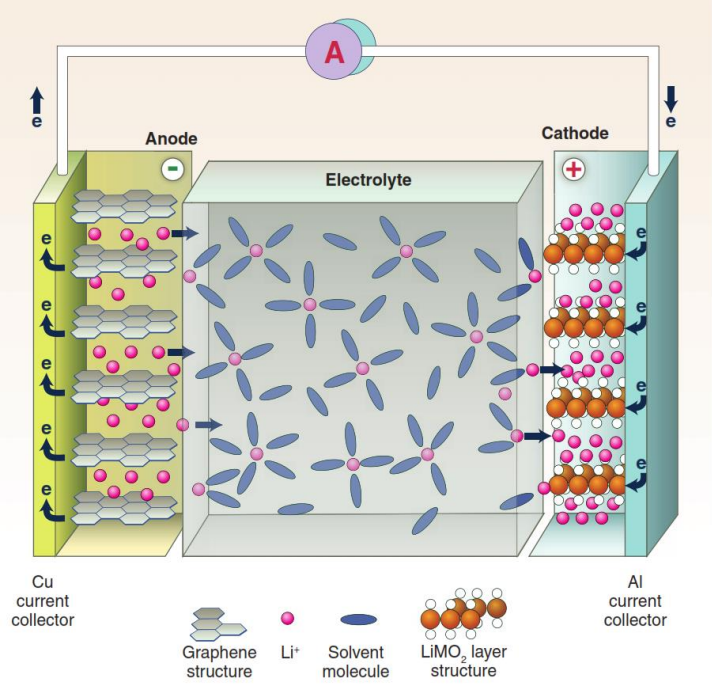

Figure 1.1.1 Schematic of a first-generation lithium-ion cell, discharge operation [21]

Specifically, during charge and discharge the following reactions occur when considering, e.g., $LiCoO_2$ as positive electrode material and graphitic carbon as the negative:

$$C_6 + xLi^+ + e^- \underset{\text{Li-ion discharge}}{\overset{\text{Li-ion charge}}{\rightleftharpoons}} Li_xC_6 \quad \text{(negative electrode)}$$

$$LiCoO_2 \underset{\text{Li-ion discharge}}{\overset{\text{Li-ion charge}}{\rightleftharpoons}} xLi^+ xe^- + Li_{1-x}CoO_2 \quad \text{(positive electrode)}$$

It is important to notice that such a cell is assembled in the fully discharged state, requiring to be charged in the first step. Upon the application of an external current, Li^+ ions are shuttled from the cathode to the anode resulting in the charging of the cell. When a charged cell is connected to a circuit, current will start to flow, and the potential will change upon time, toward the equilibrium, according to Gibbs free energy. In the fully charged state, the graphite negative electrode is characterized by an average voltage of about 0.1 V, while $LiCoO_2$ is characterized by an average voltage of about 4.1 V [9] resulting in the lithium-ion battery open circuit voltage of about 4.0 V. Each active material is characterized by a certain quantity of charge storage capability. This is called capacity [9] and it is usually expressed in Ah (1 Ah = 3600 C) and can be normalized by weight, volume or mol. The theoretical specific (normalized) capacity for a material can be calculated from Faraday's Law:

$$Q_{th} = \frac{n \times F}{M_w} \times \left(\frac{1000}{3600} \right)$$

where F is the Faraday constant (96495 C mol^{-1}), and M_w and n are, respectively, the molecular weight and the number of electrons exchanged per mole of active material. It can be easily calculated for both graphite and lithium cobalt oxide for x = 1 (C = 372 mAh g^{-1}, $LiCoO_2$ = 272 mAh g^{-1}). Practical specific capacity for a given material is usually different and is depending on several factors. While for graphite the thermodynamic limit can be approached (C_{sp} = 370 mAh g^{-1}), for $LiCoO_2$ this is limited by the number of lithium equivalents that can be reversibly exchanged, about 0.4, translating in a practical specific capacity of about 140 mAh g^{-1}. Another important parameter to mention is the current (dis-)/charge rate (C), that is the current to be applied to fully charge or discharge a given active material in a fixed amount of time, usually expressed in hours. A current rate of 1C corresponds to the current necessary to fully discharge the material in one hour. Thus, the C rate is equivalent to the active material specific capacity (e.g., mAh/g) multiplied by the weight of the active material (g) and divided by the time in hours (h).

From the discharge and charge capacity, it is possible to calculate the coulombic efficiency, that is:

$$\eta = \frac{Q_{sp\ discharge}}{Q_{sp\ charge}}$$

To calculate the energy stored in a battery, one can consider the following equation:

$$\text{energy} = \int_o^t IV(t)dt = \int_o^t P(t)dt = \int_o^Q V(q)dq$$

With I, current (A), V, voltage (V) t, time (h), P, power (W). The total exchanged capacity Q, can be calculated as follows:

$$Q = \int_o^t Idt = \int_o^Q dq$$

Energy and power can be normalized by weight (gravimetric, Wh or W kg^{-1}) or by volume (volumetric, Wh or W L^{-1}). The big advantage of lithium-ion batteries with respect to other systems lies in their outstanding energy and power densities (figure 1.1.2), coupled with long cycle life (that

is, the number of times the battery can be reversibly charged and discharged without a significant loss in capacity, namely above 80%) [8,13,15,22].

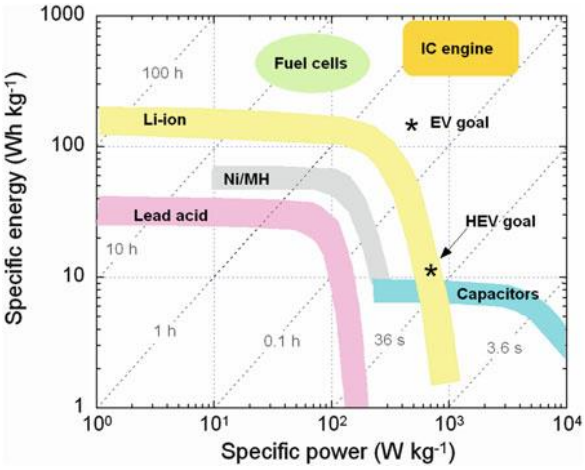

Figure 1.1.2 Ragone plot of several energy storage systems. Li-ion devices hold much promise, in particular, if coupled with capacitors, to reach the goal for electric mobility [22]

This few nomenclature and definition notions are by no means complete or exhaustive and are exclusively meant as a general reminder of a few key concepts important for understanding data here presented and comparing cell chemistries/configurations. For more detailed definitions and descriptions, few books are recommended, namely the electrochemical dictionary [13] and the Linden's Handbook of batteries, among others, in particular for the description of techniques using potentiostatic regimes and/or alternating current [9].

1.1.1 Safe operation of lithium-ion batteries

It was in the 1950s that lithium was found to be stable in organic, aprotic solvents [23]. About 20 years later it was first employed for the realization of primary lithium (metal) batteries [24]. Lithium, like other alkali metals, forms a passivation layer on its surface as soon as it is immersed in the electrolyte solution. This passivation layer is conventionally called solid electrolyte interphase (SEI, figure 1.1.1.1) [25].

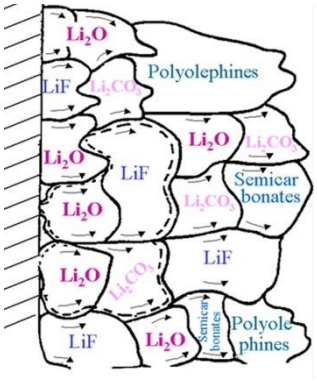

Figure 1.1.1.1 SEI mosaic model on lithium metal [26]

The SEI acts as an interphase between the electrode and the solution, effectively acting as a solid electrolyte (e^- insulating, ion conductive) and it is fundamental for safe battery operation, as first stated by Peled in 1979 [25,26]. Without a passivation layer, the metallic anode would quickly dissolve or be corroded, thus rendering battery operation impossible [26]. The physicochemical characteristics of the SEI are dependent on its structure/morphology and chemical composition, which are rather complex and dependent on the anode material, as well as on the electrolyte composition [27]. When a battery employing lithium metal is charged, however, the formation and growth of needle-like lithium crystals (dendrites, whiskers) [28] on the anode surface usually occur because the SEI is not mechanically stable. If dendrites grow through the electrolyte to the cathode surface, the negative and positive electrodes are in direct contact with negligible resistance, i.e., short-circuited (figure 1.1.1.2).

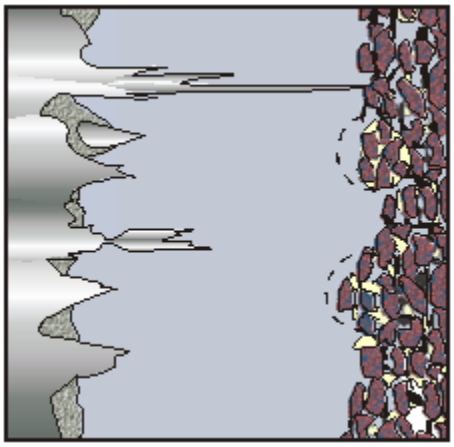

Figure 1.1.1.2 Lithium dendrite growth to the positive electrode, resulting in an internal short-circuit

The cell will consequently start to (over-)discharge at the maximum current allowed by the system (known as short-circuit current), generating heat, while several exothermic unwanted side reactions will start to take place (such as uncontrolled electrolyte decomposition). If the system cannot dissipate the generated heat, the temperature will increase, leading to the so-called "thermal runaway," which can effectively cause fire and/or the explosion of the battery pack (figure 1.1.1.3).

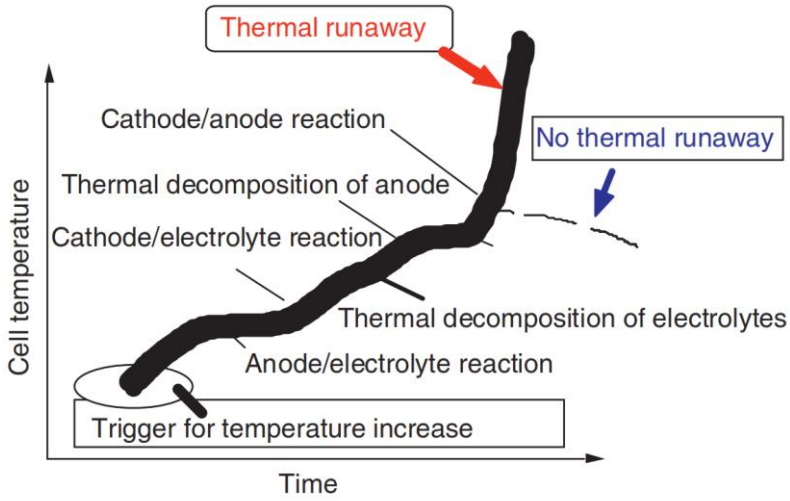

Figure 1.1.1.3 Conceptual scheme of lithium-ion battery thermal runaway [29]

Lithium metal rechargeable batteries were plagued with safety problems that even caused injury to users, and consequent product recalls, thus limiting their commercialization [30]. Replacing the metal anode with carbon (lithium-ion concept) allowed to realize safer, but still high energy, batteries that are now a commercial success [31]. The use of an intercalation anode, however, does not prevent system failures. The thermal runaway can be triggered by any event that causes the overheating of the Li-ion battery, which includes internal short circuits (such as between current collectors, between positive and negative materials or between the current collectors and the electrode materials) [32], mechanical abuse (for example, after a car crash of induced by vibrations) [32], thermal abuse and overcharge [32]. Safety is essential for a battery, with the idea that, even if the battery fails, the user of the electric device is not harmed [29]. To determine the safety of a battery pack abuse tests are employed, simulating all the events causing overheating. The results are used to evaluate the safety of the energy storage system. One way is to determine the hazard level of a battery, based on

guidelines, such as those suggested by the European Council for Automotive Research and Development (EUCAR) [32,33]. Following these guidelines, a battery can be considered safe if, in case of electrolyte leakage (loss of at least 50% of electrolyte weight), there is no fire or flame [32]. Just by considering the high flammability of conventional organic electrolytes (practically considerable as fuel) [34,35], and that upon degradation most cathode materials tend to release oxygen (oxidizer) [29], this is not trivial, considering that all the reagents necessary for a combustion [36] are inside the battery pack. Since before the first lithium-ion battery was fabricated, researchers have proposed solutions to the severe safety issues that characterize this system. The underestimation of the risks, which caused accidents in the past, always backfired, resulting in the withdrawal of products, market losses and even ban on lithium-ion batteries [34].

1.2 Anode materials – Post-graphite

In this chapter, a general overview of materials for negative electrodes in lithium and lithium-ion batteries is given. The evolution that led to the realization of the first lithium-ion battery will be described, together with the fundamentals of carbon electrodes, with attention at the reaction mechanisms that allow this material to be still the negative electrode of choice for commercial devices. In the following sub-chapters, a general overview of few post-graphite, negative electrodes is also given, specifically alloy, conversion, and conversion/alloy materials. Key advantages and unresolved issues of these different materials will be discussed, while also explaining the fundamentals allowing the formulation of new material chemistries.

1.2.1 From lithium metal to graphite

The use of lithium metal as anode material generated a new class of electrochemical energy storage devices possessing unparalleled characteristic in terms of gravimetric and volumetric energy densities [37]. The electrochemical potential of the Li/Li^+ couple is -3.04 V vs SHE. By considering the dissociation reaction,

$$Li \rightarrow Li^+ + e^-$$

it is possible to calculate the specific capacity of lithium metal, equal to 3860 mAh g^{-1}, given its mass weight of 6.941 g mol^{-1}. The first studies on lithium batteries date back to 1912, by G.N. Lewis. It was not until 1958, however, that lithium metal would be found to passivate and therefore could be successfully electroplated in aprotic solvents [38]. The first lithium primary batteries became a commercial reality in the late 60s. All these batteries included lithium metal as the anode. Building rechargeable systems, however, proved to be more challenging. It was soon found out that, when lithium metal is used as the anode in a secondary cell, dendrites could grow at the metal surface upon plating (i.e., cell charge) (figure 1.2.1.1), resulting in serious safety issues [39].

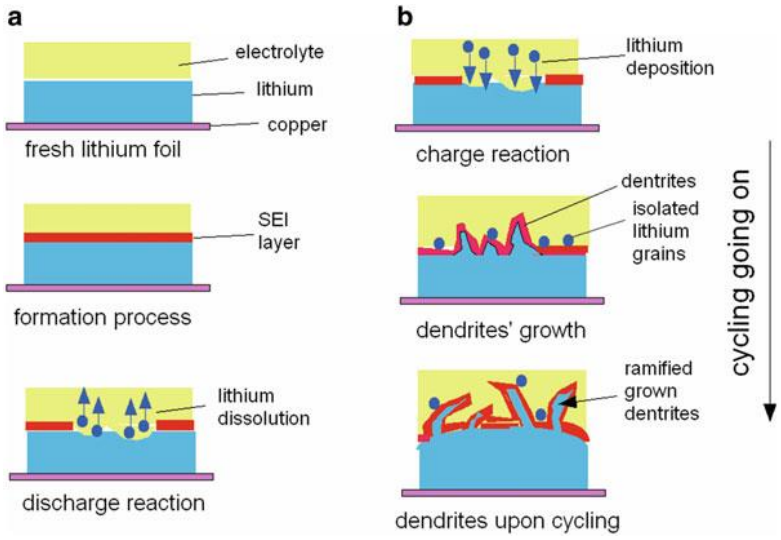

Figure 1.2.1.1 Lithium metal deposition mechanism (a) first cycle, formation of passivation layer (SEI) (b) dendrite formation and growth upon cycling [22]

The use of intercalation compounds as negative and positive electrode materials was first proposed by Armand in the 70s [19,30]. In the beginning, insertion oxides, such as WO_2, were studied as negative electrodes. However, it soon became clear that this class of materials was characterized by an average (dis-)/charge potential too high for real application, as the energy content of the resulting cell would be too low [30,31]. Carbonaceous materials were also investigated. Graphite did not seem feasible as electrode material in the beginning, mainly because the electrolytes employed at the time would result in solvent co-intercalation between the graphene layers, resulting in the irreversible degradation of the graphitic structure. Instead, polyacetylene was the first successful anode to be used as negative electrode for reversible lithium intercalation in a prototype commercial Li-ion cell, followed by hard carbons and eventually graphitized soft carbons, like vapor grown carbon fiber [40,41]. Hard carbons are a class of carbonaceous materials characterized by a sloped voltage profile, a high specific capacity of about 700 mAh g^{-1} but a relatively high average (dis-)/charge potential when compared to other carbonaceous materials [42]. The reaction mechanism involving lithium is still unclear and debated. Several models have been proposed [43], like the "house of cards" model [44], in figure 1.2.1.2, that involves the reversible adsorption of Li^+ on both faces of the graphene sheets.

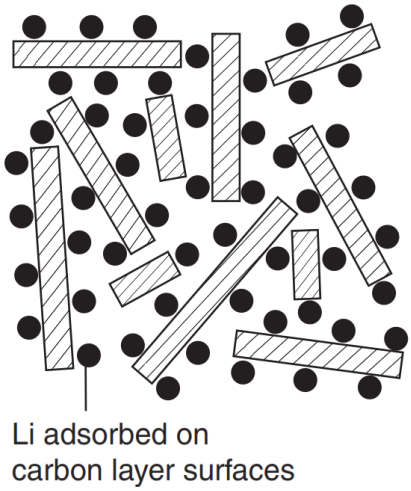

Figure 1.2.1.2 "House of cards" model for lithium-hard carbons reactivity [42]

A major improvement was allowed by the development of new electrolyte formulations. The reversible lithium intercalation inside graphitic carbons was found to be favored by the formation of a stable SEI on the carbon surface, avoiding electrolyte degradation and solvent co-intercalation. This allowed the use of other C-based anode materials, such as mesocarbon microbeads (MCMB), microcarbon fibers (MCF) and natural and synthetic graphites [45]. Lithium intercalation inside graphitic carbon is characterized by a step-wise, relatively flat voltage profile centered between 0.1 and 0.2 V, and is associated with a theoretical specific capacity of 372 mAh g^{-1} that can be calculated based on the following reaction:

$$C_6 + Li^+ + e^- \underset{\text{discharge}}{\overset{\text{charge}}{\rightleftharpoons}} LiC_6$$

Each voltage step in the graphite voltage profile is associated with a different stage, corresponding to a different arrangement of lithium inside the graphite structure. The mechanism is schematically presented in figure 1.2.1.3.

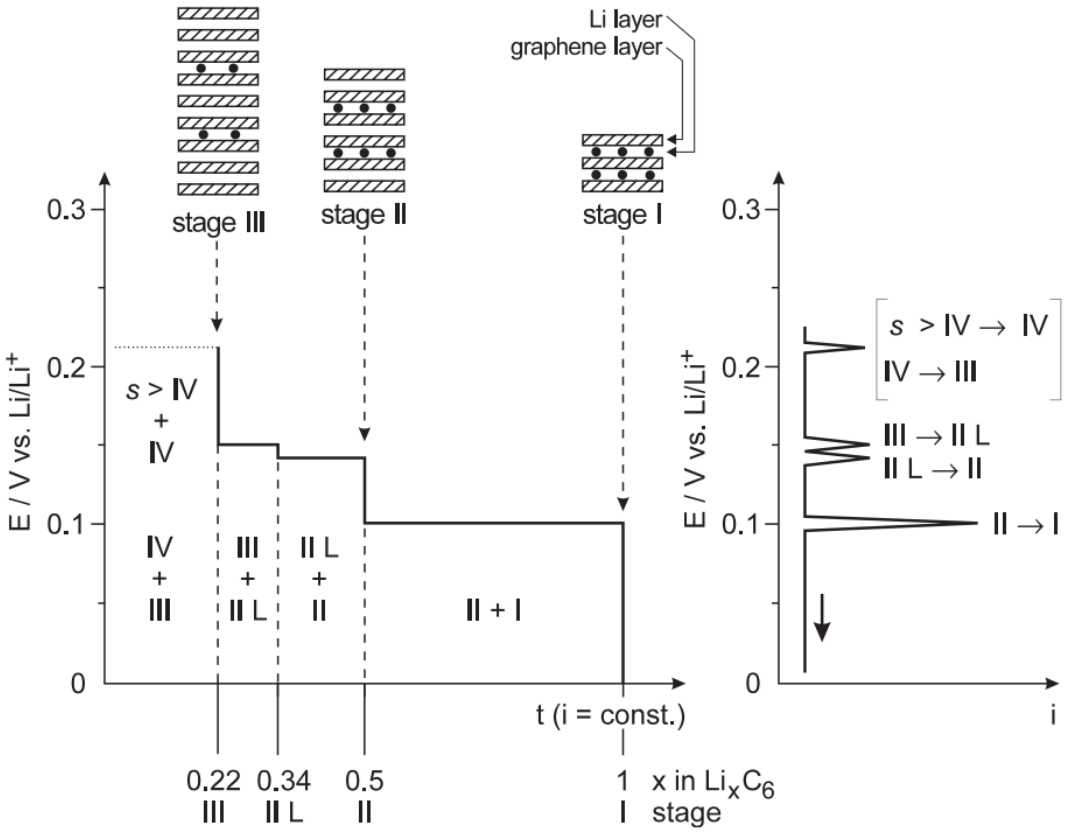

Figure 1.2.1.3 Staging mechanism for graphitic carbonaceous anodes. Left, schematic galvanostatic profile. Right, schematic voltammetric profile [46]

For many years graphite has been the material of choice to be employed as negative electrode for lithium-ion batteries, and still mostly is. Exceptions include new classes of material that have been successfully developed. Oxides, such as the $Li_4Ti_5O_{12}$ spinel (LTO), have been employed in commercial cells, thanks to their exceptional rate capabilities and safety of operation, this latter due to a relatively high average discharge potential, far from that of lithium which could result in lithium plating [31,45]. Lithium alloys also saw commercial application. Li-Al alloys were employed in high temperature, thermally activated lithium-FeS_2 batteries [47]. Similarly, the Sn-Co-C composite material, using the lithium-tin alloying process, was used as negative electrode for a cell commercialized by Sony in 2005 [37]. Also, the lithium-silicon alloy has recently received much attention, and it will probably be added to graphitic negative electrodes in the next generation of lithium batteries by Panasonic [30]. More recently, lithium metal was again proposed for possible application as negative electrode in lithium batteries. This is due to a better understanding of the

lithium/electrolyte interface, that can allow to dramatically reduce dendrite growth or to engineer materials which can effectively prevent dendrite penetration and short-circuit [48–50]. Other classes of materials include, for example, those that involve the lithium-conversion reaction with transition metal oxides. A general overview of the mechanisms of alloying and conversion anodes will be given in the next two chapters.

1.2.2 Alloys: Sn-C

Lithium alloys, for application in lithium batteries, were first investigated for thermally activated batteries, mainly because the high temperatures required to melt the electrolyte would also melt lithium. Li, alloyed with a metal, is much more thermally stable. For this reason, most of the early thermodynamics studies for these compounds were for high-temperature application [45]. For a full understanding of the compounds that can be formed, as well as of the potentials associated with the reactions, one should first take into consideration the phase diagrams of lithium-alloys and consider the (near-)/equilibrium states [45]. While a full description will not be given here as it is considered out of the scope of this thesis work, the reader should keep in mind that the electrochemistry of alloys is affected by the phases which can be formed at the (near-)/equilibrium. Potentials and reactions can vary greatly, depending on the temperature and the elements composing the alloy. For example, a binary system (such as Li-Al) can have very different characteristics from a ternary system (such as Li-Al-Sn) [45]. The reader should, therefore, consider that in this chapter mainly room temperature binary systems will be examined, with attention to two alloys, namely lithium-tin and lithium-silicon. An overview of the elements forming binary alloys with lithium is given in figure 1.2.2.1.

H																	He
Li	Be											B	C	N	O	F	Ne
Na	Mg											Al	Si	P	S	Cl	Ar
K	Ca		Sc	Ti	V	Cr	Mn	Fe	Co	Ni	Cu	Zn	Ga	Ge	As	Se	Br	Kr
Rb	Sr		Y	Zr	Nb	Mo	Tc	Ru	Rh	Pd	Ag	Cd	In	Sn	Sb	Te	I	Xe
Cs	Ba	La +	Lu	Hf	Ta	W	Re	Os	Ir	Pt	Au	Hg	Tl	Pb	Bi	Po	At	Rn
Fr	Ra	Ac +	Lr	Rf	Db	Sg	Bh	Hs	Mt	Ds	Rg	Cn	Uut	Fl	Uup	Lv	Uus	Uuo

Figure 1.2.2.1 Overview of elements which can form an alloy with lithium, marked in green (figure adapted from [51])

The lithiation of one of this elements is generally associated with high specific capacities (such as 3579 mAh g^{-1} for silicon), relatively low average (dis-)/charge voltages (V_{avg}) (however, high enough to avoid unwanted lithium electrodeposition, but low enough to ensure a high energy of the final lithium-ion cell, such as V_{avg} = 0.4 V for silicon), high 1st cycle irreversible capacity) which can be however mitigated with appropriate pre-lithiation strategies [52]), and a relatively huge volumetric expansions, up to 280% for silicon [51]. The latter is a serious drawback, that renders the use of alloys problematic, and is the key to understand why graphite is still the material of choice for negative electrodes, even though lithium alloys were employed and studied for many years before the discovery of reversible lithium intercalation in graphite. The first effect of the volume expansion is material degradation. Cycles of volume expansion/contraction induce mechanical stress in the particles, which can result in material disintegration and fast capacity fading (figure 1.2.2.2).

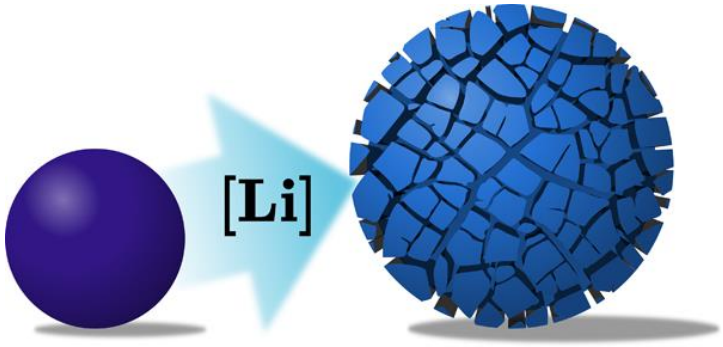

Figure 1.2.2.2 Effect of material expansion on a particle. Cracks and material loss can be observed. This is also the result of interaction between adjacent particles, which start to exercise a force on each other and can result in loss of electrical contact and electrode cracking/degradation [51,53].

This effect can be effectively minimized by preparing composite materials, such as carbon-coated materials, which can effectively buffer the volume expansion, thus preventing material degradation, and improve e^- conduction, as some materials are relatively poor electron conductors. Other strategies involve the use of additives/co-solvents, such as fluoroethylene carbonate (FEC) or vinylene carbonate (VC), which can create an elastic polymeric protective film and effectively buffer the volume changes. Other strategies involve the use of elastic binders, which can effectively reduce the stress accumulated in an electrode and eventually avoid material disintegration/loss of contact [45,51,53,54]. All these strategies, particularly when employed together in synergy, have shown exceptional improvements and allowed to reversibly (dis-)/charge silicon [55] and tin anodes for

thousands of cycles, with minimal capacity loss. The second effect of volume expansion/contraction, generally less taken into consideration, is the dramatic reduction of the volumetric capacity and volumetric energy density of this class of materials when lithiated. For a better understanding of this issue, figure 1.2.2.3 is presented.

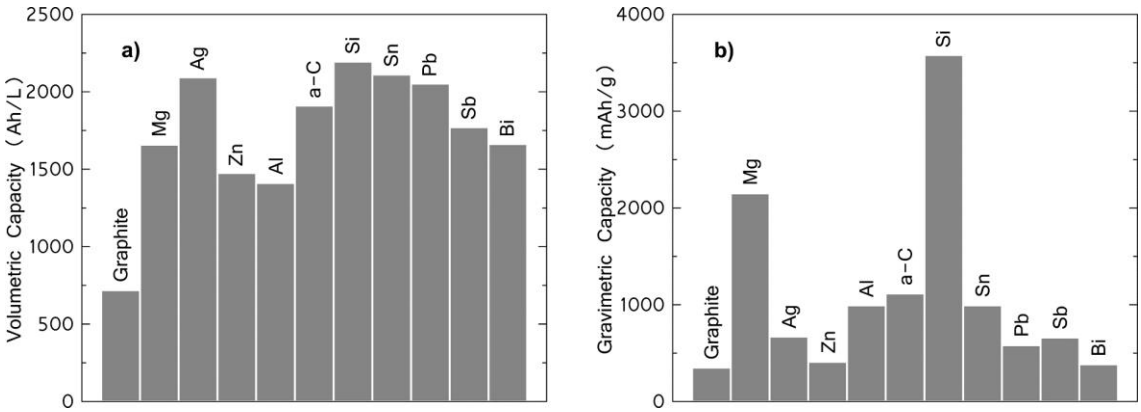

Figure 1.2.2.3 (a) Volumetric capacity at the lithiated state and (b) gravimetric capacity of selected alloy materials, with graphite as a comparison [51].

One should therefore always take into consideration these parameters for composite materials, and calculate specific capacity and energy values accordingly, to avoid overestimating advantages of a certain compound. One last fundamental point to understand is that upon (de-)/lithiation, both reversible and irreversible structural changes can be observed. The conventional redox reaction of lithium-silicon alloying, which is associated with a gravimetric specific capacity of 3579 mAh g^{-1}, is the following [51]:

1st lithiation:

$$\text{x-Si} \xrightarrow{+Li} \text{a-Li}_y\text{Si} \xrightarrow{+Li} \text{a-Li}_x\text{Si} \xrightarrow{+Li} \text{x-Li}_{15}\text{Si}_4$$

1st delithiation and subsequent cycling:

$$\text{x-Li}_{15}\text{Si}_4 \underset{+Li}{\overset{-Li}{\rightleftharpoons}} \text{a-Li}_z\text{Si} \underset{+Li}{\overset{-Li}{\rightleftharpoons}} \text{a-Si}$$

Where "x-" defines a crystalline phase and "a-" an amorphous phase. Some of these crystalline structures can co-exist during (de-)/lithiation, due to bi-phasic reaction mechanisms, and can contribute to internal mechanical stress in the material. Silicon as negative electrode, in any case, is still a viable option, in particular by considering that it is relatively low cost, environmentally friendly, non-toxic and its production and purification is very well developed, due to its use in the

semiconductor industry [56]. As previously mentioned, also tin had its share of commercial success, used as active alloy material in the Sn-Co-C composite. Tin, like silicon, can be considered non-toxic and environmentally friendly [54,57], peculiarities that suggest its application in green energy storage systems [58]. It can exchange up to 4.4 equivalents of lithium, up to a theoretical capacity of 990 mAh g^{-1}, and the alloying reaction consists of the following steps:

$$Sn \underset{+Li}{\overset{-Li}{\rightleftarrows}} Li_2Sn_5 \underset{+Li}{\overset{-Li}{\rightleftarrows}} LiSn \underset{+Li}{\overset{-Li}{\rightleftarrows}} Li_7Sn_3 \underset{+Li}{\overset{-Li}{\rightleftarrows}}$$
$$\underset{+Li}{\overset{-Li}{\rightleftarrows}} Li_5Sn_2^{*} \underset{+Li}{\overset{-Li}{\rightleftarrows}} Li_{13}Sn_5^{*} \underset{+Li}{\overset{-Li}{\rightleftarrows}} Li_7Sn_2^{*} \underset{+Li}{\overset{-Li}{\rightleftarrows}} Li_{17}Sn_4^{*}$$

In which * denotes a disordered phase [51]. A peculiarity of tin is that the spontaneously growing passivation layer (SnO_2) can be easily reduced upon lithiation, according to the following reaction, i.e., the conversion reaction of SnO_2 (another example of the phase changes that this class of materials can undergo):

$$SnO_2 + 4Li^+ + 4e^- \longrightarrow Sn + 2Li_2O$$

If the material is properly engineered, the resulting metallic tin can be reversibly cycled. More details on the fundamentals of conversion reaction will be given in the next chapter. In this work, a Sn-C nanocomposite material was employed as negative electrode material for a few applications. This material is synthesized using a conventional resorcinol formaldehyde synthesis procedure [59].

1.2.3 Conversion-alloys: $Zn_{0.9}Fe_{0.1}O_2$-C

Even though research on conversion materials dates back to the 80s [60,61], it was first believed that these reactions were only mildly reversible and would be detrimental to cell operation [62]. However, in 1997, the discovery by Idota et al. from Fujifilm of reversible tin oxide reactivity attracted great attention [63,64]. It was found that this reaction is highly reversible for nanoparticles and, soon after, conversion-based materials began being studied as negative electrodes for room temperature lithium-ion batteries [65]. The conversion-displacement reaction for transition metal oxides is the following:

$$MO+2Li^{+}+2e^{-} \rightleftharpoons M+Li_2O$$

With M being a 3d-metal, such as Mn, Fe, Co, Ni, Cu. During the first discharge, the crystalline structure of the material is lost, resulting in lattice amorphization. The product of this reaction can be described as a framework of metal nanoparticles dispersed in a Li_2O matrix [66]. The following charge results in lithium oxide decomposition and reversible formation of the transition metal oxide (figure 1.2.3.1).

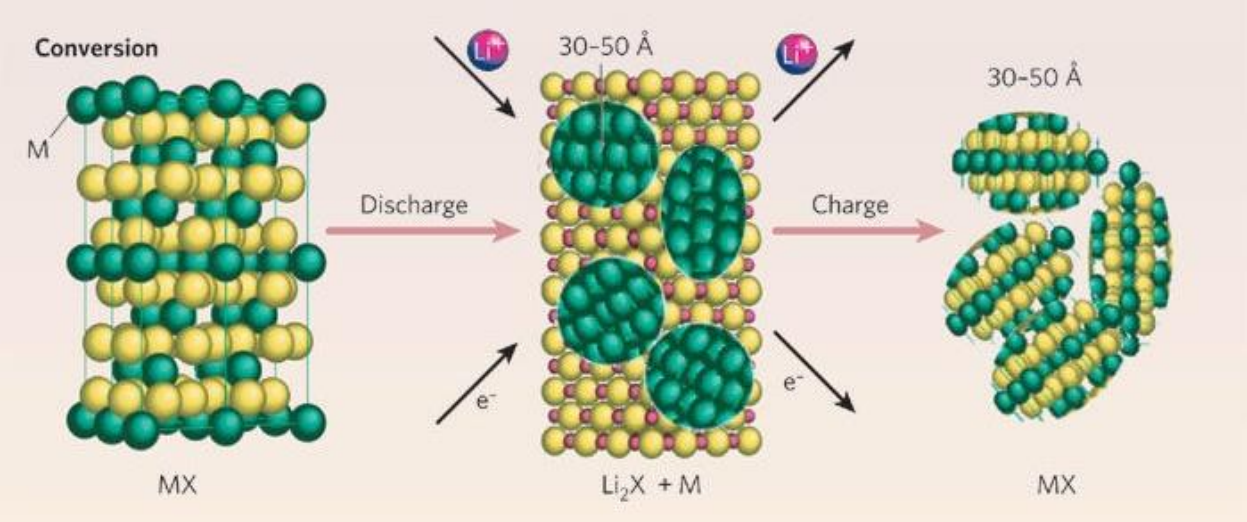

Figure 1.2.3.1 Conversion reaction (dis-)/charge mechanism [67]

The voltage profile is, usually, characterized by a plateau corresponding to the bi-phasic conversion reaction. The average voltage of this plateau depends on the transition metal(s) that are used (and, possibly, also on the anionic species. Conversion is not limited to oxide-based materials, as will be discussed in a following chapter [62]). Following this plateau, a sloping voltage region appears (at lower voltage values). This region often accounts for extra capacity with respect to the theoretical one and is mostly ascribed to either reversible electrolyte decomposition [68] or interfacial lithium storage in a capacitive-like behavior [69]. The conversion of metal oxides is associated with high capacities, typically of 1Ah g^{-1}, nearly three times that of graphite, but relatively higher average discharge potentials and larger voltage hysteresis between charge and discharge, leading to low energy efficiencies. Moreover, similarly to alloy materials, the reaction is associated with high volume changes and structural re-organizations that result in high inefficiencies during the first few cycles,

although the amorphous Li_2O formed can help releasing part of the mechanical stress [62]. During the years, several strategies have been proposed to solve these issues. One example is the synthesis of nanostructured materials which can buffer volume changes, such as hollows structured [70] or carbon coated materials, that also benefit from improved e^- conductivity and inter-particle contact [62]. The mitigation of the irreversible capacity is still an open topic, but several solutions have been proposed [52]. To reduce the average working potential, one strategy is to modify the M-O bond, by changing the species composing the active material. Another interesting strategy, which still holds much promise, is the use of an alloying-active material as the transition metal, such as Sn, Zn, Ru [71]. As discussed in the previous chapter, alloy-based materials are usually characterized by low (dis-)/charge potentials and high capacities, which would result in an additional electroactive element at the end of the conversion reaction, upon discharge. The alloy-active metal could benefit from the presence of the Li_2O matrix, which in principle can buffer the volume changes of the lithium alloy upon (de-)/lithiation [71]. Nevertheless, the use of this class of materials in commercial Li-ion batteries is still debated, due to low volumetric and gravimetric energy densities when compared to cells employing graphite anodes [72,73]. Nanostructured materials do successfully enable a few chemistries but also have severe drawbacks, like an increased catalytic decomposition of the electrolyte component [73]. Quoting Palacin et al., "nano does not always mean better" for electrochemical energy storage [73]. In this thesis, an alloying-conversion carbon coated anode is employed as an alternative negative electrode, namely $Zn_{0.9}Fe_{0.1}O_2$-C [74] (TMO-C). This anode composition benefits from an improved theoretical specific capacity of 990 mAh g^{-1}. Moreover, the synthesis involves the use of environmentally benign and low-cost materials, making TMO-C a promising green and sustainable material for the green grid.

1.3 Electrolytes - Safer alternatives

In this chapter the evolution of electrolytes is covered, starting from lithium primary batteries to the realization of the first lithium-ion commercial cells. A general overview will be given on the logic behind the choice of proper electrolyte components, as well as some of the limits for the various chemistries. The chemistry of electrolytes is very complex, in particular, that of the most modern ones employed in commercial cells, which include several, often undisclosed additives [45,75]. This aspect is out of the scope of this thesis and will not be discussed. Instead, an overview of two novel families of electrolytes, characterized by increased safety, namely ionic liquids and solid-state electrolytes, will be discussed more in-depth.

1.3.1 Conventional organic-based electrolytes

As previously mentioned, the role of the electrolyte in an electrochemical cell is to transport ions between the cathode and the anode and vice versa. Ideally, the electrolyte should be an inert component of the battery and only influence how fast the ions can diffuse between the electrodes [23]. Prior to discussion, it is imperative to understand the properties of an ideal electrolyte for a lithium battery. It should be a good ionic (Li^+) conductor, thus ensuring fast movement of ions, and an electronic insulator, avoiding self-discharge. It should be stable in a wide voltage range, i.e., have a wide electrochemical stability window including the redox reactions at the positive and negative electrodes (degradation and side reactions at the anode and the cathode are avoided). It should be inert to all cell components, including metal contacts, electrode materials and electrode additives, etc. It should be stable under abuse, so that it does not degrade under electrical, thermal and mechanical abuses, to ensure safety of the electrochemical device. It should be cheap, non-toxic and generally environmentally friendly [8,9,23]. Lithium, however, is extremely electropositive, with a potential of -3.04 V vs SHE, and it was not until the 50s that it could be studied as negative electrode for primary batteries, when it was found to be stable in aprotic solvents due to the formation of a stable film at the lithium/electrolyte interface [23]. Early commercial primary

batteries included a lithium metal anode and an electrolyte composed by an aprotic solvent, such as propylene carbonate (PC), dimethoxyethane (DME), tetrahydrofuran (THF), in which a lithium salt was dissolved, such as $LiClO_4$, $LiAsF_6$, $LiBF_4$ [24,76]. As previously mentioned, the transition to secondary batteries was very complex as it was soon found out that, upon battery charge, lithium electrodeposition results in the growth of dendrites. Dendrites can either become electrically isolated from the anode upon discharge (but still be present and extremely reactive, due to their high surface area) or penetrate the separator, grow and reach the cathode surface, generating an internal short-circuit causing unfortunate events, such as fire and eventually explosions [77]. It was therefore clear that the use of lithium metal poses a serious safety hazard and should have been replaced by different materials that could act as lithium ion hosts [10]. It was therefore necessary to find suitable electrolytes that would allow reversible reactions with a new generation of negative and positive electrodes. This required the formulation of new compositions, which would include appropriate aprotic solvents, a lithium salt and eventually additives. An appropriate solvent must meet a few criteria, namely, it should have a high dielectric constant to ensure high salt dissociation, and low viscosity to facilitate ion diffusion. It should be stable in contact with cell components, including the positive and the negative active materials, cell casing, contacts, etc., to avoid side reactions. It should be liquid in a wide temperature range, safe, non-toxic and cheap [23]. Similarly, also the choice of an appropriate lithium salt can be helped by the formulation of a few criteria. The salt should be completely dissolved in the solvent and the ions (Li^+ in particular) should have high mobility in the solution. The salt should also be stable against cell components, to avoid corrosion and other side reactions. The anion should be stable against oxidation, inert against the electrolyte solvent, thermally stable, non-toxic and cheap [23]. Historically, the first electrolyte employed for lithium electrodeposition was a solution of $LiClO_4$ in PC. PC, however, is characterized by a rather limited stability against lithium metal and cannot form a stable SEI on graphite [78], while $LiClO_4$ is unstable, both thermally and in contact with lithium metal and aluminum [79]. THF seemed also a promising candidate, but it was soon found to oxidize at 4.0 V on a platinum working electrode and, in contact with layered oxide cathode materials, the electrochemical stability window was even narrower, due to catalytic decomposition [23]. A major breakthrough was the finding, by Pistoia and Scrosati, that adding small amounts of PC (at least 9%) to ethylene carbonate (EC), solid at room temperature, would result in the formation of a melt [80]. EC was found to enhance the physicochemical properties of electrolyte solutions, such as a higher stability and conductivity, and to form a stable SEI on carbon anodes, differently from PC. Thanks to these properties, a mixture

of EC/PC was selected as the solvent used for the first generation of commercial lithium-ion batteries, which employed a coke-derived anode. Finally, in 1994, Tarascon and Guyomard described the use of dimethyl carbonate (DMC) as EC co-solvent [81,82], which is the basis of the current state-of-the-art electrolytes. The use of linear carbonates (such as DMC), mixed with EC, widens the electrochemical stability window of the electrolytes, bringing it up to 5 V, as they benefit from a synergic effect, while forming a stable SEI on the anode surface (see figure 1.3.1 and figure 1.3.2) [23].

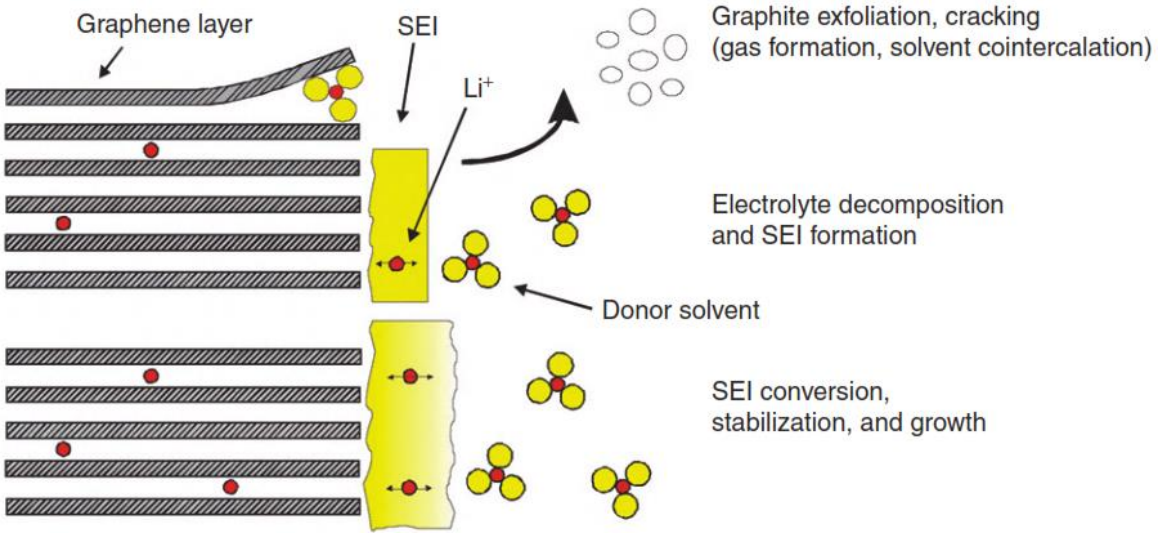

Figure 1.3.1 Top, co-intercalation of a solvent molecule, such as PC, and resulting graphite exfoliation, that destroys the pre-formed SEI. Bottom, consolidation of the SEI, resulting from more stable electrode/electrolyte interphase, without exfoliation [83].

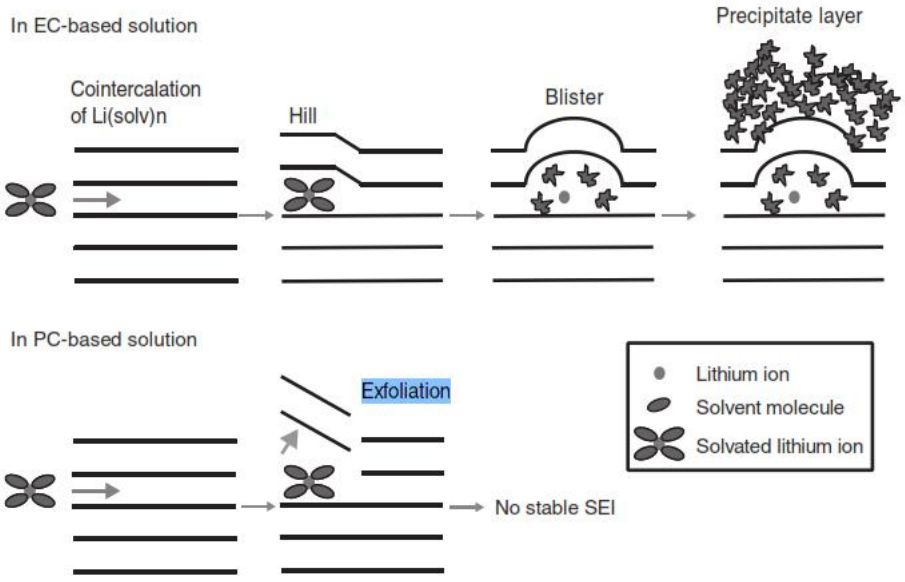

Figure 1.3.2 Top, EC effect on stabilizing the SEI. Bottom, PC-mediated graphite exfoliation [84]

The choice of a proper lithium salt was restricted to fewer compounds. As previously mentioned, $LiClO_4$ is generally considered not stable. $LiAsF_6$, even though being characterized by extremely good characteristics, such as high solubility, good SEI film forming abilities, high anodic and cathodic stability, is highly toxic. $LiBF_4$ results in a rather limited conductivity, due to its low dissociation constant. New compounds were proposed, such as lithium trifluoromethanesulfonate (LiTf) and lithium bis(trifluoromethanesulfonyl)imide (LiTFSI), but, at the time, their use was limited by the anodic dissolution of aluminum, which is commonly used as cathode current collector. The origin of aluminum corrosion is still debated today, as recent reports show that, for an electrolyte using an imide-based salt, it is due to halide impurities, rather than to the salt itself [85]. Also, in case of ionic liquid based electrolytes, aluminum corrosion is not observed when employing LiTFSI [86]. In the end, $LiPF_6$ was the salt selected for the first lithium-ion battery. Even though it does not excel in any of the characteristic possessed by the other candidates, it was the best compromise not being affected by any of their drawbacks [23]. The current generation of lithium-ion batteries still mostly employ $LiPF_6$ dissolved in mixtures of EC and linear carbonates. New electrolyte formulations are, however, actively searched. This is mainly due to the lower temperature limit of EC, which crystallizes at -20 °C even in a mixture and to the high temperature and safety limitations of $LiPF_6$, which can degrade at 50 °C to release PF_5, and/or HF in contact with water.

Moreover, as new cathode and anode materials are developed, new electrolyte compositions are required to achieve reversible cycling. It is the case of high voltage conventional cathode materials, for example, which require a wider electrochemical stability window. Also, beyond lithium-ion technologies, like lithium-air and lithium-sulfur, involve different reaction mechanisms and, thus, issues concerning those of conventional lithium-ion technologies. Similarly, the formulation of new high energy anode materials, such as the alloy-based, require the development of alternative formulation due to the different chemistry of the SEI and issues concerning graphitic carbons [86,87]. While some of these issues can be mitigated by using additives [88] in the electrolyte solution, which can improve the stability and safety of the battery, some of the limits of the solvents and the salts cannot be overcome. For this reason, alternative formulations, new compounds and new families of electrolytes are being actively developed and explored. This also includes polymer, liquid-gel, solid-state and ionic-liquid-based electrolytes [86,89–91].

1.3.2 Ionic liquids

During the last 20 years, ionic liquids [92]received much attention, reflected in an increasing amount of publications per year [93]. Many different molecules with very different properties belong to this category of materials [93]. They have been successfully applied as rocket propellants [94], flame retardants [95], lubricants [96], solvents [97], catalytic medias [98], just to name a few. Also, possible application in very diverse fields, from analytical chemistry to biology, medicine, and electrochemistry [99] have been already demonstrated. Room temperature ionic liquids (RTILs, i.e., molten salts at room temperature) are an appealing alternative to conventional electrolytes [100,101] for many diverse applications. It is important to note that in case of ionic-liquid-based electrolytes there is no solvent, as they are effectively mixtures of molten salts, resulting from the thermal disintegration of the salt lattice [23]. RTILs can be engineered by tuning their structure, e.g., changing either one or both the anion and cation [102], thus tailoring their properties to contemporarily meet various important needs such as high ionic conductivity, interfacial and electrochemical stabilities as well as thermal stability and low-flammability [91,103]. These features allow the realization of safer electrochemical storage devices such as super-capacitors [104–106], batteries [107–115] and solar cells [116]. Among the several RTILs developed for lithium-ion

batteries, imidazolium-based [117–120], piperidinium-based [121–124] and pyrrolidinium-based [125–130] electrolytes have demonstrated the best performance. Indeed, RTILs may be considered the solvents of choice for next-generation electrolytes for application in safe and more sustainable Li-ion batteries, although the widespread use in commercial application is still limited due to their relatively high cost [99]. This thesis work has been focused mainly on four mixtures of RTILs (namely, N-butyl-N-methylpyrrolidinium bis(trifluoromethanesulfonyl)imide (Pyr_{14}TFSI), *N*-butyl-*N*-methyl-pyrrolidinium bis(fluorosulfonyl)imide (Pyr_{14}FSI), N-methoxy-ethyl-N-methylpyrrolidinium bis(trifluoromethanesulfonyl)imide (Pyr_{12O1}TFSI) or N-N-diethyl-N-methyl-N-(2-methoxyethyl)ammonium bis(trifluoromethanesulfonyl)imide (DEMETFSI) [126–128,130]) with lithium bis(trifluoromethanesulfonyl)imide (LiTFSI), which have been comparatively evaluated for application as electrolytes in Li-ion batteries (see structural details in Fig. 1.3.2.1). The Pyr_{14}TFSI-based electrolyte is characterized by remarkable electrochemical stability in lithium cell and by suitable ionic conductivity [113,131,132]. However, the main issue of this excellent electrolyte is represented by its high viscosity, which limits the electrochemical performance at high currents and low to ambient temperatures. Pyr_{14}FSI, differing from Pyr_{14}TFSI by the anion structure (compare Fig. 1.3.2.1d and a), is indeed characterized by a lower viscosity, but at the expense of a higher, sometimes beneficial, chemical reactivity. Hence, electrolytes based on Pyr_{14}FSI show higher ionic conductivity and enhanced SEI film forming ability with respect to Pyr_{14}TFSI [126,133]. A recent study has shown that Li/$LiCoO_2$ battery employing FSI-based electrolyte is characterized by a greatly improved rate capability compared to TFSI-based one [134]. Besides the change of the anion in the electrolyte formulation, also the cation can be modified to obtain enhanced characteristics. The substitution in the alkyl side chain of Pyr_{14} of one carbon by oxygen leads to Pyr_{12O1} bearing an ether group granting higher bond flexibility bond of the side chain (Fig. 1.3.2.1b). In fact, the Pyr_{12O1}TFSI-based electrolyte has a lower viscosity and higher conductivity than the Pyr_{14}TFSI-based one [135]. Recent studies suggested suitable electrochemical performances in lithium battery of ILs formed by aliphatic quaternary ammonium cations, such as DEME (Fig. 1.3.2.1c) [136,137], even comparable to pyrrolidinium-based ILs [138].

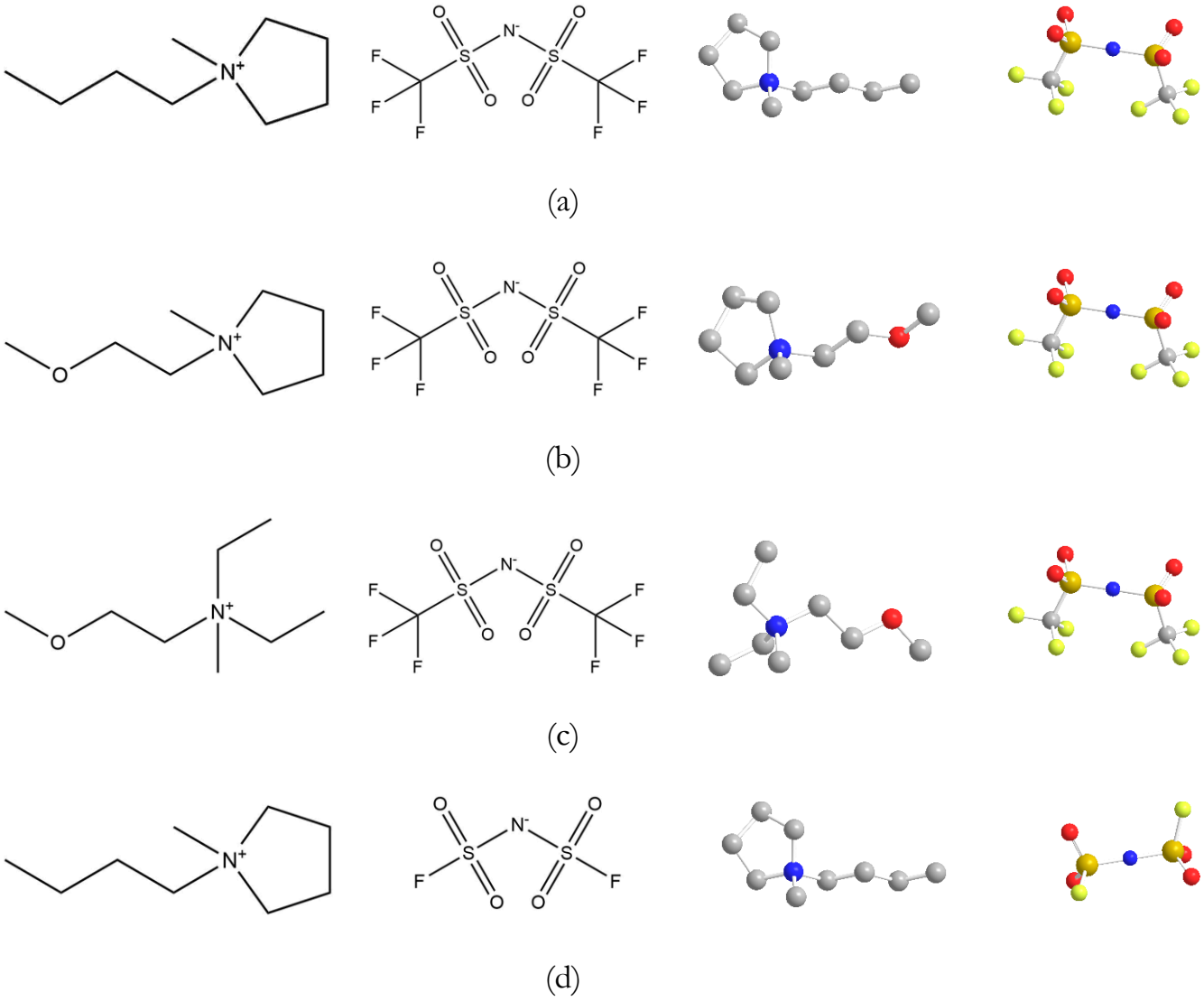

Figure 1.3.2.1 Graphical representation of the structures of the studied ionic liquids. a) N-butyl-N-methylpyrrolidinium bis(trifluoromethanesulfonyl)imide ($Pyr_{14}TFSI$), b) N-methoxy-ethyl-N-methylpyrrolidinium bis(trifluoromethane-sulfonyl)imide ($Pyr_{12O1}TFSI$) , c) N-N-diethyl-N-methyl-N-(2-methoxyethyl)ammonium bis(trifluoromethanesulfonyl)imide (DEMETFSI), d) *N*-butyl-*N*-methyl-pyrrolidinium bis(fluoro-sulfonyl)imide ($Pyr_{14}FSI$)

1.3.3 Solid state electrolytes

The replacement of the liquid-organic electrolyte with polymeric membranes [139–142] or inorganic solid-state lithium-ion conducting materials, such as those based on oxides [143] and sulfides [144–

148], may enhance the safety content of lithium batteries and further promote their large-scale diffusion. Inorganic solid-state electrolytes have attractive features for practical applications such as non-flammability, a rather wide electrochemical stability window, high ionic conductivity, comparable to that of liquid electrolyte (figure 1.3.3.1), as well as lithium transference number (t_{Li+}, that is the contribution of Li^+ to the overall ionic conductivity of the electrolyte solution) approaching the unity [23,149–151].

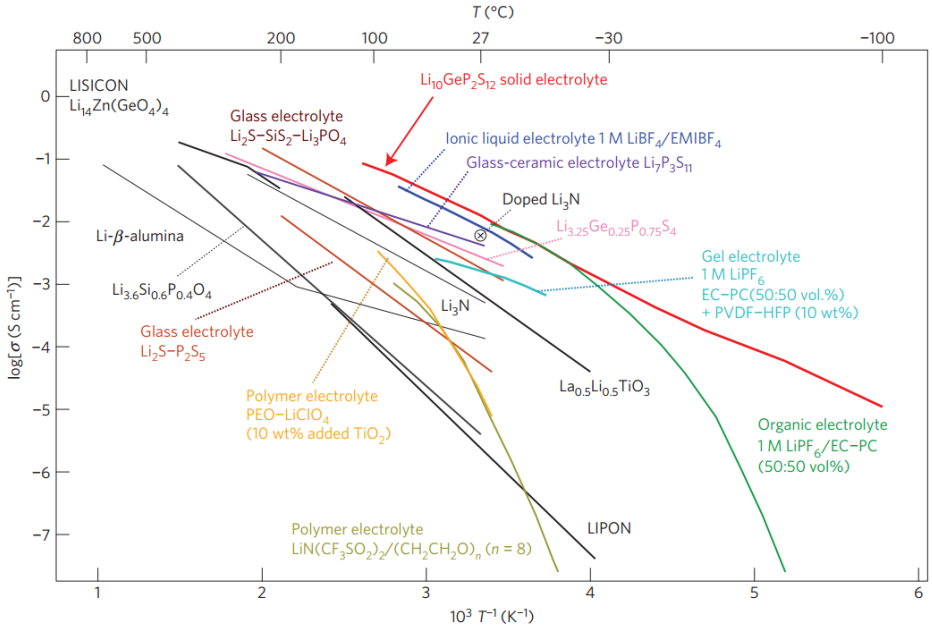

Figure 1.3.3.1 Conductivity Arrhenius plot of all-solid-state, polymer and gel electrolytes [152]

To understand the benefit originating from this last property (t_{Li+} = 1), one should consider the different ion conduction mechanisms. In conventional organic-based liquid electrolytes, cations (including solvated Li^+ ions) and anions both move in the solvent (Figure 1.3.3.2a). This results in several charged species moving at the same time, which translates into a lower amount of effective Li^+ charge transferred, i.e., the lithium transference number ranges between 0.2 and 0.5 [151]. In solid-state electrolytes (Figure 1.3.3.2b), Li^+ must migrate between stable sites through a higher energy environment. In good approximation, it can be considered as the only charged species able to move, meaning that the lithium transference number approaches the unit [151,153].

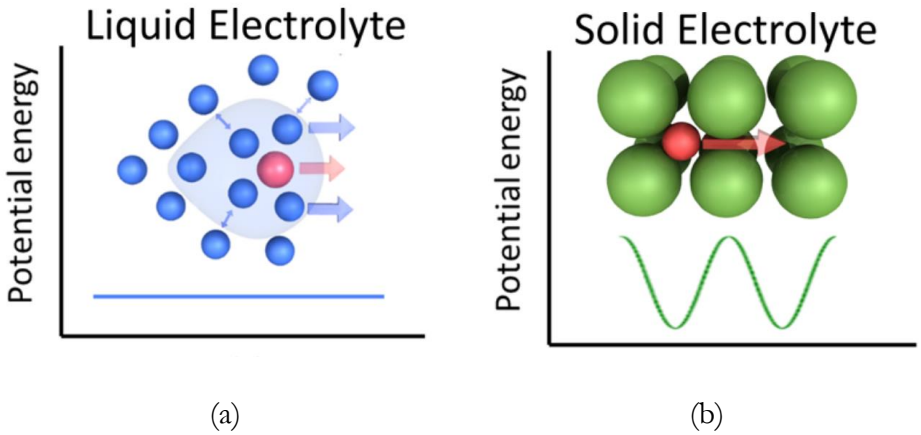

Figure 1.3.3.2 (a) Li^+ ion, in red, moving with solvating molecules in blue. Anions and negatively charged ion-triplets may, however, move in the other direction thus reducing the effective Li^+ cations transfer between the two electrodes. The potential energy of mobile lithium ions can be assumed as constant, considering a fast exchange between solvating/solvated species and a homogenous distribution of the species. (b) Li^+ ion, in red, moving between stable crystallographic sites. Lithium-ion has to overcome an energy barrier to move between energy minima, typically located at stable crystallographic sites [151].

Oxide-based solid-state electrolytes have been applied successfully with remarkable performance to conventional lithium-ion [154], lithium-air [155] and lithium-sulfur [156]. Oxide-based electrolytes with high Li^+ conduction are usually characterized by a high chemical reactivity with lithium metal, often requiring the use of a liquid organic electrolyte interlayer. The use of this class of electrolytes, moreover, requires a sintering procedure at high temperature to obtain a non-porous, mechanically stable membrane [89]. Sulfide-based glass-type electrolytes, such as Li_2S-P_2S_5, Li_2S-SiS_2 or $Li_{10}GeP_2S_{12}$ [152,157,158] and more recently oxysulfide-based electrolytes [159] have the additional advantages of being chemically stable in contact with lithium metal [145,160], chemically resistant to dry air, such as LiI-Li_4SnS_4 [161], and easily formed and pelletized by pressing [162] without additional sintering procedures at high temperature [89]. Finally, synthesis is relatively simple, and the highly ionic conductive phase can be stabilized by addition of inorganic compounds, e.g., Li_2SO_4, LiI [163]. Addition of lithium halogens is particularly beneficial in improving the ionic conductivity of sulfide-based inorganic conductors. The halide anions favor the formation of face-sharing tetrahedral sites. Tetrahedral sites are found to be the most energetically stable sites for Li. By having

a shared face, Li^+ cation movement is greatly favored, since the energy barrier to overcome is greatly lowered [153]. LiI-Li_3PS_4 (LPSI) [164] is a good example, with an ionic conductivity of about 10^{-3} S cm^{-1} at room temperature. Moreover, this class of solid electrolytes is often associated with the formation of a stable lithium-electrolyte interface, one of the main drawbacks of many inorganic lithium-ion conductors [165].

1.4 Cathode materials

In the next section, a general overview of the history of cathode materials, as well as current state of the art and beyond lithium-ion cathodes, is given. Most attention is dedicated to the materials that were part of this thesis work, namely, $LiFePO_4$ (LFP) and $LiCo_{1/3}Ni_{1/3}Mn_{1/3}O_2$ (NMC) for conventional lithium-ion cells, and oxygen and sulfur/metal sulfides for beyond lithium-ion cells.

1.4.1 History and state of the art cathode materials

Even though the first commercial lithium-ion battery was first placed on the market in 1991 by Sony (thanks to the great efforts of Yoshino et al. from Asahi Kasei [40]) using $LiCoO_2$ as cathode material, many before that were proposed [30]. The first working prototype of a lithium-ion cell is attributed to Scrosati and Lazzari [20], for which TiS_2 was used as cathode material. This material was seen, in the early age of lithium batteries technology development, i.e., in the 70s, as the best candidate for positive electrodes together with several other metal sulfides [31]. To fully understand why these sulfide-based cathode materials were so promising, one should first understand the properties of an ideal cathode in a rechargeable lithium battery, which were very well summarized in 2004 by M.S. Whittingham [166]. Briefly, the material should contain a readily reducible/oxidable ion, such as a transition metal. The reaction must be reversible. The reaction with lithium should be fully reversible and associated with fast kinetics and a highly negative energy ($\Delta G << 0$). The material should be a good electronic conductor, stable and not degrade in non-ideal conditions, such as upon over(-charge)/-discharge. Finally, the ideal cathode material should be low cost and environmentally benign [166]. Theoretically, TiS_2 can reversibly intercalate up to 1 equivalent of lithium:

$$xLi + TiS_2 \underset{\text{charge}}{\overset{\text{discharge}}{\rightleftharpoons}} Li_xTiS_2$$

This reaction is associated with a theoretical voltage of ca. 2.5 V [31], high reversibility and a single-phase transition, in which the lithium ions reversibly insert, or more specifically intercalate, between the TiS_2 layers, as shown in figure 1.4.1.1.

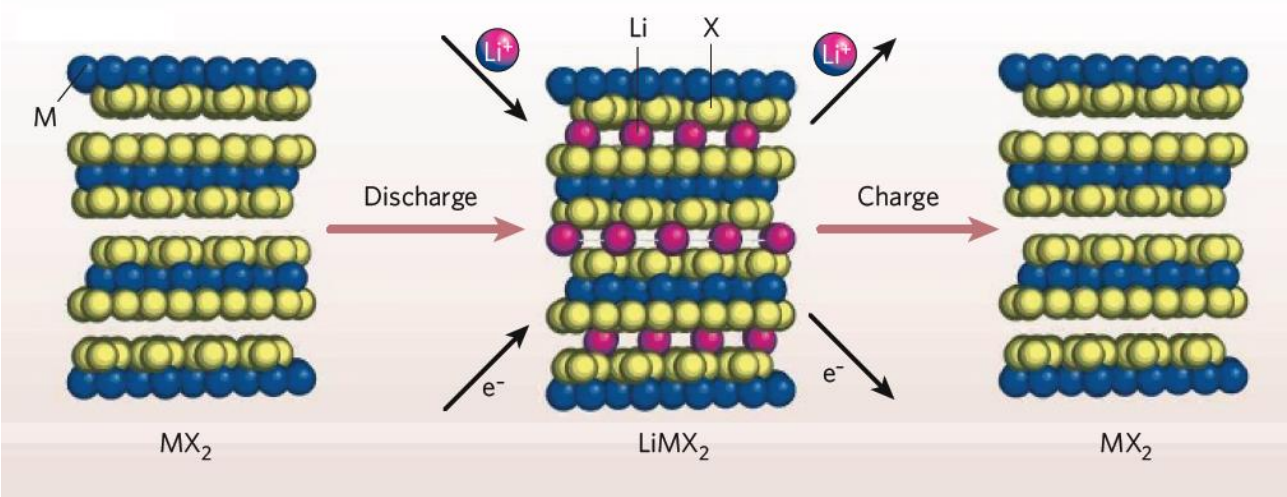

Figure 1.4.1.1 Intercalation mechanism in layered structured metal oxides/sulfides [67]

Moreover, TiS_2 has a relatively high e^- conductivity, and it is rather environmentally benign. Indeed, during the late 70s, Exxon first proposed Li/TiS_2 cells and later commercialized $LiAl/TiS_2$ [167] batteries [31]. These configurations, however, had several limitations. Battery operation, for example, required the use of a perchlorate-based electrolyte and, for the Li/TiS_2, included lithium metal as the anode, thus posing severe safety issues.

Later, a breakthrough came from Goodenough by using lithium transition metal oxides (such as $LiCoO_2$)as the positive material [168]. The layer stacking of this material is similar to that of other dichalcogenides, such as TiS_2, and lithium intercalates between the CoO_2 layers.

$$xLi + Li_{1-x}CoO_2 \underset{\text{charge}}{\overset{\text{discharge}}{\rightleftharpoons}} LiCoO_2, \quad (x \leq 0.4)$$

Upon extensive de-lithiation, however, Li_xCoO_2 undergoes structural changes leading to CoO_2 which is electrochemically inactive as cathode material. This implies that only a certain amount of lithium can be removed from the structure before the material becomes electrochemically inactive, i.e., the full reversibility can be attained only for values in the range of $0 \leq x \leq 0.4$. Within this limit,

however, the lithium insertion in this material is very reversible and characterized by a capacity of about 140 mAh g^{-1} and an average (dis-)/charge voltage of about 4.1 V [9], resulting in an energy content much higher than that of dichalcogenides [166,169]. Moreover, this material is much more stable against water and oxygen, particularly because it is synthesized in the discharged (lithiated) state. An additional benefit of the presence of lithium in the as-synthesized materials is that metallic lithium is not required at the negative electrode [31]. These advantages made it the perfect candidate to be employed as the positive material for LIBs. During the years, many other lithium-containing layered oxide materials were studied, trying to reduce or avoid the use of cobalt, which is expensive and toxic. Much effort was made to find more environmentally friendly alternative materials with higher energy content. $LiNiO_2$, a $LiCoO_2$ isostructural, was a promising alternative [170]. Whereas by tuning the synthesis condition it was possible to solve some of the limitations of this material (Li-Ni cationic disorder, formation of defective phase clusters, such as NiO) and achieve capacities as high as 200 mAh g^{-1} [171], this material is characterized by a very limited thermal stability (only up to 200 °C) [77,172]. Moreover, in the delithiated state, $Li_{1-x}NiO_2$ is thermodynamically unstable and can release oxygen, which poses a serious safety risk. Another promising isostructural of $LiCoO_2$ was $LiMnO_2$. Even though manganese is non-toxic and cost-effective, the layered phase is not stable. Indeed, at temperatures higher than 400 °C the spinel phase $LiMn_2O_4$ and the monoclinic phase Li_2MnO_3 are favored. The spinel phase is another promising alternative [173], but its application is still mostly limited by irreversible phase transitions due to manganese dissolution in the electrolyte. On the other hand, the monoclinic phase, if used as is, has a very limited electrochemical activity [174]. The main issue of the layered lithium manganese oxide lies in its structural instability. Upon prolonged cycling, $LiMnO_2$ undergoes a phase transition into the thermodynamically more stable spinel phase. This implies a changing working potential, as well as a progressive capacity fading and reduced electrochemical activity due to manganese dissolution from the spinel phase into the electrolyte [173,174]. One of the proposed solutions to the issues of these layered analogs is the synthesis of layered mixed metal oxides as positive materials [175]. Of special interest is the ternary system including nickel, manganese, and cobalt. A triangular phase diagram is proposed in figure 1.4.1.2 as an aid in the description of this rather big family of compounds.

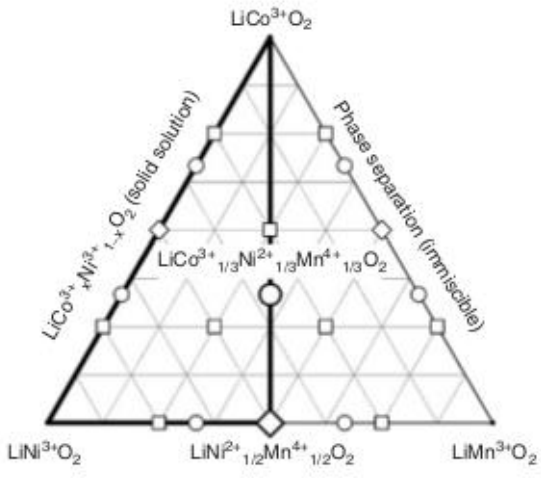

Fig.1.4.1.2 Triangular phase diagram, $LiNiO_2$-$LiMnO_2$-$LiCoO_2$ [176]

As evidenced by the phase diagram, $LiCoO_2$ e $LiMnO_2$ are immiscible, i.e., do not form a homogeneous phase that could help stabilize the final mixed material. $LiCoO_2$ and $LiNiO_2$ give a solid solution, which can reversibly cycle up to 4.3 V with a reversible capacity up to 175 mAh/g. The further development of this binary system eventually led to the addition of aluminum, which was found to substantially improve the safety of the material plagued by a very limited thermal and structural stability in the charged state. The resulting ternary system rich in nickel, that is $LiNi_{0.8}Co_{0.15}Al_{0.05}O_2$ (NCA), is currently used in commercial cells by SAFT and Panasonic for high energy and high power systems, such as EVs [30]. $LiMnO_2$ and $LiNiO_2$ [177] form a stable compound if the ratio between the two transition metals is 1:1. This is not a solid solution, but rather a whole new compound in which Ni has an oxidation state of +2 and Mn is characterized by an oxidation state of +4 [178,179]. The material is characterized by a high practical specific capacity of about 180-200 mAh g^{-1}. The limitation of this material is the need of the Mn:Ni ratio to be strictly 1:1, otherwise defective phases rich in electrochemically inactive Li_2MnO_3 domains form. See figure 1.4.1.3 for a better understanding of the crystalline structure [180].

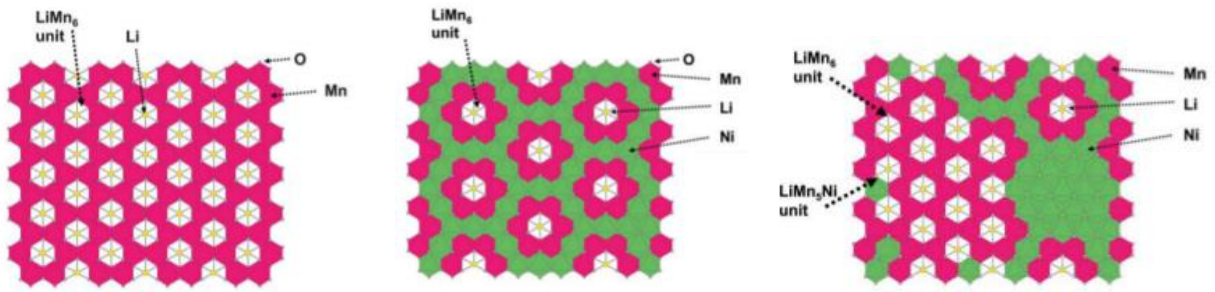

Fig.1.4.1.3 From left to right, transition metal layer of Li_2MnO_3, $LiNi_{1/2}Mn_{1/2}O_2$, $Li_{1+x}(Ni1_{/2}Mn_{1/2})_{1-x}O_2$ defective phase [180]

Research on this system eventually led to the formulation by T. Ohzuku and Y. Nakimura in 2001 of a ternary system including cobalt, which was believed to be able to stabilize the structure [181]. $LiCo_{1/3}Ni_{1/3}Mn_{1/3}O_2$ (NMC) was another breakthrough and was soon integrated into commercial batteries, in particular for consumer electronics and EVs [30,31]. Cobalt reduces the amount of defective nickel in the lithium layer (Li-Ni cationic disorder) while manganese ensures higher structural stability, even if defects are present (see figure 1.4.1.4).

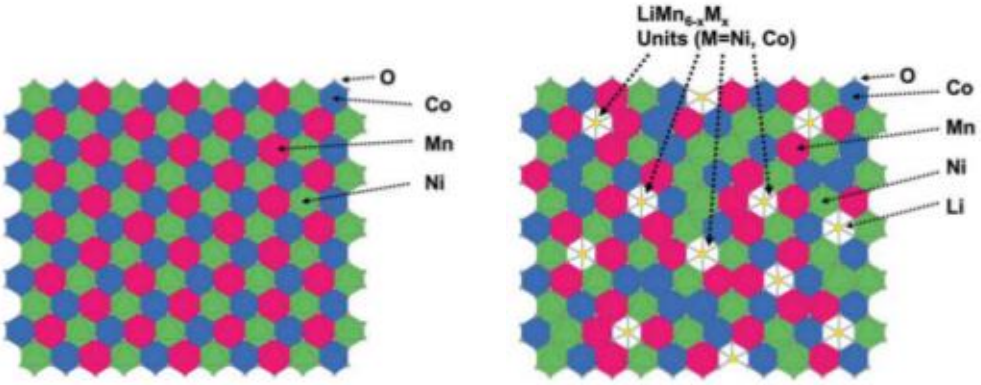

Fig.1.4.1.3 From left to right, transition metal layer of $LiNi_{1/3}Co_{1/3}Mn_{1/3}O_2$, $Li_{1+x(}Ni_{1/3}Co_{1/3}Mn_{1/3})_{1-x}O_2$ defective phase. Li_2MnO_3 formation is not observed [180]

In this material, Ni has an oxidation state of +2, Co of +3 and Mn of +4, while the crystal structure is analog to that of $LiCoO_2$. The reversible redox reaction is the following:

$$xLi + Li_{1-x}Ni_{1/3}Co_{1/3}Mn_{1/3}O_2 \underset{\text{charge}}{\overset{\text{discharge}}{\rightleftharpoons}} LiNi_{1/3}Co_{1/3}Mn_{1/3}O_2, (x \leq 0.6\text{-}0.7)$$

With nickel oxidizing, upon charge, from Ni^{2+} to Ni^{4+}, for $0 \leq x \leq 0.67$ (lower potentials) and cobalt oxidizing from Co^{3+} to Co^{4+}, for $0.67 \leq x \leq 1$ (higher potentials) [182,183]. This material is characterized by a sloped voltage profile, with an average discharge potential of about 4.0 V, a practical specific capacity of about 160 mAh g^{-1} and high thermal stability, over 350 °C, among several other advantages [166]. Research on this promising ternary system is far from being concluded. New frontiers include Li-rich, (Li/Mn)-rich and Ni-rich NMCs, which are proposed for the next generation of lithium batteries for EVs [5,169]. Another successful family of cathode materials is represented by olivine-structured materials, in particular, $LiFePO_4$ (LFP) [184]. This material is characterized by an average discharge potential of about 3.5 V and practical specific capacity of about 170 mAh g^{-1}. It can (dis-)/charge at high currents if properly synthesized and is relatively cheap and environmentally benign if compared to $LiCoO_2$ and analog materials. The crystalline structure, reported in figure 1.4.1.4, as well as the reaction mechanism of lithium (de-)/insertion, differs much from that of the layered structured materials [185].

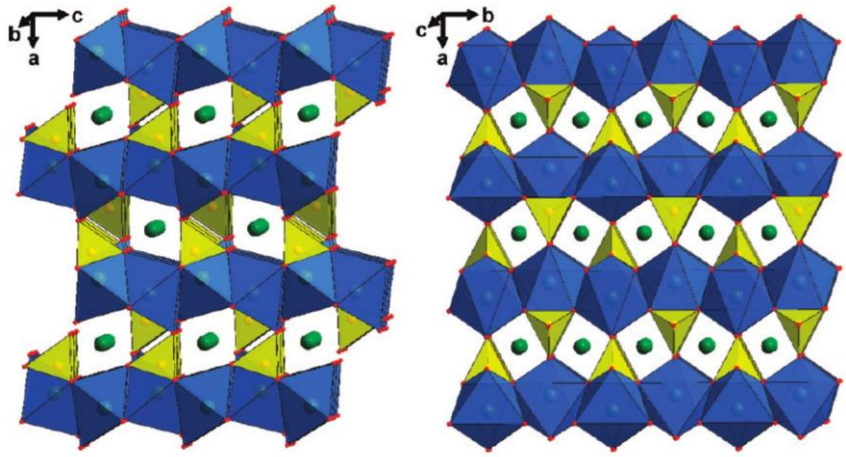

Fig.1.4.1.3 $LiFePO_4$ olivine structure. Iron octahedra in blue, phosphate tetrahedral in yellow, lithium ions in green. [185]

Upon charge, the material undergoes a bi-phasic change, characterized by a very flat discharge potential. The second phase is orthorhombic $FePO_4$, which is characterized by the same space group as $LiFePO_4$. This phase change begins at the surface of the material particle and soon becomes limited by lithium diffusion inside the particle. Moreover, depending on the material crystal size, a

sloped voltage profile can be observed at the beginning and the end of the lithiation process. This corresponds to a solid solution insertion mechanism related to the single phases of $Li_{1-x}FePO_4$ and Li_xFePO_4 for values of $x \approx 0$ and is most evident in nanometric materials. [185,186] Some of the drawbacks of this material include a limited e^- conductivity, that is addressed by preparing composite materials, such as carbon-coated LFP, and a lithium (de-)/insertion controlled by Li^+ diffusivity, dominated by one-dimensional movement of Li^+ ions along the [010] channels, requiring the synthesis of materials with a preferential (010) face orientation. LFP is also characterized by a relatively low energy content when compared to other positive materials and, to improve this aspect, much research is directed toward the partial substitution of iron with other transition metals, such as cobalt or manganese [166,169,185–187]. LFP, in any case, is successfully employed in commercial cells, in particular for high power applications such as power tools [30]. The last important family of cathode materials is that of spinels, such as the previously mentioned $LiMn_2O_4$ (LMO), which also saw real application for high power application [174]. Many other class of materials, of course, have been proposed during the years, such as vanadium oxides, iron phosphorous sulfides, etc. Among the several alternatives for next generation lithium-ion batteries, those based on conversion reactions hold much promise.

1.4.2 Conversion reactions

The current generation of commercial batteries involves the use of insertion cathode materials, as previously discussed. Thanks to joint research efforts from academia and industry, LIBs are on a good path to utilize the theoretical gravimetric energy densities of current generation insertion cathodes, of about 650-750 Wh kg^{-1} [5]. This is considered by car makers, however, as the minimum critical target to be reached for cathode materials [5], to ensure widespread distribution of zero-emission [4] full electric vehicles [5–7]. For this purpose, alternative chemistries, in particular those involving conversion reactions [4,5], are widely studied, since they hold much promise from the theoretical point of view. It is in this category that we find cathode materials with substantially improved energy densities [10]. An overview of two different, promising systems is given in the next paragraphs, namely Li/O_2 and Li/S. Both these chemistries are characterized by safe, non-toxic and cheap materials, offering theoretical gravimetric energy densities of 3458 Wh kg^{-1} and 2510 Wh kg^{-1},

for Li/O_2 and Li/S respectively, thus holding much promise for beyond lithium-ion battery technologies [188].

1.4.2.1 Sulfur and metal sulfides

To improve the energy density of lithium-ion batteries [10] alternative chemistries are required. Among possible choices, those that involve the sulfur conversion reaction at the positive electrode are considered one of the most promising for the next generation of lithium-ion batteries [87]. Furthermore, sulfur is the 15th most abundant element in earth's crust. Being also non-toxic and environmentally benign, it is of a rather low-cost when compared with the present cathode materials employing transition metal oxides based on nickel and cobalt [189–191]. In fact, the use of sulfur as active material has already seen real application in stationary storage, being employed in high-temperature, Na-S batteries [192]. The conversion reaction of sulfur with lithium, $S+2Li \rightleftharpoons Li_2S$, is associated with a theoretical specific capacity of 1672 mAh g^{-1} and an average discharge voltage of 2.15 V, translating in a gravimetric energy density up to 2510 Wh kg^{-1} [87,193], This value is three to five times higher than that of cathodes employed in the current generation of lithium-ion batteries [5]. Unfortunately, its practical application is still hindered by a few issues that effectively limit both the practical energy density and the cycle life of lithium-sulfur batteries [193]. Several of these technical challenges relate to the conversion reaction mechanism of sulfur, pictured in figure 1.4.2.1.1a. The most stable allotrope of sulfur at 25 °C is orthorhombic, cyclic α-S_8. Upon reduction, the octahedral ring will open, with the formation of several high- and low-order polysulfides [193,194], finally leading to the formation of lithium disulfide. An ideal voltage profile relative to this reaction using conventional ether-based electrolytes [86], presented in figure 1.4.2.1.1b, is generally characterized by two main plateaus (the exact discharge process is much more complex and highly dependent on the electrolyte formulation [194,195]).

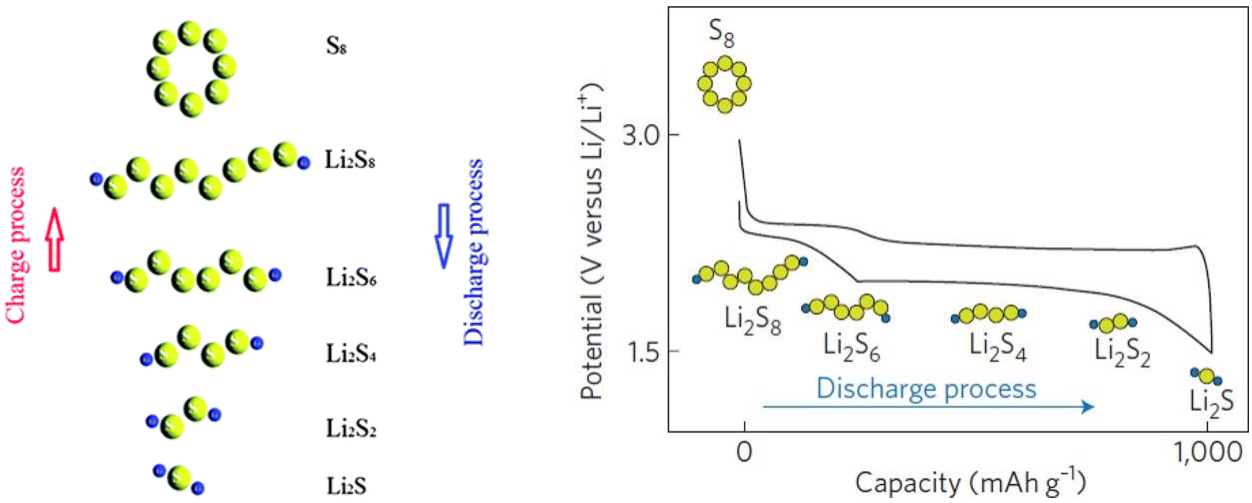

Figure 1.4.2.1.1 (a) Electrochemical process of a lithium-sulfur cell, (b) associated voltage profile [87,193]

Polysulfides are highly soluble in conventional liquid electrolytes. They tend to shuttle between the anode and the cathode upon cycling, resulting in high self-discharges and positive and negative electrodes degradation, due to both the active material dissolution and the reactivity of the intermediate polysulfides [193]. The issue is schematically pictured in figure 1.4.2.1.2a. The situation is aggravated by a high volumetric expansion/contraction upon cycling (figure 1.4.2.1.2b) of about 80% [193], which facilitates polysulfide dissolution as well as causes major structural and morphological changes, which can then result in loss of contact and fast battery performance degradation.

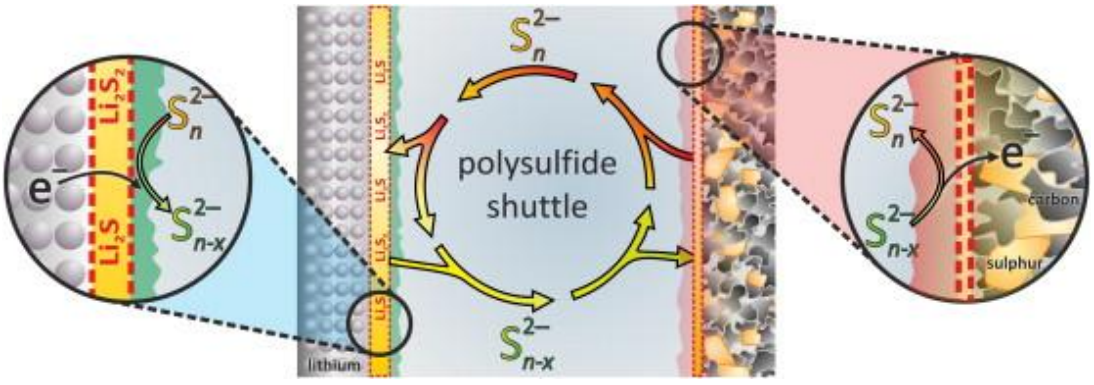

(a)

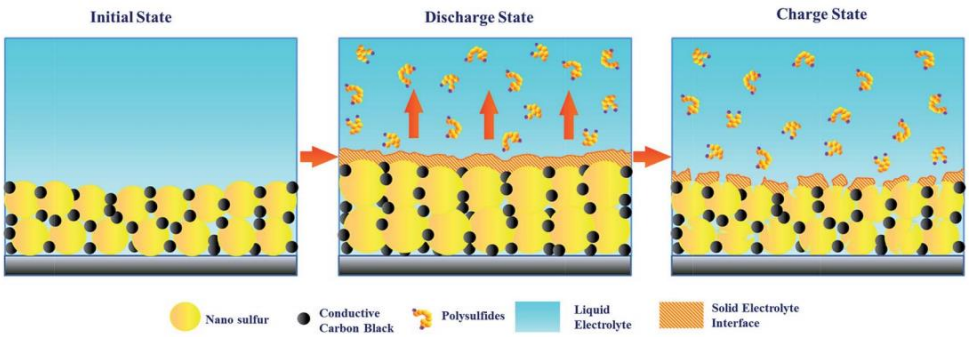

(b)

Figure 1.4.2.1.2 (a) Parasitic polysulfide shuttle effect in conventional liquid electrolytes. High order polysulfides diffuse to the negative electrode, corroding the anode and reducing to low order polysulfides, which migrate to the positive electrode and get oxidized back to high order polysulfides [196] (b) The breakdown-reconstruction of a passivation layer on the cathode, caused by huge volume changes connected with the sulfur conversion reaction, accelerates the dissolution of polysulfides in the liquid electrolyte [195]

Finally, sulfur, lithium disulfide and all reaction intermediates are characterized by a very low e^- conductivity [193]. In the past years, several strategies have been developed to address the abovementioned issues. Some involve the use of composite cathode materials, e.g., sulfur-carbon [197] (with particular attention at functionalized carbon [198]), sulfur-transition metal oxides [199], sulfur metal sulfides [200], sulfur-graphene [201], sulfur-polymer [202], etc. Composites benefit from increased e^- conductivity, lower polysulfide dissolution due to trapping effects, volume expansion/contraction buffering, and a more stable electrode/electrolyte interface, while the additional compounds may participate in the redox reaction as active materials [193,203,204]. Electrolyte additives [205], polysulfide-saturated [206] or solvent-in-salt [207] solutions have also shown promising results in reducing anode materials degradation and improving the reaction kinetics while reducing the polysulfide dissolution. Polymeric [208] and gel electrolytes [209,210], also in hybrid systems using ceramic interlayers [211,212], have been proposed to cope with the abovementioned issues. However, all solid-state devices [213,214] employing sulfide-based electrolytes, offer several advantages [164,215,216]. Apart from the typical benefits of sulfide-based electrolytes, which are added safety and formation of a stable lithium/solid electrolyte interphase [215], all-solid-state cells can effectively prevent polysulfide dissolution and, consequently, their shuttling, thus ensuring high performance over hundreds of cycles [164,217,218]. It should be noted

that the (dis-)/charge mechanism of all-solid-state lithium-sulfur batteries is radically different from that observed in most of the conventional, liquid electrolyte-based ones. In fact, the voltage profiles are generally characterized by a single pseudo-plateau, corresponding to the direct conversion of sulfur to form lithium disulfide [219,220]. Still, given the generally low electron conductivity and the large volume expansion associated with the conversion reaction, composite materials are required to achieve good performance and long cycle life. Carbon matrixes [221], and more recently transition metal sulfides [204] (which are known to have a positive effect on liquid electrolyte-based systems [203]) seem to positively affect the conversion reaction taking place in all-solid-state cells [222]. These reactions can also involve the reversible oxidation/reduction of the solid electrolyte (as in the case of sulfide glasses), which is added to the cathode composite to ensure adequate ionic conductivity [154]. However, the sulfide glass becomes electrochemically active when intimately mixed with carbon [164,223]. Transition metal sulfides are also electrochemically active in a similar voltage range of sulfur [203,204]. The conventional redox reactions between transition metal sulfides and lithium (MS_2 or MS, with M = Fe, Mo, Co, Ti, …) usually involve insertion and/or conversion reactions [204], depending on the transition metal and the sulfide crystalline structure. Their use in the battery field is by no mean a novelty [31,166]. However, thanks to recent advances in material science and nano-engineering [204], as well as in the understanding of the issues associated with sulfur/polysulfide conversion, these materials are nowadays being revisited as viable alternative cathodes. It is now known that in conventional liquid systems they can show an anchoring/trapping effect on lithium polysulfides [203], thus effectively mediating sulfur conversion to lithium disulfide. However, their effect on all-solid-state lithium-sulfur batteries is still not fully understood nor widely studied and, therefore, prompts further investigation and research.

1.4.2.2 Oxygen

Non-aqueous lithium-oxygen batteries [224], involving the reversible electrochemical reaction of lithium with oxygen to form lithium peroxide, are characterized by a high theoretical gravimetric energy density [225], i.e., 3458 Wh kg^{-1}, which largely exceeds the maximum value of 750 Wh kg^{-1} associated with the current generation commercial cathodes [5]. However, Li/O_2 batteries (Figure 1.4.2.2.1) are still far from practical application, due to issues limiting the reversibility of the

electrochemical process and the practical energy density of the battery [225,226]. The most severe issues are related to parasitic side reactions that occur during both the oxygen reduction reaction (ORR, discharge) and the oxygen evolution reaction (OER, charge) [227].

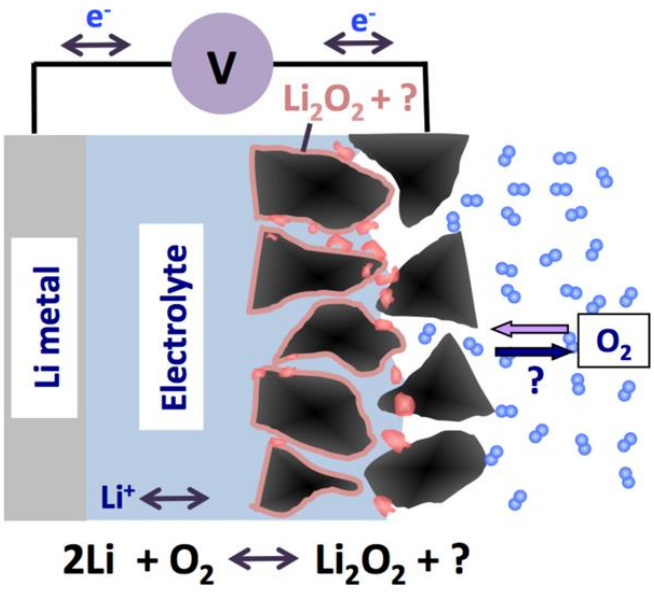

Figure 1.4.2.2.1 Schematic representation of a Li-O_2 battery. Side reactions can form unwanted products, leading to limited cycling life [225].

These undesired reactions are mainly ascribed to the degradation of the organic electrolyte and the composite acting as the positive electrode, conventionally consisting of a high surface area carbon and a polymeric binder [228–231]. Thus, besides the conventional, organic carbonate-based electrolytes, which are known to undergo severe degradation upon ORR and subsequent OER [230,232], several other electrolytes have been proposed with promising performance, such as polymers [224,233], lithium superionic conductors (LISICONs) [234,235], ethers, glymes, nitriles, amides, sulfones and dimethyl sulfoxide (DMSO)-based [86,225]. More recently, increasing attention has been devoted to the use of ionic liquids (ILs) as electrolytes for application in lithium-oxygen batteries [86,227,236,237]. As already mentioned in paragraph 1.3.2, the structure of ILs can be endlessly modified to tune their physical-chemical properties, leading to favorable characteristics such as low vapor pressure, thus, low-flammability and remarkable thermal stability, and high electrochemical stability and ionic conductivity [91,103]. The use of IL electrolytes in Li/O_2 batteries is favored by a low OER average potential [238,239], good stability against $O_2^{\cdot-}$ nucleophilic attack [240], and enhanced ORR/OER reversibility [241–244]. Among these very promising materials,

imidazolium- [245,246] and pyrrolidinium-based [112,247–249] electrolytes have demonstrated promising performance. In particular, $Pyr_{14}TFSI$ has revealed to be suitable for lithium-air batteries showing low OER polarization and remarkable electrochemical performance [238]. DEMETFSI, characterized by a lower viscosity then the former, was also proposed for application as electrolyte component for lithium-air batteries [250]. The choice of a proper composite electrode for supporting the oxygen redox processes also plays a key role in determining the cell performance. Indeed, important characteristics favoring the ORR/OER are high surface area and porosity, to favor the reaction and accommodate the reaction products, electron conductivity and stability in the reactive environment of the Li-O_2 battery [251–253]. Carbon is one of the most suitable, low-cost materials for use in the positive electrode of Li/O_2 batteries. Many different carbon morphologies and structures, i.e., 1-D [254,255], 2-D [256,257] and 3-D [258,259] structured materials, have been studied all showing promising performance and cycle life. The chemical nature of the polymeric additive binding the Li/O_2 battery positive electrodes, as well as the traces of the solvent used for slurry preparation, may also have a significant impact on the nature of the final discharge product and the reversibility of the electrochemical process, as recently evidenced by research works [260–262]. Therefore, the choice of suitable materials and proper electrode preparation represent relevant topics presently explored for the improvement of Li/O_2 batteries. Attention has also been devoted to the anode side of the cell, where several studies focused on alternative materials to lithium metal, such as nanostructures based on lithiated tin and silicon materials dispersed in carbon matrixes that have demonstrated relevant stability and satisfactory capacity in lithium and lithium-ion cells [59,263–265].

1.5 Aim of the work

The objective of this thesis work is to propose innovative, safer lithium and lithium-ion configurations, by replacing the conventional graphite anode and organic based electrolyte components, and/or proposing alternative cathode chemistries for higher energy, beyond lithium-ion batteries. In chapter 2, the use of a nanostructured alloy-based material, Sn-C, coupled with safer ionic liquid-based electrolytes, is explored. This chapter is mainly focused on the realization of high performance, safe lithium-ion battery configurations. The use of an olivine-structured, $LiFePO_4$ cathode material ensures an added safety value to the full cell configuration, while the use of a layer-structured $LiNi_{1/3}Co_{1/3}Mn_{1/3}O_2$ is proposed to demonstrate that ionic liquid-based electrolytes can be successfully employed also for higher energy systems. Moreover, in this chapter, one of the key properties of ionic liquids is evidenced. It is their flexibility in physicochemical properties, which can be modified by properly engineering their molecular structure. The studies in this chapter mainly employ electrochemical techniques, which are supported by morphological/structural analysis. A similar approach is used in chapter 3, where the use of ionic liquid-based electrolytes is expanded to beyond lithium-ion systems, namely Li-O_2. The use of this class of safe electrolytes is evaluated with the idea of realizing full lithium-ion-oxygen cells. To this end, a carbon-coated $Zn_{0.9}Fe_{0.1}O$ lithium-alloy-conversion anode is used as negative electrode to realize an advanced configuration. The electrolyte employed is not only thermally and electrochemically stable, but also effectively mediates and allows reversible formation of Li_2O_2, which cannot be obtained by using conventional, organic-based liquid electrolytes. The promising characteristic of the ionic liquid-based Li-O_2 cell is further demonstrated by engineering advanced cathode configurations and evidenced by realizing a full lithium-ion-oxygen battery employing alternative, Sn-C, anode material. Finally, the use of safe, all-solid-state electrolytes for lithium-sulfur batteries is proposed, as an alternative strategy to avoid polysulfide dissolution. Novel cathode architectures are investigated, employing low cost, environmentally friendly materials, such as FeS_2 and elemental sulfur, and a facile mechanochemical synthesis procedure. The experimental data show that the issues of beyond lithium-ion technologies can be effectively mitigated thus improving both the performance and the safety content of the energy storage system. This can be doneby adopting alternative strategies involving the use of novel electrolyte formulations.

Chapter 2: Lithium-ion systems

In this chapter, two different lithium-ion systems employing alternative, alloy-based anodes and safe, ionic-liquid based electrolytes are explored. The first part deals with a general physicochemical and electrochemical characterization of all the ionic liquid based electrolytes described in chapter one, i.e., Pyr_{14}FSI-LiTFSI, Pyr_{14}TFSI-LiTFSI, DEMETFSI-LiTFSI, and Pyr_{12O1}TFSI-LiTFSI. Pyr_{14}FSI-LiTFSI. Pyr_{14}FSI-LiTFSI, which shows outstanding characteristics, but is relatively limited by its anodic stability, is studied in full lithium-ion cell employing LFP cathode. The obtained results highlight the outstanding cycle life, with capacity retention close to 100% over 2000 cycles, rate capability extending up to 500 mA g^{-1} and energy content as high as 480 Wh kg^{-1} (referred to the cathode weight only). The stability of this system is further highlighted by electrochemical impedance spectroscopy (EIS) and scanning electron microscopy (SEM) studies. In the following paragraph, Pyr_{14}TFSI-LiTFSI, which is characterized by a higher anodic stability, is coupled with a layered NMC cathode. This allows the realization of a full cell which delivers a capacity of about 140 mAh g^{-1} as referred to the NMC cathode weight for more than 400 cycles with a retention higher than 99%. Also in this case, the favorable electrode-electrolyte interface is investigated by EIS, while the prolonged structural stability of the electrode materials is revealed using scanning electron microscopy. Both cells are expected to have a high safety level, thanks to the use of non-volatile and non-flammable ionic liquid based electrolytes [266–268]. Moreover, one of the most interesting characteristics of ionic liquids is evidenced, that is the possibility of changing their physicochemical properties by tuning the structure of the molecules, thus meeting different needs required by different systems.

Chapter 2 Experimental

The ionic liquid based electrolytes were prepared by mixing 0.2 mol of LiTFSI (3M, battery grade) per kg of either Pyr_{14}TFSI, Pyr_{14}FSI, Pyr_{12O1}TFSI or DEMETFSI in an argon-filled glove box (MBRAUN), with oxygen and water content lower than 1 ppm. The electrolytes were dried under

vacuum for 24 hours at 120°C (Pyr_{14}TFSI-LiTFSI), 60°C (Pyr_{14}FSI-LiTFSI), 60°C (Pyr_{12O1}TFSI-LiTFSI) and 80°C (DEMETFSI-LiTFSI) until the water content was reduced to less than 5 ppm (detection limit) as determined by Karl Fischer titration. The drying conditions have been chosen considering the thermal stability of each IL-based electrolyte, to avoid possible decomposition promoted by the presence of water traces during the initial stages of the drying process [269,270]. The lithium salt concentration in the ionic liquid-based electrolytes, i.e., 0.2 mol kg^{-1}, has been demonstrated as an optimal compromise allowing a high lithium ion conductivity and charge transport and contemporary avoiding undesired viscosity increase, thus leading to satisfactory cell performance in terms of delivered capacity, low polarization and high rate capability [269,270]. The electrolyte conductivity Arrhenius plots were obtained by electrochemical impedance spectroscopy (EIS, Mmates-Biologic) using sealed Pt-black/Pt-black cells (Mmates) with a K value of 1 cm^{-1}, using a Peltier system for cooling/heating as temperature control. The reported conductivity plots are performed upon heating, after eighteen hours of aging at -40 °C, using an increment of 5°C/hour. The cell constant was confirmed using the standard 0.1M KCl water solution (Fluka). The viscosity of the electrolytes was evaluated at various temperatures in a dry room environment using an Anton-Paar Physica MCR102 rheometer, applying constant shear rates, and using a Peltier system for cooling/heating. The viscosity plots are performed upon heating, after six hours of aging at -40 °C, using an increment of 10°C/hour. The cycling stability of the lithium metal in the IL-based electrolytes was evaluated by continuous stripping/deposition tests on symmetrical Li/Li cells in coin cell cases, reversing the current (0.1 mA cm^{-2}) every 1 hour. The electrochemical anodic stability of the electrolytes was evaluated by linear sweep voltammetry (scan rate of 0.1 mV s^{-1}) using a composite carbon (Super C65, Imerys) coated on aluminum foil as the working electrode. The current versus time plots for the anodic stability were obtained by applying increasing voltage steps of 0.1 V (each lasting one hour). The cathodic stability was determined by cyclic voltammetry in the 0.01-2 V potential range at 0.1 mV s^{-1} scan rate employing a composite carbon electrode (Super C65, Imerys) coated on a copper foil as the working electrode. These experiments were performed on Swagelok-type cells with lithium metal as reference electrode. All the electrochemical tests were carried at 40°C temperature in thermostatic climatic chambers with a possible deviation of ± 1°C. Composite electrodes were prepared by doctor-blade technique, coating a slurry composed of C-NERGY Super C65 (Imerys), Polyvinylidene fluoride (PVDF, 6020 Solef, Solvay) and the active materials (LFP, NMC, or Sn-C) in a 1:1:8 weight ratio, dispersed in N-methyl-2-pyrrolidinone (NMP, Aldrich 99.9 %) and casted either on aluminum (LFP, NMC) or copper (Sn-C) foils. After

drying, the coated foils were punched in disk-shaped electrodes having a diameter of 14 mm (LFP) or 16 mm (Sn-C), the residual solvent and water traces were removed under vacuum at 110 °C overnight. The electrode mass loading was about 2-3 mg cm^{-2} for Sn-C, 3-4 mg cm^{-2} for NMC and about 4-5 mg cm^{-2} for LFP. Specific capacity and currents were evaluated taking into account a maximum error of 5% mostly due to the uncertainty in the electrode loadings (±0.1 mg). NMC was acquired from BASF. The Sn–C nanocomposite (Sn/C weight ratio of approximately 40:60) was prepared as previously described [59] while the LFP was reported in a previous work [271]. The theoretical specific capacity of the nanocomposite material was calculated to be approximately 440 mAh g^{-1} at room temperature, assuming contributions of tin and carbon of 380 and 60 mAh g^{-1}, respectively.

The electrochemical characterization for lithium half cells was performed using stainless steel 2032 coin cells, with lithium metal as the counter electrode, a sheet of Whatman glass fiber GF/A soaked by the electrolyte as separator and either NMC, LFP or pre-lithiated Li_xSn-C as the working electrode. Prior to half and full cell assembling, the Sn–C anode was pre-lithiated by placing the electrode in contact with a Li foil wetted by a LP30 solution to compensate for the irreversible capacity shown by this material upon the 1st lithiation [263,264] and allow the formation of a stable SEI layer at the anode surface, as reported in literature [264,272]. The same pre-lithiation procedure was attempted by directly pressing the anode in the presence of the IL-based electrolyte instead of the conventional one. However, this resulted in a mechanical degradation of the anode, avoiding the proper pre-activation, and, SEI film formation. The cycling tests of Li/IL-based electrolyte/LFP cells were carried out applying increasing specific currents (from 25 to 250 mA g^{-1}) in the voltage range 2.2-4 V, while those of Li/Pyr_{14}FSI-LiTFSI/Sn-C cells were performed applying increasing specific currents from 25 mA g^{-1} to 200 mA g^{-1} in the voltage range 0.01-2 V. The Sn-C/Pyr_{14}FSI-LiTFSI/LFP cell was tested in the voltage range 2-3.8 V at specific currents increasing from 25 to 250 mA g^{-1}, while a fingerprint test was performed employing a specific current of 500 mA g^{-1}, lowered to 25 mA g^{-1} for three cycles every 45 cycles. The galvanostatic cycling tests of the Li/Pyr_{14}TFSI-LiTFSI/NMC cells were performed using a current of 25 mA g^{-1} at 25°C and 40°C. The Li/Pyr_{14}TFSI-LiTFSI/Sn-C cells were tested at 25°C, 40°C and 60°C also using a current of 25 mA g^{-1} and additionally characterized at 40°C using various current rates, i.e. 25, 50, 100 mA g^{-1}. The galvanostatic test of the Sn-C/ Pyr_{14}TFSI-LiTFSI/NMC cell was performed using a current of 25 mA g^{-1} within the 2.5-4 V cut-off voltage and 40°C. Before the measurements, all the cells were

kept at the desired temperature for at least 24 hours to reach thermal equilibrium. All galvanostatic cycling tests were carried out in thermostatic climatic chamber (with a possible deviation of ± 1°C) using a Maccor 4000 Battery Test System. The specific current and the specific capacity are referred to the cathode (LFP, NMC) weight. The impedance measurements were performed within the frequency range from 200 kHz to 10 mHz applying a 10 mV sinusoidal amplitude using a VMP3 Potentiostat/Galvanostat/EIS (Bio-Logic). The ex-situ morphological characterization was performed using field emission scanning electron microscopy (SEM, Zeiss LEO1550VP Gemini). Before the SEM analyses, the studied electrodes were rinsed using dimethyl carbonate (DMC) to remove residual electrolyte components.

2.1 Sn-C/Pyr_{14}FSI-LiTFSI/LFP

The electrolytes' conductivities and viscosities are reported in Figure 2.1.1. The Arrhenius plot shown in Figure 2.1.1a evidence as Pyr_{14}FSI-LiTFSI (black dots) is characterized by the highest ionic conductivity, with values ranging from 15 mS cm^{-1} at 60 °C to 0.3 mS cm^{-1} at -30 °C. A progressively decreasing conductivity values are shown by Pyr_{12O1}TFSI-LiTFSI (blue dots, 10 mS cm^{-1} at 60 °C and 0.05 mS cm^{-1} at -30 °C), Pyr_{14}TFSI-LiTFSI (green dots, 7 mS cm^{-1} at 60 °C and 0.03 mS cm^{-1} at -30 °C) and DEMETFSI-LiTFSI (red dots, 7 mS cm^{-1} at 60 °C and 0.02 mS cm^{-1} at -30°C). Thus, all the investigated samples reveal suitable conductivity for battery application only above room temperature. Figure 2.1.1b reports the viscosity versus temperature plots and shows that Pyr_{14}FSI-LiTFSI electrolyte (black dots, 13 mP s at 80°C, 1573 mP s at -30°C) is characterized by the lowest viscosity, followed by Pyr_{12O1}TFSI-LiTFSI (blue dots, 14 mP s at 80°C, 5730 mP s at -30°C). Instead, Pyr_{14}TFSI-LiTFSI (green dots, 16 mP s at 80°C, 12250 mP s at -30°C) and DEMETFSI-LiTFSI (red dots, 14 mP s at 80°C, 15565 mP s at -30°C) reveal the highest viscosity values.

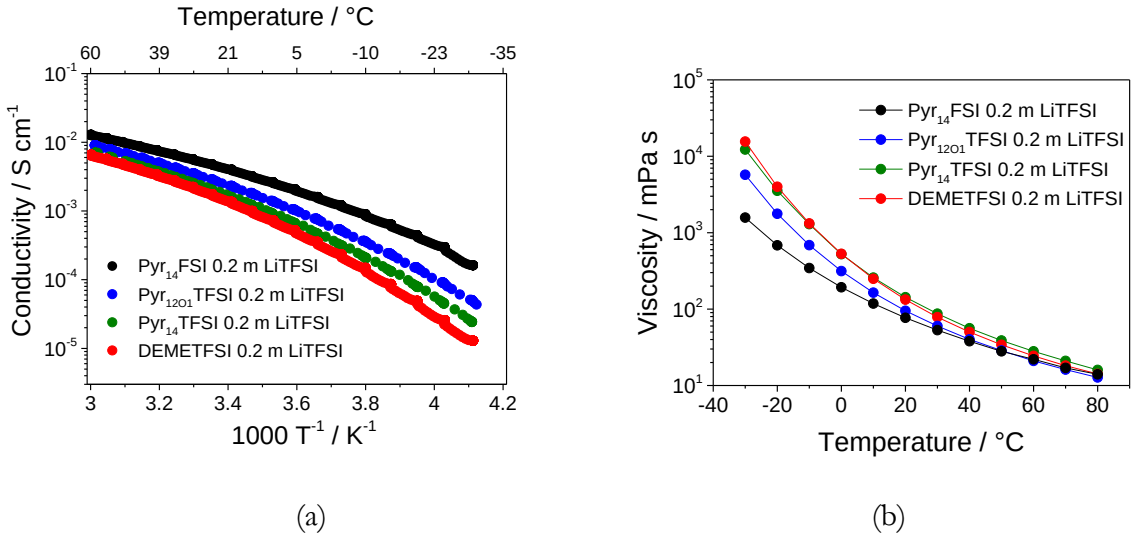

Figure 2.1.1 (a) Conductivity and (b) viscosity Arrhenius plot of Pyr_{14}TFSI-LiTFSI (green dot), Pyr_{14}FSI-LiTFSI (black dot), Pyr_{12O1}TFSI-LiTFSI (blue dot), DEMETFSI-LiTFSI (red dot).

The viscosity and the conductivity trends reported in Figure 2.1.1 deviate from the linear behavior expected for the Arrhenius-type curve but can be properly described by the Vogel-Tammann-Fulcher (VTF) model, in particular at low temperatures [102]. The model is mathematically expressed by the VTF equation (2.1) for conductivity, and (2.2) for viscosity, with the introduction of the T_0 (K) correction parameter.

$$\sigma(T) = \sigma_\infty \exp\left(-\frac{E_{a\sigma}}{k_B(T-T_0)}\right) \quad (2.1)$$

$$\eta(T) = \eta_\infty \exp\left(-\frac{E_{a\eta}}{k_B(T-T_0)}\right) \quad (2.2)$$

This value, often referred as zero configurational entropy and correlated to the glass transition temperature Tg (K) of each ionic liquid, is about 30 K lower than the Tg [102]. The other parameters in the equations (2.1) and (2.2) are the ionic conductivity at infinite temperature σ_∞ (S cm^{-1}), the maximum dynamic viscosity η_∞ (mP s), the activation energy for ion conduction $E_{a\sigma}$ (eV), the dynamic viscosity activation energy $E_{a\eta}$ (eV) and the Boltzmann constant k_B (8.62 10^{-5} eV K^{-1}). Table 1 and 2 report the results obtained by Non-Linear-Least-Square (NLLSQ) fit of conductivity and viscosity VTF curves, respectively, for Pyr_{14}TFSI-LiTFSI, Pyr_{14}FSI-LiTFSI, Pyr_{12O1}TFSI-LiTFSI, DEMETFSI-LiTFSI electrolytes (See Appendix 2, Figure A2.1, for corresponding linearized VTF plots, a, c, e and g for conductivity, b, d, f and h for viscosity) [273,274],

	σ_∞ [S cm^{-1}]	E_a [eV]	T_0 [K]
Pyr_{14}FSI 0.2m LiTFSI	0.6 ± 0.1	5.9 x 10^{-2} ± 0.1 x 10^{-2}	159 ± 3
Pyr_{14}TFSI 0.2m LiTFSI	0.7 ± 0.1	6.4 x 10^{-2} ± 0.1 x 10^{-2}	172 ± 3
Pyr_{12O1}TFSI 0.2m LiTFSI	0.7 ± 0.1	6.1 x 10^{-2} ± 0.1 x 10^{-2}	170 ± 3
DEMETFSI 0.2m LiTFSI	0.5 ± 0.1	5.5 x 10^{-2} ± 0.1 x 10^{-2}	186 ± 3

Table 2.1.1 Value of the ionic conductivity at infinite temperature, of activation energy and T_0 obtained by the VTF fit of the conductivity plots.

	η_∞ [mP s]	E_a [eV]	T_0 [K]
Pyr_{14}FSI 0.2m LiTFSI	0.31 ± 0.05	6.84 x 10^{-2} ± 0.1 x 10^{-2}	154 ± 3
Pyr_{14}TFSI 0.2m LiTFSI	0.14 ± 0.03	7.33 x 10^{-2} ± 0.1 x 10^{-2}	168 ± 3
Pyr_{12O1}TFSI 0.2m LiTFSI	0.18 ± 0.04	6.84 x 10^{-2} ± 0.1 x 10^{-2}	167 ± 3
DEMETFSI 0.2m LiTFSI	0.14 ± 0.03	7.15 x 10^{-2} ± 0.1 x 10^{-2}	172 ± 3

Table 2.1.2 Value of the maximum dynamic viscosity, activation energy and T_0 obtained by the VTF fit of the viscosity plots.

The trends of Fig. 2.1.1b well agree with the Walden rule, thus suggesting an ionic conductivity controlled by viscosity within the investigated temperature range and operating conditions [273]. Previous papers have shown possible liquid-solid phase transition for Pyr_{14}TFSI-LiTFSI and Pyr_{14}FSI-LiTFSI by quenching the samples with liquid nitrogen [268,275] that is, however, not revealed in this experimental setup. To avoid possible drawbacks due to electrode and separator wetting and considering the conductivity and viscosity trends above, 40°C was selected as the preferred temperature for testing the IL-based electrolytes in half and full-cell configurations, [274]. The cyclic voltammetry (CV) scans of the cathodic region recorded with the investigated electrolytes in contact with composite carbon working electrodes are reported in Figure 2.1.2a. The initial cycle evidence, for all electrolytes, the irreversible peak associated with the SEI formation at the carbon-based working electrode (Super C65). However, such a peak is seen to occur at rather different potentials depending on the electrolyte composition, i.e., at about 1.3V vs Li/Li^+ for the Pyr_{14}FSI-LiTFSI (black) [131] and 0.6V vs Li/Li^+ for Pyr_{14}TFSI-LiTFSI (green), Pyr_{12O1}TFSI-LiTFSI (blue) and DEMETFSI-LiTFSI (red) [276–278]. The higher SEI formation potential observed for the former electrolyte may be ascribed to the FSI anion decomposition known to have enhanced film-forming ability than TFSI [279]. The second cycle, reported in the lower panel, reveals the exclusive presence of reversible peaks in the 0.0-0.2 V vs. Li/Li^+ region associated to the lithium uptake in the carbon working electrode [280], thus suggesting the formation of a stable SEI with all investigated electrolytes which prevents any further decomposition process during the following cycles.

The anodic stability of the electrolytes is evaluated by measuring the current evolution during a stepwise potential sweep, increasing by 0.1 V each one hour, (Fig. 2.1.2b). All the investigated electrolytes reveal no current flow below 4.5 V vs. Li/Li^+. At higher potential values, i.e., 4.6 V vs. Li/Li^+, DEMETFSI-LiTFSI electrolyte (red line) shows negligible current flow, associated to side reactions, that slightly increases at 4.7-4.8 V vs. Li/Li^+, to finally reaching about 10 μA cm^{-2} at 4.9 V vs Li/Li^+, most likely due to the electrolyte decomposition. Instead, Pyr_{12O1}TFSI-LiTFSI (blue line) and Pyr_{14}FSI-LiTFSI (black line) show negligible current flow until 4.9 V vs Li/Li^+, while at 5 V vs Li/Li^+ the current flow of about 10 μA cm^{-2} can be noticed. Overall, Pyr_{14}TFSI-LiTFSI (green line) shows the best electrochemical stability, with only minor current flowing below 5.1 V vs. Li/Li^+. The inset of Fig. 2.1.2b, reporting the linear scan voltammetry (LSV) tests of the investigated electrolytes performed at the scan rate of 0.1 mV s^{-1}, well confirms the data obtained by the stepwise potential measurement. Indeed, the anodic stability of the investigated electrolytes may be summarized as following: Pyr_{14}TFSI-LiTFSI (5.1 V vs Li/Li^+); Pyr_{14}FSI-LiTFSI (4.8-4.9 V vs Li/Li^+); Pyr_{12O1}TFSI-LiTFSI DEMETFSI-LiTFSI (4.8-4.9 V vs Li/Li^+); DEMETFSI-LiTFSI (4.7 V vs Li/Li^+). Figure 2.1.2c reports the polarization versus time signatures of the stripping/deposition tests in symmetrical Li/electrolyte/Li, used to determine the compatibility of the electrolytes against lithium metal under current flow. The cells employing DEMETFSI-LiTFSI (red), Pyr_{12O1}TFSI-LiTFSI (blue) and Pyr_{14}FSI-LiTFSI (black) electrolytes show a lithium stripping/deposition polarization stably limited to about 55, 45, 15 mV, respectively, thus suggesting an optimized SEI formation at the lithium surface. The various resistance values may be attributed to different morphologies and compositions of the SEI formed at the lithium surface by changing the IL-electrolyte media. Instead, the cell using Pyr_{14}TFSI-LiTFSI electrolyte shows a polarization increasing up to 95 mV after 40 days (480 cycles, 960 h) most likely ascribed to the growth of the SEI layer. Previous works indicated the replacement of the lithium metal anode by a Li-alloying anode as a suitable pathway for solving this issue [132]. Remarkably, despite the mid-high temperature range (40°C) used for stripping/deposition measurements, the cell stability extends over 480 cycles, i.e., 40 days of continuous cell operation, thus suggesting enhanced characteristics of the lithium/IL-electrolyte interface.

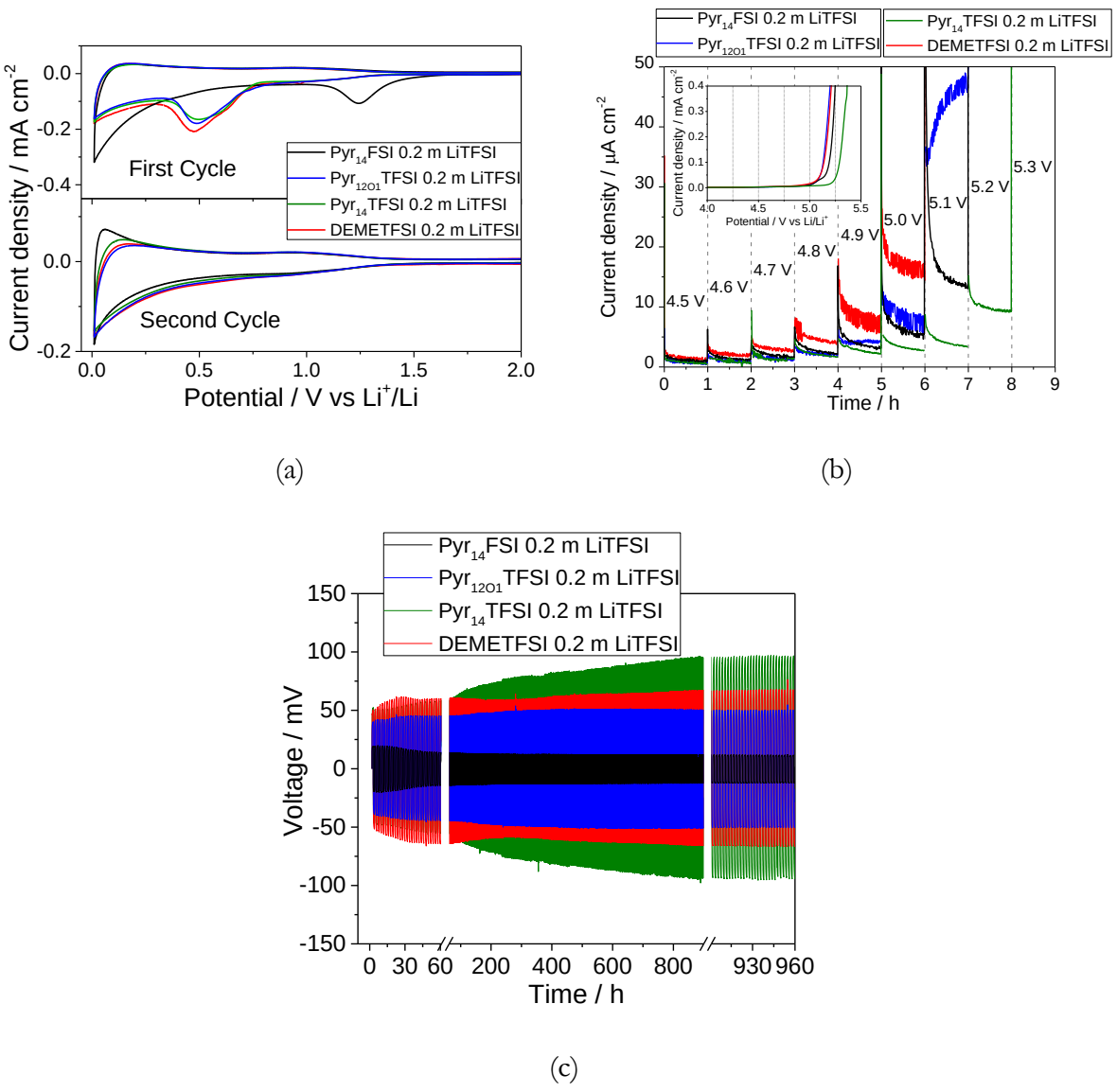

Figure 2.1.2 (a) Cyclic voltammograms of Li/ IL /Super-C65 cells recorded at a scan rate of 0.1mV s^{-1} (first and second cycle). (b) Current vs time profile of the Li/ IL /Super-C65 cells subject to a stepwise potential sweep (the inset shows the current vs potential plot upon linear sweep voltammetry on Li/ IL /Super-C65 cells at a scan rate of 0.1mV s^{-1}, (c) Voltage vs time plot recorded upon stripping/deposition measurement performed on asymmetrical Li/ IL /Li cells using a current of 0.1 mA cm^{-2} and a deposition-stripping time of 1 hours. Pyr_{14}TFSI-LiTFSI (green), Pyr_{14}FSI-LiTFSI (black), Pyr_{12O1}TFSI-LiTFSI (blue), DEMETFSI-LiTFSI (red) electrolytes. All measurements at 40°C.

The suitability of the IL-based electrolytes was further evaluated by galvanostatic cycling in Li//LFP cells. Figure 2.1.3a shows the voltage signature during a steady state cycle of the cells employing the

four investigated electrolytes at a specific current of 25 mA g^{-1} (corresponding to ca. C/7 rate) in the 2.2-4 V voltage range, performed at 40°C. The voltage signatures reflect the typical flat voltage profile associated to the reversible insertion of lithium ions in LFP olivine structure [166,184,281,282] with very low (dis-)charge polarization and only minor differences between the electrolytes (magnified in the inset of Figure 2.1.3a). The highest reversible capacity (about 165 mAh g^{-1}, i.e., 97 % of the theoretical value) is shown by the cells employing Pyr_{12O1}TFSI-LiTFSI (blue line) and Pyr_{14}FSI-LiTFSI (black line), while a capacity of 161 mAh g^{-1} is shown by employing Pyr_{14}TFSI-LiTFSI (green line) and DEMETFSI-LiTFSI (red line). The detailed evaluation of the average cell polarization reported in Figure A2.2a (Appendix 2) shows a value of about 70 mV for the cell using Pyr_{14}FSI-LiTFSI, 100 mV for Pyr_{12O1}TFSI-LiTFSI, 110 mV for Pyr_{14}TFSI-LiTFSI and 120 mV for DEMETFSI-LiTFSI electrolyte. Increasing current leads to more marked differences in (dis-)charge polarization, as evidenced in Figure 2.1.3b reporting the voltage signature of the 70th galvanostatic cycle performed at 250 mA g^{-1} (ca. 1.5 C). The best performance is achieved by employing the Pyr_{14}FSI-LiTFSI electrolyte (Fig. 2.1.3b, black line) which retains 95% of the capacity upon the tenfold increase of current, i.e. from 25 mA g^{-1} (Fig. 2.1.3a) to 250 mA g^{-1} (Fig. 2.1.3b), with an average polarization of 230 mV (Fig. A2.2b, Appendix 2). Instead, the cell employing the Pyr_{12O1}TFSI-LiTFSI electrolyte (Fig. 2.1.3b, blue circles) can deliver at the higher current a capacity of 100 mAh g^{-1} with an average polarization of 430 mV (Fig. A2.2b, Appendix 2), while the cells employing the DEMETFSI-LiTFSI (Fig. 2.1.3b, red line) and Pyr_{14}TFSI-LiTFSI (Fig. 2.1.3b, green line) electrolytes deliver a capacity of about 65 mAh g^{-1} and 70 mAh g^{-1} with an average polarization of 450 mV and 480 mV, respectively (Fig. A2.2b, Appendix 2). The polarization of the cells employing the various IL-based electrolytes appears in line with the conductivity and viscosity trends, as well as the lithium/electrolyte interface stability. In spite, the cell using Py_{14}TFSI-LiTFSI shows an increased polarization when the current is lowered back to 25 mA g^{-1} at the 90th cycle (Fig. A2.2c, Appendix 2) compared to the initial cycles (compare with Fig. A2.2a, Appendix 2). This is certainly due to the progressive growth of a more resistive SEI at the lithium metal anode. This trend matches that already observed by stripping-deposition measurements in symmetrical lithium cell reported in figure 2.1.2c. Figure 2.1.3c, overlapping the cycling trends at increasing currents of the lithium cells above discussed (see corresponding voltage profiles in Fig. 2.1.3a and 2.1.3b), shows only minor capacity fading with retention of about 95% after 100 cycles for the cell employing Pyr_{14}TFSI-LiTFSI. Remarkably, the cells using Pyr_{12O1}TFSI-LiTFSI, Pyr_{14}FSI-LiTFSI and DEMETFSI-LiTFSI electrolytes evidence negligible capacity fading and retention higher than 99%.

Figure 2.1.3c remarks the good rate capability for all the investigated electrolytes and the excellent response of $Pyr_{14}FSI$-LiTFSI due to its higher ionic conductivity and lower viscosity. Furthermore, the cell employing this electrolyte shows a very high coulombic efficiency (about 99.9 %) concerning those using $Pyr_{12O1}TFSI$-LiTFSI and DEMETFSI-LiTFSI (about 98%). Instead, $Pyr_{14}TFSI$-LiTFSI electrolyte shows a high coulombic efficiency (99.9%) only during the initial cycling stage at the lower current (25 mA g^{-1}) and remarkably lower efficiency (92%) at the higher current (250 mA g^{-1}). The efficiency is calculated basing on the electricity accumulated and delivered by the battery during the faradic processes involving electron transfer reactions at the interface between electrode and electrolyte in the course of lithium (de)insertion at the cathode and (de)alloying at the anode, while capacitive effects are considered negligible due to the very limited electrode surface [283]. Hence, the lower efficiency of the latter cell by increasing the C-rate may be attributed to kinetic effects of the current, promoted by the high viscosity of the electrolyte (Fig. 2.1.1b), and favoring the irreversible parasitic reactions concerning the reversible charge transfer process. Furthermore, the increased cell polarization upon charge at high C-rates, which results in higher and lower voltages experienced by the electrolyte at, respectively, the positive and negative electrodes, may indeed favor the occurrence of irreversible parasitic reactions, resulting in decreased efficiency.

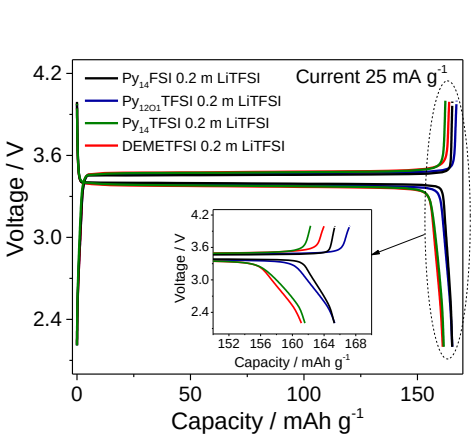

(a)

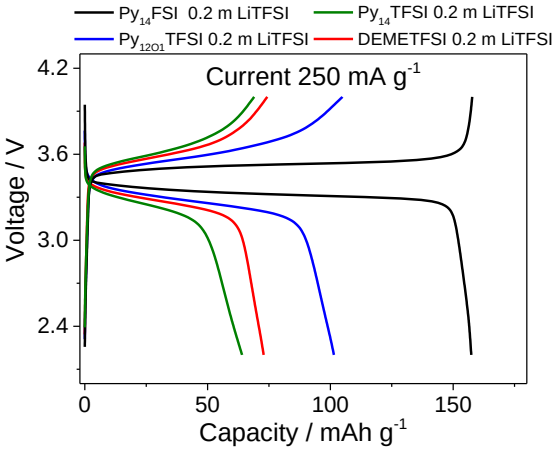

(b)

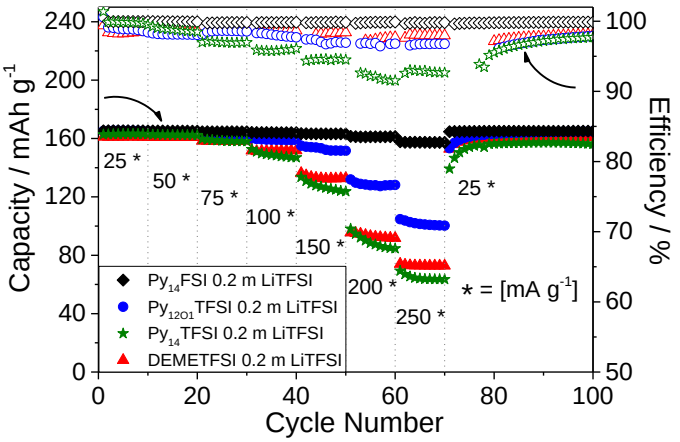

(c)

Figure 2.1.3 Steady-state voltage signatures of Li/IL/LFP cells galvanostatically cycled at (a) 25 mA g^{-1} and (b) 250 mA g^{-1}. (c) Cycling trend and coulombic efficiency of the Li/IL/LFP cells at increasing currents, i.e., 25, 50, 75, 100, 150, 200 and 250 mA g^{-1} (cut-off voltages 2.2 and 4 V). Pyr_{14}TFSI-LiTFSI (green), Pyr_{14}FSI-LiTFSI (black), Pyr_{12O1}TFSI-LiTFSI (blue), DEMETFSI-LiTFSI (red). All measurements at 40°C.

Based on the above-reported results, Pyr_{14}FSI-LiTFSI was selected as the electrolyte of choice for the realization of the lithium-ion cell prototype employing a Sn-C nanocomposite anode [59,263]. Before full cell assembly, the Sn-C electrode was pre-lithiated to eliminate its first cycle irreversible capacity, thus allowing proper cell balancing and operation [264,284]. The voltage profile of the Li/Pyr_{14}FSI-LiTFSI/Sn-C half-cell (Fig. A2.3a in Appendix 2) shows the typical signature ascribed to the reversible alloying of lithium with the tin [51,263,285]. The Li/Pyr_{14}FSI-LiTFSI/Sn-C cell delivers a capacity of 400 mAh g^{-1} over 400 cycles, with a coulombic efficiency as high as 99.9% (Fig. A2.3b in Appendix 2) and a very good rate capability (Fig. A2.3c, A2.3d in Appendix 2). This performance confirms Sn-C as a suitable anode for application in efficient and effective lithium-ion cells as well as the remarkable SEI forming ability of the electrolyte employing the FSI^- anion. The nature and composition of the SEI formed at the alloy anode surface in IL-based electrolytes has been clarified by a recent work [133]. The study reveals that FSI^- anion can decompose during the reduction process at the alloy anode (S-F bond breaking). This process leads to the formation of SO_2 and LiO at the anode/electrolyte interface and consolidation the SEI layer by adherent compounds such as LiF, LiO, LiOH, and Li_2SO_4. Figure 2.1.4a shows the steady state voltage signature of the

Sn-C/Pyr_{14}FSI-LiTFSI/$LiFePO_4$ cell at a current of 25, 75, 150 and 250 mA g^{-1} (all specific values of the lithium-ion cell refer to the active cathode material mass). The voltage shape reflects the combination of the flat profile of the LFP cathode and the sloping profile of the Sn-C anode, following the overall electrochemical process:

$$Li_xSn\text{-}C + LiFePO_4 \rightleftharpoons Li_{x+y}Sn\text{-}C + Li_{(1-y)}FePO_4$$

The cell delivers a specific capacity as high as 160 mAh g^{-1} at the lower current (25 mA g^{-1}) and a still satisfactory value of 105 mAh g^{-1} at the higher one (250 mA g^{-1}), with rather remarkable rate capability, cycling trend and coulombic efficiency (Fig. 2.1.4b). The cycling test of the Li-ion cell at the current density of 100 mA g^{-1} (Fig. 2.1.4c) reveals reversible capacity of 150 mA g^{-1} with negligible capacity fading, coulombic efficiency higher than 99.9 %, resulting in the cycle life extending over 1000 cycles, and average working voltage change by cycles limited to about 100 mV (Fig. 2.1.4d). A further long-term test, aimed to determine the cell cycle-life, was performed using a test procedure in which low (25 mA g^{-1}) and high current (500 mA g^{-1}) cycles were continuously repeated (Fig. 2.1.4e). Although subjected to these stressful conditions, the cell could reversibly deliver specific capacity well over 80 mAh g^{-1} at the highest current, fully recovering to its pristine value of 160 mAh g^{-1} at the lower current. Overall, the cell showed capacity retention of about 98% over more than 2000 cycles and coulombic efficiency close to 100%. Figure 2.1.4f shows the comparison of the voltage profiles during the 2^{nd} and 2018^{th} low current cycles and the 20^{th} and 2030^{th} high current cycles. The figure remarkably reveals a working voltage change limited to about 100 mV between the initial and the final cycles. Based on the cycling response at various current rates, we determined the theoretical energy and power densities of the cell as referred to the cathode weight. Furthermore, the system reveals good electrochemical performance even at the lowest temperature, i.e., 20°C, as evidenced by the cycling test reported in figure A2.4 in Appendix 2. The results reveal at 25 mA g^{-1} a capacity of 150 mAh g^{-1}, which is slightly lower than that delivered at 40 °C, but with comparably stable trend, high efficiency and low polarization. However, lower capacity and higher polarization are observed by raising the current, as indeed expected for the lower ionic conductivity (i.e., higher viscosity) of the electrolyte at 20°C (see Figure 2.1.1).

The plot of Figure A2.5 (Appendix 2) reports the energy density (left y-axis) and the power density (right y-axis) of the Sn-C/Pyr_{14}FSI-LiTFSI/LFP lithium-ion cell reported as a function of the operating current. The cell reaches maximum values of specific gravimetric energy and power

densities of 460 Wh kg^{-1} and 1400 W kg^{-1}, respectively, that may likely reflect into practical values well suited for efficient and high-performance energy storage applications. The relevant performance of the Pyr_{14}FSI-LiTFSI with respect to the other investigated IL solutions is further evidenced by the comparison of the Sn-C/ LFP cell performances using the various electrolytes, reported in figure A2.6 in Appendix 2. The figure reveals higher delivered capacity and coulombic efficiency for the cell employing the Pyr_{14}FSI-LiTFSI electrolyte.

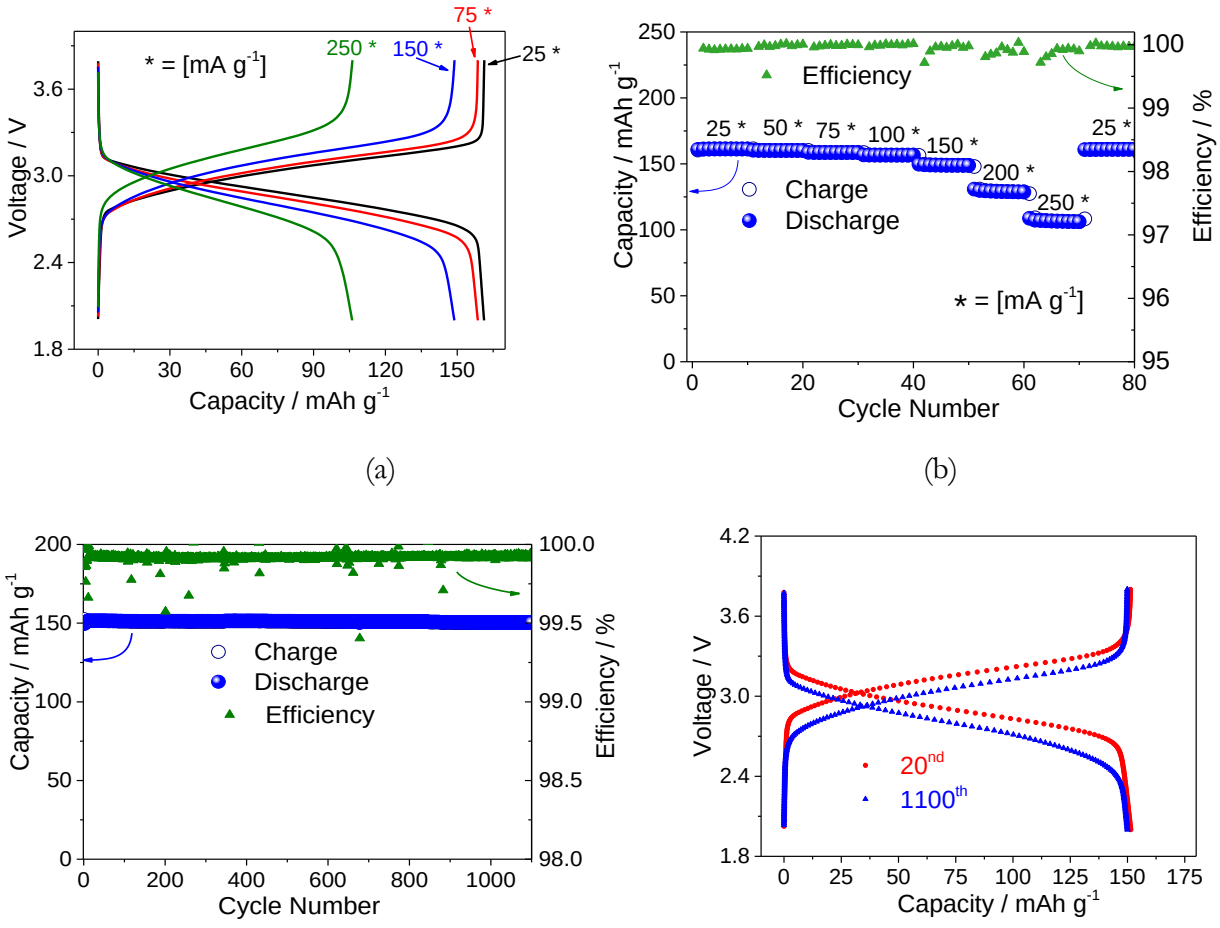

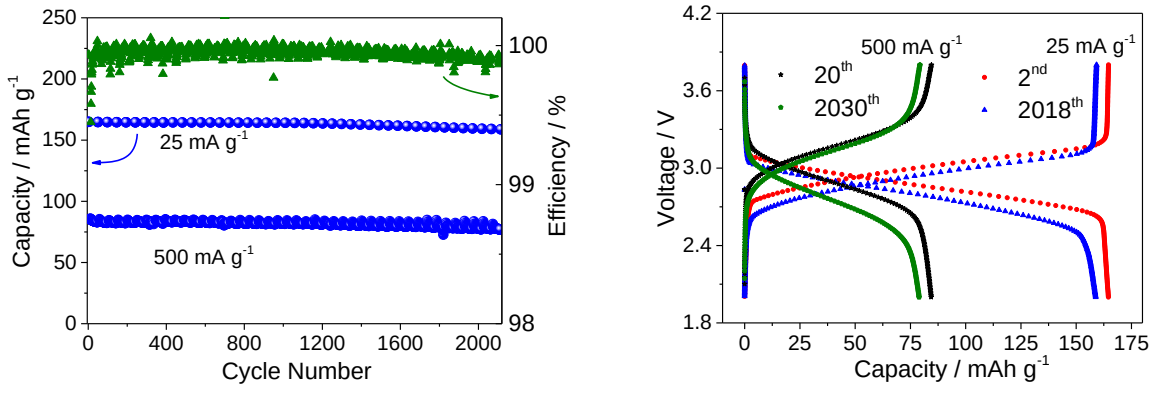

(e) (f)

Figure 2.1.4 (a) Steady state voltage signatures and (b) cycling behavior with coulombic efficiency of the Sn-C/Pyr_{14}FSI-LiTFSI/LFP cell galvanostatically measured at increasing currents, i.e., 25, 50, 75, 100, 150, 200 and 250 mA g^{-1}. (c) Coulombic efficiency and (d) steady state voltage signatures of the Sn-C/Pyr_{14}FSI-LiTFSI/LFP cell upon long-term galvanostatic cycling test at 100 mA g^{-1}. (e) Coulombic efficiency and (f) steady state voltage signatures of the Sn-C/Pyr_{14}FSI-LiTFSI/LFP cell galvanostatically cycled at different currents, i.e., 25 and 500 mA g^{-1}. All measurements at 40°C and cut off voltage 2-3.8 V.

The exceptional performance of the Sn-C/Pyr_{14}FSI-LiTFSI/$LiFePO_4$ cell may be clarified by the evolution of the cell impedance upon cycling (Figure 2.1.5a), obtained by analyzing the EIS response reported in Figure A2.7a (Appendix 2) together with the equivalent circuit (figure A2.7b) used for the Nonlinear Least Square (NLLSQ) fit procedure [286,287]. The cell shows a very low overall cell internal resistance at the open circuit voltage (OCV, 16 Ω), slightly increasing during the initial 10 cycles due to SEI film formation and consolidation at the electrode surfaces [288,289], and finally stabilizing to about 25 Ω over 200 cycles, with only small changes considered within the experimental error of the measurement. Accordingly, the SEI film formation at the electrode surface is completed upon 10 charge/discharge cycles. Further proof of the cell interface stability is given by ex-situ SEM micrographs of Sn-C (Fig. 2.1.5b) and of LFP (Fig. 2.1.5c) electrodes, performed after cell assembly (OCV), upon 10 cycles and 200 cycles. The figure clearly reveals negligible morphological changes for the two materials upon cycling, thus further accounting for the extended stability of the electrodes/electrolyte interface.

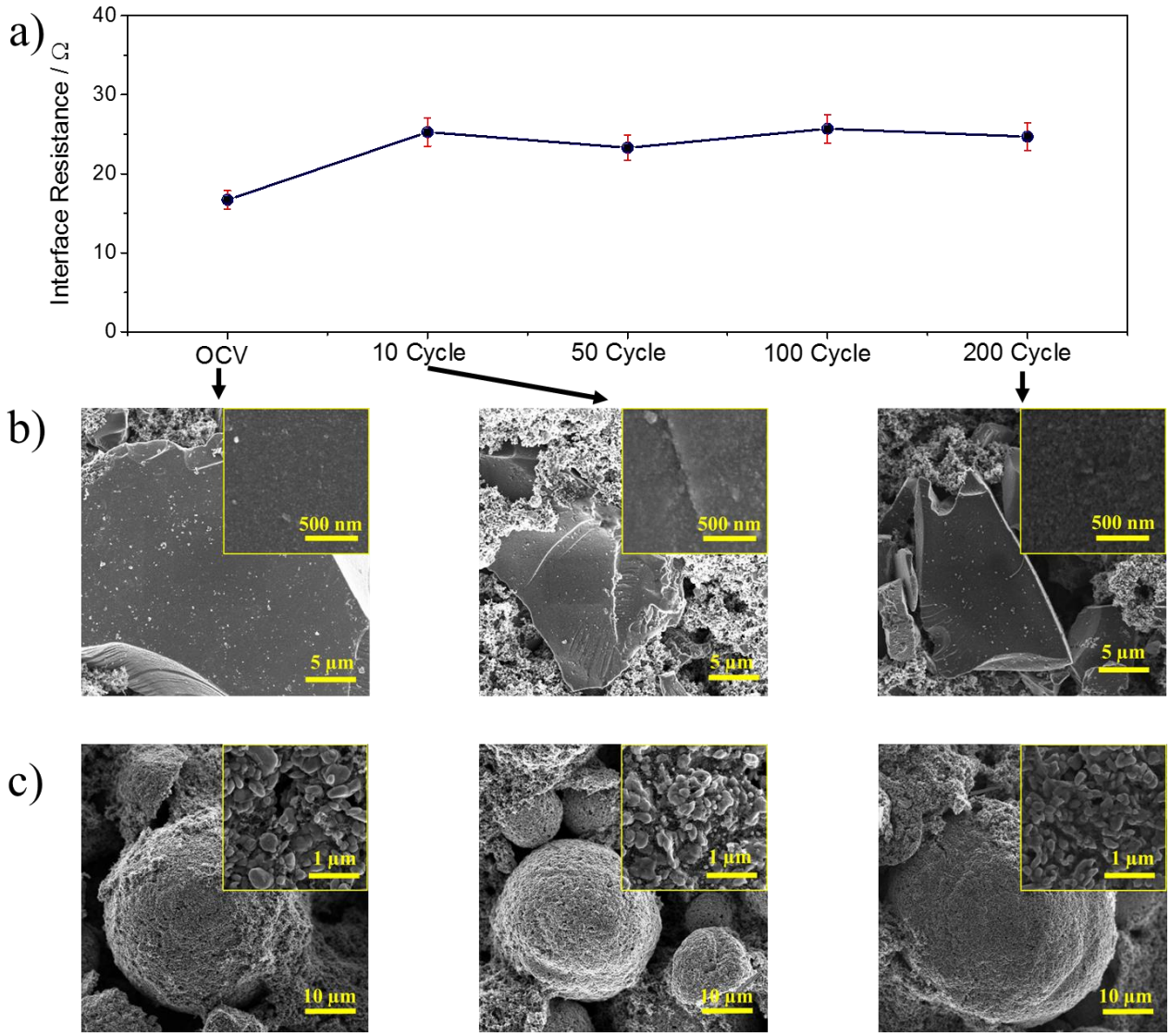

Figure 2.1.5 (a) Evolution of the interface resistance of the Sn-C/Pyr_{14}FSI-LiTFSI/LFP cell upon cycling, including the error bar. (b-c) Ex-situ SEM images of the electrode materials (Sn-C and LFP) subjected to galvanostatic cycling.

2.2 Sn-C/Pyr_{14}TFSI-LiTFSI/NMC

Figure 2.2.1a shows steady-state charge and discharge behavior of the Li/NMC cell at 25°C and 40°C. At the lower temperature, the material reversibly delivers a rather low capacity, i.e., of about 75 mAh g^{-1} with relevant (dis-)charge polarization. This trend is certainly ascribed to the low RT conductivity of the IL-electrolyte (10^{-3} S cm^{-1} vs. 10^{-2} S cm^{-1} of a conventional liquid electrolyte), but also to its high RT viscosity (see Figure 2.1.1). Indeed, the high viscosity of the IL may induce poor electrode interface wetting [35] and, consequently, high polarization leading to the above reported poor cell behavior. Increasing the temperature to 40°C leads to a remarkable improvement of the cell characteristics both in terms of steady state voltage profile (Figure 2.2.1a), now reflecting the expected slope associated to the efficient (de-)intercalation of the lithium into layered $LiNi_{1/3}Co_{1/3}Mn_{1/3}O_2$ structure, and in terms of delivered capacity (150 mAh g^{-1}). Furthermore, the cell operating at 40°C shows a coulombic efficiency approaching 99% and retains 97% of its initial capacity by 40 charge/discharge cycles (Figure 2.2.1b), thus suggesting good stability of the electrode-electrolyte interface and the electrolyte media [121,126,128].

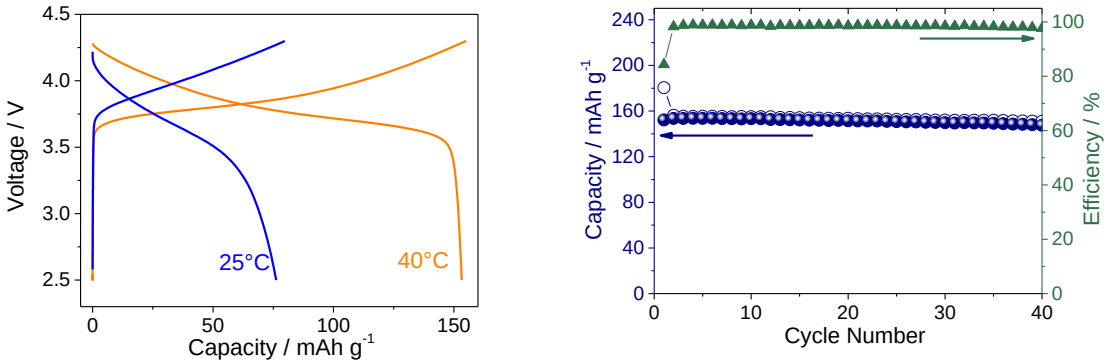

(a) (b)

Figure 2.2.1 Comparison of the steady-state voltage signature of the Li/Pyr_{14}TFSI-LiTFSI/NMC cell at 25°C and 40°C, employing a 25 mA g^{-1} current. (b) Cycling behavior and steady-state voltage signature (inset) of the Li/Pyr_{14}TFSI-LiTFSI/NMC cell employing a 25 mA g^{-1} current at 40°C.

The ionic liquid-based electrolyte was also investigated in combination with the Sn-C nano-composite anode in half-cell configuration [59]. The Sn-C material is characterized by a carbon micrometric structure trapping the active tin nanoparticles, i.e., a morphology ensuring unique chemical and electrochemical stability and limiting the pulverization of the Sn particles during cell operation [59]. Figure 2.2.2 shows a summary of the electrochemical properties of the Sn-C electrode in lithium half-cell at various temperatures and current rates. The voltage profiles (Fig. 2.2.2a) of the cell at 25, 40, and 60 °C evidence an increasing reversible capacity from about 300 mAh g^{-1} at 25 °C to about 450 mAh g^{-1} at 40°C, i.e., a value approaching the theoretical value of the Sn-C material. Further increase of the temperature up to 60°C increases the reversible capacity to 600 mAh g^{-1} that well exceeds the theoretical one. This anomaly may be ascribed to an additional contribution of the carbon matrix [280] evidenced by the differential capacity curves (Fig. 2.2.2b), revealing an increase of the intensity of the peaks at about 0.8V in oxidation and 0.2V in the reduction, ascribed to lithium-uptake process in amorphous carbon [46]. The cell shows remarkable cycling behavior upon increasing temperature, with capacity retention higher than 80% when the temperature is decreased to the initial value (25°C, Fig. 2.2.2c). Figure 2.2.2d, reports the cycling trend at various specific currents (25, 50, and 100 mA g^{-1}) performed at 40°C. The results evidence satisfactory rate capability of the cell, with capacity values ranging from 450 to 250 mAh g^{-1} by repeated increasing of the current from 25 to 100 mA g^{-1}.

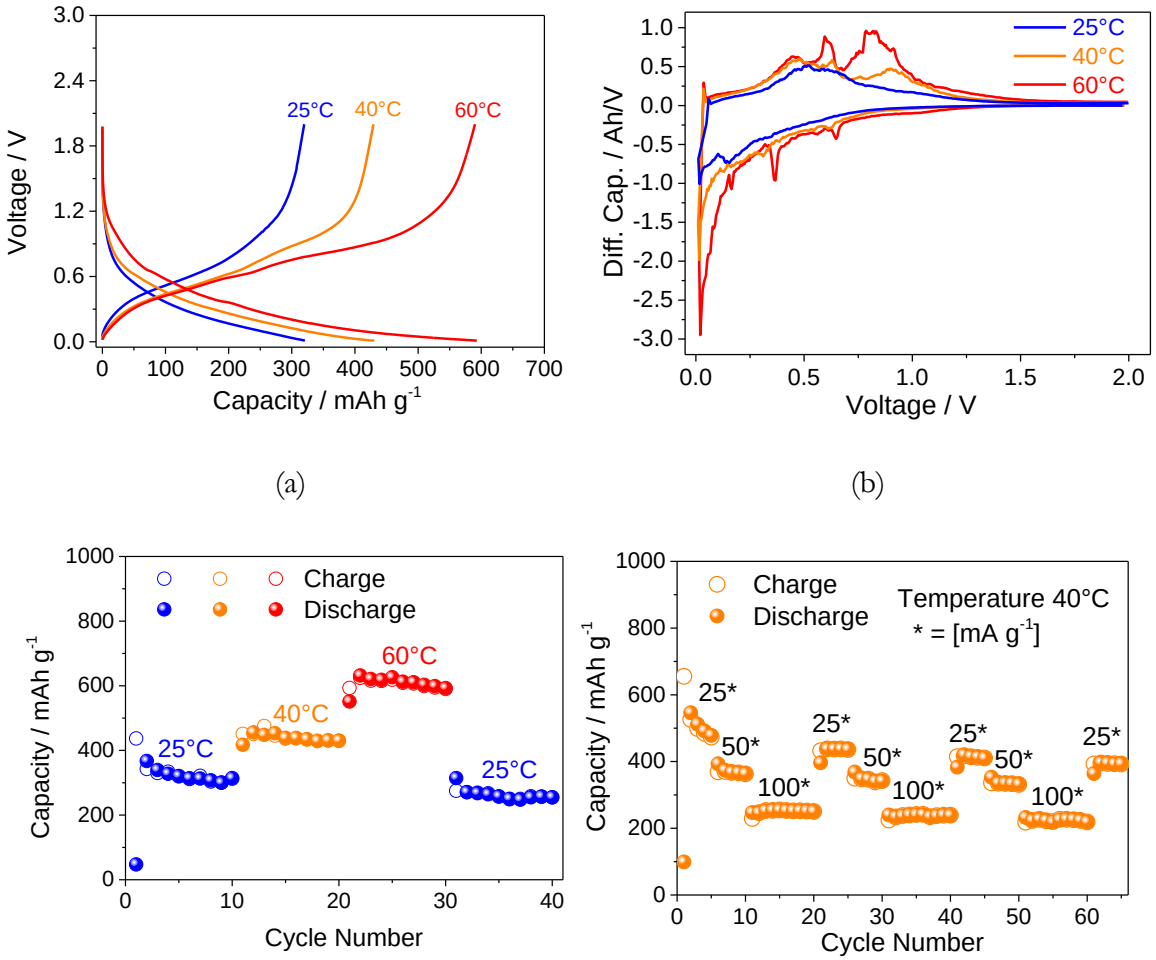

Figure 2.2.2 Steady state voltage signatures (a), differential capacity profiles (b) and cycling behavior (c) of the Li/Pyr_{14}TFSI-LiTFSI/Li_xSn-C cell galvanostatically measured at 25 mA g^{-1} current at increasing temperatures, i.e., 25°C, 40°C and 60 °C. (d) Cycling trend of the Li/Pyr_{14}TFSI-LiTFSI/Li_xSn-C cell at 40°C and increasing currents, i.e., 25, 50 and 100 mA g^{-1}.

The promising results gathered from the half-cell tests suggest the suitability of the NMC and Sn-C materials in a cathode-limited full lithium-ion cell employing Pyr_{14}TFSI-LiTFSI as the electrolyte. Figure 2.2.3 reports the performance of such a full-cell at 40°C, using a current of 25 mA g^{-1}, in terms of both the cycling behavior (a) and the voltage profile (b). Fig. 2.2.3a reveals the excellent long-term cycling response of the cell offering the stable capacity (about 140 mAh $g^{-1}_{cathode}$) with a coulombic efficiency approaching 100% after the first cycle (first cycle energy efficiency 80%). In

fact, the cell capacity did not show any significant decay (capacity retention close to 100%) upon more than 400 cycles, corresponding to a continuous cycling operation of about 140 days. Such an outstanding cycle performance, combined with the use of the non-flammable (IL-based) electrolyte, match with the stringent long-life, high energy density (expected to practically approach 200 Wh kg^{-1}), and safety requirements of the electric vehicles market.

Fig. 2.2.3b reveals the typical voltage signature reflecting the combination of the lithium intercalation process at the NMC layered cathode and lithium-alloying reaction within Sn-C anode. The figure shows that the profiles well reproduce the electrochemical process centered at about 3.4V even after 400 cycles. The slight decrease of the working voltage is most likely due to the SEI film consolidation at the electrodes' surfaces.

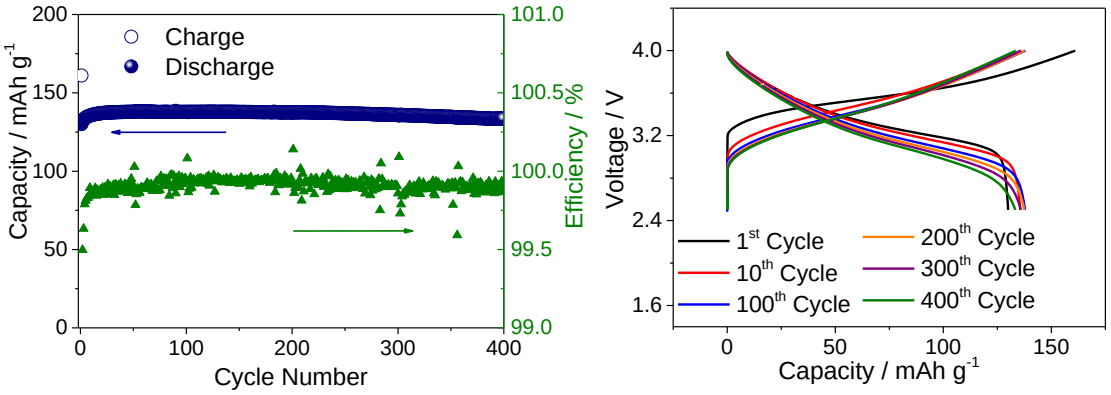

(a) (b)

Figure 2.2.3 (a) Prolonged cycling behavior and (b) voltage signature of the Sn-C/Pyr_{14}TFSI-LiTFSI/NMC cell galvanostatically characterized at 25 mA g^{-1} current at 40°C.

To verify this hypothesis, the interface of the Sn-C/Pyr_{14}TFSI-LiTFSI/NMC cell was investigated via in-situ electrochemical impedance spectroscopy and ex-situ scanning electron microscopy upon prolonged cycling. Figure 2.2.4 (top panel) reports the evolution of the cell impedance during cycling, the corresponding SEM image of the electrodes (middle panel) as well as the Nyquist impedance plots and equivalent circuit used for the analysis (bottom panel) [268]. The figure evidences a very slight increase of the resistance value, thus indicating the stable electrode-electrolyte interfaces and leading to the relevant cycle life (Fig. 2.2.3a) and the limited voltage-profile change

(Fig. 2.2.3b). The Nonlinear Least Square analysis of the impedance spectra [286,287] has been performed employing a $R_e(R_fQ_f)(R_{tc}Q_f)Q_g$ equivalent circuit (See Appendix 2, Fig. A2.7b), where R_e represents the resistance of the electrolyte R_f represent the resistance of the film and R_{tc} represent the resistance of the charge transfer process. The overall interface resistance remains stable at about 15 **Ω** that is considered a remarkably low value allowing a modest ohmic drop of the cell upon cycling. Furthermore, the SEM images (Fig. 2.2.4, middle panel) of the Sn-C anode and NMC cathode at the pristine state and after the 10^{th}, 50^{th}, 100^{th}, and 200^{th} cycle. The SEM images of the Sn-C anode show that the typical micrometric carbon matrix (inset) is retained during cycling without significant modification or relevant formation of decomposition products [59]. Meanwhile, the SEM images of the NMC cathode show the micrometric particle with a size of about 10 μm, with primary particles of about 500 nm (inset) both at the pristine state and after 200 cycles. In summary, both the SEM images and the EIS measurement account for the structural stability of the electrode materials during cycling and suggest the limited formation of side products at the electrode surface by electrolyte decomposition, thus revealing the enhanced characteristics of the electrode/IL-electrolyte studied herein.

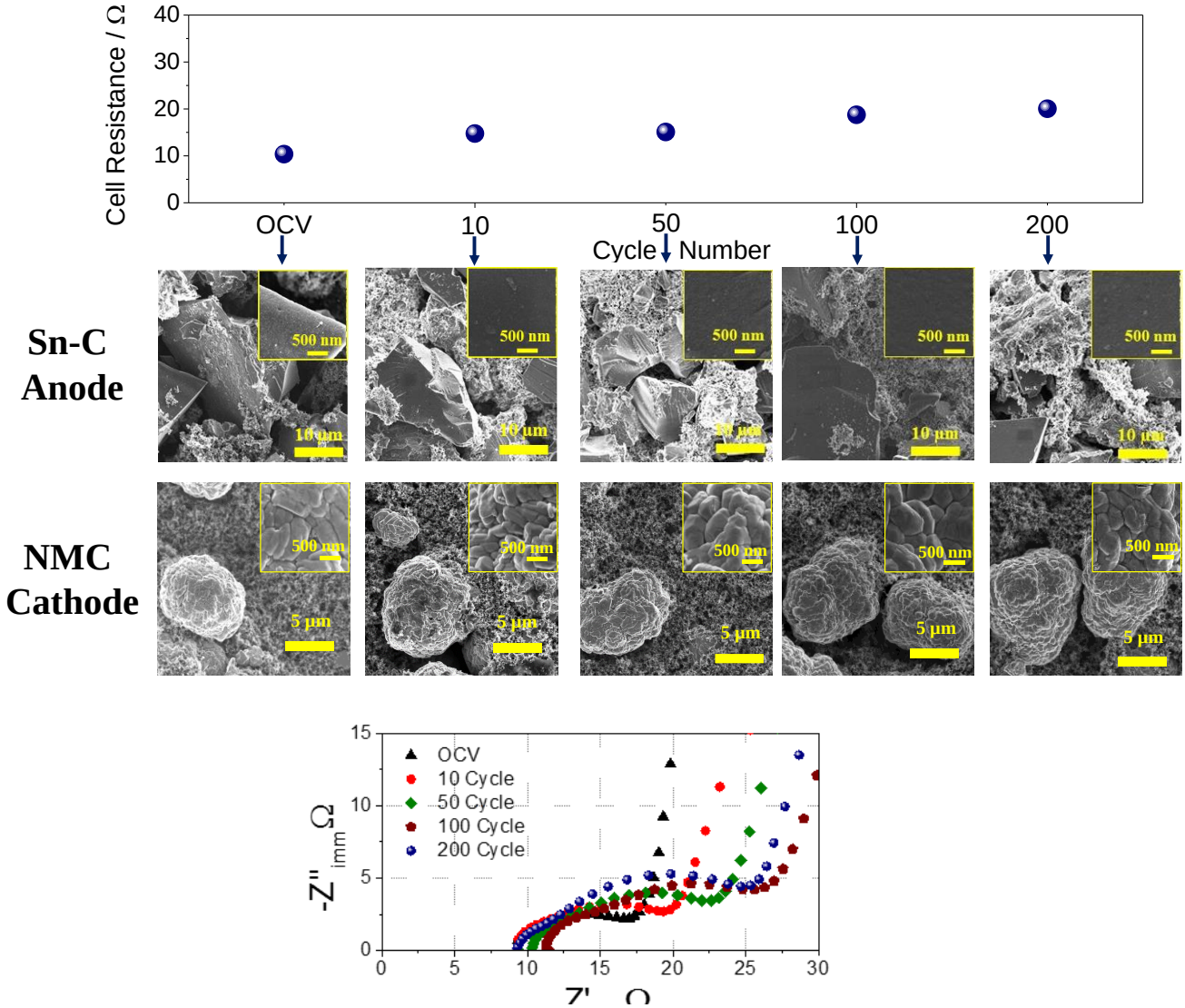

Figure 2.2.4 Evolution of the interface resistance of the Sn-C/Pyr_{14}TFSI-LiTFSI/NMC cell upon cycling (top panel), corresponding ex-situ SEM images of the electrode materials (Sn-C and NMC, middle panel) and Nyquist plot of the cell impedance data (bottom panel). Frequency range 1 MHz-10 mHz (10 mV signal amplitude), 40°C temperature.

2.3 Summary

In chapter 2, the investigation of a class of enhanced ionic liquid-based electrolytes for application in long life and safe lithium-ion batteries is reported. All the investigated electrolytes have shown suitable ionic conductivity and excellent electrochemical stability. Vogel-Tammann-Fulcher (VTF) model well represented the behavior of conductivity and viscosity of the electrolytes, thus leading to parameters calculated by linear plots in good agreement to the Walden law within the explored temperature range. Pyr14FSI-LiTFSI revealed the highest ionic conductivity, lowest viscosity, most suitable lithium/electrolyte interface and remarkably low polarization under current flow, while Pyr_{14}TFSI-LiTFSI showed the widest electrochemical stability window. The favorable characteristics of Pyr_{14}FSI-LiTFSI are reflected into the outstanding performance of the Sn-C/Pyr_{14}FSI-LiTFSI/LFP lithium-ion cell, delivering a maximum capacity of 160 mAh g^{-1} at an average working voltage of 3V with a coulombic efficiency higher than 99.9% over more than 2000 charge/discharge cycles. Such performance is achieved because of the exceptionally stable cell impedance upon cycling, as demonstrated by in-situ EIS measurements and ex-situ SEM characterization. The Sn-C/Pyr_{14}TFSI-LiTFSI/$LiNi_{1/3}Co_{1/3}Mn_{1/3}O_2$ (NMC) cell reported in chapter 2.2 shows outstanding characteristics in terms of relevant cycle life, efficiency, optimal electrodes/electrolyte interface features and energy density. The employment of $LiNi_{1/3}Co_{1/3}Mn_{1/3}O_2$ layered cathode, owning remarkable structural integrity as demonstrated by SEM study, grants a rather high cell energy density and long-term stability. Indeed, the cell, characterized by the reversible capacity referred to the cathode mass of about 140 mAh g^{-1} and average working voltage of about 3.4 V, has a theoretical energy density of about 476 Wh kg^{-1} as referred to the cathode that reflects into a practical energy density exceeding 200 Wh kg^{-1} considering electrochemically inactive cell components, such as cell casing, electrolyte, and current collectors. These values, in addition to the stability exceeding 400 cycles, efficiency and capacity retention approaching 100%, extremely limited volatility, thus expected non-flammability of the IL-based electrolyte, appear very attracting characteristics for electric vehicles application and, more in general, advanced electrochemical energy storage systems. Together, the two studies demonstrate that lithium-ion batteries using safer, alternative electrolyte formulations, are a viable option for several different cell configurations using

commercially available positive electrodes and, most importantly, it emphasizes the flexibility given by engineering ionic liquid structures to meet different needs.

Appendix 2

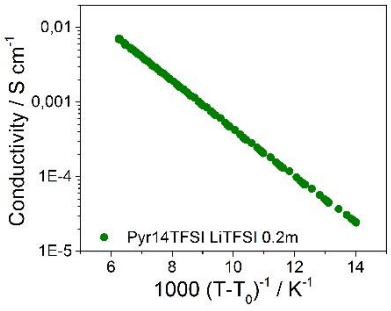

(a)

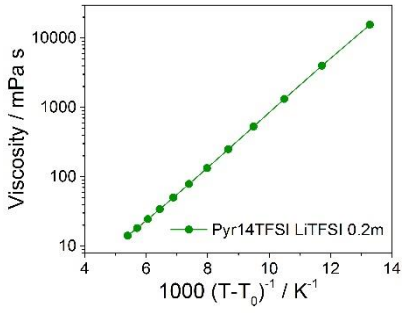

(b)

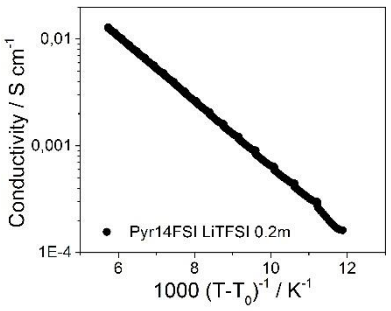

(c)

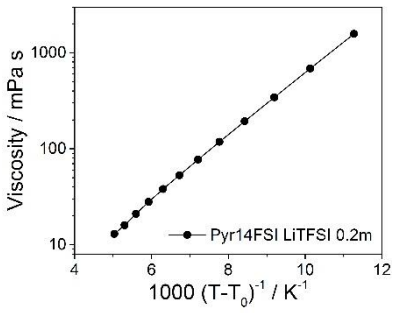

(d)

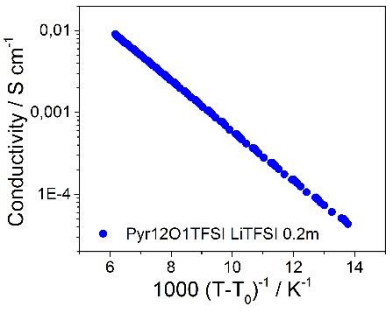

(c)

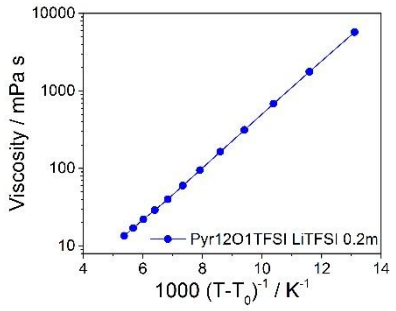

(d)

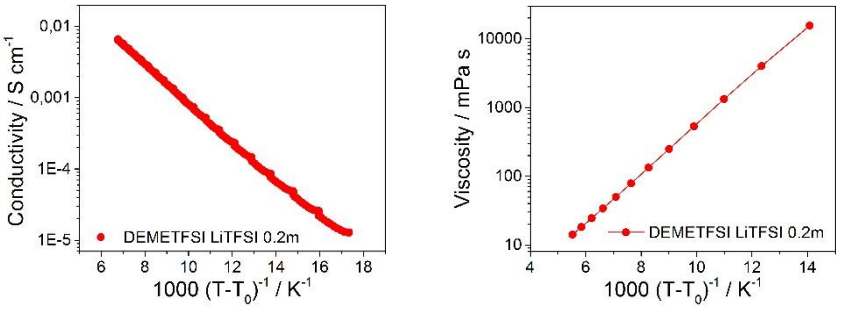

(c) (d)

Figure A2.1 Vogel-Tammann-Fulcher (VTF) plot of conductivity and viscosity reported vs. $1000/(T-T_0)$. $Pyr_{14}TFSI$-LiTFSI in green (a,b), $Pyr_{14}FSI$-LiTFSI in black (c,d), $Pyr_{12O1}TFSI$-LiTFSI in blue (e,f) and DEMETFSI-LiTFSI in red (g,h).

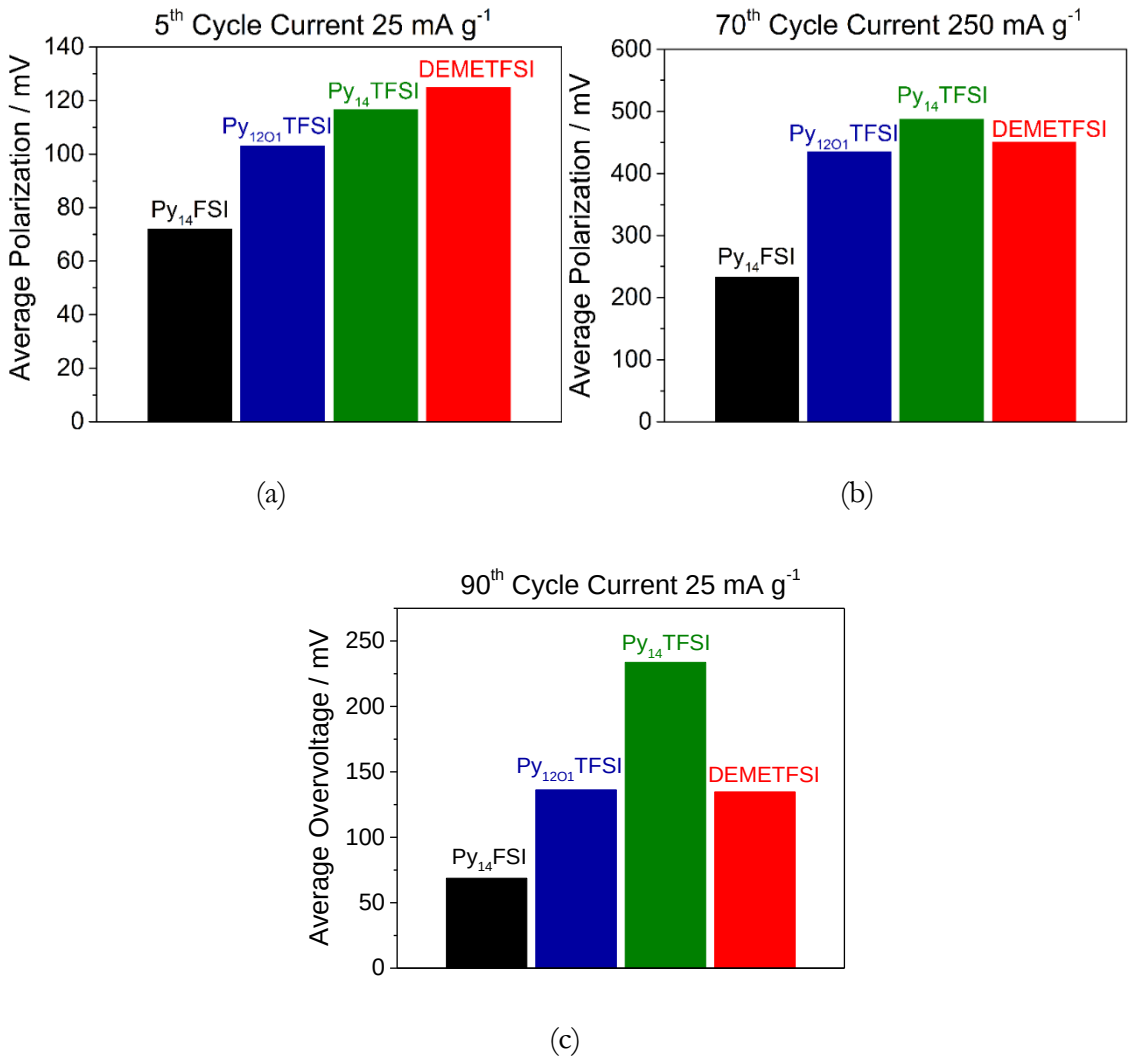

Figure A2.2 Average polarization during (a) the 5th cycle measured at 25 mA g^{-1} (0.12 mA cm^{-2}) current, (b) the 70th cycle measured at 250 mA g^{-1} (1.2 mA cm^{-2}) current and (c) the 90th cycle measured at 25 mA g^{-1} (0.12 mA cm^{-2}) of the Li/IL/LFP cells employing the Pyr$_{14}$FSI-LiTFSI (black), the Pyr$_{12O1}$TFSI-LiTFSI (blue), the Pyr$_{14}$TFSI-LiTFSI (green) and the DEMETFSI-LiTFSI (red) electrolytes 40°C temperature cut off voltage 2.2-4 V.

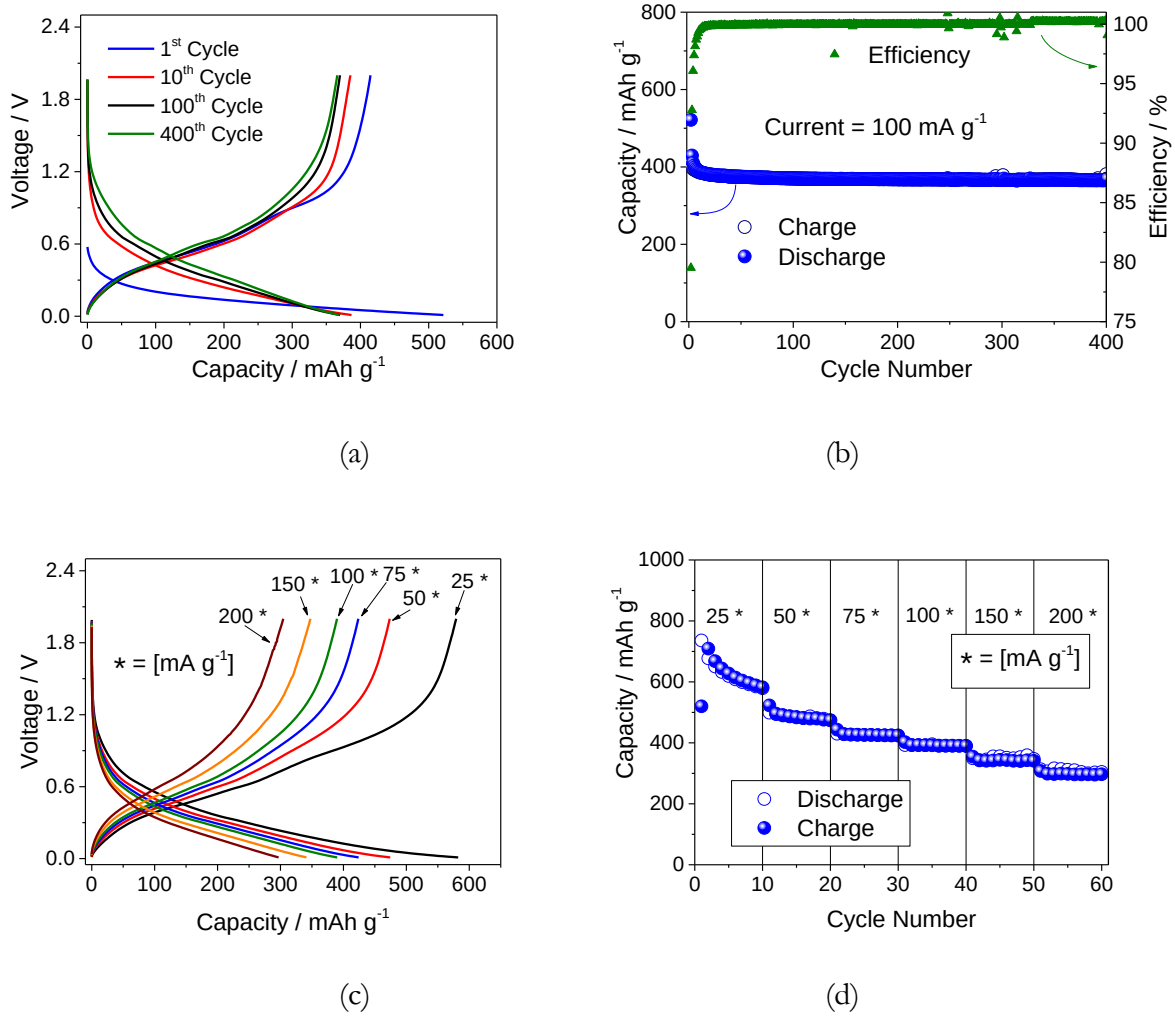

Figure A2.3 Voltage signatures (a) and cycling behavior (b) of the Li/Pyr_{14}FSI-LiTFSI/Sn-C cell galvanostatically measured 100 mA g^{-1} (0.25 mA cm^{-2}). Voltage signatures (c) and cycling behavior (d), of the Li/Pyr_{14}FSI-LiTFSI/Sn-C cell galvanostatically measured at increasing currents, i.e., 25, 50, 75, 100, 150 and 200 mA g^{-1} (0.065, 0.1875, 0.25, 0.375, 0.5 mA $cm^{-2,}$ respectively). Temperature 40°C cut off voltage 0.01-2 V.

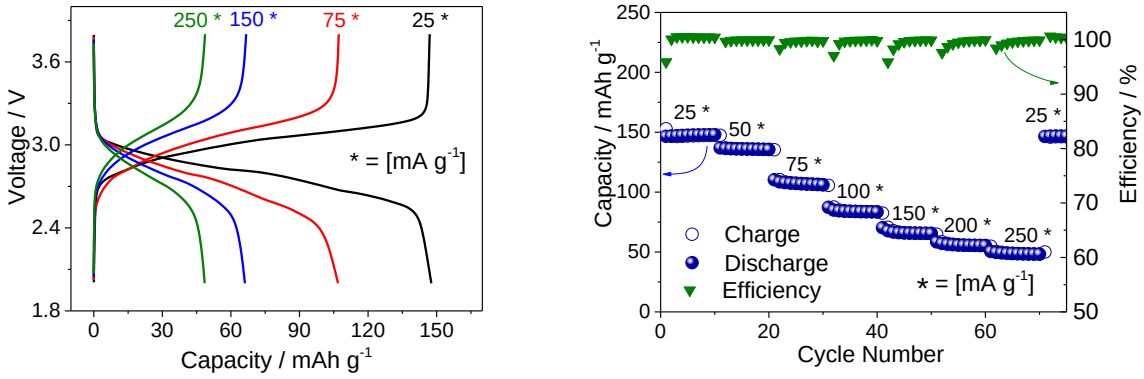

Figure A2.4 (a) Selected voltage signatures and (c) cycling behavior with coulombic efficiency of the Sn-C/Pyr_{14}FSI-LiTFSI/LFP cell galvanostatically cycled at increasing currents, i.e., 25, 50, 75, 100, 150, 200 and 250 mA g^{-1} (0.12, 0.24, 0.36, 0.48, 0.72, 0.96, 1.2 mA cm^{-2}, respectively) at 20 °C. Voltage cut-off 2-3.8 V.

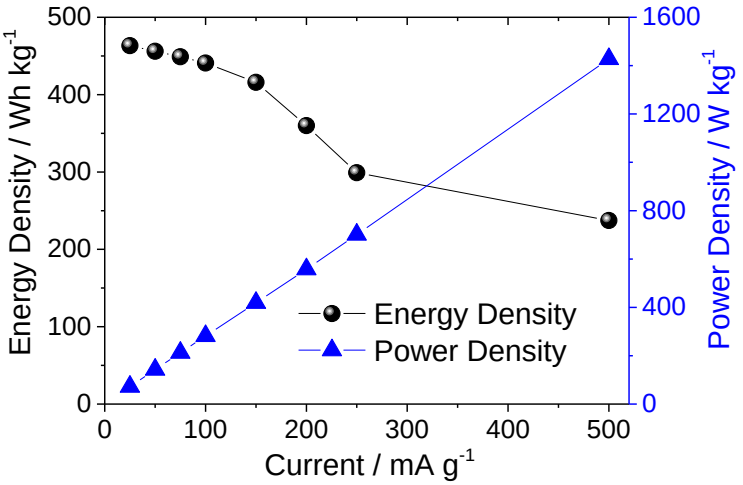

Figure A2.5 Energy density and power density of the Sn-C/Pyr_{14}FSI-LiTFSI/LFP lithium ion cell vs. the discharge current.

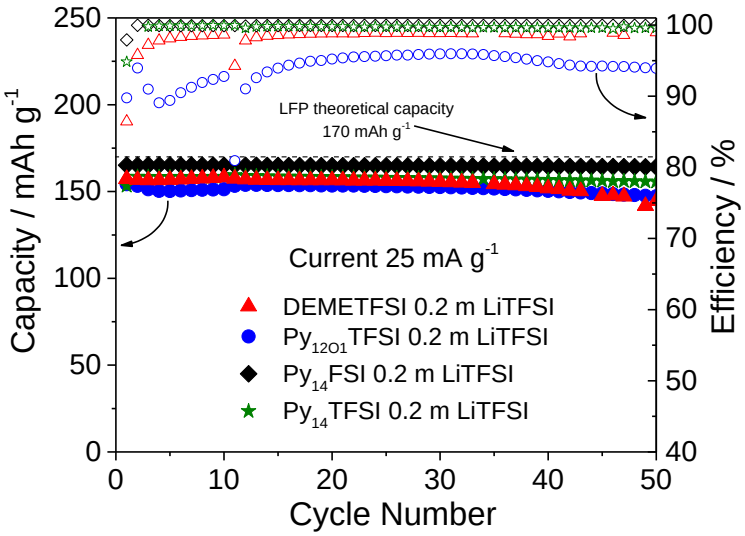

Figure A2.6 Cycling trend and coulombic efficiency of the Sn-C/IL/LFP cells at 25 mA g^{-1} current (0.12 mA cm^{-2}). Voltage cut-off 2.2-4 V. Pyr_{14}TFSI-LiTFSI (green), Pyr_{14}FSI-LiTFSI (black), Pyr_{12O1}TFSI-LiTFSI (blue), DEMETFSI-LiTFSI (red). All measurements at 40°C

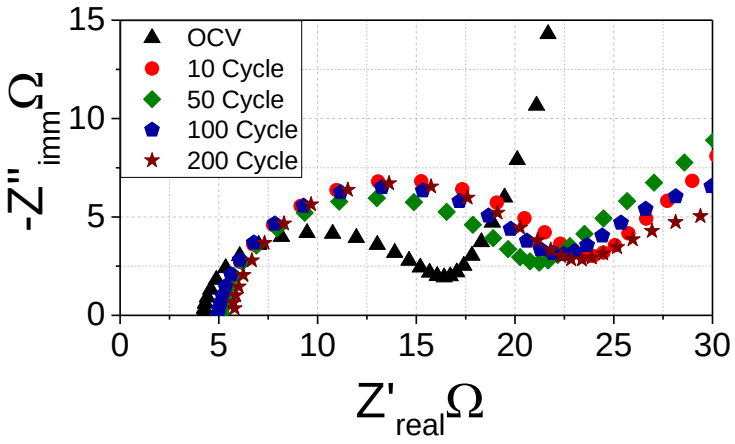

(a)

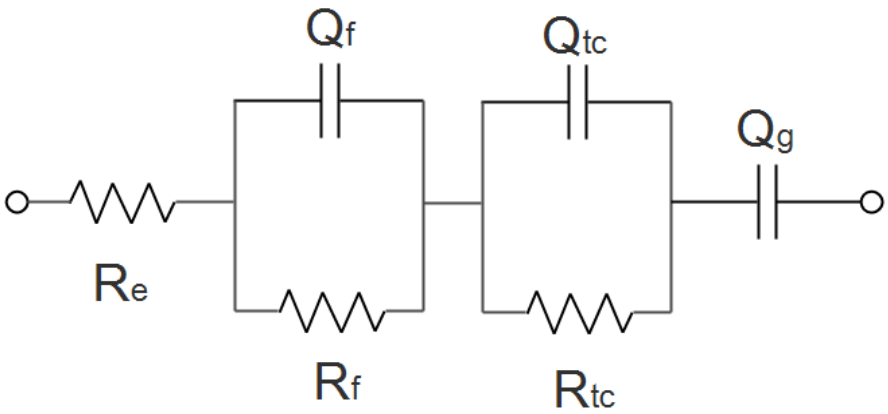

(b)

Figure A2.7 a) Electrochemical impedance spectroscopy (EIS) Nyquist plot during cycling of the Sn-C/Pyr_{14}FSI-LiTFSI/LFP cell. Frequency range 1 MHz-10 mHz (10 mV signal amplitude), cycling test at 100 mA g^{-1} of current, voltage limits 2-3.8 V, 40°C temperature. b) $R_e(R_fQ_f)(R_{tc}Q_{tc})Q_g$ equivalent circuit, where R_e represents the resistance of the electrolyte, R_f and Q_f the resistance and the capacitance of the SEI film, R_{tc} and Q_{tc} the resistance and capacitance of the charge transfer process and Q_g the cell capacitance, respectively.

Chapter 3: Beyond lithium-ion systems

In this chapter, two different beyond lithium-ion systems will be studied, namely Li-O_2 and Li-Sulfur, using alternative, safer electrolytes with respect to conventional ones. *N*,*N*-diethyl-*N*-(2-methoxyethyl)-*N*-methylammonium bis(trifluoromethanesulfonyl)imide (DEMETFSI) is used for application as electrolyte component in lithium-oxygen cells. In chapter 3.1, the previous study is extended by fully characterizing the DEMETFSI-based electrolyte in terms of electrochemical and chemical stabilities, as well as charge-discharge cycling in lithium-oxygen cells at various temperatures. The reversibility of the electrochemical process is studied by ex-situ powder X-ray diffraction (XRD) and supported by scanning electron microscopy (SEM). It is found that increasing temperature results in changing the morphology of the Li_2O_2 deposited at the cathode and increasing the cell energy efficiency. Additionally, the suitability of the DEMETFSI–based electrolyte for application in lithium-ion-oxygen cells is demonstrated, using a carbon-coated $Zn_{0.9}Fe_{0.1}O$ (TMO-C) lithium-alloy-conversion anode. In chapter 3.2 the electrochemical behavior of Li/O_2 cells formed by employing new positive electrode configurations is studied in the same IL-based electrolyte, that is DEMETFSI-LiTFSI. The electrodes supporting the O_2 reaction have been prepared both by either roll pressing or spray deposition on glass fiber, of high surface area, electron conductive carbon black (Ketjenblack) using polytetrafluoroethylene (PTFE) as a binder, known to enhance the ORR/OER reversibility [227,290]. The electrochemical study is supported by scanning electron microscopy (SEM), to understand the effects of the cathode preparation technique and morphology on the cell performance. The optimal electrode configuration is employed in a promising Li-ion oxygen cell in which the lithium metal is replaced by lithiated Sn-C nanostructured electrode. In chapter 3.3, an all-solid-state lithium-sulfur battery configuration is investigated. Three different carbon, iron disulfide, sulfur (C-FeS_2-S)-based composites are proposed as alternative cathodes. The composites are characterized by an increasing sulfur content, namely C:FeS_2 40:60 (wt.%, referred as sample CF), C:FeS_2:Sulfur 40:50:10 (wt.%, referred as sample CFS(8:2)), C:FeS_2:Sulfur 40:30:30 (wt.%, referred as sample CFS(5:5)). The composites are synthesized by a facile and relatively cheap, single-step ball milling procedure. It is shown that the crystalline structure (evaluated by XRD) and the morphology of the materials (evaluated by SEM) are greatly influenced by the ratio of the components, in particular by the FeS_2:S ratio. For all-solid-state cell assembly, a

LiI added, sulfide-based electrolyte is used, namely LiI-Li_3PS_4 [164]. Differential capacity plots, derived from galvanostatic cycling, are used to discuss the peculiar electrochemical features of these materials. The cells, which benefit from the use of a lithium metal anode, can deliver a capacity as high as 1200 mAh g^{-1}_{AM} at the intermediate loading of 1mg_{AM} cm^{-2}, and up to 4.10 mAh cm^{-2}, using active material loadings as high as of 5mg_{AM} cm^{-2} at 20 °C, that is one of the targets for Li/S batteries commercialization [193].

Chapter 3 Experimental

DEMETFSI ionic liquid was synthesized from N,N-diethylmethylamine (Sigma Aldrich) and 2-bromoethyl methyl ether (Sigma Aldrich). After N,N-diethylmethylamine distillation, the two chemicals were mixed in a 1:1 molar ration. The same volume of THF was added as buffer solvent. The solution was kept in a sealed glass holder under continuous stirring at 40°C for one week. The synthesized precursor was then completely dried in a rotary evaporator. Subsequent anion exchange was performed to replace Br^- with $TFSI^-$ in ultrapure water using LiTFSI as the anion source. Further 3% mole of LiTFSI was added to ensure complete reaction. The final product, DEMETFSI was insoluble in water. The latter was first rinsed with water several times, to remove bromide, and finally purified with activated charcoal and alumina using ethyl acetate as a solvent. Finally, DEMETFSI was dried stepwise in the range of 500 to 10^{-7} mbar at 80°C. The water content was measured to be less than 5ppm (detection limit) as determined by Karl Fischer titration. The electrolyte solution was prepared by mixing 0.2 mol kg^{-1} of lithium bis(trifluoromethanesulfonyl)imide (LiTFSI, 3M, battery grade) with *N*,*N*-diethyl-*N*-(2-methoxyethyl)-*N*-methylammonium bis(trifluoromethanesulfonyl)imide (DEMETFSI) ionic liquid, in an argon-filled glove box with oxygen and water contents below 1 ppm. The DEMETFSI-LiTFSI electrolyte mixture was dried stepwise in the range of 500 to 10^{-7} mbar at 80°C until the water content was reduced to less than 5 ppm (detection limit) as determined by Karl Fischer titration. The electrolyte conductivity Arrhenius plot was obtained by electrochemical impedance spectroscopy (EIS, Mmates-Biologic) using sealed Pt-black/Pt-black cells (Mmates) with a K value of 1 cm^{-1} in a Julabo FP50 refrigerated/heating circulator for temperature control. The cell constant was confirmed using a standard 0.1M KCl water solution (Fluka). The viscosity of the DEMETFSI-

LiTFSI electrolyte was evaluated at various temperatures in a dry room environment using an Anton-Paar Physica MCR301 rheometer, applying constant shear rates using a liquid nitrogen-based cooling unit and an electrical oven heating. The lithium/electrolyte interface stability was evaluated using impedance spectroscopy of symmetrical Li/DEME-LiTFSI/Li cells during storage time at various temperatures (30, 40 and 60 °C) using coin cell cases. The impedance measurements were performed within the frequency range from 200 kHz to 10 mHz, applying a sinusoidal voltage perturbation with an amplitude of 10 mV. The cycling stability of lithium metal in the DEMETFSI-LiTFSI electrolyte was evaluated at various temperatures (30, 40, and 60 °C) by stripping/deposition cycle tests on symmetrical Li/DEMETFSI-LiTFSI/Li cells using a current of 0.1 mA cm^{-2} and deposition/stripping times of 1 hour (each) using coin cell cases. The electrochemical anodic stability of the electrolyte was evaluated by linear sweep voltammetry with a scan rate of 0.1 mV s^{-1}, using the Super-C65 working electrode coated on aluminum foil. The cathodic stability was determined by cyclic voltammetry in a 0.01-2 V potential range at 0.1 mV s^{-1} scan rate employing a Super-C65 working electrode coated on copper foil. The electrochemical stability window was evaluated at different temperatures, i.e. 30, 40 and 60 °C, using Swagelok-type cells with lithium metal as reference electrode. All electrochemical tests were carried out in thermostated climatic chambers with a deviation of ± 1°C. The cathodes for the lithium-oxygen cycling tests presented in sub-chapter 3.1 were prepared by doctor-blade technique, casting a slurry composed of C-NERGY Super C65 (Imerys) and PVDF (6020 Solef, Solvay) in an 8:2 weight ratio, dispersed in N-methyl-2-pyrrolidinone (NMP, Aldrich 99.9 %) on a gas diffusion layer (GDL, SGL-35BC carbon paper, SGL). After drying, the GDL were punched in disk-shaped electrodes having a diameter of 16 mm. The residual solvent was removed under vacuum at 110 °C overnight. The Super C65 carbon electrodes loading ranged from 0.5 to 0.8 mg cm^{-2}. Cycling tests were carried out galvanostatically at various temperatures (30, 40, and 60 °C) by liming the capacity to 500 and 1500 mAh g^{-1} (applying a specific current of 50 mA g^{-1} and 100 mA g^{-1}, respectively). To determine the achievable capacity of this system, the cells were cycled in the full voltage range, i.e., 2.0-4.0 V, using a current of 100 mA g^{-1} at 30 °C temperature. The cathodes for the lithium-oxygen cycling tests presented in sub-chapter 3.2, were prepared either as self-standing electrodes (SSEs) or as spray deposited electrodes (SDEs) The preparation of SSEs involved the use of ketjenblack EC-600JD and polytetrafluoroethylene (60 wt.% PTFE dispersion in H_2O; Sigma Aldrich). The two compounds were homogeneously mixed in a 90:10 w:w ratio (carbon:PTFE) using an agate mortar until obtaining a rubber-like composite. The obtained composite was first hand-rolled on a Mylar foil, and then roll-pressed between two Mylar

foils using a calendaring machine, until a thickness lower than 300μm was achieved. Finally, the obtained tape was cut into 16 mm disks which were dried under vacuum at 110°C overnight (Figure 3.1a). The preparation of SDEs also involved the use of ketjenblack EC-600JD and polytetrafluoroethylene 60 wt. % dispersion in H_2O. The two compounds were mixed by stirring for 24 hours a slurry of carbon:PTFE (9:1 weight ratio dispersed in a mixture of water and isopropyl alcohol (8:2 w:w). The obtained dispersion was spray deposited on a Whatman® GF/A glass fiber separator. Finally, disks of 16 mm diameter were cut and dried under vacuum at 110°C overnight (Figure 3.2b). The properties of the developed electrodes are summarized in Table 3.1.

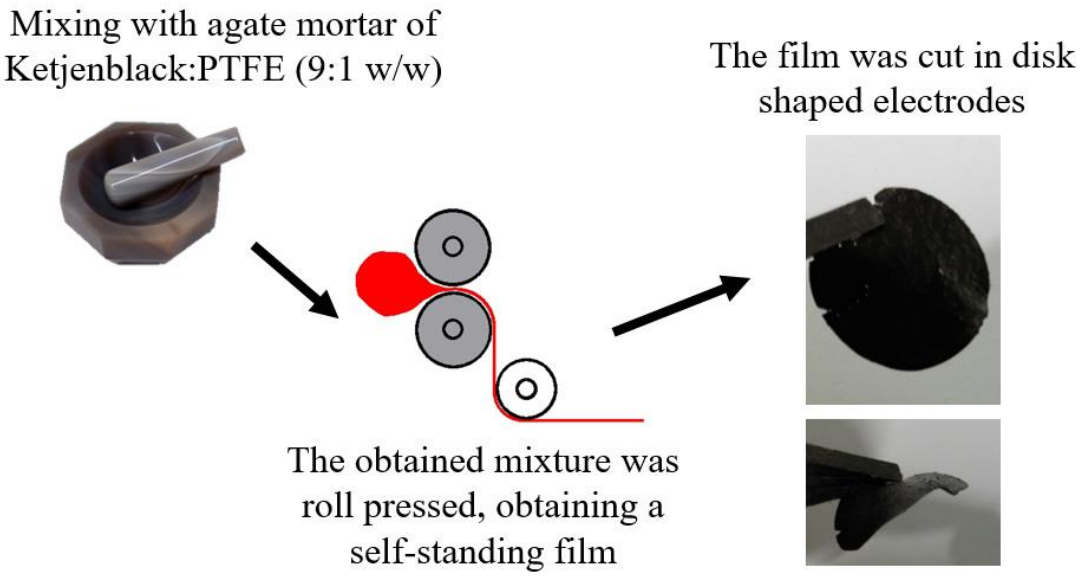

(a)

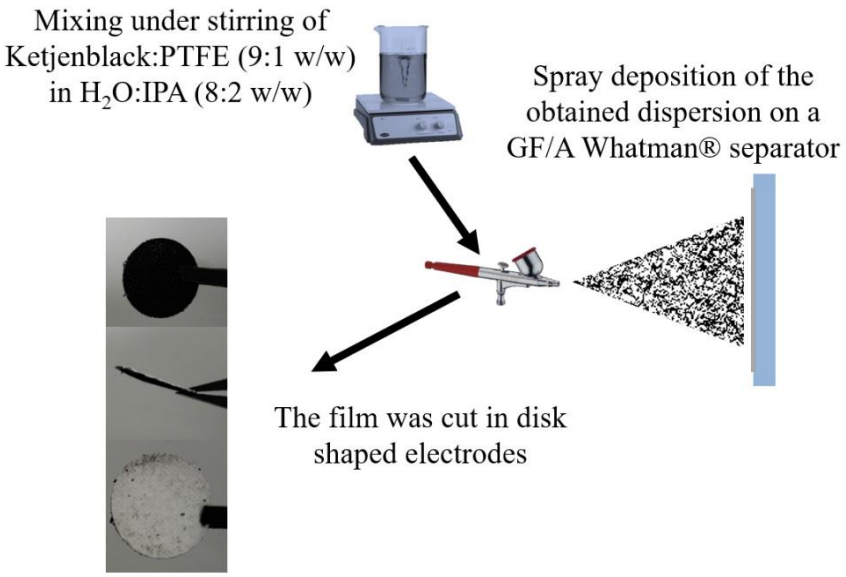

(b)

Figure 3.1 (a) Scheme of the preparation of the SSE. (b) Scheme of the preparation of the SDE. For electrode's acronym see experimental section.

Cathode	Thickness	Loading	Thickness (with support)	Loading (with support)
SSE	200-250 μm	15-20 mg cm^{-2}	200-250 μm	15-20 mg cm^{-2}
SDE	30-40 μm	0.8-1.5 mg cm^{-2}	290-300 μm	6.2-6.9 mg cm^{-2}

Table 3.1. Characteristics of the SSE and SDE samples.

The cycling behavior of the Li/O_2 cells employing both SDEs, SSEs and DEMETFSI-LiTFSI electrolyte was evaluated at 60 °C applying constant currents of 50 or100 μA cm^{-2}, but limiting the delivered capacity to 0.5 or 1 mAh cm^{-2}. The carbon-coated $Zn_{0.9}Fe_{0.1}O_2$ (TMO-C), used in sub-

chapter 3.1, was prepared using a procedure described in a previous paper, but with higher carbon content, namely 40% [74]. The electrode was obtained by casting a slurry composed of 70% active material, 20% C-NERGY Super C65 (Imerys) and 10 % PVDF (6020 Solef, Solvay) dispersed in N-methyl-2-pyrrolidinone (NMP, Aldrich 99.9 %) on a copper foil. After drying, the copper foil was punched in disk-shaped electrodes having a diameter of 16 mm. The residual solvent was removed under vacuum at 110 °C overnight. The TMO-C electrodes loading ranged from 2 to 3 mg cm^{-2}. The electrochemical characterization of the anode was performed using a 2032 coin-cell and lithium metal as anode, a sheet of Whatman glass fiber GF/A soaked with the electrolyte as separator, and the TMO-C electrodes as cathode. The full lithium-ion-oxygen cell was assembled using TMO-C as anode [272,291]. The "$Li_xZn_{0.9}Fe_{0.1}O_2$"-C/DEMETFSI-LiTFSI/O_2 cell was cycled using a constant current of 50 mA g^{-1} and limiting the capacity to 500 mAh g^{-1} at 30 °C temperature. "$Li_xZn_{0.9}Fe_{0.1}O_2$" is a symbolic expression for the phase mixture resulting from the partial lithiation of $Zn_{0.9}Fe_{0.1}O_2$, according to the following reaction:

$$Zn_{0.9}Fe_{0.1}O + 2.9Li^+ + 2.9e^- \rightleftharpoons 0.9LiZn + 0.1Fe^0 + Li_2O$$

The Sn-C material, used in sub-chapter 3.2, was synthesized according to the procedure reported in the literature by impregnating a porous, hydro-gel, resorcinol-formaldehyde matrix with a tin-organometallic precursor (therbuthylphenyl-tin) followed by annealing at 700 °C for 2h [263]. The electrode was prepared by wet casting on a dendritic copper foil a slurry composed by Sn-C, C-NERGY Super C65 (Imerys) and PVDF (6020 Solef, Solvay) in the 8:1:1 weight ratio, using N-methyl-2-pyrrolidinone (Aldrich 99.9 %) as a dispersing agent. The electrodes, with an average loading of about 4 mg cm^{-2}, were cut as disks (16 mm diameter) dried under vacuum at 110°C overnight. The so prepared Sn-C electrodes were subsequently pre-activated using lithium metal and the controlled force-time method [264]. The procedure consisted in pressing a lithium metal foil wet by the LP30 solution (EC:DMC, 1:1, $LiPF_6$, 1M) against the Sn-C electrode at 4 kg/cm^2 for 3 hours. In this way, fully lithiated Sn-C electrodes were obtained. The cycling behavior of the Sn-C electrode at various temperatures was evaluated in T-type cells, using DEMETFSI-LiTFSI as the electrolyte, by galvanostatic cycling at 25 mA g^{-1}, within 0.01-2V voltage range. Li_xSn-C/DEMETFSI 0.2 m LiTFSI/SSE,O_2 full lithium-ion cells were assembled coupling lithiated Sn-C and SSE electrodes. These cells were cycled limiting the capacity to 0.5 mAh cm^{-2} at a current of 50 μA cm^{-2}. All galvanostatic cycling tests were performed using a Maccor 4000 Battery Test System. Gravimetric specific current and gravimetric specific capacity are referred to the Super C65 carbon mass on the

cathode. Areal capacities are referred to the cathode surface of 2.0 cm^2 (disks with Ø16mm). All electrochemical tests were carried in thermostated climatic chamber with a maximum deviation of ± 1°C. The electrochemical characterization of lithium and lithium-ion oxygen cells was performed using a top-meshed 2032 coin-cell, lithium metal as anode, a sheet of Whatman glass fiber GF/A soaked by the electrolyte as separator, and carbon electrodes as cathode. Each cell was kept in static O_2 atmosphere using an air-tight glass tube flushed (Figure 3.1) for 15min with ultrapure oxygen (ALPHAGAZ™ 2, 99.9995%, Air liquid).

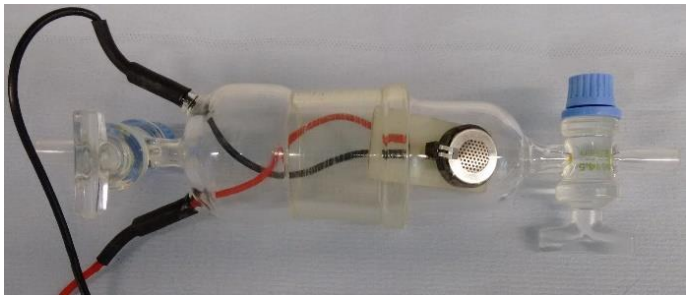

Figure 3.1 Air-tight glass tube for Li/O_2 cells tests

For the synthesis of the materials presented in sub-chapter 3.3, MAXSORB activated carbon (KANSAI COKE AND CHEMICALS CO., LTD.), elemental sulfur (99.998%, Sigma-Aldrich) and FeS_2 (-325 mesh, 99.8%, Sigma-Aldrich) were dried and transferred in an Ar-filled UNIlab glove box (MBRAUN, O_2 and H_2O concentration < 0.1ppm). Three different composites were synthesized, with an increasing sulfur content, namely C:FeS_2 40:60 (wt.%, referred as sample CF), C:FeS_2:Sulfur 40:50:10 (wt.%, referred as sample CFS(8:2)), C:FeS_2:Sulfur 40:30:30 (wt.%, referred as sample CFS(5:5)). The materials were weighted in the desired ratio and ground in an agate mortar. Each mixture was then transferred in ZrO_2 80mL jars filled with 10g Ø0.1cm, 17 Ø0.5cm and 10 Ø10cm ZrO_2 balls. The jars were sealed under inert Ar atmosphere using parafilm and an additional clamping system to avoid exposure to air atmosphere. Finally, the materials were ball-milled in a Pulverisette 4 (FRITSCH), alternating a ball-milling step at 360rpm (45min) with a cooling step (15min). This procedure was repeated for 17 times (total ball-milling time of ca. 13h). The jars were then transferred in an Ar-filled glove box, the mixtures were recovered and separated from the ZrO_2 balls, ground in an agate mortar and mixed in a 1:1 weight ratio with a Li_3PS_4-LiI (LPSI) solid electrolyte (solid electrolyte was synthesized according to a procedure previously reported [164]). The mixtures were then transferred in ZrO_2 45mL jars filled with 10g Ø0.1cm, 17 Ø0.5cm and 10 Ø10cm ZrO_2 balls. The jars were sealed under inert Ar atmosphere using parafilm and an additional

clamping system to avoid exposure to air atmosphere. Finally, the materials were ball-milled in a Pulverisette 4 (FRITSCH), alternating a ball-milling step at 360rpm (45min) with a cooling step (15min). The jars were then transferred in an Ar-filled glove box, the material was recovered and ground in an agate mortar, then used for the electrochemical characterization as cathode. The final, solid electrolyte-added composites, were labeled as CF-LPSI, CFS(8:2)-LPSI and CFS(5:5)-LPSI. For cell assembly, an in-house Ø1.3cm two electrode cell setup was employed [144]. This setup (figure 3.2a) allows the cell pellet to be prepared directly inside the casing. After closing, by using a screw in the upper part and by employing a precision torque wrench, a constant force can be applied to the pelletized cell (figure 3.3b and c). Specifically, a cylindrical Teflon insulator case with an internal Ø1.3 cm hole is used to prepare the pellet. The holder is filled with ca. 300 mg of Li_3PS_4-LiI (LPSI) and hand pressed to form a pre-pellet. Following varying amounts of solid electrolyte-cathode composites were inserted in the top of the pre-pellet, spread on the surface and hand pressed. Active material loading was of 1.0-5.0 mg cm^{-2}, and the total amount of $S+FeS_2$ was considered. A lithium metal disk (thickness = 30 μm, Ø1.2cm. Honjo Metal, Osaka) was used as the anode. The pre-formed electrodes/electrolyte pellet is finally pressed at 10 MPa for 30 s, at 25 °C, using a YLJ-24 hydraulic press (MTI corp.). After assembling the solid cell and the upper current collectors, the top screw was fastened by applying a torque of 3Nm using a preset torque wrench, i.e., a condition suitable for maintaining the proper contact between cell components and ensuring mechanical stability of the formed pellet. The electrochemical tests were carried out in sealed aluminum bags under Ar atmosphere, to avoid possible exposure of the sample to the air. Ionic conductivity tests were performed using stainless steel working and counter electrodes, and by determining the solid electrolyte pellet thickness after the final step involving the hydraulic press. Ionic conductivity has been determined by potentiostatic electrochemical impedance spectroscopy, using a potentiostat/galvanostat Solartron Ametek SI1260+1287, in the 0.1 Hz – 10 MHz frequency range, using a 10 mV amplitude, in a -20 – 70 °C temperature range. All galvanostatic cycling tests were performed in the 1.3-3.1 V voltage range, using a Maccor 4000 Battery Test System, at 20 °C. All electrochemical tests were performed in thermostated climatic chambers at with a maximum deviation of ± 1°C. The cells were held at OCV for 12 hours before testing and between temperature changes.

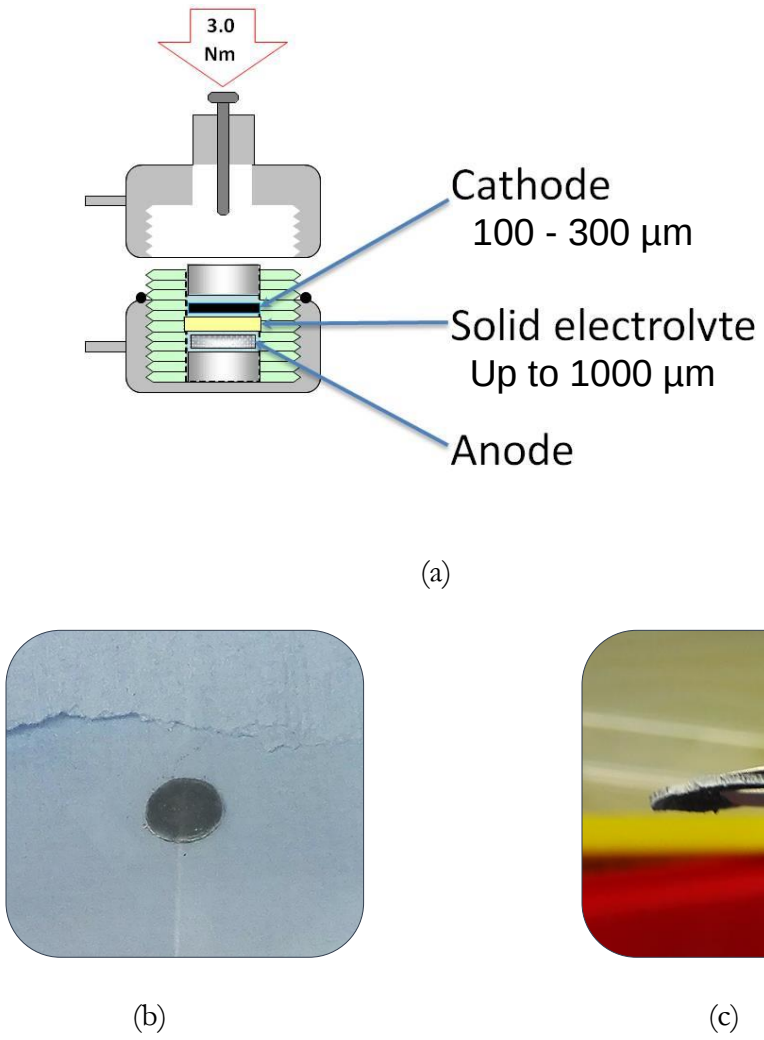

Figure 3.2 (a) Cylindrical cell configuration, (b) pelletized cell, Ø 1.3 cm, (c) pelletized cell, 0.9mm thickness

The morphological and structural characterization for all the samples were performed by field emission scanning electron microscopy (Zeiss LEO1550VP Gemini) and powder X-ray diffraction (Bruker D8 Advance diffractometer, Bragg-Brentano theta-2theta configuration, equipped with a Cu K_α source λ=0.154 nm). For air-sensitive materials (ex-situ and sulfide-based materials), an airtight, Ar-filled sample holder was used to transfer the samples from the glovebox to the SEM chamber. For XRD measurements, either Kapton tape and air-tight samples holders were employed to avoid sample degradation. Before SEM and XRD analyses, the studied electrodes used for ex-situ analysis were rinsed using dimethyl carbonate to remove residual salt and/or ionic liquid and carefully dried under vacuum. Thermo-gravimetric analysis (TGA) was performed under N_2 stream, using air-tight

aluminum pans sealed under Ar atmosphere, in a temperature range of 30-600 °C, with a constant heating rate of 10°C/min by using a Discovery TGA (TA Instruments).

3.1 Ionic liquids: $Zn_{0.9}Fe_{0.1}O_2$-C/DEMETFSI-LiTFSI/O_2

Figure 3.1.1 illustrates the electrochemical properties of the DEMETFSI-LiTFSI electrolyte. The Arrhenius plot within 0-60 °C temperature range (Fig. 3.1.1a) reveals a conductivity value of $3.5x10^{-4}$ S cm^{-1} at 0°C, which greatly improves with temperature to reach 2.2 $x10^{-3}$ S cm^{-1} at 30 °C, 3.4 $x10^{-3}$ S cm^{-1} at 40 °C and 6.6 $x10^{-3}$ S cm^{-1} at 60 °C, i.e. values considered suitable for application in high performances lithium-oxygen batteries [86]. The inset of Fig. 3.1.1a shows the viscosity of the DEMETFSI-LiTFSI electrolyte within the same temperature range. The graph shows a relatively high value at 0 °C (above 500 mP s) that rapidly decreases by raising the temperature to 30 °C (80 mP s) and 60 °C (24 mP s). Conductivity and viscosity, correlated according to the Walden rule in this temperature range and operating conditions [273], deviate from the linear Arrhenius-type behavior and are more properly described by the Vogel-Fulcher-Tammann (VFT) model [102] in the low-temperature domain. A more detailed description, according to the VFT mathematical model, is reported in the previous section (chapter 2.1). The increase of the electrolyte conductivity at higher temperatures, directly related to the decreased viscosity [91,102], is expected to greatly improve the electrochemical performance of the system [23]. Therefore, the features of the electrolyte have been investigated at various temperatures. Fig. 3.1.1b reports the electrochemical stability window of the electrolyte the carbon electrode at various temperatures, i.e., 30°C (blue line) 40°C (orange line) 60°C (red line). The first cathodic scan reveals a broad peak (circled in green), which has no corresponding peak in the following anodic scan. Thus, it is associated with the irreversible solid electrolyte interphase (SEI) formation at the carbon surface [292–294], which limits further electrolyte decomposition during the following cycles (see 2nd cycle in inset of Fig. 3.1.1b). The irreversible peak associated to the SEI formation shifts to higher potential values by increasing the temperature, i.e., from 0.4 V at 30 °C (blue curve) to 0.5 V at 40 °C (orange curve) and to 0.6 V at 60 °C (red curve) [280]. In fact, the higher temperatures may lead to faster kinetics of the reductive formation of the SEI layer and to an increased electrolyte conductivity [280]. Consequently, the electrolyte decomposition takes place at higher potentials. At the lowest temperature (30 °C), a shoulder on the anodic side of the SEI-formation peak is observed, which might be related to the IL cation insertion into the carbon occurring before SEI formation. Following the first irreversible peak a second reversible (an anodic counter peak is also shown) peak

appears at about 0.1 V vs. Li/Li^+, associated to the lithium storage in the amorphous carbon electrode [46,280]. The intensity of this peak increases with temperature as a results of the increased electrolyte conductivity as well as electrochemical activity at higher temperature [280]. The second cycle (inset of Fig. 3.1.1b) shows only the features corresponding to the electrochemical lithium uptake into amorphous carbon (no further evidences of electrolyte decomposition processes), revealing the stability of the SEI film at the electrode surface. The corresponding anodic scans in Fig. 3.1.1b indicate a decrease of the oxidative degradation potential of the IL-electrolyte by heating, as expected, owing to the enhanced decomposition reaction kinetics. Accordingly, the DEMETFSI-LiTFSI electrolyte shows a stability extended up to 5.00 V vs. Li/Li^+ at 30 °C (blue curve), decreasing to 4.87 V vs. Li/Li^+ at 40 °C (orange curve) and finally to 4.68 V vs. Li/Li^+ at 60 °C (red curve). The voltage values are associated with an increase of current density of at least 8 $\mu A\ cm^{-2}$. The stability of the lithium/electrolyte interface was investigated by monitoring the impedance evolution of symmetrical Li/DEMETFSI-LiTFSI/Li cells at various temperatures. Non-linear least square (NLLSQ) analysis [286,287] of the Nyquist impedance spectra (see Appendix 3, Fig. A3.1) has been performed. The obtained time-evolution of the interface resistance at various temperatures is reported in Fig. 3.1.1c. The figure evidences a quite stable trend at 30°C (blue), 40°C (orange) as well as at 60°C (red). With increasing temperatures, the value of the interface resistance decreased from 200 **Ω** at 30 °C, to 120 **Ω** at 40 °C and finally to 40 **Ω** at 60 °C. This trend may be ascribed to the decrease of the resistivity of the SEI formed at the lithium metal surface when exposed to elevated temperatures as reported in the literature [295]. The very modest increase of the resistance at the higher temperatures indicates that the reactivity of the electrolyte with lithium metal does not sharply increase with temperature, confirming that a stable lithium/electrolyte interface is established within the investigated temperature range. The ability of the electrolyte to sustain an efficient lithium dissolution/plating process was investigated by stripping/deposition measurements at various temperatures. Figure 3.1.1d reports the voltage profile of the measurement performed at 30°C (blue), 40°C (orange) and 60°C (blue) with current density of $\pm 0.1\ mA\ cm^{-2}$. The data reveal a decrease of the polarization associated to lithium dissolution/plating process by increasing temperature, i.e., from a value of about 0.1 V at 30°C to 0.05 V at 40°C and finally to 0.025 V at 60°C. This trend is ascribed to the increase of the ionic conductivity of the electrolyte promoted by the decrease of its viscosity upon heating, and of to the concomitant decrease of the interfacial resistance of the cell. Furthermore, the measurement shows a stable polarization upon time, further

evidenced by the magnification of the voltage profiles related to selected cycles (1st, 2nd, 123rd, 124th), reported in the inset of Fig. 3.1.1d. The V(t) plots reveal very stable trend, without signs of voltage spikes or irregularities which are usually a hint of unstable SEI formation/reconstruction [296,297], and occasionally observed in other ionic liquid based electrolytes [295]. This behavior is particularly relevant for the cells at higher temperatures, in which a steady, flat profile is observed from the 2nd cycle onwards, thus again suggesting a very stable lithium/electrolyte interface even upon plating/stripping.

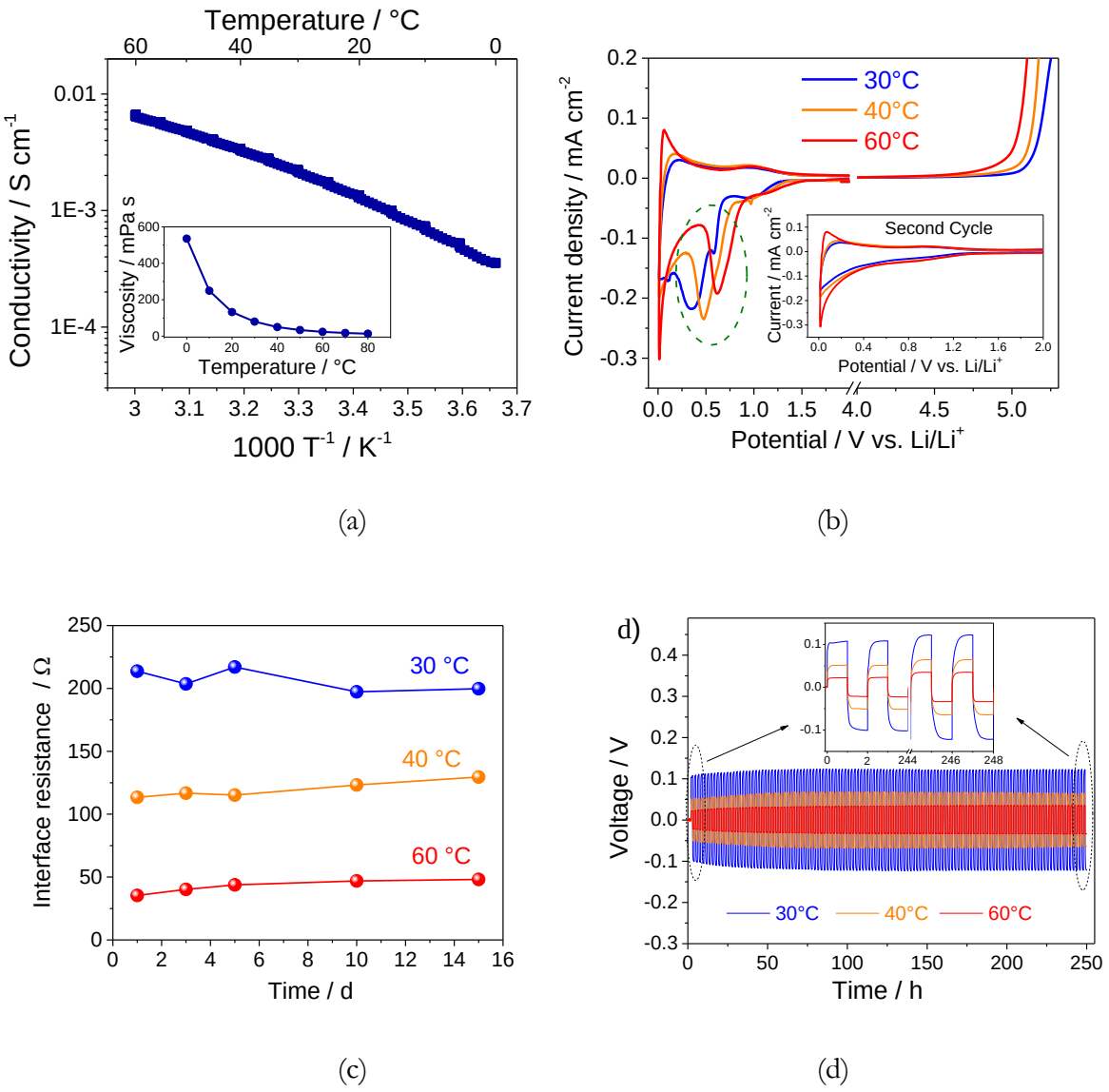

Figure 3.1.1 (a) Arrhenius plot of the DEMETFSI-LiTFSI electrolyte with the viscosity vs. temperature plot (inset) (b) Current vs. potential plot of the LSV and of the CV performed on a Li/DEMETFSI-LiTFSI/Super-C65 cell using a scan rate of 0.1 mV s^{-1} at various temperatures: 30 °C (blue), 40 °C (orange), 60 °C (red). (c) Time evolution of the interphase resistance of symmetrical Li/DEMETFSI-LiTFSI/Li at various temperatures: 30 °C (blue), 40 °C (orange), 60 °C (red). (d) Time evolution of the cell voltage and, in inset, magnification of the 1st, 2nd, 123rd and 124th cycle during stripping-deposition measurements performed on a symmetrical Li/DEMETFSI-LiTFSI/Li cell using a current of 0.1 mA cm^{-2} and a deposition-stripping time of 1 hour at various temperatures: 30 °C (blue), 40 °C (orange), 60 °C (red).

The DEMETFSI-LiTFSI electrolyte was subsequently tested in lithium-oxygen cells using a carbon-based cathode. Fig. 3.1.2a reports the voltage signature of the cell cycled at 100 mA g^{-1} within 2V

and 4 V at 30°C. The cell shows a flat discharge at about 2.5 V due to the electrochemical deposition of lithium peroxide at the carbon electrode surface, resulting in the delivered capacity of about 13 Ah g^{-1}_{carbon}. This extremely high capacity leads to a theoretical energy density of about 32.5 kWh kg^{-1}_{carbon}, which is extremely promising even considering the reduction factor originating from the additional weight coming from other cell components, including casing, membranes for oxygen separation from air, which is considered a requirement for transitioning from Li-O_2 to Li-air systems [298,299], and the battery management system (BMS). Moreover, the cell shows good reversibility and a coulombic efficiency of 94%, considered a good value in this voltage range, given the current state of the art of electrolytes for Li-O_2 batteries [225,237]. The reversibility of the electrochemical process is also suggested by the ex situ XRD and SEM studies. Fig. 3.1.2b shows the SEM micrograph of the pristine carbon electrode, evidencing the typical morphology of Super C65. Upon full discharge process (Fig. 3.1.2c) the SEM micrograph of the cathode reveals the formation of lithium peroxide Li_2O_2 showing disk-like particles' morphology, which, to the best to our knowledge, is originally observed in this study. The SEM micrograph of the cathode upon full recharge (Fig. 3.1.2d) shows, once more, the morphology associated to pristine carbon as, indeed, expected from the high reversibility of the electrochemical process indicating the almost complete dissolution of the Li_2O_2 formed during discharge. Further proof of the process reversibility is given by ex-situ XRD measurements of the carbon electrode performed after the (dis-)charge process (Fig. 3.1.2 e-g). Indeed, the XRD pattern before cycling (Fig. 3.1.2e) evidences broad reflection peaks at 2θ values of 45 and 50 degree attributed to the carbon-based electrode. Two new peaks at 2θ values of 32 and 35 degrees, ascribed to Li_2O_2 (indexed by JCPDS 96-210-0228), appear after full discharge (Fig. 3.1.2f). However, after the following charge these Li_2O_2-related reflections almost vanish (Fig. 3.1.2g). This suggests the reversible deposition and subsequent dissolution of the lithium peroxide during the electrochemical processes, which is, in fact, in agreement with the results of the SEM study (compare panels b-d and e-g in Fig 3.1.2).

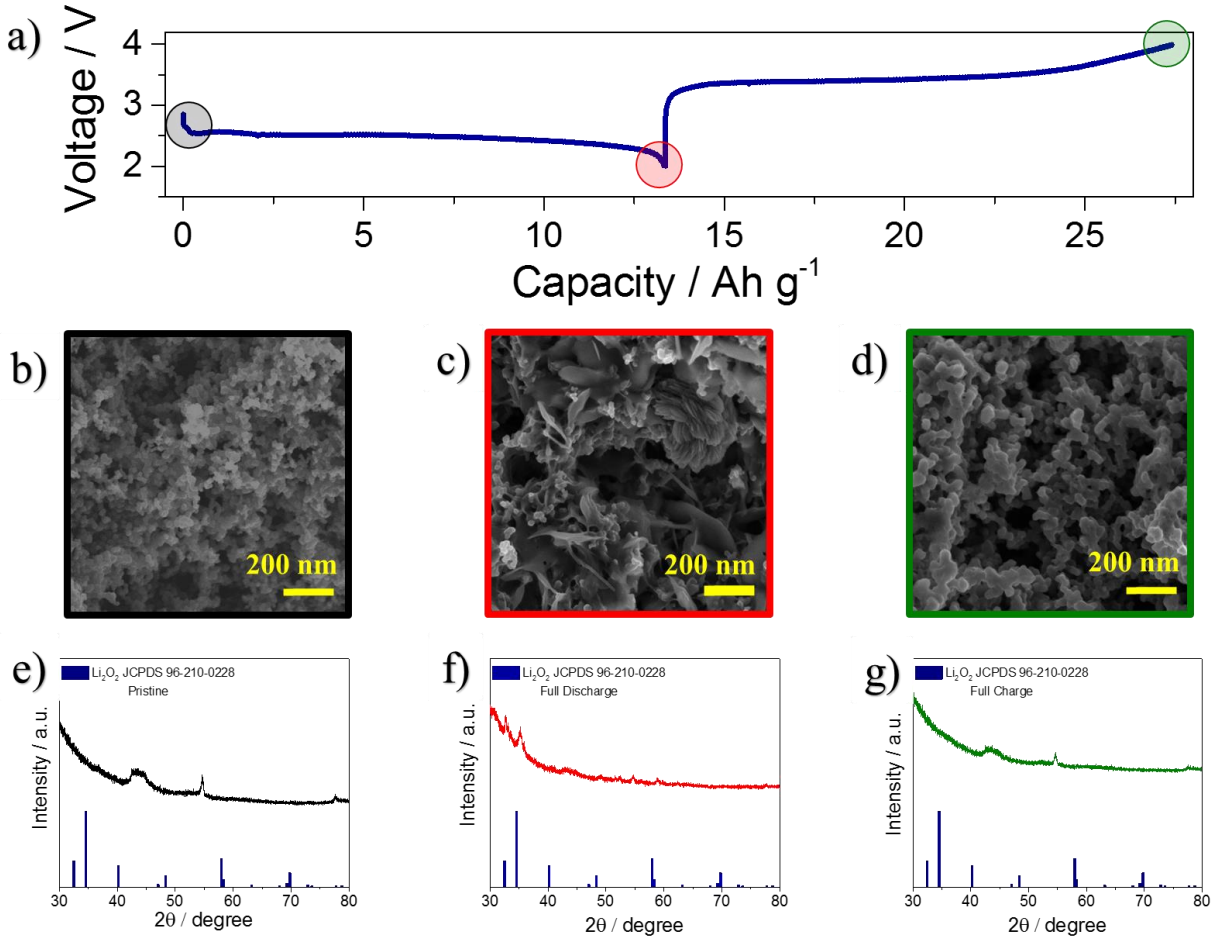

Figure 3.1.2 Structural and morphological characterization of the carbon-based electrode collected from a Li/DEMETFSI-LiTFSI/O_2 cell galvanostatically cycled within the 2-4 V voltage range at 100 mA g^{-1} at 30 °C. (a) Voltage profile of the 1st cycle. The circles indicate the state of charge at which *ex-situ* XRD and SEM analyses of the pristine (b, e), fully charged (c, f) and fully discharged (d, g) electrode, was performed.

Figure 3.1.3a shows the electrochemical performance of the Li/DEMETFSI-LiTFSI/O_2 cell galvanostatically cycled by limiting the delivered capacity to 500 mAh g^{-1} at various temperatures, i.e., 30°C (blue curve) 40°C (orange curve) and 60°C (red curve). The limited capacity condition used for cycling has been already proposed for lithium oxygen cell as the optimal condition for allowing a stable, continuous, charge/discharge operation [238,300]. During the first stages at 30 °C (top left of Fig. 3.1.3a, blue curves) the cell is characterized by stable behaviour and remarkable overlapping of the voltage profiles upon cycling, with a polarization between the (dis-)charge processes of about 0.6 V. At this temperature, slight voltage drops are associated with small temperature variations.

Increasing the temperature during the following cycles results in a significant polarization decrease, i.e., down to 0.55 V at 40 °C (top center of Fig. 3.1.3a, orange curves) and to a value as low as 0.45 V at 60 °C (top right of Fig. 3.1.3a, red curves). This behavior is expected from the combination of the increased ionic conductivity of the electrolyte, the lower value of the electrode/electrolyte interface resistance as well as by the improved kinetics of the electrochemical reaction at higher temperatures. Lowering back the temperature to 30 °C (Fig. 3.1.3a bottom left blue curves) evidence an increase of the cell polarization with respect to the initial cycles (compare with Fig. 3.1.3a top left blue curve), most likely due to possible side reactions at the higher operating temperatures [301]. Likely, further increase of the temperature from 30 °C to 40 °C (bottom center of Fig. 3.1.3a, orange curves) and 60 °C (bottom right of Fig. 3.1.3a red curves) leads to notably decreased cell polarization. Fig. 3.1.3b reports the evolution of the corresponding Li/DEMETFSI-LiTFSI/O_2 energy efficiency upon continuous cycling with changing temperature and evidences the improvement of the cell energy efficiency by heating. Furthermore, the results indicate a stable trend and only minor effects of the repeated heating/cooling on the cell performance.

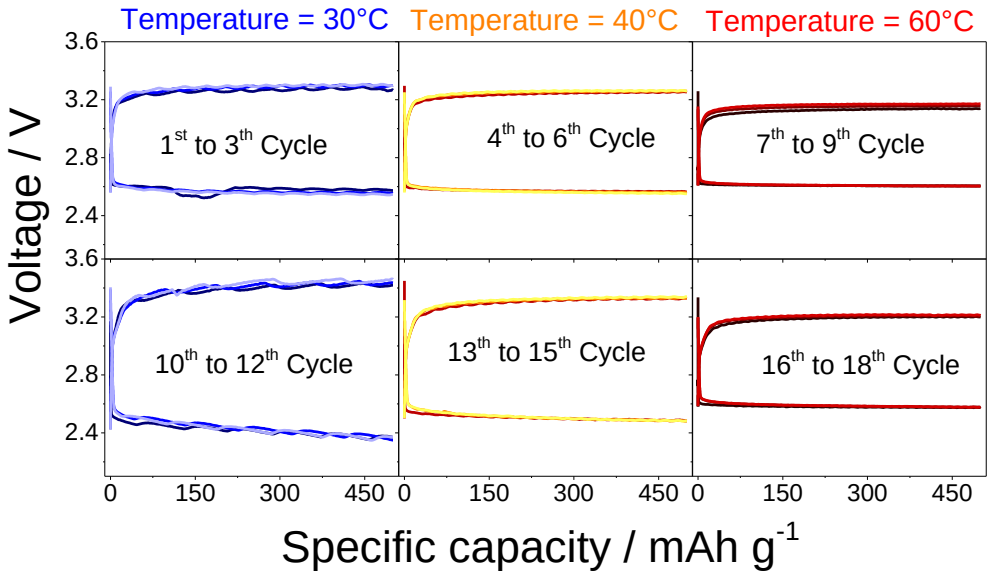

(a)

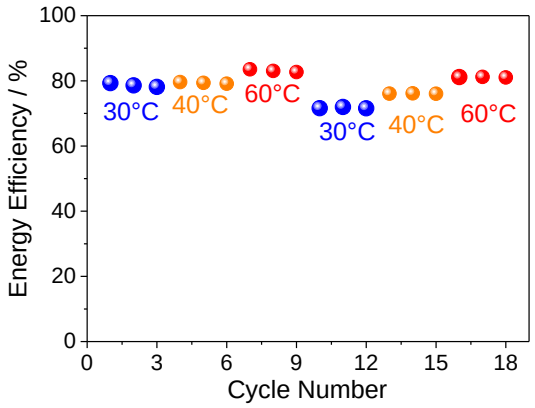

(b)

Figure 3.1.3 Voltage profile (a) and energy efficiency upon cycling (b) of the Li/DEMETFSI-LiTFSI/O_2 cell cycled at various temperatures: 30 °C (blue), 40 °C (orange), 60 °C (red). Current density 50 mA g^{-1}. Capacity limited to 500 mAh g^{-1}.

The Li/DEMETFSI-LiTFSI/O_2 cell has been also investigated by increasing the delivered capacity limit up to 1500 mAh g^{-1}, which corresponds to a geometric surface capacity of about 2.4 mA cm^{-2}, at the various temperatures, i.e., 30°C (Fig. 3.1.4a), 40°C (Fig. 3.1.4b), 60°C (Fig. 3.1.4c). Despite the higher capacity, the cell shows stable cycling performance and reveals the already mentioned reduction of the cell polarization by increasing the temperature with consequent improvement of the energy efficiency (see Appendix 3 Fig. A3.2). Remarkably, only a limited increase of the cell polarization, due to excess deposition of lithium peroxide [229,302] or side reactions at the lithium side [272,303,304], is observed by increasing the capacity limit from 500 to 1500 mAh g^{-1}. Figures 3.1.4d-f report the SEM micrographs of the carbon cathode upon discharge up to 1500 mAh g^{-1} at various operating temperatures. The images evidence, for the first time, the evolution of the discharge product morphology from flat-shape particles at 30 °C to toroidal, flower-shaped particles at 60 °C. An intermediate morphology comprising both shapes is evident at 40 °C. The different morphologies of the discharge products may be ascribed to the electrochemical Li_2O_2 deposition process following two different pathways involving particles growth both at the electrode surface and into the electrolyte. This reaction mechanism is greatly influenced by the temperature, current density, and by the electrolyte ability to stabilize the intermediate superoxide species [305–307]. In summary, we reasonably assume that the positive effect of the temperature increase on the cell

energy efficiency may be ascribed to the improved kinetics of the electrochemical lithium peroxide deposition process, influencing both the reaction pathway and the morphology of the formed products. However, further investigation is still needed to fully clarify this aspect.

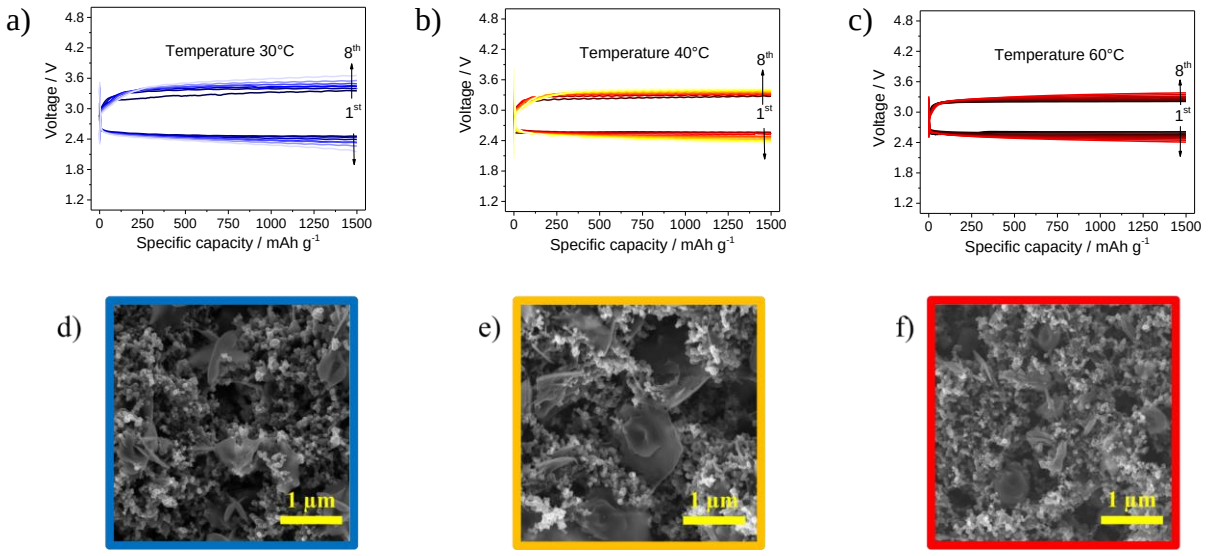

Figure 3.1.4 Voltage profile of the Li/DEMETFSI-LiTFSI/O_2 cell cycled at various temperatures: 30 °C (a), 40 °C (b), 60 °C (c). Current density 100 mA g^{-1}, capacity limited to 1500 mAh g^{-1}. SEM images of the electrode recovered from the cell discharged limiting the capacity to 1500 mAh g^{-1} at a temperature of 30 °C (d, blue), 40 °C (e, orange), 60 °C (f, red).

Approaching the replacement of the lithium metal by a Li-ion anode, carbon-coated $Zn_{0.9}Fe_{0.1}O$ (TMO-C) conversion/alloying anode [74] was used to make a Li-ion-O_2 cell. Figure 3.1.5 (red curve) reports the voltage profile of the Li/DEMETFSI-LiTFSI/$Zn_{0.9}Fe_{0.1}O_2$-C half-cell, evidencing the expected sloping voltage profile associated to the reversible conversion/alloy reaction (3.1.1) [74]:

$$Zn_{0.9}Fe_{0.1}O + 2.9Li^+ + 2.9e \rightleftharpoons 0.9LiZn + 0.1Fe^0 + Li_2O \quad (3.1.1)$$

In half-cell configuration the conversion/alloying material delivers about 550 mAh g^{-1}, with a satisfactory coulombic efficiency, approaching the already demonstrated electrochemical performance in conventional carbonate-based electrolyte [74]. Before assembling the Li-ion-O_2 cell,

the anode was electrochemically fully discharged down to 0.01 V and then coupled with the carbon-based cathode [272,291]. The "$Li_xZn_{0.9}Fe_{0.1}O$"-C/DEMETFSI-LiTFSI/O_2 Li-ion-oxygen cell reported in Fig. 3.1.5a (blue curve) shows a (dis-)charge voltage profile reflecting the combination of the flat profiles associated to the Li/O_2 electrochemical process (black curve) and the sloping profile of the Li/"$Li_xZn0_{.9}Fe_{0.1}O$"-C electrochemical process (red curve) described by the electrochemical reaction (3.1.2):

$$1.45\ O_2 + 0.9LiZn + 0.1Fe + Li_2O \rightleftharpoons Zn_{0.9}Fe_{0.1}O + 1.45\ Li_2O_2 \quad (3.1.2)$$

Indeed, the proof-of-concept cell has a discharge working voltage centered at about 1.6 V and delivers a reversible capacity of about 500 mAh g^{-1} of carbon, however, with a relatively high polarization mostly attributed to the conversion reaction. Figure 3.1.5b, which reports the first and second cycle (dis-)charge profiles of the full cell, evidences the satisfactory reversibility of the process. Indeed, the second cycle is characterized by a similar (dis-)charge profile and a slight drop in the working potential due to several factors including oxygen cross-over, irreversible reactions due to the conversion reaction and to possible electrolyte degradation [74,303,308]. Although long-term cycling is still required, particularly in air rather than in pure oxygen, the cell here originally reported may represent a promising and safe energy storage system.

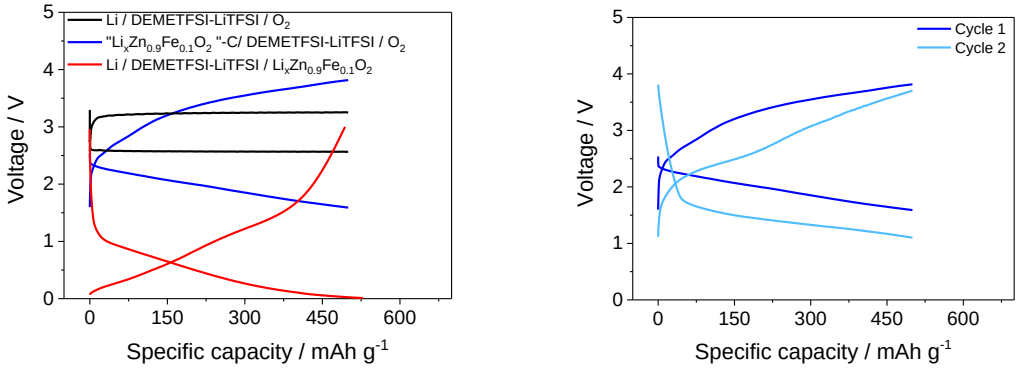

(a) (b)

Figure 3.1.5 (a) Galvanostatic cycling profiles of Li/DEMETFSI-LiTFSI/"$Li_xZn_{0.9}Fe_{0.1}O$"-C (red), Li/DEMETFSI-LiTFSI/O_2 (black) half-cells and "$Li_xZn_{0.9}Fe_{0.1}$"-C/DEMETFSI-LiTFSI/O_2 full-cell (blue). Current density 50 mA g^{-1}, capacity limited to 500 mAh g^{-1} for all the Li/O_2 half-cell and full cell, cut off voltage for the Li/"$Li_xZn_{0.9}Fe_{0.1}O$"-C half cell 0.01-3 V. (b) Galvanostatic cycling profiles of "$Li_xZn_{0.9}Fe_{0.1}O$"-C/DEMETFSI-LiTFSI/O_2 full-cell, first cycle (blue) and second cycle (light blue)

3.2 Ionic liquids: Li/DEMETFSI-LiTFSI/O_2 using alternative cathodes

The performance of the two composite electrode designs developed herein (SSE and SDE) was first verified in Li/O_2 oxygen cells using the DEMETFSI-LiTFSI electrolyte at 60°C, in a limited capacity regime. This testing protocol, in fact, allows the more stable and reversible Li/O_2 charge/discharge process [300]. Applied current and delivered capacity were normalized based on electrode surface, rather than carbon loading, considering that only a small portion of the cathode support can be considered as electrochemically active [309]. Figure 3.2.1a reports the voltage signature of the Li/DEMETFSI 0.2 m LiTFSI/SSE-O_2 cell cycled at 50 μA cm^{-2} within a limited delivered capacity (0.5 mAh cm^{-2}). The cell reveals a remarkably low polarization, i.e., about 0.4 V between the ORR/OER reactions, and an average discharge voltage of about 2.7 V, corresponding to estimated energy efficiency above 88%. The electrochemical performance of the Li/DEMETFSI 0.2 m LiTFSI/SSE-O_2 cell has been further evaluated by increasing the current density up to 100 μA cm^{-2} and the delivered capacity limit to 1 mAh cm^{-2}. The voltage signature of this cell, reported in Figure 3.2.1b, shows good electrochemical behavior despite the increased current rate and capacity limit. However, the figure reveals a slightly lower energy efficiency for the system due to an increased polarization during the charging process, which is in good agreement with previous literature reports for higher depth of discharge [262].

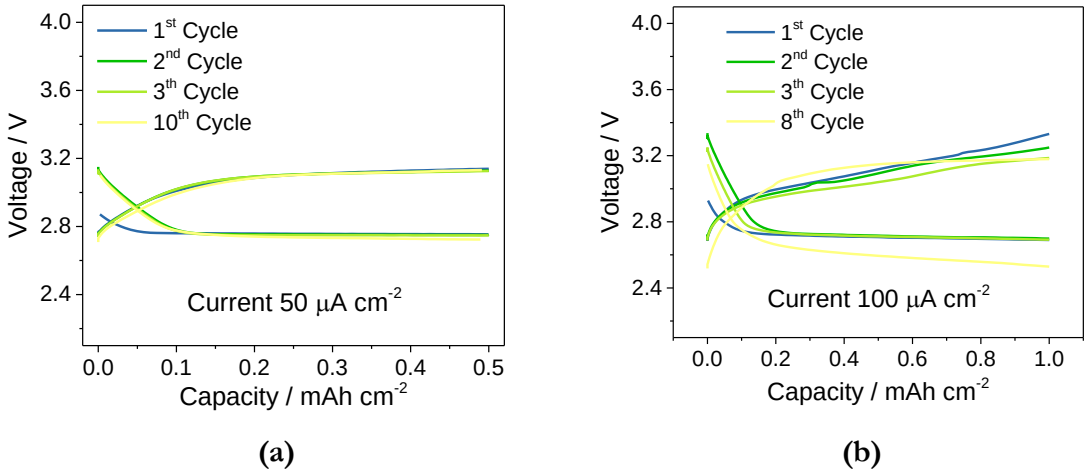

Figure 3.2.1 (a) Voltage signatures of the galvanostatic cycling test of Li/DEMETFSI 0.2 m LiTFSI /SSE,O_2 cell, limited capacity to 0.5 mAh cm^{-2} at a current of 50 μA cm^{-2}. (b) Voltage signatures of the galvanostatic cycling test of Li/DEMETFSI 0.2 m LiTFSI /SSE,O_2 cell, limited capacity to 1 mAh cm^{-2} at a current of 100 μA cm^{-2}. Temperature 60°C. For electrode's acronym see experimental section.

Analogously, Figure 3.2.2a reports the electrochemical trend of a spray-deposited electrode in a Li/SDE-O_2 cell using the DEMETFSI-LiTFSI electrolyte. The voltage signature at 60°C of the cell cycled using a current of 50 μA cm^{-2} and limiting the delivered capacity to 0.5 mAh cm^{-2} shows a stable cycling trend, but polarization of about 0.6 V, which is 50% higher than that reported for the SSE (compare Figure 3.2.1a and 3.2.2a). Analogously, the ORR reaction occurs, using the SDE, at a slightly lower average voltage, i.e., about 2.6 V, than with the SSE. Moreover, the higher (dis-)charge polarization using the SDE instead of SSE reflects a lower energy efficiency, which is only of about 80%. The electrochemical performance of the SDE-based cell was also evaluated increasing the current to 100 μA cm^{-2} and extending the delivered capacity to 1 mAh cm^{-2}. Figure 3.2.2b, reporting the voltage signature of the lithium oxygen cell using the SDE under this condition, evidences the expected cell polarization increase leading to decreased energy efficiency. Hence, the cycling trends of Figure 3.2.1 and Figure 3.2.2 suggest the SSE as the most suitable electrode for achieving ORR/OER reactions with high energy efficiency, which is most probably ascribed to its morphology enhancing the formation and dissolution of lithium peroxide.

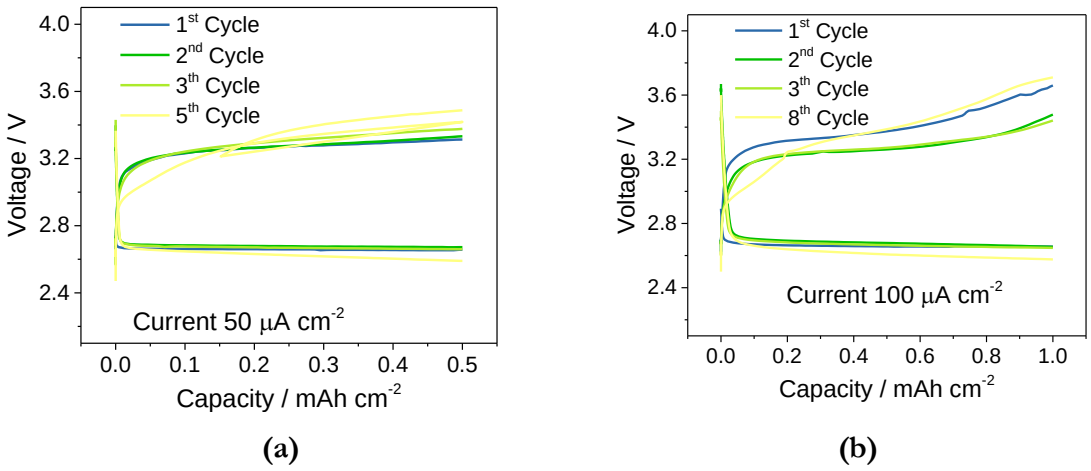

Figure 3.2.2 (a) Voltage signature of the galvanostatic cycling test of Li/DEMETFSI 0.2 m LiTFSI /SDE,O_2 cell, limited capacity to 0.5 mAh cm^{-2} at a current of 50 μA cm^{-2}. (b) Voltage signatures of the galvanostatic cycling test of Li/DEMETFSI 0.2 m LiTFSI /SDE,O_2 cell, limited capacity to 1 mAh cm^{-2} at a current of 100 μA cm^{-2}. Temperature 60°C. For electrode's acronym see experimental section.

The SEM images of the self-standing electrode (SSE, Figure 3.2.3a) and the spray deposited electrode (SDE, Figure 3.2.3b) evidence the different morphologies of the two composites. Carbon black is homogeneously distributed in both samples, without signs of PTFE segregation. However, SSE (Figure 3.2.3a) shows a smoother packing of the nanometric carbon with respect to SDE (Figure 3.2.3b), which reveals a rougher and more granular morphology. These characteristics are expected to directly influence the electrochemical performances of the Li/O_2 cells by affecting oxygen diffusion, electrode wettability, morphology of the ORR products, and, therefore, the charge/discharge polarization, as already observed in figures 3.2.1 and 3.2.2. It is worth noticing that an optimal electrode morphology certainly favors the tri-phase reaction mechanism at the carbon-oxygen-electrolyte interface, avoids electrode flooding which may limit the oxygen diffusion and carbon utilization, thus enhancing the ORR/OER reactions [310]. Therefore, the morphology of the SSE electrode after charge and discharge was further investigated via ex-situ scanning electron microscopy. Figure 3.2.3c and 3.2.3d show the micrographs of, respectively, an electrode after discharge to 0.5 mAh cm^{-2} and subsequent charge, respectively, both at 50 μA cm^{-2}. The typical sub-micrometric toroidal [311] morphology of the discharge product observed in Figure 3.2.3c, with an average particle size of about 900-1000 nm, suggests a solution mechanism accounting for the Li_2O_2 formation, which is a favorable pathway for improving the cell performance [227]. Despite only

qualitatively, the SEM image of the charged SSE (Figure 3.2.3d) reveals almost complete dissolution of the discharge products upon OER, thus well supporting the highly reversible nature of the lithium-oxygen (dis-)charge reaction suggested by the electrochemical test of Figure 3.2.1 for Li/DEMETFSI 0.2 m LiTFSI/O_2-SSE cell.

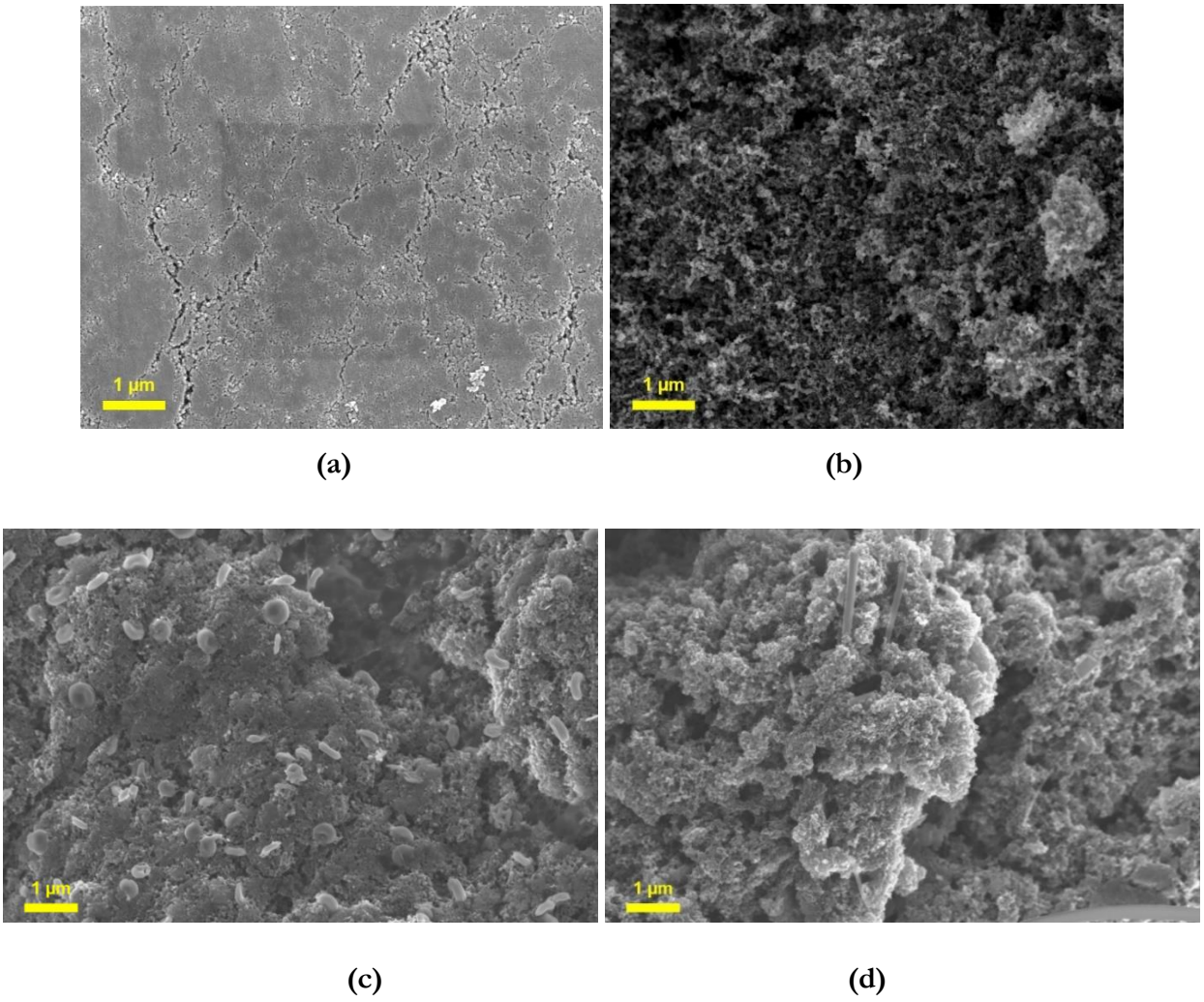

Figure 3.2.3. Scanning electron microscopy images of pristine (a) SSE, and (b) SDE. Ex-situ scanning electron microscopy images of SSE cycled by limiting the capacity to 0.5 mAh cm^{-2} at a current of 50 µA cm^{-2}. (c) SSE, Discharge. (d) SSE, Charge. Cycling temperature 60°C. For electrode's acronym see experimental section.

SSE was also employed in the realization of a lithium ion oxygen (Li-ion/O_2) cell, using a fully lithiated, nanostructured Sn-C electrode (Figure 3.2.4). This lithiated Sn-C electrode (indicated as Li_xSn-C) was characterized in half-cell at various temperatures, i.e., 25, 40, 60 °C (see experimental section for the lithiation procedure) using a lithium metal anode and DEMETFSI 0.2 m LiTFSI electrolyte. Figure 3.2.4 shows the voltage profile (a) and the cycling behavior (b) of the cell at increasing operative temperatures. The figure reveals a very limited lithiation capacity during the first discharge, as indeed expected by the almost full pre-lithiation of the Li_xSn-C electrode (i.e., $Li_{4.4}Sn$-C). This is extremely important since this electrode would act as the only lithium reservoir in the Li-ion/O_2 cell. The subsequent reversible cycles reveal an increase of the delivered capacity from 370 mAh g^{-1} at 25°C to 450 mAh g^{-1} at 40°C, and finally to a capacity of 600 mAh g^{-1} at 60°C. The increase of the delivered capacity can be ascribed to the higher contribution of the carbon matrix (C in Li_xSn-C) at higher temperature due to lower Li^+ ion diffusion limitation in the electrolyte, resulting in the larger utilization of the low voltage carbon capacity [312]. Figure 3.2.4c illustrates one charge/discharge cycle of the Li_xSn-C/DEMETFSI 0.2 m LiTFSI/O_2-SSE full cell performed at 60°C and 50 μA cm^{-2}, but limiting the delivered capacity to 0.5 mAh cm^{-2}. The voltage profile of Figure 3.2.4c clearly reflects the combination of the expected electrochemical processes, i.e., the ORR forming lithium peroxide at the SSE cathode and the de-lithiation of the Li_xSn-C at the anode during discharge, and the OER with Li/Sn-C alloying during the charge, as already reported in a previous work [272]. The full cell shows very low polarization and high reversibility, thus confirming the optimal electrochemical performance of the employed materials as the cathode (SSE), anode (Li_xSn-C) and electrolyte (DEMETFSI-LiTFSI) sides. It is important to point out that the Li-ion/O_2 cell here reported represents only a proof of concept because it does not offer a solution to the oxygen crossover through the electrolyte leading to the direct oxidation of the anode in turns causing the fast decay of the electrochemical performance [272,303,313].

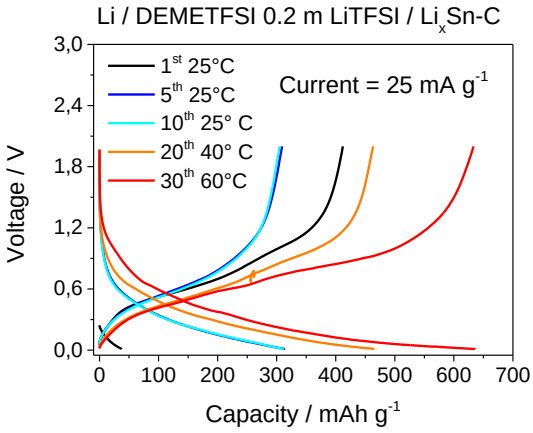

(a)

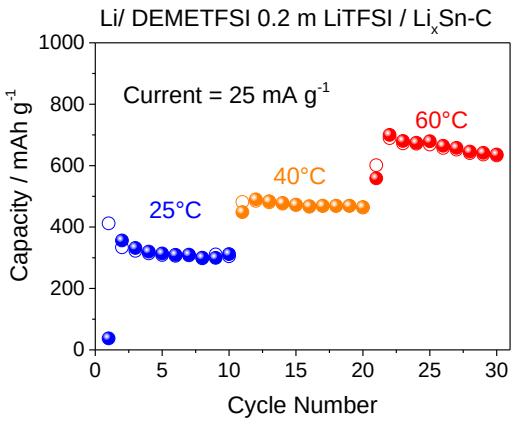

(b)

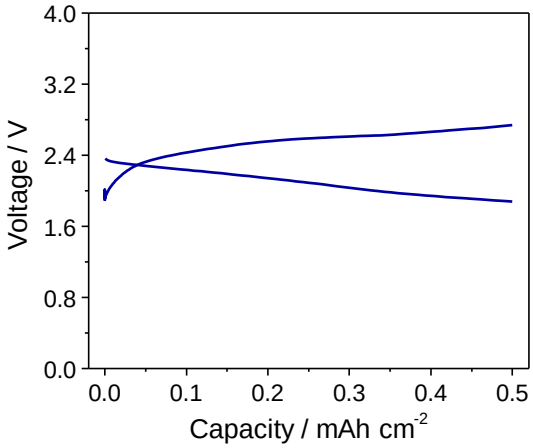

(c)

Figure 3.2.4 (a) Voltage signatures and (b) cycling behavior of the galvanostatic cycling test of Li/ DEMETFSI 0.2 m LiTFSI/ Li_xSn-C. Current rate 25 mA g^{-1}. Cycling test at increasing temperature (25, 40, 60 °C). (c) Voltage signature obtained by galvanostatic cycling tests of Li_xSn-C/DEMETFSI 0.2 m LiTFSI /SSE,O_2 cell, limited capacity to 0.5 mAh cm^{-2} at a current of 50 μA cm^{-2}. Temperature 60°C.

3.3 Solid state: Li/LiI-Li_2S-P_2S_5/S+FeS_2

The Arrhenius plot of the LPSI electrolyte is reported in figure 3.3.1. By assuming a t_{Li+} of 1, Li^+ ionic conductivities value are between ca. 10^{-4} - 10^{-2} S cm^{-1} in the -20 – 70 °C range, and is equal to about 10^{-3} S cm^{-1} at 20 °C, approaching values of organic based liquid electrolytes [152]. As expected, the ionic conductivity values are very well fitted by the Arrhenius equation (3.3.1):

$$\sigma = \sigma_0 + e^{-\frac{Ea}{RT}} \quad (3.3.1)$$

By linearizing the equation and fitting the data, the activation energy for the ion movement has been calculated and is equal to 31.9 kJ mol^{-1} (0.33eV), in line with materials that belong to this class of electrolytes, i.e., argyrodites [153].

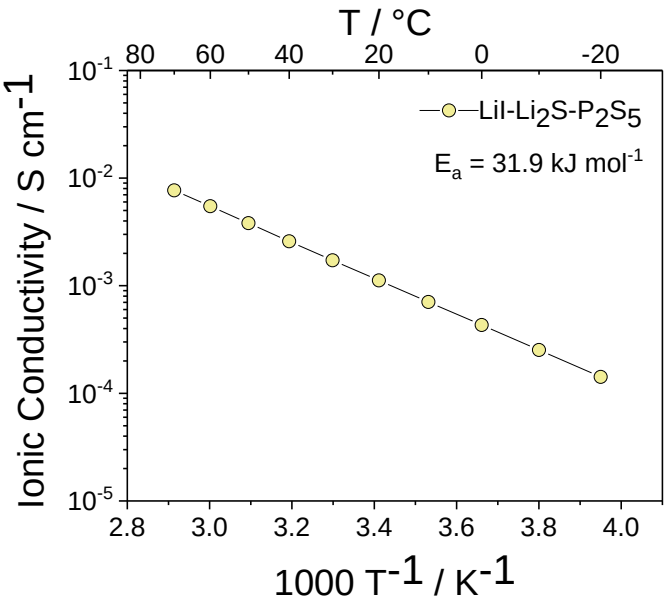

Figure 3.3.1 (a) Arrhenius plot of the LPSI electrolyte. Temperature range, -20 to 70 °C. Activation energy calculated according to Arrhenius equation, equal to 31.9 kJ mol^{-1} (0.33eV)

The cathode composites' crystalline structure was first characterized by powder X-ray diffraction, and it is reported in figure 3.3.2. The diffraction patterns of the composites after the first ball milling

procedure (figure 3.3.2a) reveal that when no elemental sulfur is added (CF sample, in blue) a sulfur defective phase is detected, that is $Fe_{(1-x)}S$ (pyrrhotite, ICSD 190010, monoclinic, P1211(4) space group), along with crystalline FeS_2 (pyrite, ICDD PDF 01-071-0053, cubic, Pa-3(205) space group). The formation of this phase appears to be hindered when 10% of sulfur is added, but it still present, as evidenced by the diffraction pattern of the CFS(8:2) sample (orange). When the sulfur content is higher, on the other hand, the formation of pyrrhotite is suppressed, as only crystalline FeS_2 is detected in the CFS(5:5) sample (green), containing 30 wt.% of elemental sulfur. The diffraction patterns of the composites after the second ball milling step (Figure 3.3.2b), that is when the solid electrolyte is added, are in line with the previous observations. All samples are characterized by an additional broad reflection between 38-52 2θ degrees, that is ascribed to the amorphous solid electrolyte and, possibly, to the activated carbon (see appendix 3, figure A3.3a). Interestingly, the second ball milling step seems to promote the formation of the sulfur defective phase, particularly when no sulfur is added or is present in low amounts, as evidenced by the diffraction patterns of CF-LPSI (light blue) and CFS(8:2)-LPSI (light orange). Pyrite, on the other hand, is predominant in the sample with a higher sulfur content (light green, sample CFS(5:5)-LPSI). Small traces of pyrrhotite might be present too, as a faint peak at ca. 44.1 2θ degrees is observed. Carbon retains an amorphous structure throughout the whole synthesis procedure, as no feature can be ascribed to a graphitic structure (even at angles lower than 30 2θ degrees, data not reported). The formation of the sulfur defective phase can be likely ascribed to a mechanochemical reaction between carbon and iron disulfide during the milling steps. Indeed, as evidenced by the diffraction patterns reported in Appendix 3, figure A3.3b, when pyrite is ball-milled without carbon, only a general amorphization of the material can be observed. The addition of elemental sulfur might create a more oxidative environment, or, most probably, is more easily adsorbed on the carbon surface, thus helping in retaining phase-pure pyrite. Moreover, sulfur is entirely amorphous, as no diffraction peak is observed. The stoichiometry of all materials has also been verified by thermogravimetric analysis (see appendix 3, figure A3.3 and table A1) and is consistent, within the experimental error, for every sample.

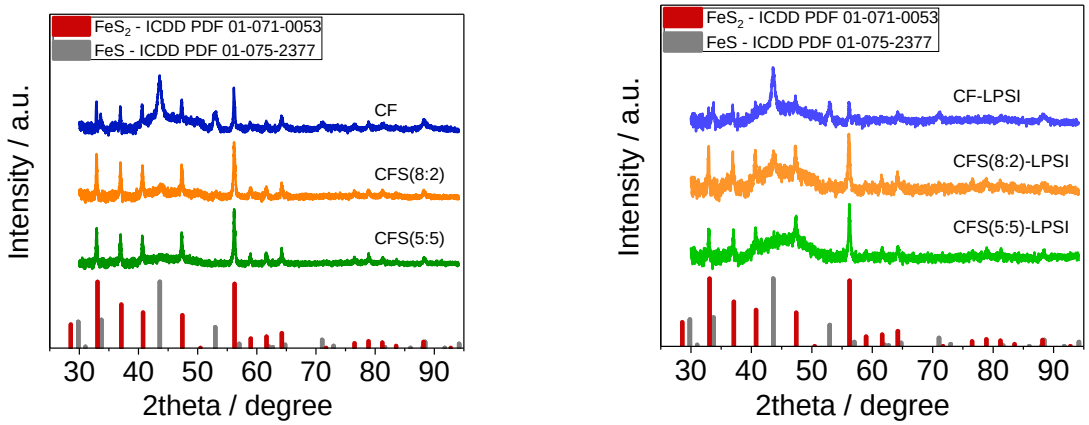

Figure 3.3.2 XRD patterns of (a) active materials after the first ball milling procedure, CF-dark blue, CFS(8:2)-dark orange, CFS(5:5)-dark green, and (b) cathode composites after the second ball milling procedure, CF-LPSI-light blue, CFS(8:2)-LPSI-light orange, CFS(5:5)-LSPI-light green.

The morphology of selected materials has been studied by scanning electron microscopy and is reported in figure 3.3.3. From figure 3.3.3a, aggregates of submicrometric particles can be observed for FeS_2. Activated carbon (figure 3.3.3b) is characterized by bigger aggregates with a broad size distribution. When the two materials are mixed, and ball milled (CF sample, figure 3.3.3c) the activated carbon seems to mostly retain its morphology, while the iron sulfide aggregates are broken, and the submicrometric particles are homogeneously dispersed on the activated carbon. When sulfur is added to the synthesis, a more noticeable particle size reduction can be observed. This is particularly evident from the SEM micrograph of the sample relatively rich in sulfur (sample CFS(5:5), figure 3.3.3d). It is known that Sulfur can effectively trigger mechanically induced self-propagating reactions (MSR) [314,315] and, given the high temperatures reached during a mechanochemical synthesis, could melt or sublimate/evaporate [314]. In this way, it can act as wetting agent and hinder the material re-aggregation thus reducing the particle size [316]. The second ball milling step, which includes the solid electrolyte, yields materials with a more homogeneous morphology (Figure 3.3.3e and f). In particular, the sample with a higher sulfur content (CFS(5:5)-LPSI, figure 3.3.3f) is characterized by a more regular, spherical morphology.

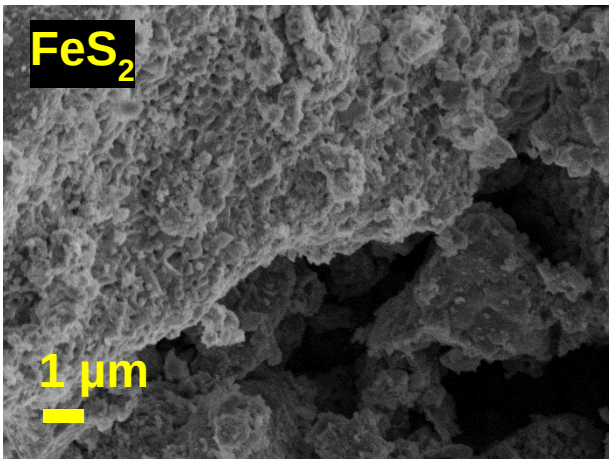

(a)

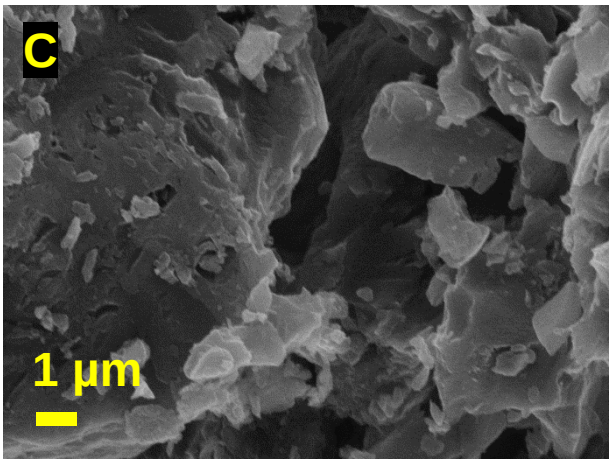

(b)

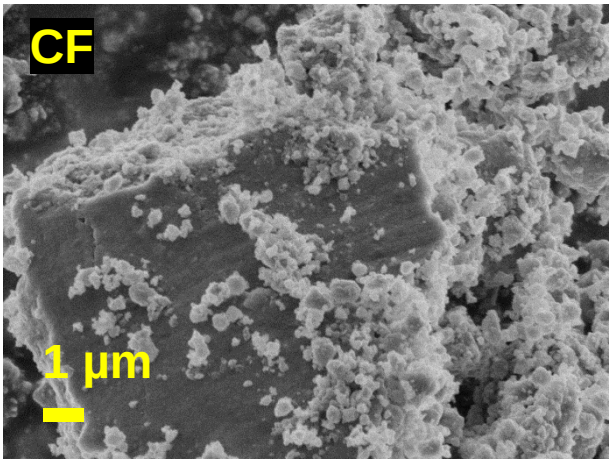

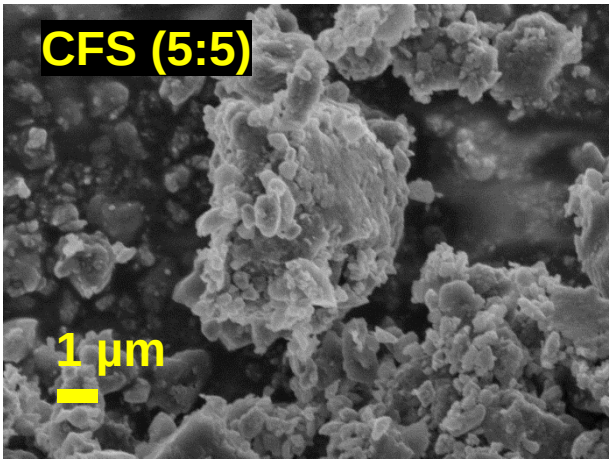

(b) (d)

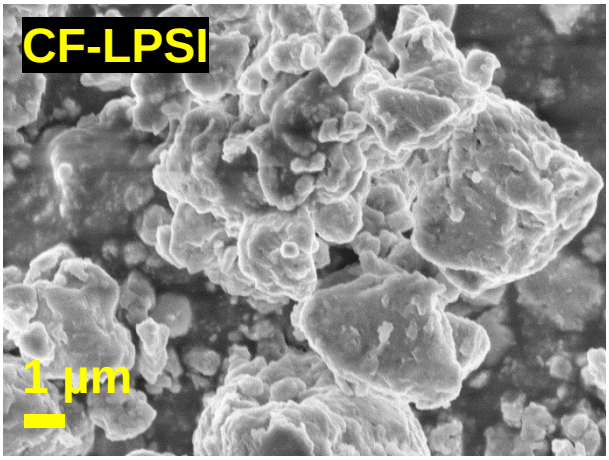

(e)

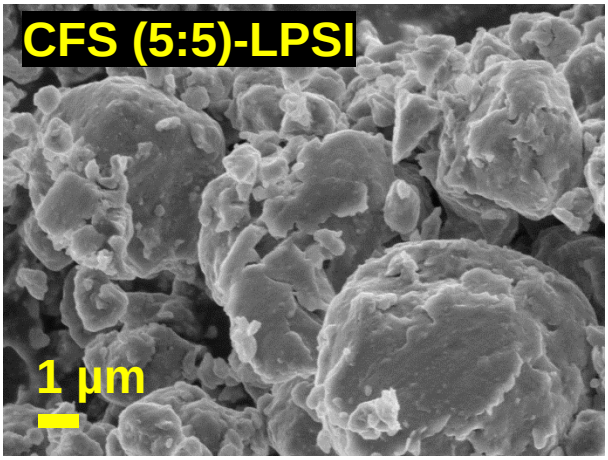

(f)

Figure 3.3.3 SEM micrographs of (a) FeS_2, (b) activated carbon, (c) CF, (d) CFS(5:5) (e) CF-LPSI (f) CFS(5:5)-LSPI

The electrochemical behavior of the materials obtained at the end of the second ball milling procedure was evaluated by galvanostatic cycling of lithium all solid-state half cells, using LPSI as electrolyte, with an active material loading of 1.0 mg cm^{-2} at 20 °C. The differential plots were employed to evaluate the redox processes taking place, as well as to evaluate the reversibility of (dis-)/charge and are reported in figure 3.3.4. The 1st discharge of the Li/LPSI/CF-LPSI cell (Figure 3.3.4a) is characterized by a sharp peak centered at about 1.34 V, and a small shoulder to this peak, centered at ca. 1.5 V. The shoulder is most probably associated with the intercalation of lithium into iron disulfide to form Li_2FeS_2.

$$FeS_2 + 2Li^+ + 2e^- \rightarrow Li_2FeS_2 \quad (3.3.2)$$

The main peak, centered at 1.34V, can be attributed, on a first instance, to the iron sulfide (pyrrhotite) conversion reaction.

$$FeS + 2Li^+ + 2e^- \rightarrow Li_2S + Fe \quad (3.3.3)$$

Both reactions have already been observed in conventional, organic based liquid electrolytes [317,318]. In this voltage range, the conversion of Li_2FeS_2 is also expected.

$$Li_2FeS_2 + 2Li^+ + 2e^- \rightarrow Li_2S + Fe \quad (3.3.4)$$

The following charge is characterized by one main peak centered at ca. 1.8 V, most probably attributed to the oxidation of iron,

$$Fe+Li_2S \rightarrow Li_{2-x}FeS_2+xLi^+ +xe^- \quad (3.3.5)$$

followed by a very broad feature, extending from ca. 1.9 V to 2.4 V, which can be associated with the oxidation of lithium iron sulfide.

$$Li_2FeS_2 \rightarrow Li_{2-x}FeS_2+xLi^+ +xe^- \quad (3.3.6)$$

The following peak centered at 2.5 V is associated with lithium iron sulfide disproportionation [317,319].

$$Li_{2-x}FeS_2 \rightarrow 0.8FeS_2+0.2FeS_y+0.2(2-y)S+(2-x)Li^+ +(2-x)e^- \quad (3.3.7)$$

Another large feature upon charge, common to all the materials and centered at ca. 2.5-2.7 V, can be ascribed to the solid electrolyte electrochemical activity. When the solid electrolyte is added to the cathode composite, it is known to show a reversible cycling behavior [164]. This is also evident from Figure A3.5a in appendix 3, which shows the differential capacity plot of a Li/LPSI/C-LPSI cell, in which the cathode composite is obtained by ball-milling carbon with the LPSI electrolyte. The differential capacity plots of the 2nd and 5th cycles, relative to the Li/LPSI/CF-LPSI cell (Figure 3.3.4a), show different features. The broad cathodic peak, centered at about 2.25V, can be ascribed to the conversion of sulfur generated during the first charge by the electrochemically active Li_2S-containing electrolyte (Figure A3.5a, Supporting information). The material is also active in the 1.9-2.2 V voltage range. (see inset of figure 3.3.4a). A similar feature was observed by Yersak et al., and could be ascribed to the formation of $Li_{2-x}FeS_2$ from non-stoichiometric FeS_y and S, generated by disproportionation of lithium iron sulfide (Equation 3.3.7) in the previous charge.

$$FeS_y+(2-y)S+2Li^+ +2e^- \rightarrow Li_{2-x}FeS_2 \quad (3.3.8)$$

Two distinct peaks are also present in the lower voltage area (< 1.75 V), and can be attributed to the lithiation of $Li_{2-x}FeS_2$ (peak at ca. 1.65 V),

$$Li_{2-x}FeS_2+xLi^+ +xe^- \rightarrow Li_2FeS_2 \quad (3.3.9)$$

and to the lithiation of FeS_2 (equation 3.3.2, peak at 1.5 V). The broad feature at lower voltage ranges (extending from ca. 1.4 V) is attributed to the conversion of Li_2FeS_2 (Equation 3.3.4). The absence of the peak at 1.34 V could be explained by an irreversible phase transition. During the first cycle, we have a defective phase ($Fe_{(1-x)}S$, pyrrhotite), as evidenced by the XRD pattern, which is mostly lost upon an irreversible structural reorganization and is therefore absent during the following cycles. The role of the elemental sulfur, probably present as a by-product of the synthesis procedure, is still unclear. However, it is evident that the reaction mechanism is changing upon cycling, as suggested by the evolution of the anodic peaks centered at 1.8 V and 2.5 V during charge. Figure 3.3.4b, relative to the Li/LPSI/CFS(8:2)-LPSI half-cell, seems to follow the same reaction mechanism previously proposed. The first cathodic process at 1.5 V (equation 3.3.2), is, however, more prominent, due to the larger amount of FeS_2. The fact that during the following discharges this electrochemical process is present suggests that cubic FeS_2 is formed upon cycling. In turn, the pyrrhotite phase, still present in the CFS(8:2)-LPSI sample, but in a lower amount, seems to be characterized by the same peak centered at about 1.35 V (equation 3.3.3), which shows a much lower intensity (compare 3.3.4a and 3.3.4b). Upon charge, the material is generally characterized by the same features observed for the CF-LPSI cathode composite. Interestingly though, during the following discharge cycles, electrochemical activity between 1.9-2.2 V becomes much more prominent. This could be partially ascribed to the increasing contribution from conversion of sulfur (figure A3.5b, appendix 3), which is also included in the composite), and to the formation of $Li_{2-x}FeS_2$ (equation 3.3.8) from FeS_y and S. As previously mentioned, these charge products are the result of Li_2FeS_2 disproportionation, which is apparently activated during cycling, as evidenced by the increased intensity of the anodic feature at 2.5 V. The differential capacity plot of the Li/LPSI/CFS(5:5)-LPSI half-cell (figure 3.3.4c), where the cathode composite is characterized by a higher percentage of sulfur, evidence a behavior that substantially differs from the previous samples. The first discharge of this cell is characterized by a very broad peak, extending between ca. 2.2 V and 1.65 V. This peak is clearly associated with the redox reaction of sulfur to form Li_2S (figure A3.5b, appendix 3) [164]. The following peak at 1.6 V is unique to this material and could be associated with the presence of other FeS defective phases that react to form Li_2FeS_2 [204]. This is subsequently converted between 1.5 V and 1.3 V, together with phase pure FeS_2 (similarly to other samples), into Li_2S and Fe [320]. Most importantly, the absence of sharp peaks below 1.5 V suggests that the electrochemical activity in this region is mostly associated with the pyrrhotite phase, whose formation is mostly suppressed in the CFS(5:5)-LPSI sample, as suggested by the XRD pattern in

figure 3.3.2b. Upon charge a more evident electrochemical activity at higher voltages is detected (peaks at 2.25V and 2.7V). This additional contribution to the total capacity is attributed to the formation of elemental sulfur from lithium disulfide (figure A3.5b, appendix 3). An increasing peak upon cycling, corresponding to Li_2FeS_2 disproportionation is also evident at 2.5 V, similarly to previous samples. Sulfur is reduced upon discharge in the 2.3-1.66 V voltage range during the following cycles, with additional contributions to the capacity attributed to the solid electrolyte electrochemical activity, as well as to the increasing electrochemical activity upon cycling of residual FeS_y phases (disproportionation products). At lower voltages, the peak at 1.6 V, present during the first discharge, is absent. However, in this low voltage range, the profile is characterized by similar features of the CFS(8:2)-LPSI samples, but lower intensities, again, suggesting that this voltage range is ascribed to mostly pyrrhotite impurities, which could still be present, but in much lower amounts, as suggested by the XRD data (Figure 3.3.2b). The following charges are characterized by the reversible formation of sulfur from lithium disulfide and the increasing contribution from Li_2FeS_2 to form FeS_y and S. It should be noted that the redox activity of iron sulfides is relatively complex and debated, particularly when more phases are included, and will require further validation [157,320–324].

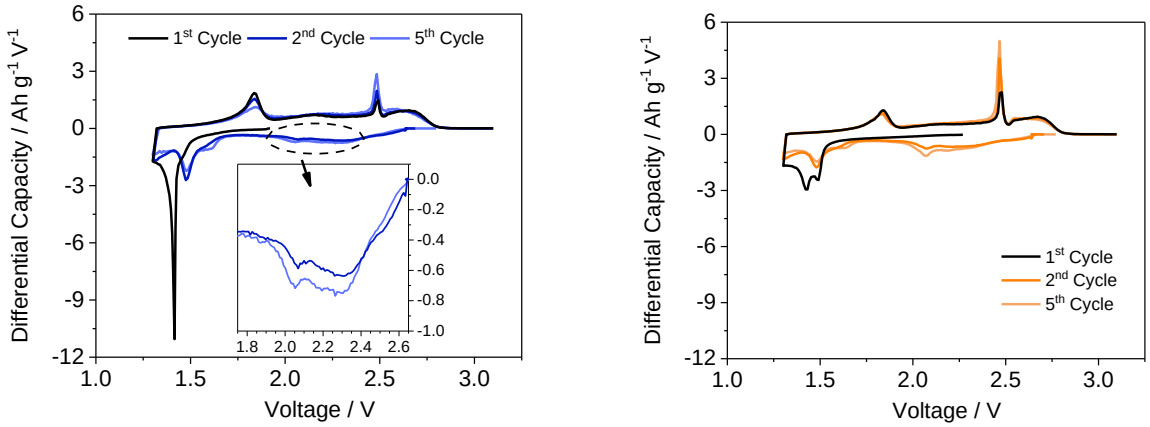

(a) (b)

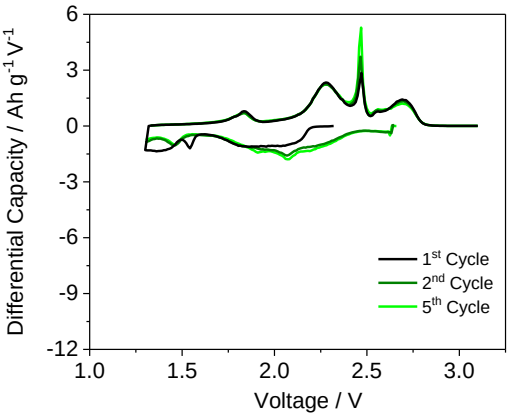

(c)

Figure 3.3.4 Differential capacity plots derived from galvanostatic cycling of lithium all solid state half cells. (a) Li/LPSI/CF-LPSI, magnification in inset, (b) Li/LPSI/CFS(8:2)-LPSI, (c) Li/LPSI/CFS(5:5)-LPSI. Current rate 83.5 mA g^{-1}. Active material loading, 1.0mg cm^{-2}. Cutoff voltage 1.3-3.1 V. Cycling test at 20 °C.

The (dis-)/charge voltage profiles of the Li/LPSI/CF-LPSI cell, reported in Figure 3.3.5a, reveal a discharge pseudo-plateau centered at ca. 1.34 V evident from cycle 1, as suggested by the differential capacity plot, which delivers a capacity over 600 mAh g^{-1}. The first charge is characterized by a much larger capacity (910 mAh g^{-1}), justified by the reversible oxidation of the electrolyte in the cathode composite (figure A3.6, Appendix 3). Upon following (dis-)/charges, a general increase in the electrochemical activity of the material can be observed, with a capacity exceeding 970 mAh g^{-1}, with a relatively low and constant polarization. After the 6th cycle, however, a general decay in capacity and an increasing polarization can be observed, most evident from the 20th cycle. The capacity stabilizes at about 800 mAh g^{-1} after the 10th cycle for over 20 cycles (figure 3.3.5b), with a coulombic efficiency (calculated as $\eta = C_{disch} / C_{ch}$) ranging between 98-101% (excluding the 1st cycle) and an average coulombic efficiency between the 5th and 10th cycle of 100.3%. The data suggest, therefore, possible increased irreversibility that could result in partial material deactivation. The (dis-)/charge voltage profiles of the Li/LPSI/CF(8:2)-LPSI cell, are reported in Figure 3.3.5c. The first cycle is characterized by a sloped feature between 2.3 V and 1.55 V, which accounts for about 100 mAh g^{-1}, followed by a pseudo-plateau in the low voltage area. The 1st discharge and charge are characterized, respectively, by capacities of about 600 mAh g^{-1} and 800 mAh g^{-1}. Upon

cycling, a relatively low polarization can be observed, with an average V_{disch} of 1.89 V and V_{ch} of 2.26 V at the 20th cycle, with increasing reversible capacity up to 960 mAh g^{-1}. Coulombic efficiency stabilizes at about 99.99% after the third cycle, as evidenced by the cycling behavior reported in figure 3.3.5d. The Li/LPSI/CF(5:5)-LPSI cell (figure 3.3.5e and f) is characterized by a similar trend and improved performance. The voltage profiles show a more sloped shape and a much higher, increasing capacity approaching 1200 mAh g^{-1}, as result of the sulfur addition. Polarization is still relatively low, with an average V_{disch} of 1.94 V and V_{ch} of 2.34 V at the 20th cycle. Coulombic efficiency is also promising, stabilizing at about 99.99% after the 4th cycle. The Li/LPSI/CF(5:5)-LPSI cell configuration appears as the best performing, as evidenced from figure A3.7b, appendix 3 in which a comparison of the cycling behavior of all solid-state cell configurations is reported.

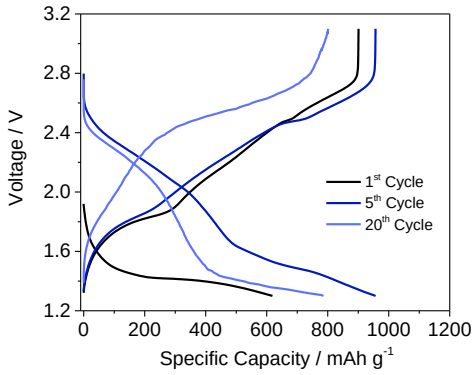

(a)

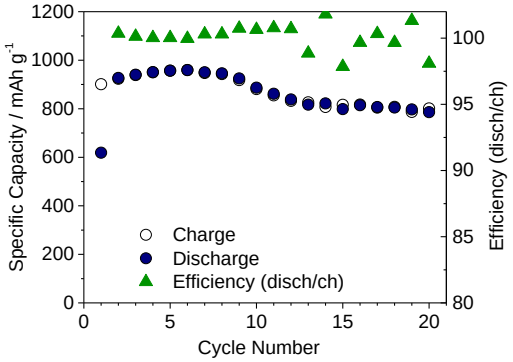

(b)

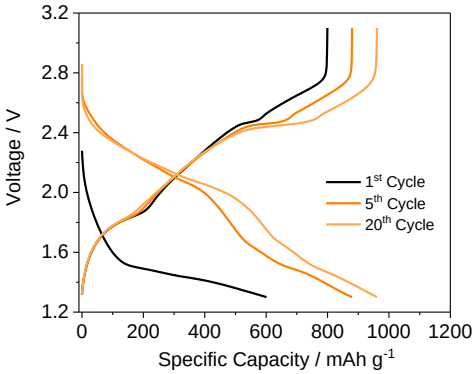

(c)

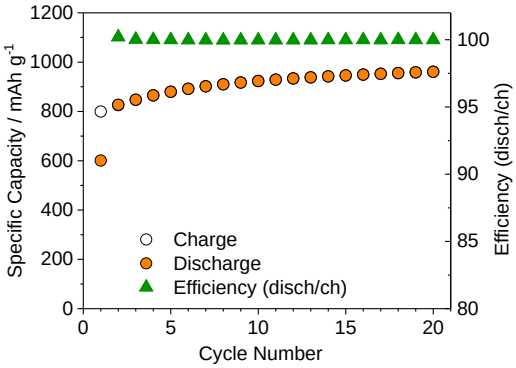

(d)

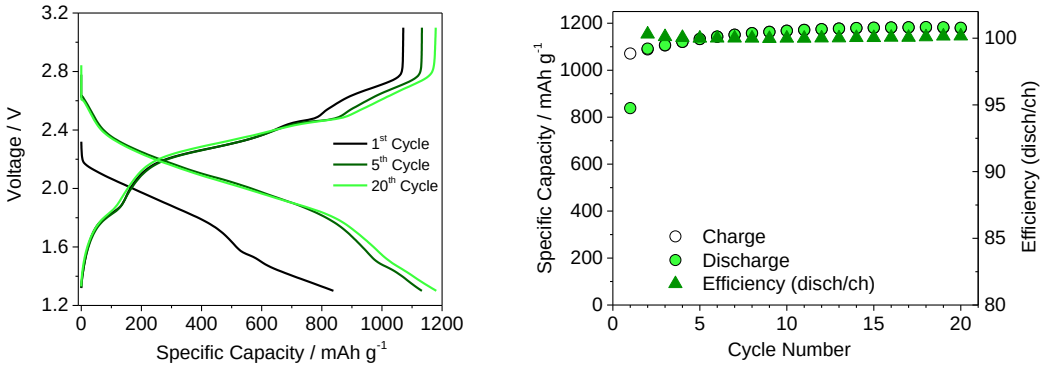

(e) (f)

Figure 3.3.5 (a) Voltage signatures and (b) cycling behavior of the galvanostatic cycling test of Li/LPSI/CF-LPSI. (c) Voltage signatures and (d) cycling behavior of the galvanostatic cycling test of Li/LPSI/CFS(8:2)-LPSI. (e) Voltage signatures and (f) cycling behavior of the galvanostatic cycling test of Li/LPSI/CFS(5:5)-LPSI. Current rate 83.5 mA g^{-1}. Active material loading, 1.0 mg cm^{-2}. Cutoff voltage 1.3-3.1 V. Cycling test at 20 °C.

All-solid-state cells with a high active material loading, i.e., 4-5 mg cm^{-2}, that is considered one of the targets Li/S batteries commercialization, were therefore tested using the CFS(5:5)-LPSI cathode composite as the active material. The results, reported in figure 3.3.6a and b, are relative to the galvanostatic cycling of Li/LPSI/CFS(5:5)-LPSI cells with an active material loading of 4 mg cm^{-2} and 5 mg cm^{-2} respectively, cycled at 20 °C between 1.3-3.1 V, using a current density of 16.70 mA g^{-1}. The (dis-)charge profiles are consistent with those observed at lower active material loadings. The cell with an active material loading of 4 mg cm^{-2} (figure 3.3.6a) is characterized by a discharge capacity, at the second cycle, of about 990 mAh g^{-1}, equivalent to 3.96 mAh cm^{-2}, with a coulombic efficiency of 97.6%. When the active material loading is incremented to 5 mg cm^{-2} (figure 3.3.6b), this cell configuration still delivers a reversible capacity of about 820 mAh g^{-1}, equivalent to 4.10 mAh cm^{-2}, with a coulombic efficiency of 98.6%. Similar results, to the best of our knowledge, have never been reported in the literature for all-solid-state lithium sulfur or lithium sulfide batteries and evidence that the all-solid-state configuration is a promising alternative for next generation, safer batteries.

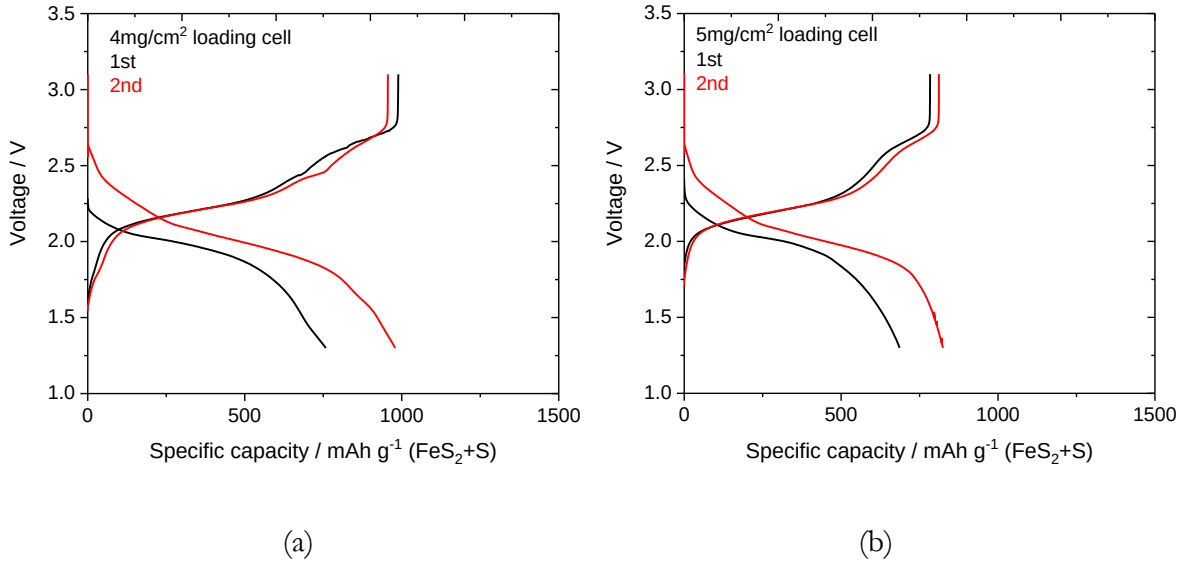

(a) (b)

Figure 3.3.6 (a) Voltage signatures of Li/LPSI/CFS(5:5)-LPSI. Active material loading, (a) 4.0 mg_{am} cm^{-2}. (b) 5.0 mg_{am} cm^{-2}. Current rate 16.70 mA g^{-1}. Cutoff voltage 1.3-3.1 V. Cycling test at 20 °C.

3.4 Summary

The suitability of a DEMETFSI-based ionic liquid for efficient use in high-performance lithium-oxygen batteries is demonstrated for two different lithium-oxygen systems. In chapter 3.1, a cell with maximum capacity as high as 13 Ah g^{-1} is reported, which revealed high reversibility as detected with SEM and XRD. Furthermore, the effect of temperature on the reaction mechanism and products morphology was investigated. The study reveals increasing cell's energy efficiencies with increasing temperatures. Additionally, the change of discharge product morphology ranging from flat-shape particles at 30 °C to toroidal flower-shaped particles at 60 °C is reported. These morphological changes are attributed to different electrochemical process, implying Li_2O_2-growth both at the electrode surface and through the electrolyte. Finally, we presented the proof-of-concept, lithium-ion-oxygen cell including a conversion/alloying based anode instead of lithium metal. The cell delivered a reversible capacity of 500 mAh g^{-1} with the working voltage centered at about 1.6 V, hence a theoretical energy density of about 900 Wh kg^{-1} that is considered well suitable for Li-ion battery applications. In chapter 3.2, the same electrolyte was employed to characterize two oxygen electrode morphologies, differing by the preparation technique. The electrodes' morphology, resulting from the different preparation method, affects the ORR/OER in the Li/O_2 cells as clearly demonstrated by electrochemical tests combined with SEM analysis. Remarkably, the thicker, self-standing electrodes (SSE) prepared via roll pressing offer rather limited cell polarization (0.4V) and high energy efficiency (up to 88%), while the thinner, spray deposited electrodes (SDE) yield to higher polarization (about 0.6V) and lower energy efficiency (80%). The suitability of the SSE/DEMETFSI-LiTFSI electrode/electrolyte couple for lithium oxygen cell is confirmed by morphological SEM analysis, revealing the high reversibility of the redox process. The ORR occurs through the solution mechanism yielding toroidal shaped discharge products. The Li-ion/O_2 cell using the SSE, DEMETFSI-LiTFSI and nanostructured Sn-C alloying anode, cell shows the lowest polarization, and thus highest energy efficiency, so far reported in literature. In chapter 3.3 a novel cathode composite based on iron disulfide is reported for high-performance lithium-sulfur batteries at high loading. The materials are synthesized by a simple, one-step mechanochemical procedure. Their crystalline structure, as well as their morphology, are favorably affected by sulfur addition and is key in stabilizing the pyrite phase. The materials reveal a complex, yet novel (dis-)/charge

behavior, as expected considering the all-solid-state configuration. The cells, which benefit from the use of a lithium metal anode, can deliver a capacity as high as 1200 mAh g^{-1} at the intermediate loading of 1mg cm^{-2} over 20 cycles and up to 4.10 mAh cm^{-2}, using active material loadings as high as of 5mg cm^{-2} at 20 °C, that is one of the targets for Li/S batteries commercialization. This is the first report of an all-solid-state Li/S cell employing a carbon-sulfur-transition metal sulfide material which can cycle at such high loading using lithium metal as the anode and, as such, is proposed as a promising alternative for the realization of next generation, Li/S batteries. All three systems benefit from added safety. The ionic liquid based and the all-solid-state electrolytes, although very different in the working principle, share the common characteristic of being incombustible and both hold promise as alternative media for efficiently mitigating some of the issues of beyond lithium-ion technologies.

Appendix 3

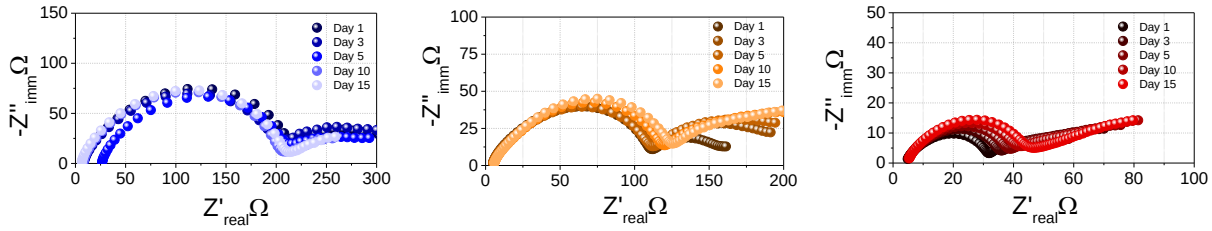

Figure A3.1 Nyquist plot of the electrochemical impedance spectroscopy of a symmetrical Li/ DEMETFSI-LiTFSI / Li upon time at various temperatures: 30 °C (a-blue), 40 °C (b-orange), 60 °C (c-red).

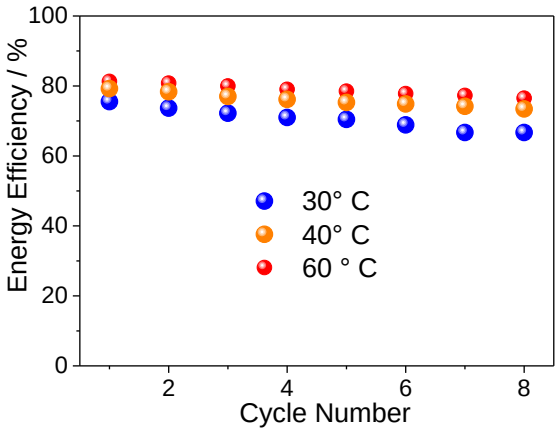

Figure A3.2 Energy efficiency during cycling of the Li/ DEMETFSI-LiTFSI / O_2 cell cycled at various temperatures, 30 °C (blue), 40 °C (orange), 60 °C (red). Current density 100 mA g^{-1}, specific capacity limited to 1500 mAh g^{-1}.

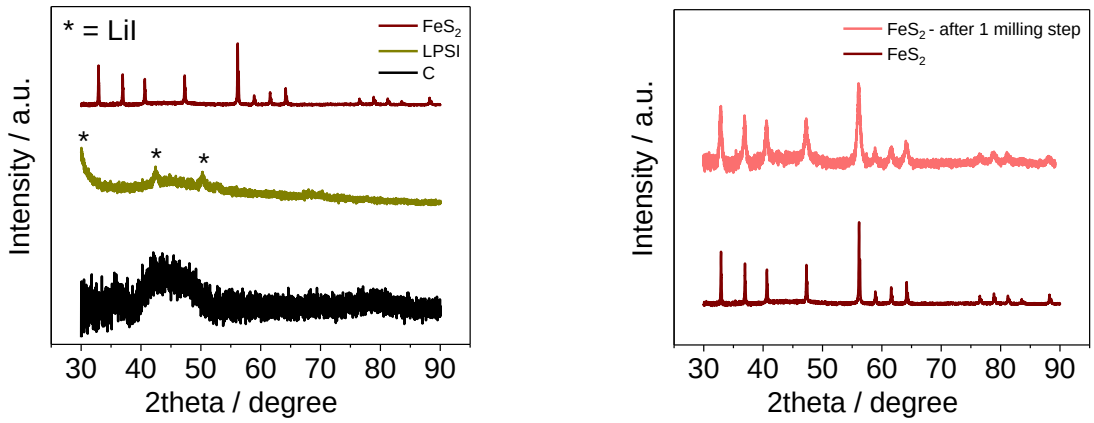

Figure A3.3 Powder X-ray diffraction patterns of (a) starting materials, activated carbon (black), LPSI (dark yellow), FeS_2 (dark red) and of (b) FeS_2 before the ball milling step (dark red) and after the 1st ball milling step (pink). LPSI diffraction pattern is consistent with the one previously reported for the same electrolyte [164].

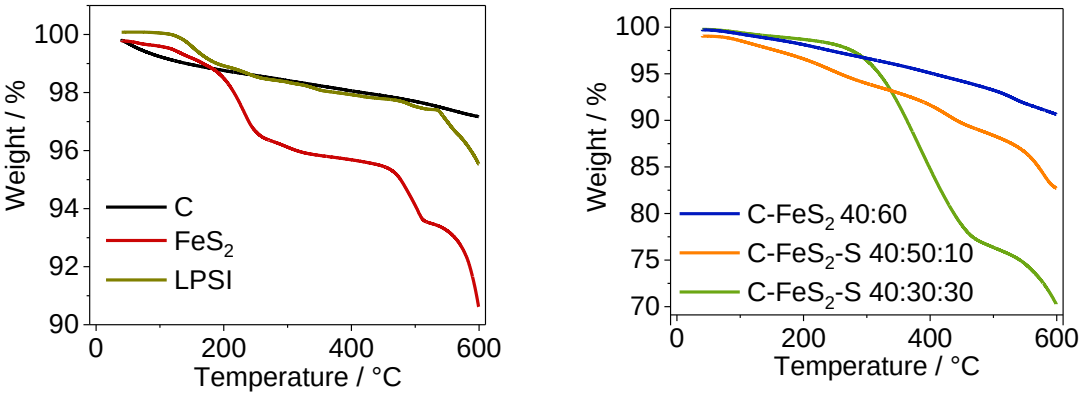

(a) (b)

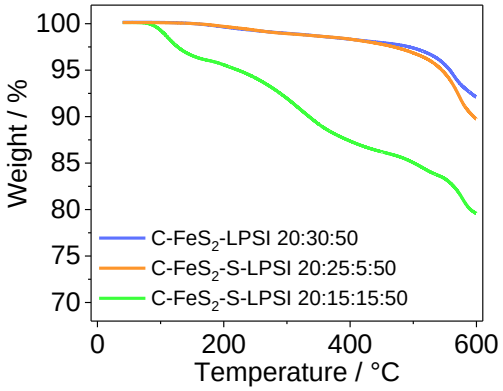

(c)

Figure A3.4 Thermogravimetric analysis under N_2 gas stream (a) starting materials, AC-black, FeS2-dark red, LPSI-dark yellow, (b) active materials, after first ball milling procedure, CF-dark blue, CFS(8:2)-dark orange, CFS(5:5)-dark green, (c) cathode composites, after second ball milling procedure, CF-LPSI-light blue, CFS(8:2)-LPSI-light orange, CFS(5:5)-LSPI-light green.

The stoichiometry has been verified by considering the mass loss of the starting materials

C: 2.5%, FeS2: 9%, SE: 4.5%, sulfur: 100% (not reported)

The expected mass loss was then calculated and compared. Results are reported in table A3.1 and are within the experimental error.

	CF	**CFS(8:2)**	**CFS(5:5)**	**CF-LPSI**	**CFS(8:2)-LPSI**	**CFS(5:5)-LPSI**
Expected	6.5%	15.5%	33%	5.5%	10%	19%
Measured	9%	16%	29%	8%	10%	21%

Table A3.1 TGA analysis results, comparison of expected and measured mass losses for each material.

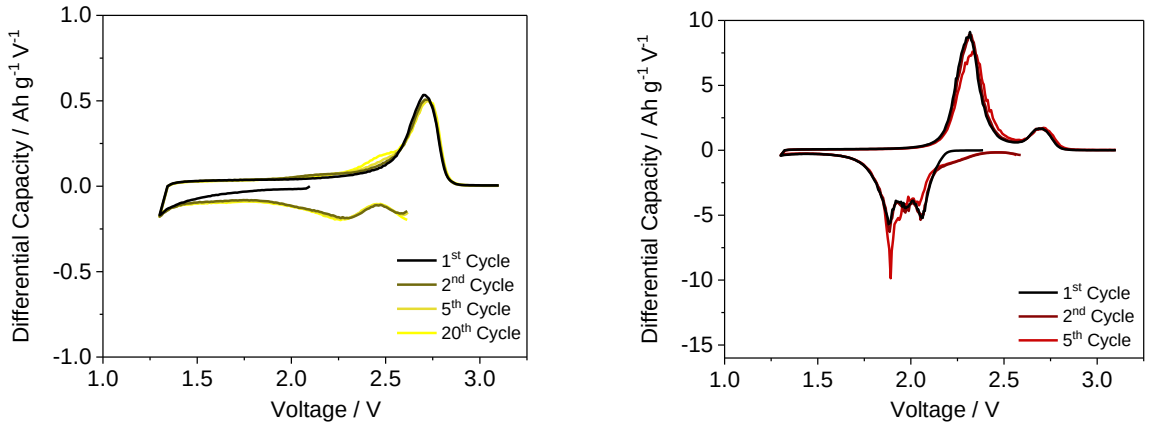

Figure A3.5 Differential capacity plot derived from galvanostatic cycling of lithium all solid-state half-cell. (a) Li/LPSI/C-LPSI half-cell, using as active material a composite consisting of 28.5% activated carbon and 72.5% solid electrolyte. (b) Li/LPSI/C-S-LPSI half-cell, using as active material a composite consisting of 20% activated carbon, 30% sulfur and 50% solid electrolyte. Both samples were synthesized following the same procedure reported for the previous composites including iron disulfide.

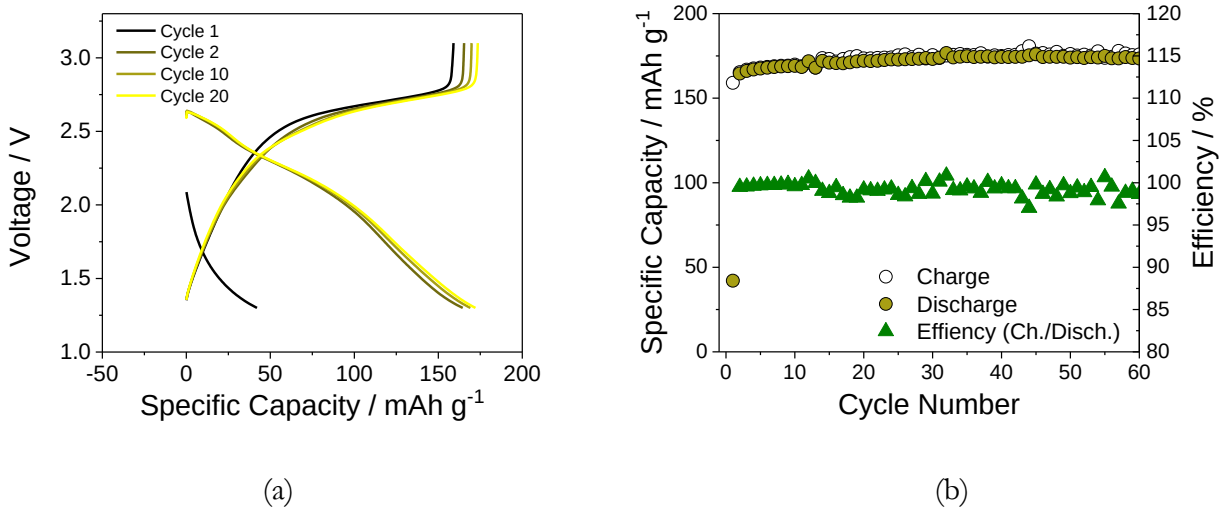

Figure A3.6 (a) Voltage signatures and (b) cycling behavior of the galvanostatic cycling test of Li/LPSI/LPSI-C. Current rate 83.5 mA g^{-1}. Active material loading, 1.0mg_{am} cm^{-2}. Cutoff voltage 1.3-3.1 V. Cycling test at 20 °C.

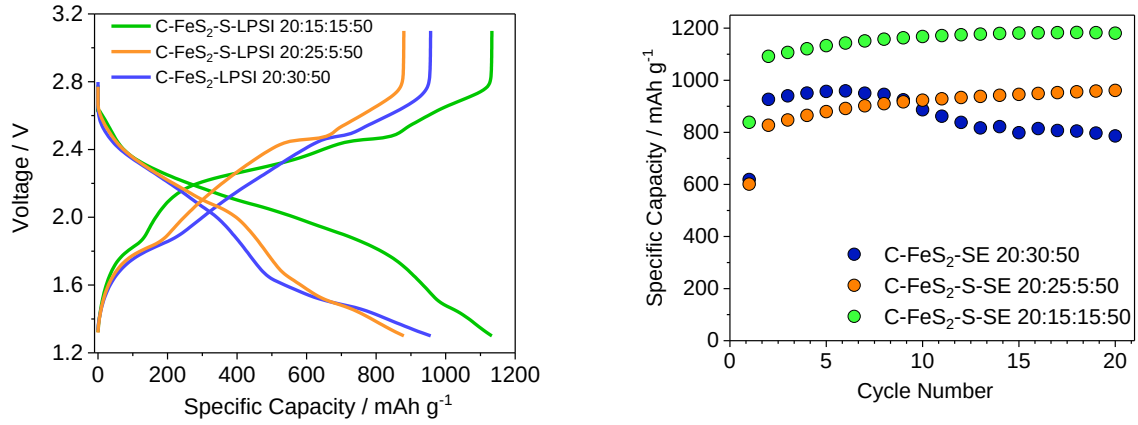

(a) (b)

Figure A3.7 (a) Voltage signatures of the 5th cycle and (b) discharge cycling behavior of the galvanostatic cycling test of Li/LPSI/CF-LPSI (blue), Li/LPSI/CFS(8:2)-LPSI (orange), Li/LPSI/CFS(5:5)-LPSI (green). Current rate 83.5 mA g^{-1}. Active material loading, 1.0mg_{am} cm^{-2}. Cutoff voltage 1.3-3.1 V. Cycling test at 20 °C.

Chapter 4: General remarks and conclusion

In this thesis work, several approaches to realize safer, alternative lithium and lithium-ion configurations have been proposed. It has been demonstrated that alternative electrolytes hold much promise. Their use enables the operation of safer, high-performance lithium-ion batteries, employing conventional cathode materials. It has been demonstrated that the choice of a proper molecular structure for ionic liquids can be advantageous to meet specific needs and this fact should motivate further research, as the possibilities to modify this class of very diverse materials is indeed endless and can potentially lead to significant improvements in the battery field. Moving to beyond lithium-ion technologies is by no means a simple task for the future. However, electrolyte choice has been demonstrated to be again a key factor to enable their exploitation. Lithium-oxygen batteries reversibility can be indeed significantly improved by using ionic liquids and by engineering alternative cathode designs. This system, even though far for commercialization, should be regarded as a promising, given its intrinsic high energy density. Even though ORR/OER reversibility is questioned, so was for the early lithium-ion batteries that employed graphite in PC-based solvents. Also, lithium-sulfur can significantly benefit from an alternative configuration. By avoiding liquid electrolytes, the polysulfide shuttling is prevented. Moreover, the synthesis of new cathodes composites reveals very favorable characteristics, and transition metal sulfides should again be regarded as promising, alternative cathode materials, given their low cost. In general, the applicability of all these systems (conventional and beyond lithium-ion) has been tested by realizing full lithium-ion batteries or high loading cells already at lab-scale. This approach is not conventional in the battery field since every part of the system must be compatible with the other. However, it can significantly help identify critical aspects and applicability of anode, cathode, electrolyte materials in the realization of more realistic battery configurations.

Chapter 5: Related publications

(1) T. Yamada, S. Ito, R. Omoda, T. Watanabe, Y. Aihara, M. Agostini, U. Ulissi, J. Hassoun, B. Scrosati, All Solid-State Lithium-Sulfur Battery Using a Glass-Type P_2S_5-Li_2S Electrolyte: Benefits on Anode Kinetics, J. Electrochem. Soc. 162 (2015) A646–A651. doi:10.1149/2.0441504jes.

(2) M. Agostini, U. Ulissi, D. Di Lecce, Y. Ahiara, S. Ito, J. Hassoun, A Lithium-Ion Battery based on an Ionic Liquid Electrolyte, Tin-Carbon Nanostructured Anode, and Li_2O-ZrO_2-Coated $Li[Ni_{0.8}Co_{0.15}Al_{0.05}]O_2$Cathode, Energy Technol. 3 (2015) 632–637. doi:10.1002/ente.201402226.

(3) U. Ulissi, M. Agostini, S. Ito, Y. Aihara, J. Hassoun, All solid-state battery using layered oxide cathode, lithium-carbon composite anode and thio-LISICON electrolyte, Solid State Ionics. 296 (2016) 13–17. doi:10.1016/j.ssi.2016.08.014.

(4) G.A. Elia*, U. Ulissi*, F. Mueller, J. Reiter, N. Tsiouvaras, Y.K. Sun, B. Scrosati, S. Passerini, J. Hassoun, A Long-Life Lithium Ion Battery with Enhanced Electrode/Electrolyte Interface by Using an Ionic Liquid Solution, Chem. - A Eur. J. 22 (2016) 6808–6814. doi:10.1002/chem.201505192.

(5) G.A. Elia*, U. Ulissi*, S. Jeong, S. Passerini, J. Hassoun, Exceptional long-life performance of lithium-ion batteries using ionic liquid-based electrolytes, Energy Environ. Sci. 9 (2016) 3210–3220. doi:10.1039/C6EE01295G.

(6) U. Ulissi, J. Zimmermann, S. Brutti, J. Hassoun, Investigation of the electrochemical features of carbon-coated TiO_2 anode for application in lithium-ion battery using high voltage $LiNi_{0.5}Mn_{1.5}O_4$ spinel cathode, Electrochim. Acta. 201 (2016) 158–164. doi:10.1016/j.electacta.2016.03.174.

(7) U. Ulissi*, G.A. Elia*, S. Jeong, J. Reiter, N. Tsiouvaras, S. Passerini, J. Hassoun, Alternative Electrode and Electrolyte Configurations for New Lithium-Oxygen Battery, Chem. - A Eur. J., Under revision process

(8) U. Ulissi*, G.A. Elia*, S. Jeong, F. Mueller, J. Reiter, N. Tsiouvaras, Y.K. Sun, B. Scrosati, S. Passerini, J. Hassoun, Electrochemical features of a low-polarization lithium oxygen battery using

N,N-diethyl-N-(2-methoxyethyl)-N-methylammonium bis(trifluoromethanesulphonyl) imide (DEMETFSI) ionic liquid electrolyte, ChemSusChem, 10.1002/cssc.201701696

(9) C. Torre, G.B. Appetecchi, U. Ulissi, A. Varzi, A. Varez, S. Passerini, NASICON-ionic liquid hybrid electrolytes: an approach for realizing solid-state sodium-ion batteries?, Submitted to Journal of Power Sources

(10) U. Ulissi, A. Varzi, S. Ito, Y. Aihara, S. Passerini, Novel pyrite-based composite cathodes for solid-state Li/S batteries, Under submission process

(11) Y. Ma, U. Ulissi, D. Bresser, Y. Ma, Y. Ji, S. Passerini, Manganese silicate hollow spheres enclosed in reduced graphene oxide as anode for lithium-ion batteries, Submitted to Electrochimica Acta

Paper 4, 5, 7, 8, 10 are included in this thesis work.

In paper 4, 5, 7, 8 Dr. S. Jeong performed the synthesis of the ionic liquid based electrolytes. Mr. U. Ulissi and Dr. G.A. Elia performed the rest of experimental work (electrolyte characterization, anode synthesis, half and full cell fabrication, ex-situ measurements), equally contributing to data analysis and manuscript writing. Prof. Passerini and Prof. Hassoun supervised and directed the activity. The other authors participated in data analysis and discussion.

In paper 10, Dr. S. Ito provided the as-synthesized solid electrolyte. Mr. U. Ulissi performed the experimental work, data analysis, and manuscript writing. Prof. Passerini supervised and directed the activity. The other authors participated in data analysis and discussion.

* = Co-first author

5.1 Patent applications

(a) Paper (7) and (8) are part of an international patent application, number PCT/EP2017/070375, in collaboration with BMW AG

(b) Paper (10) is part of a Japanese patent application, in collaboration with SAMSUNG R&D, Japan

Chapter 6: Bibliography

[1] S. Chu, A. Majumdar, Opportunities and challenges for a sustainable energy future, Nature. 488 (2012) 294–303. doi:10.1038/nature11475.

[2] S. Chu, Y. Cui, N. Liu, The path towards sustainable energy, Nat. Mater. 16 (2016) 16–22. doi:10.1038/nmat4834.

[3] Z. Yang, J. Zhang, M.C.W. Kintner-Meyer, X. Lu, D. Choi, J.P. Lemmon, J. Liu, Electrochemical energy storage for green grid, Chem. Rev. 111 (2011) 3577–3613. doi:10.1021/cr100290v.

[4] M.A. Hannan, M.M. Hoque, A. Mohamed, A. Ayob, Review of energy storage systems for electric vehicle applications: Issues and challenges, Renew. Sustain. Energy Rev. 69 (2017) 771–789. doi:10.1016/j.rser.2016.11.171.

[5] D. Andre, S.-J. Kim, P. Lamp, S.F. Lux, F. Maglia, O. Paschos, B. Stiaszny, Future generations of cathode materials: an automotive industry perspective, J. Mater. Chem. A. 3 (2015) 6709–6732. doi:10.1039/C5TA00361J.

[6] J.Y. Yong, V.K. Ramachandaramurthy, K.M. Tan, N. Mithulananthan, A review on the state-of-the-art technologies of electric vehicle, its impacts and prospects, Renew. Sustain. Energy Rev. 49 (2015) 365–385. doi:10.1016/j.rser.2015.04.130.

[7] J.M. Tarascon, M. Armand, Issues and challenges facing rechargeable lithium batteries, Nature. 414 (2001) 359–367. doi:10.1038/35104644.

[8] A.J. Bard, L.R. Faulkner, Electrochemical Methods: Fundamentals and Applications, 2nd ed., John Wiley & Sons Inc., 2000.

[9] T.B. Reddy, Linden's Handbook of Batteries, 4th ed., McGraw-Hill Education, 2011.

[10] B. Scrosati, K.M. Abraham, J. Hassoun, W. Van Schalkwijk, Lithium Batteries: Advanced Technologies and Applications, John Wiley & Sons, Inc., 2013. doi:10.1002/9781118615515.

[11] R. Parsons, Electrochemical nomenclature, Pure Appl. Chem. 37 (1974). doi:10.1351/pac197437040499.

[12] G. Gritzner, G. Kreysa, Nomenclature, symbols and definitions in electrochemical engineering (IUPAC Recommendations 1993), J. Electroanal. Chem. 360 (1993) 351–362. doi:10.1016/0022-0728(93)87029-U.

[13] A.J. Bard, G. Inzelt, F. Scholz, eds., Electrochemical Dictionary, Springer Berlin, 2012. doi:10.1007/978-3-642-29551-5.

[14] J. McDowall, BATTERIES | Parallel and Series Connections, in: Encycl. Electrochem. Power Sources, Elsevier, 2009: pp. 499–509. doi:10.1016/B978-044452745-5.00850-9.

[15] P. Kurzweil, BATTERIES | Nomenclature, in: Encycl. Electrochem. Power Sources, Elsevier, 2009: pp. 381–394. doi:10.1016/B978-044452745-5.00042-3.

[16] J.O. Bockris, A.K.N. Reddy, Modern Electrochemistry 1, Springer US, 2002. doi:10.1007/b114546.

[17] T.R. Jow, K. Xu, O. Borodin, M. Ue, eds., Electrolytes for Lithium and Lithium-Ion Batteries, Springer New York, New York, USA, 2014. doi:10.1007/978-1-4939-0302-3.

[18] P. Arora, Z. Zhang, Battery Separators, Chem. Rev. 104 (2004) 4419–4462. doi:10.1021/cr020738u.

[19] M.B. Armand, Intercalation Electrodes, in: Mater. Adv. Batter., Springer US, 1980: pp. 145–161. doi:10.1007/978-1-4684-3851-2_7.

[20] M. Lazzari, B. Scrosati, A Cyclable Lithium Organic Electrolyte Cell Based on Two Intercalation Electrodes, J. Electrochem. Soc. 127 (1980) 773. doi:10.1149/1.2129753.

[21] B. Dunn, H. Kamath, J.M. Tarascon, Electrical energy storage for the grid: A battery of choices, Science 334 (2011) 928–935. doi:10.1126/science.1212741.

[22] C. Julien, A. Mauger, A. Vijh, K. Zaghib, Lithium Batteries, Springer International Publishing, 2016. doi:10.1007/978-3-319-19108-9.

[23] K. Xu, Nonaqueous liquid electrolytes for lithium-based rechargeable batteries, Chem. Rev. 104 (2004) 4303–4417. doi:10.1021/cr030203g.

[24] K. Kordesch, W. Taucher-Mautner, HISTORY | Primary Batteries, in: Encycl. Electrochem. Power Sources, Elsevier, 2009: pp. 555–564. doi:10.1016/B978-044452745-5.00003-4.

[25] E. Peled, The Electrochemical Behavior of Alkali and Alkaline Earth Metals in Nonaqueous Battery Systems—The Solid Electrolyte Interphase Model, J. Electrochem. Soc. 126 (1979) 2047. doi:10.1149/1.2128859.

[26] E. Peled, S. Menkin, Review—SEI: Past, Present and Future, J. Electrochem. Soc. 164 (2017) A1703–A1719. doi:10.1149/2.1441707jes.

[27] X.B. Cheng, R. Zhang, C.Z. Zhao, F. Wei, J.G. Zhang, Q. Zhang, A review of solid electrolyte interphases on lithium metal anode, Adv. Sci. 3 (2015) 1500213. doi:10.1002/advs.201500213.

[28] P. Bai, J. Li, F.R. Brushett, M.Z. Bazant, Transition of lithium growth mechanisms in liquid electrolytes, Energy Environ. Sci. 9 (2016) 3221–3229. doi:10.1039/C6EE01674J.

[29] S. Tobishima, SECONDARY BATTERIES – LITHIUM RECHARGEABLE SYSTEMS – LITHIUM-ION | Thermal Runaway, in: Encycl. Electrochem. Power Sources, Elsevier, 2009: pp. 409–417. doi:10.1016/B978-044452745-5.00873-X.

[30] G.E. Blomgren, The Development and Future of Lithium Ion Batteries, J. Electrochem. Soc. 164 (2017) A5019–A5025. doi:10.1149/2.0251701jes.

[31] M.S. Whittingham, History, evolution, and future status of energy storage, Proc. IEEE. 100 (2012) 1518–1534. doi:10.1109/JPROC.2012.2190170.

[32] S. Abada, G. Marlair, A. Lecocq, M. Petit, V. Sauvant-Moynot, F. Huet, Safety focused modeling of lithium-ion batteries: A review, J. Power Sources. 306 (2016) 178–192. doi:10.1016/j.jpowsour.2015.11.100.

[33] C. Ashtiani, Analysis of Battery Safety and Hazards' Risk Mitigation, in: ECS Trans., ECS, 2008: pp. 1–11. doi:10.1149/1.2897967.

[34] P.G. Balakrishnan, R. Ramesh, T. Prem Kumar, Safety mechanisms in lithium-ion batteries, J. Power Sources. 155 (2006) 401–414. doi:10.1016/j.jpowsour.2005.12.002.

[35] M. Armand, F. Endres, D.R. MacFarlane, H. Ohno, B. Scrosati, Ionic-liquid materials for the electrochemical challenges of the future, Nat. Mater. 8 (2009) 621–629. doi:10.1038/nmat2448.

[36] J. Akhavan, The chemistry of explosives, 3rd ed., Royal Society of Chemistry, 2011.

[37] C. Julien, A. Mauger, A. Vijh, K. Zaghib, Anodes for Li-Ion Batteries, in: Lithium Batter., Springer International Publishing, 2016: pp. 323–429. doi:10.1007/978-3-319-19108-9_10.

[38] R. Jasinski, High-energy batteries, 1st ed., Springer US, 1967.

[39] R. Fong, H. Al-Janby, J.R. Dahn, Carbonaceous electrodes for lithium cells, WO1990013924A2, 1991.

[40] A. Yoshino, K. Sanechika, T. Nakajima, Secondary battery, US4668595A, 1985.

[41] A. Yoshino, The birth of the lithium-ion battery, Angew. Chemie - Int. Ed. 51 (2012) 5798–5800. doi:10.1002/anie.201105006.

[42] J. Yang, J. -l. Wang, SECONDARY BATTERIES – LITHIUM RECHARGEABLE SYSTEMS – LITHIUM-ION | Negative Electrodes: Lithium Alloys, in: Encycl. Electrochem. Power Sources, Elsevier, 2009: pp. 225–236. doi:10.1016/B978-044452745-5.00190-8.

[43] M. Nagao, C. Pitteloud, T. Kamiyama, T. Otomo, K. Itoh, T. Fukunaga, K. Tatsumi, R. Kanno, Structure Characterization and Lithiation Mechanism of Nongraphitized Carbon for Lithium Secondary Batteries, J. Electrochem. Soc. 153 (2006) A914. doi:10.1149/1.2184908.

[44] A. Mabuchi, Charge-Discharge Characteristics of the Mesocarbon Miocrobeads Heat-Treated at Different Temperatures, J. Electrochem. Soc. 142 (1995) 1041. doi:10.1149/1.2044128.

[45] G. Nazri, G. Pistoia, Lithium Batteries: Science and Technology, Springer US, 2003. doi:10.1007/978-0-387-92675-9.

[46] M. Winter, J.O. Besenhard, M.E. Spahr, P. Novák, Insertion electrode materials for rechargeable lithium batteries, Adv. Mater. 10 (1998) 725–763. doi:10.1002/(SICI)1521-4095(199807)10:10<725::AID-ADMA725>3.0.CO;2-Z.

[47] A.N. Jansen, SECONDARY BATTERIES – LITHIUM RECHARGEABLE SYSTEMS | Lithium–Iron Sulfide, in: Encycl. Electrochem. Power Sources, Elsevier, 2009: pp. 145–150. doi:10.1016/B978-044452745-5.00183-0.

[48] C. Yang, K. Fu, Y. Zhang, E. Hitz, L. Hu, Protected Lithium-Metal Anodes in Batteries:

From Liquid to Solid, Adv. Mater. 29 (2017) 1701169. doi:10.1002/adma.201701169.

[49] X.B. Cheng, R. Zhang, C.Z. Zhao, Q. Zhang, Toward Safe Lithium Metal Anode in Rechargeable Batteries: A Review, Chem. Rev. 117 (2017) 10403–10473. doi:10.1021/acs.chemrev.7b00115.

[50] Y. Guo, H. Li, T. Zhai, Reviving Lithium-Metal Anodes for Next-Generation High-Energy Batteries, Adv. Mater. 29 (2017) 1700007. doi:10.1002/adma.201700007.

[51] M.N. Obrovac, V.L. Chevrier, Alloy negative electrodes for Li-ion batteries, Chem. Rev. 114 (2014) 11444–11502. doi:10.1021/cr500207g.

[52] V. Aravindan, Y.S. Lee, S. Madhavi, Best Practices for Mitigating Irreversible Capacity Loss of Negative Electrodes in Li-Ion Batteries, Adv. Energy Mater. 7 (2017) 1602607. doi:10.1002/aenm.201602607.

[53] R.A. Huggins, Lithium alloy negative electrodes, J. Power Sources. 81–82 (1999) 13–19. doi:10.1016/S0378-7753(99)00124-X.

[54] W.J. Zhang, A review of the electrochemical performance of alloy anodes for lithium-ion batteries, J. Power Sources. 196 (2011) 13–24. doi:10.1016/j.jpowsour.2010.07.020.

[55] X. Zuo, J. Zhu, P. Müller-Buschbaum, Y.-J. Cheng, Silicon based lithium-ion battery anodes: A chronicle perspective review, Nano Energy. 31 (2017) 113–143. doi:10.1016/j.nanoen.2016.11.013.

[56] W. Zulehner, B. Neuer, G. Rau, Silicon, in: Ullmann's Encycl. Ind. Chem., Wiley-VCH Verlag GmbH & Co. KGaA, 2000. doi:10.1002/14356007.a23_721.

[57] G.G. Graf, Tin, Tin Alloys, and Tin Compounds, in: Ullmann's Encycl. Ind. Chem., Wiley-VCH Verlag GmbH & Co. KGaA, 2000: pp. 119–126. doi:10.1002/14356007.a27_049.

[58] D. Deng, M.G. Kim, J.Y. Lee, J. Cho, Green energy storage materials: Nanostructured TiO_2 and Sn-based anodes for lithium-ion batteries, Energy Environ. Sci. 2 (2009) 818. doi:10.1039/b823474d.

[59] G. Derrien, J. Hassoun, S. Panero, B. Scrosati, Nanostructured Sn-C composite as an advanced anode material in high-performance lithium-ion batteries, Adv. Mater. 19 (2007)

2336–2340. doi:10.1002/adma.200700748.

[60] N.A. Godshall, I.D. Raistrick, R.A. Huggins, Thermodynamic investigations of ternary lithium-transition metal-oxygen cathode materials, Mater. Res. Bull. 15 (1980) 561–570. doi:10.1016/0025-5408(80)90135-X.

[61] M.M. Thackeray, J. Coetzer, A preliminary investigation of the electrochemical performance of α-Fe_2O_3 and Fe_3O_4 cathodes in high-temperature cells, Mater. Res. Bull. 16 (1981) 591–597. doi:10.1016/0025-5408(81)90126-4.

[62] J. Cabana, L. Monconduit, D. Larcher, M.R. Palacín, Beyond intercalation-based Li-ion batteries: The state of the art and challenges of electrode materials reacting through conversion reactions, Adv. Mater. 22 (2010) E170–E192. doi:10.1002/adma.201000717.

[63] Y. Idota, T. Kubota, A. Matsufuji, Y. Maekawa, T. Miyasaka, Tin-based amorphous oxide: A high-capacity lithium-ion-storage material, Science 276 (1997) 1395–1397. doi:10.1126/science.276.5317.1395.

[64] H. Li, Z. Wang, L. Chen, X. Huang, Research on advanced materials for Li-ion batteries, Adv. Mater. 21 (2009) 4593–4607. doi:10.1002/adma.200901710.

[65] H. Bin Wu, J.S. Chen, H.H. Hng, X. Wen Lou, Nanostructured metal oxide-based materials as advanced anodes for lithium-ion batteries, Nanoscale. 4 (2012) 2526. doi:10.1039/c2nr11966h.

[66] F. Lin, D. Nordlund, T.C. Weng, Y. Zhu, C. Ban, R.M. Richards, H.L. Xin, Phase evolution for conversion reaction electrodes in lithium-ion batteries, Nat. Commun. 5 (2014). doi:10.1038/ncomms4358.

[67] M. Armand, J.-M. Tarascon, Building better batteries, Nature. 451 (2008) 652–657. doi:10.1038/451652a.

[68] S. Laruelle, S. Grugeon, P. Poizot, M. Dollé, L. Dupont, J.-M. Tarascon, On the Origin of the Extra Electrochemical Capacity Displayed by MO/Li Cells at Low Potential, J. Electrochem. Soc. 149 (2002) A627. doi:10.1149/1.1467947.

[69] Y.F. Zhukovskii, E.A. Kotomin, P. Balaya, J. Maier, Enhanced interfacial lithium storage in nanocomposites of transition metals with LiF and Li_2O: Comparison of DFT calculations

and experimental studies, Solid State Sci. 10 (2008) 491–495. doi:10.1016/j.solidstatesciences.2007.12.030.

[70] Z. Wang, L. Zhou, X.W. Lou, Metal oxide hollow nanostructures for lithium-ion batteries, Adv. Mater. 24 (2012) 1903–1911. doi:10.1002/adma.201200469.

[71] D. Bresser, S. Passerini, B. Scrosati, Leveraging valuable synergies by combining alloying and conversion for lithium-ion anodes, Energy Environ. Sci. 9 (2016) 3348–3367. doi:10.1039/C6EE02346K.

[72] P. Simon, J.M. Tarascon, Electrochemical energy storage: The benefits of nanomaterials, in: Nanotechnol. Energy Chall. Second Ed., 2013: pp. 277–298. doi:10.1002/9783527665105.ch10.

[73] M.R. Palacín, P. Simon, J.M. Tarascon, Nanomaterials for Electrochemical Energy Storage: the Good and the Bad, Acta Chim. Slov. (2016) 417–423. doi:10.17344/acsi.2016.2314.

[74] D. Bresser, F. Mueller, M. Fiedler, S. Krueger, R. Kloepsch, D. Baither, M. Winter, E. Paillard, S. Passerini, Transition-metal-doped zinc oxide nanoparticles as a new lithium-ion anode material, Chem. Mater. 25 (2013) 4977–4985. doi:10.1021/cm403443t.

[75] K. Abe, Nonaqueous Electrolytes and Advances in Additives, in: Electrolytes Lithium Lithium-Ion Batter., 2014: pp. 167–207. doi:10.1007/978-1-4939-0302-3_3.

[76] B.B. Owens, P. Reale, B. Scrosati, PRIMARY BATTERIES | Overview, in: Encycl. Electrochem. Power Sources, Elsevier, 2009: pp. 22–27. doi:10.1016/B978-044452745-5.00096-4.

[77] Y. Guo, SAFETY | Thermal Runaway, in: Encycl. Electrochem. Power Sources, Elsevier, 2009: pp. 241–253. doi:10.1016/B978-044452745-5.00394-4.

[78] S. Passerini, W.A. Henderson, SECONDARY BATTERIES – LITHIUM RECHARGEABLE SYSTEMS | Electrolytes: Ionic Liquids, in: Encycl. Electrochem. Power Sources, Elsevier, 2009: pp. 85–91. doi:10.1016/B978-044452745-5.00835-2.

[79] R. Marom, O. Haik, D. Aurbach, I.C. Halalay, Revisiting $LiClO_4$ as an Electrolyte for Rechargeable Lithium-Ion Batteries, J. Electrochem. Soc. 157 (2010) A972. doi:10.1149/1.3447750.

[80] G. Pistoia, M. De Rossi, B. Scrosati, Study of the Behavior of Ethylene Carbonate as a Nonaqueous Battery Solvent, J. Electrochem. Soc. 117 (1970) 500. doi:10.1149/1.2407550.

[81] J.M. Tarascon, D. Guyomard, New electrolyte compositions stable over the 0 to 5 V voltage range and compatible with the $Li_{1+x}Mn_2O_4$/carbon Li-ion cells, Solid State Ionics. 69 (1994) 293–305. doi:10.1016/0167-2738(94)90418-9.

[82] D. Guyomard, Rechargeable $Li_{1+x}Mn_2O_4$/Carbon Cells with a New Electrolyte Composition, J. Electrochem. Soc. 140 (1993) 3071. doi:10.1149/1.2220987.

[83] J. Vetter, M. Winter, M. Wohlfahrt-Mehrens, SECONDARY BATTERIES – LITHIUM RECHARGEABLE SYSTEMS – LITHIUM-ION | Aging Mechanisms, in: Encycl. Electrochem. Power Sources, Elsevier, 2009: pp. 393–403. doi:10.1016/B978-044452745-5.00922-9.

[84] M. Inaba, SECONDARY BATTERIES – LITHIUM RECHARGEABLE SYSTEMS – LITHIUM-ION | Negative Electrodes: Graphite, in: Encycl. Electrochem. Power Sources, Elsevier, 2009: pp. 198–208. doi:10.1016/B978-044452745-5.00189-1.

[85] H.B. Han, S.S. Zhou, D.J. Zhang, S.W. Feng, L.F. Li, K. Liu, W.F. Feng, J. Nie, H. Li, X.J. Huang, M. Armand, Z. Bin Zhou, Lithium bis(fluorosulfonyl)imide (LiFSI) as conducting salt for nonaqueous liquid electrolytes for lithium-ion batteries: Physicochemical and electrochemical properties, J. Power Sources. 196 (2011) 3623–3632. doi:10.1016/j.jpowsour.2010.12.040.

[86] K. Xu, Electrolytes and interphases in Li-ion batteries and beyond, Chem. Rev. 114 (2014) 11503–11618. doi:10.1021/cr500003w.

[87] B. Scrosati, J. Hassoun, Y.-K. Sun, Lithium-ion batteries. A look into the future, Energy Environ. Sci. 4 (2011) 3287. doi:10.1039/c1ee01388b.

[88] S.S. Zhang, A review on electrolyte additives for lithium-ion batteries, J. Power Sources. 162 (2006) 1379–1394. doi:10.1016/j.jpowsour.2006.07.074.

[89] P. Knauth, Inorganic solid Li ion conductors: An overview, Solid State Ionics. 180 (2009) 911–916. doi:10.1016/j.ssi.2009.03.022.

[90] J.W. Fergus, Ceramic and polymeric solid electrolytes for lithium-ion batteries, J. Power

Sources. 195 (2010) 4554–4569. doi:10.1016/j.jpowsour.2010.01.076.

[91] G.B. Appetecchi, M. Montanino, S. Passerini, Ionic liquid-based electrolytes for high energy, safer lithium batteries, in: ACS Symp. Ser., 2012: pp. 67–128. doi:10.1021/bk-2012-1117.ch004.

[92] R. Hayes, G.G. Warr, R. Atkin, Structure and Nanostructure in Ionic Liquids, Chem. Rev. 115 (2015) 6357–6426. doi:10.1021/cr500411q.

[93] A.E. Visser, N.J. Bridges, R.D. Rogers, eds., Ionic Liquids: Science and Applications, American Chemical Society, 2012. doi:10.1021/bk-2012-1117.

[94] S. Schneider, T. Hawkins, Y. Ahmed, M. Rosander, L. Hudgens, J. Mills, Green bipropellants: Hydrogen-rich ionic liquids that are hypergolic with hydrogen peroxide, Angew. Chemie - Int. Ed. 50 (2011) 5886–5888. doi:10.1002/anie.201101752.

[95] H. Nakagawa, Y. Fujino, S. Kozono, Y. Katayama, T. Nukuda, H. Sakaebe, H. Matsumoto, K. Tatsumi, Application of nonflammable electrolyte with room temperature ionic liquids (RTILs) for lithium-ion cells, J. Power Sources. 174 (2007) 1021–1026. doi:10.1016/j.jpowsour.2007.06.133.

[96] F. Zhou, Y. Liang, W. Liu, Ionic liquid lubricants: designed chemistry for engineering applications, Chem. Soc. Rev. 38 (2009) 2590. doi:10.1039/b817899m.

[97] M.J. Earle, K.R. Seddon, Ionic liquids. Green solvents for the future, in: Pure Appl. Chem., 2000: pp. 10–25. doi:10.1351/pac200072071391.

[98] G.G. Graf, Tin, Tin Alloys, and Tin Compounds, in: Ullmann's Encycl. Ind. Chem., Wiley-VCH Verlag GmbH & Co. KGaA, 2000: pp. 157–189. doi:10.1002/14356007.a27_049.

[99] N. V. Plechkova, K.R. Seddon, Applications of ionic liquids in the chemical industry, Chem. Soc. Rev. 37 (2008) 123–150. doi:10.1039/B006677J.

[100] K.N. Marsh, J.A. Boxall, R. Lichtenthaler, Room temperature ionic liquids and their mixtures - A review, Fluid Phase Equilib. 219 (2004) 93–98. doi:10.1016/j.fluid.2004.02.003.

[101] D.R. MacFarlane, M. Forsyth, P.C. Howlett, M. Kar, S. Passerini, J.M. Pringle, H. Ohno, M. Watanabe, F. Yan, W. Zheng, S. Zhang, J. Zhang, Ionic liquids and their solid-state analogues

as materials for energy generation and storage, Nat. Rev. Mater. 1 (2016) 15005. doi:10.1038/natrevmats.2015.5.

[102] H. Ohno, Electrochemical Aspects of Ionic Liquids, John Wiley & Sons Inc., 2005. doi:10.1002/0471762512.

[103] G.G. Eshetu, S. Grugeon, H. Kim, S. Jeong, L. Wu, G. Gachot, S. Laruelle, M. Armand, S. Passerini, Comprehensive Insights into the Reactivity of Electrolytes Based on Sodium Ions, ChemSusChem. 9 (2016) 462–471. doi:10.1002/cssc.201501605.

[104] Y. Chen, X. Zhang, D. Zhang, P. Yu, Y. Ma, High performance supercapacitors based on reduced graphene oxide in aqueous and ionic liquid electrolytes, Carbon N. Y. 49 (2011) 573–580. doi:10.1016/j.carbon.2010.09.060.

[105] B. Xu, F. Wu, R. Chen, G. Cao, S. Chen, Y. Yang, Mesoporous activated carbon fiber as electrode material for high-performance electrochemical double layer capacitors with ionic liquid electrolyte, J. Power Sources. 195 (2010) 2118–2124. doi:10.1016/j.jpowsour.2009.09.077.

[106] F. Pettersson, J. Keskinen, T. Remonen, L. von Hertzen, E. Jansson, K. Tappura, Y. Zhang, C.-E. Wilén, R. Österbacka, Printed environmentally friendly supercapacitors with ionic liquid electrolytes on paper, J. Power Sources. 271 (2014) 298–304. doi:10.1016/j.jpowsour.2014.08.020.

[107] T. Yamamoto, T. Nohira, R. Hagiwara, A. Fukunaga, S. Sakai, K. Nitta, S. Inazawa, Charge–discharge behavior of tin negative electrode for a sodium secondary battery using intermediate temperature ionic liquid sodium bis(fluorosulfonyl)amide–potassium bis(fluorosulfonyl)amide, J. Power Sources. 217 (2012) 479–484. doi:10.1016/j.jpowsour.2012.05.110.

[108] I. Hasa, S. Passerini, J. Hassoun, Characteristics of an ionic liquid electrolyte for sodium-ion batteries, J. Power Sources. 303 (2016) 203–207. doi:10.1016/j.jpowsour.2015.10.100.

[109] D. Monti, E. Jónsson, M.R. Palacín, P. Johansson, Ionic liquid based electrolytes for sodium-ion batteries: Na^+ solvation and ionic conductivity, J. Power Sources. 245 (2014) 630–636. doi:10.1016/j.jpowsour.2013.06.153.

[110] S. Menne, T. Vogl, A. Balducci, The synthesis and electrochemical characterization of bis(fluorosulfonyl)imide-based protic ionic liquids, Chem. Commun. 51 (2015) 3656–3659. doi:10.1039/C4CC09665G.

[111] G.A. Elia, R. Bernhard, J. Hassoun, A lithium-ion oxygen battery using a polyethylene glyme electrolyte mixed with an ionic liquid, RSC Adv. 5 (2015) 21360–21365. doi:10.1039/C4RA17277A.

[112] D. Di Lecce, S. Brutti, S. Panero, J. Hassoun, A new Sn-C/$LiFe_{0.1}Co_{0.9}PO_4$ full lithium-ion cell with ionic liquid-based electrolyte, Mater. Lett. 139 (2015) 329–332. doi:10.1016/j.matlet.2014.10.089.

[113] M. Nádherná, J. Reiter, J. Moškon, R. Dominko, Lithium bis(fluorosulfonyl)imide-PYR_{14}TFSI ionic liquid electrolyte compatible with graphite, J. Power Sources. 196 (2011) 7700–7706. doi:10.1016/j.jpowsour.2011.04.033.

[114] L.G. Chagas, D. Buchholz, L. Wu, B. Vortmann, S. Passerini, Unexpected performance of layered sodium-ion cathode material in ionic liquid-based electrolyte, J. Power Sources. 247 (2014) 377–383. doi:10.1016/j.jpowsour.2013.08.118.

[115] J.K. Kim, F. Mueller, H. Kim, S. Jeong, J.S. Park, S. Passerini, Y. Kim, Eco-Friendly Energy Storage System: Seawater and Ionic Liquid Electrolyte, ChemSusChem. 9 (2016) 42–49. doi:10.1002/cssc.201501328.

[116] Y. Qin, Y. Hu, S. Koehler, L. Cai, J. Wen, X. Tan, W.L. Xu, Q. Sheng, X. Hou, J. Xue, M. Yu, D. Weitz, Ultrafast Nanofiltration through Large-Area Single-Layered Graphene Membranes, ACS Appl. Mater. Interfaces. 9 (2017) 9239–9244. doi:10.1021/acsami.7b00504.

[117] B. Garcia, S. Lavallée, G. Perron, C. Michot, M. Armand, Room temperature molten salts as lithium battery electrolyte, Electrochim. Acta. 49 (2004) 4583–4588. doi:10.1016/j.electacta.2004.04.041.

[118] S. Seki, Y. Kobayashi, H. Miyashiro, Y. Ohno, A. Usami, Y. Mita, N. Kihira, M. Watanabe, N. Terada, Lithium secondary batteries using modified-imidazolium room-temperature ionic liquid, J. Phys. Chem. B. 110 (2006) 10228–10230. doi:10.1021/jp0620872.

[119] S. Seki, Y. Ohno, Y. Kobayashi, H. Miyashiro, A. Usami, Y. Mita, H. Tokuda, M. Watanabe,

K. Hayamizu, S. Tsuzuki, M. Hattori, N. Terada, Imidazolium-Based Room-Temperature Ionic Liquid for Lithium Secondary Batteries, J. Electrochem. Soc. 154 (2007) A173. doi:10.1149/1.2426871.

[120] J.K. Kim, A. Matic, J.H. Ahn, P. Jacobsson, An imidazolium based ionic liquid electrolyte for lithium batteries, J. Power Sources. 195 (2010) 7639–7643. doi:10.1016/j.jpowsour.2010.06.005.

[121] G.B. Appetecchi, S. Scaccia, C. Tizzani, F. Alessandrini, S. Passerini, Synthesis of Hydrophobic Ionic Liquids for Electrochemical Applications, J. Electrochem. Soc. 153 (2006) A1685. doi:10.1149/1.2213420.

[122] T. Dong, L. Zhang, S. Chen, X. Lu, S. Zhang, A piperidinium-based ionic liquid electrolyte to enhance the electrochemical properties of $LiFePO_4$ battery, Ionics (Kiel). 21 (2015) 2109–2117. doi:10.1007/s11581-015-1388-0.

[123] I.A. Profatilova, N.S. Choi, S.W. Roh, S.S. Kim, Electrochemical and thermal properties of graphite electrodes with imidazolium- and piperidinium-based ionic liquids, J. Power Sources. 192 (2009) 636–643. doi:10.1016/j.jpowsour.2009.03.041.

[124] J. Xiang, F. Wu, R. Chen, L. Li, H. Yu, High voltage and safe electrolytes based on ionic liquid and sulfone for lithium-ion batteries, J. Power Sources. 233 (2013) 115–120. doi:10.1016/j.jpowsour.2013.01.123.

[125] D.R. MacFarlane, P. Meakin, J. Sun, N. Amini, M. Forsyth, Pyrrolidinium Imides: A New Family of Molten Salts and Conductive Plastic Crystal Phases, J. Phys. Chem. B. 103 (1999) 4164–4170. doi:10.1021/jp984145s.

[126] E. Paillard, Q. Zhou, W.A. Henderson, G.B. Appetecchi, M. Montanino, S. Passerini, Electrochemical and Physicochemical Properties of $PY_{14}FSI$-Based Electrolytes with LiFSI, J. Electrochem. Soc. 156 (2009) A891. doi:10.1149/1.3208048.

[127] V. Borgel, E. Markevich, D. Aurbach, G. Semrau, M. Schmidt, On the application of ionic liquids for rechargeable Li batteries: High voltage systems, J. Power Sources. 189 (2009) 331–336. doi:10.1016/j.jpowsour.2008.08.099.

[128] A.I. Bhatt, A.S. Best, J. Huang, A.F. Hollenkamp, Application of the N-propyl-N-methyl-

pyrrolidinium Bis(fluorosulfonyl)imide RTIL Containing Lithium Bis(fluorosulfonyl)imide in Ionic Liquid Based Lithium Batteries, J. Electrochem. Soc. 157 (2010) A66. doi:10.1149/1.3257978.

[129] A.P. Lewandowski, A.F. Hollenkamp, S.W. Donne, A.S. Best, Cycling and rate performance of Li-$LiFePO_4$ cells in mixed FSI-TFSI room temperature ionic liquids, J. Power Sources. 195 (2010) 2029–2035. doi:10.1016/j.jpowsour.2009.10.059.

[130] J. Mun, T. Yim, S. Jurng, J.H. Park, S.Y. Lee, J.H. Ryu, Y.G. Kim, S.M. Oh, The feasibility of a pyrrolidinium-based ionic liquid solvent for non-graphitic carbon electrodes, Electrochem. Commun. 13 (2011) 1256–1259. doi:10.1016/j.elecom.2011.08.030.

[131] J. Reiter, M. Nádherná, R. Dominko, Graphite and $LiCo_{1/3}Mn_{1/3}Ni_{1/3}O_2$ electrodes with piperidinium ionic liquid and lithium bis(fluorosulfonyl)imide for Li-ion batteries, J. Power Sources. 205 (2012) 402–407. doi:10.1016/j.jpowsour.2012.01.003.

[132] G.A. Elia, U. Ulissi, F. Mueller, J. Reiter, N. Tsiouvaras, Y.K. Sun, B. Scrosati, S. Passerini, J. Hassoun, A Long-Life Lithium Ion Battery with Enhanced Electrode/Electrolyte Interface by Using an Ionic Liquid Solution, Chem. - A Eur. J. 22 (2016) 6808–6814. doi:10.1002/chem.201505192.

[133] D.M. Piper, T. Evans, K. Leung, T. Watkins, J. Olson, S.C. Kim, S.S. Han, V. Bhat, K.H. Oh, D.A. Buttry, S.H. Lee, Stable silicon-ionic liquid interface for next-generation lithium-ion batteries, Nat. Commun. 6 (2015) 6230. doi:10.1038/ncomms7230.

[134] H. Matsumoto, H. Sakaebe, K. Tatsumi, M. Kikuta, E. Ishiko, M. Kono, Fast cycling of $Li/LiCoO_2$ cell with low-viscosity ionic liquids based on bis(fluorosulfonyl)imide [FSI]−, J. Power Sources. 160 (2006) 1308–1313. doi:10.1016/j.jpowsour.2006.02.018.

[135] J. Reiter, E. Paillard, L. Grande, M. Winter, S. Passerini, Physicochemical properties of N-methoxyethyl-N-methylpyrrolidinum ionic liquids with perfluorinated anions, Electrochim. Acta. 91 (2013) 101–107. doi:10.1016/j.electacta.2012.12.086.

[136] H. Matsumoto, H. Sakaebe, K. Tatsumi, $Li/LiCoO_2$ Cell Performance Using Ionic Liquids Composed of N,N-Diethyl-N-methyl-N-(2-methoxyethyl)ammonium - Effect of Anionic Structure, in: ECS Trans., ECS, 2009: pp. 59–66. doi:10.1149/1.3123128.

[137] M.L.P. Le, N.A. Tran, H.P.K. Ngo, T.G. Nguyen, V.M. Tran, Liquid Electrolytes Based on Ionic Liquids for Lithium-Ion Batteries, J. Solution Chem. 44 (2015) 2332–2343. doi:10.1007/s10953-015-0408-z.

[138] T. Sato, T. Maruo, S. Marukane, K. Takagi, Ionic liquids containing carbonate solvent as electrolytes for lithium ion cells, J. Power Sources. 138 (2004) 253–261. doi:10.1016/j.jpowsour.2004.06.027.

[139] Y. Aihara, J. Kuratomi, T. Bando, T. Iguchi, H. Yoshida, T. Ono, K. Kuwana, Investigation on solvent-free solid polymer electrolytes for advanced lithium batteries and their performance, J. Power Sources. 114 (2003) 96–104. doi:10.1016/S0378-7753(02)00529-3.

[140] P. Lightfoot, M.A. Mehta, P.G. Bruce, Crystal Structure of the Polymer Electrolyte Poly(ethylene oxide)$_3$:LiCF_3SO_3, Science 262 (1993) 883–885. doi:10.1126/science.262.5135.883.

[141] G.B. Appetecchi, S. Passerini, PEO-carbon composite lithium polymer electrolyte, Electrochim. Acta. 45 (2000) 2139–2145. doi:10.1016/S0013-4686(99)00437-5.

[142] J.-H. Shin, W.A. Henderson, C. Tizzani, S. Passerini, S.-S. Jeong, K.-W. Kim, Characterization of Solvent-Free Polymer Electrolytes Consisting of Ternary PEO–LiTFSI–PYR_{14}TFSI, J. Electrochem. Soc. 153 (2006) A1649. doi:10.1149/1.2211928.

[143] V. Thangadurai, S. Narayanan, D. Pinzaru, Garnet-type solid-state fast Li ion conductors for Li batteries: critical review, Chem. Soc. Rev. 43 (2014) 4714. doi:10.1039/c4cs00020j.

[144] S. Ito, S. Fujiki, T. Yamada, Y. Aihara, Y. Park, T.Y. Kim, S.-W. Baek, J.-M. Lee, S. Doo, N. Machida, A rocking chair type all-solid-state lithium ion battery adopting Li_2O–ZrO_2 coated $LiNi_{0.8}Co_{0.15}Al_{0.05}O_2$ and a sulfide based electrolyte, J. Power Sources. 248 (2014) 943–950. doi:10.1016/j.jpowsour.2013.10.005.

[145] R. Kanno, M. Murayama, Lithium Ionic Conductor Thio-LISICON: The Li_2S-GeS_2-P_2S_5 System, J. Electrochem. Soc. 148 (2001) A742. doi:10.1149/1.1379028.

[146] A. Hayashi, Preparation and Characterization of Glassy Materials for All-Solid-State Lithium Secondary Batteries, J. Ceram. Soc. Japan. 115 (2007) 110–117. doi:10.2109/jcersj.115.110.

[147] T. Takeuchi, H. Kageyama, K. Nakanishi, M. Tabuchi, H. Sakaebe, T. Ohta, H. Senoh, T.

Sakai, K. Tatsumi, All-Solid-State Lithium Secondary Battery with Li_2S–C Composite Positive Electrode Prepared by Spark-Plasma-Sintering Process, J. Electrochem. Soc. 157 (2010) A1196. doi:10.1149/1.3486083.

[148] N. Machida, H. Yamamoto, S. Asano, T. Shigematsu, Preparation of amorphous $75Li_2S$-xP_2S_3-$(25-x)P_2S_5$ (mol%) solid electrolytes by a high-energy ball-milling process and their application for an all-solid-state lithium battery, Solid State Ionics. 176 (2005) 473–479. doi:10.1016/j.ssi.2004.08.019.

[149] M. Nagao, A. Hayashi, M. Tatsumisago, Fabrication of favorable interface between sulfide solid electrolyte and Li metal electrode for bulk-type solid-state Li/S battery, Electrochem. Commun. 22 (2012) 177–180. doi:10.1016/j.elecom.2012.06.015.

[150] N. Machida, J. Kashiwagi, M. Naito, T. Shigematsu, Electrochemical properties of all-solid-state batteries with ZrO_2-coated $LiNi_{1/3}Mn_{1/3}Co_{1/3}O_2$ as cathode materials, Solid State Ionics. 225 (2012) 354–358. doi:10.1016/j.ssi.2011.11.026.

[151] J.C. Bachman, S. Muy, A. Grimaud, H.H. Chang, N. Pour, S.F. Lux, O. Paschos, F. Maglia, S. Lupart, P. Lamp, L. Giordano, Y. Shao-Horn, Inorganic Solid-State Electrolytes for Lithium Batteries: Mechanisms and Properties Governing Ion Conduction, Chem. Rev. 116 (2016) 140–162. doi:10.1021/acs.chemrev.5b00563.

[152] N. Kamaya, K. Homma, Y. Yamakawa, M. Hirayama, R. Kanno, M. Yonemura, T. Kamiyama, Y. Kato, S. Hama, K. Kawamoto, A. Mitsui, A lithium superionic conductor, Nat. Mater. 10 (2011) 682–686. doi:10.1038/nmat3066.

[153] Y. Wang, W.D. Richards, S.P. Ong, L.J. Miara, J.C. Kim, Y. Mo, G. Ceder, Design principles for solid-state lithium superionic conductors, Nat. Mater. 14 (2015) 1026–1031. doi:10.1038/nmat4369.

[154] C. Sun, J. Liu, Y. Gong, D.P. Wilkinson, J. Zhang, Recent advances in all-solid-state rechargeable lithium batteries, Nano Energy. 33 (2017) 363–386. doi:10.1016/j.nanoen.2017.01.028.

[155] Y. Wang, H. Zhou, A lithium-air battery with a potential to continuously reduce O_2 from air for delivering energy, J. Power Sources. 195 (2010) 358–361.

doi:10.1016/j.jpowsour.2009.06.109.

[156] L. Wang, Y. Wang, Y. Xia, A high performance lithium-ion sulfur battery based on a Li_2S cathode using a dual-phase electrolyte, Energy Environ. Sci. 8 (2015) 1551–1558. doi:10.1039/C5EE00058K.

[157] K. Takada, Lithium iron sulfide as an electrode material in a solid state lithium battery, Solid State Ionics. 117 (1999) 273–276. doi:10.1016/S0167-2738(98)00413-5.

[158] N. Ohta, K. Takada, L. Zhang, R. Ma, M. Osada, T. Sasaki, Enhancement of the high-rate capability of solid-state lithium batteries by nanoscale interfacial modification, Adv. Mater. 18 (2006) 2226–2229. doi:10.1002/adma.200502604.

[159] K. Suzuki, M. Sakuma, S. Hori, T. Nakazawa, M. Nagao, M. Yonemura, M. Hirayama, R. Kanno, Synthesis, structure, and electrochemical properties of crystalline Li–P–S–O solid electrolytes: Novel lithium-conducting oxysulfides of $Li_{10}GeP_2S_{12}$ family, Solid State Ionics. 288 (2016) 229–234. doi:10.1016/j.ssi.2016.02.002.

[160] R. Kanno, M. Murayama, K. Sakamoto, New Lithium Solid Electrolytes, Thio-Lisicon: Materials Design Concept and Application To Solid State Battery, in: Solid State Ionics, World Scientific, 2002: pp. 13–22. doi:10.1142/9789812776259_0003.

[161] K.H. Park, D.Y. Oh, Y.E. Choi, Y.J. Nam, L. Han, J.Y. Kim, H. Xin, F. Lin, S.M. Oh, Y.S. Jung, Solution-Processable Glass LiI-Li_4SnS_4 Superionic Conductors for All-Solid-State Li-Ion Batteries, Adv. Mater. 28 (2016) 1874–1883. doi:10.1002/adma.201505008.

[162] A. Hayashi, S. Hama, H. Morimoto, M. Tatsumisago, T. Minami, Preparation of Li_2S-P_2S_5 Amorphous Solid Electrolytes by Mechanical Milling, J. Am. Ceram. Soc. 84 (2004) 477–79. doi:10.1111/j.1151-2916.2001.tb00685.x.

[163] S. Choi, M. Eom, C. Park, S. Son, G. Lee, D. Shin, Effect of Li_2SO_4 on the properties of Li_2S-P_2S_5 glass-ceramic solid electrolytes, Ceram. Int. 42 (2015) 6738–6742. doi:10.1016/j.ceramint.2016.01.045.

[164] Y. Aihara, S. Ito, R. Omoda, T. Yamada, S. Fujiki, T. Watanabe, Y. Park, S. Doo, The Electrochemical Characteristics and Applicability of an Amorphous Sulfide-Based Solid Ion Conductor for the Next-Generation Solid-State Lithium Secondary Batteries, Front. Energy

Res. 4 (2016) 1–8. doi:10.3389/fenrg.2016.00018.

[165] P. Bron, B. Roling, S. Dehnen, Impedance characterization reveals mixed conducting interphases between sulfidic superionic conductors and lithium metal electrodes, J. Power Sources. 352 (2017) 127–134. doi:10.1016/j.jpowsour.2017.03.103.

[166] M.S. Whittingham, Lithium batteries and cathode materials, Chem. Rev. 104 (2004) 4271–4301. doi:10.1021/cr020731c.

[167] B.M.L. Rao, Lithium-Aluminum Electrode, J. Electrochem. Soc. 124 (1977) 1490. doi:10.1149/1.2133098.

[168] K. Mizushima, P.C. Jones, P.J. Wiseman, J.B. Goodenough, Li_xCoO_2 (0<x<-1): A new cathode material for batteries of high energy density, Mater. Res. Bull. 15 (1980) 783–789. doi:10.1016/0025-5408(80)90012-4.

[169] M.S. Whittingham, Ultimate limits to intercalation reactions for lithium batteries, Chem. Rev. 114 (2014) 11414–11443. doi:10.1021/cr5003003.

[170] T. Ohzuku, Electrochemistry and Structural Chemistry of $LiNiO_2$ (R3m) for 4 Volt Secondary Lithium Cells, J. Electrochem. Soc. 140 (1993) 1862. doi:10.1149/1.2220730.

[171] S. Yamada, M. Fujiwara, M. Kanda, Synthesis and properties of $LiNiO_2$ as cathode material for secondary batteries, J. Power Sources. 54 (1995) 209–213. doi:10.1016/0378-7753(94)02068-E.

[172] R. Kanno, SECONDARY BATTERIES – LITHIUM RECHARGEABLE SYSTEMS – LITHIUM-ION | Positive Electrode: Lithium Nickel Oxide, in: Encycl. Electrochem. Power Sources, Elsevier, 2009: pp. 297–306. doi:10.1016/B978-044452745-5.00195-7.

[173] M. Wohlfahrt-Mehrens, SECONDARY BATTERIES – LITHIUM RECHARGEABLE SYSTEMS – LITHIUM-ION | Positive Electrode: Manganese Spinel Oxides, in: Encycl. Electrochem. Power Sources, Elsevier, 2009: pp. 318–327. doi:10.1016/B978-044452745-5.00198-2.

[174] M. Yoshio, H. Noguchi, SECONDARY BATTERIES – LITHIUM RECHARGEABLE SYSTEMS – LITHIUM-ION | Positive Electrode: Manganese Oxides, in: Encycl. Electrochem. Power Sources, Elsevier, 2009: pp. 307–317. doi:10.1016/B978-044452745-

5.00200-8.

[175] Y. Makimura, T. Ohzuku, SECONDARY BATTERIES – LITHIUM RECHARGEABLE SYSTEMS – LITHIUM-ION | Positive Electrode: Layered Mixed Metal Oxides, in: Encycl. Electrochem. Power Sources, Elsevier, 2009: pp. 249–257. doi:10.1016/B978-044452745-5.00196-9.

[176] S.-H. Kang, P. Kempgens, S. Greenbaum, A.J. Kropf, K. Amine, M.M. Thackeray, Interpreting the structural and electrochemical complexity of $0.5Li_2MnO_3$-$0.5LiMO_2$ electrodes for lithium batteries (M = $Mn_{0.5-x}Ni_{0.5-x}Co_{2x}$, $0 \leq x \leq 0.5$), J. Mater. Chem. 17 (2007) 2069–2077. doi:10.1039/B618715C.

[177] E. Rossen, C.D.W. Jones, J.R. Dahn, Structure and electrochemistry of $Li_xMn_yNi_{1-y}O_2$, Solid State Ionics. 57 (1992) 311–318. doi:10.1016/0167-2738(92)90164-K.

[178] M.E. Spahr, P. Novák, B. Schnyder, O. Haas, R. Nesper, Characterization of Layered Lithium Nickel Manganese Oxides Synthesized by a Novel Oxidative Coprecipitation Method and Their Electrochemical Performance as Lithium Insertion Electrode Materials, J. Electrochem. Soc. 145 (1998) 1113–1121. doi:10.1149/1.1838425.

[179] T. Ohzuku, Y. Makimura, Layered Lithium Insertion Material of $LiNi_{1/2}Mn_{1/2}O_2$: A Possible Alternative to $LiCoO_2$ for Advanced Lithium-Ion Batteries, Chem. Lett. 30 (2001) 744–745. doi:10.1246/cl.2001.744.

[180] M.M. Thackeray, S.-H. Kang, C.S. Johnson, J.T. Vaughey, R. Benedek, S.A. Hackney, Li_2MnO_3-stabilized $LiMO_2$ (M = Mn, Ni, Co) electrodes for lithium-ion batteries, J. Mater. Chem. 17 (2007) 3112. doi:10.1039/b702425h.

[181] T. Ohzuku, Y. Makimura, Layered Lithium Insertion Material of $LiCo_{1/3}Ni_{1/3}Mn_{1/3}O_2$ for Lithium-Ion Batteries, Chem. Lett. 30 (2001) 642–643. doi:10.1246/cl.2001.642.

[182] H. Kobayashi, Y. Arachi, S. Emura, H. Kageyama, K. Tatsumi, T. Kamiyama, Investigation on lithium de-intercalation mechanism for $Li_{1-y}Ni_{1/3}Mn_{1/3}Co_{1/3}O_2$, J. Power Sources. 146 (2005) 640–644. doi:10.1016/j.jpowsour.2005.03.081.

[183] B.J. Hwang, Y.W. Tsai, D. Carlier, G. Ceder, A combined computational/experimental study on $LiNi_{1/3}Co_{1/3}Mn_{1/3}O_2$, Chem. Mater. 15 (2003) 3676–3682. doi:10.1021/cm030299v.

[184] A.K. Padhi, Phospho-olivines as Positive-Electrode Materials for Rechargeable Lithium Batteries, J. Electrochem. Soc. 144 (1997) 1188. doi:10.1149/1.1837571.

[185] B.L. Ellis, K.T. Lee, L.F. Nazar, Positive electrode materials for Li-Ion and Li-batteries, Chem. Mater. 22 (2010) 691–714. doi:10.1021/cm902696j.

[186] K. Zaghib, A. Mauger, F. Gendron, C.M. Julien, J.B. Goodenough, SECONDARY BATTERIES – LITHIUM RECHARGEABLE SYSTEMS – LITHIUM-ION | Positive Electrode: Lithium Iron Phosphate, in: Encycl. Electrochem. Power Sources, Elsevier, 2009: pp. 264–296. doi:10.1016/B978-044452745-5.00204-5.

[187] Y. Wang, P. He, H. Zhou, Olivine $LiFePO_4$: development and future, Energy Environ. Sci. 4 (2011) 805–817. doi:10.1039/C0EE00176G.

[188] J.W. Choi, D. Aurbach, Promise and reality of post-lithium-ion batteries with high energy densities, Nat. Rev. Mater. 1 (2016) 16013. doi:10.1038/natrevmats.2016.13.

[189] W. Nehb, K. Vydra, Sulfur, in: Ullmann's Encycl. Ind. Chem., Wiley-VCH Verlag GmbH & Co. KGaA, 2006. doi:10.1002/14356007.a25_507.pub2.

[190] D.G.E. Kerfoot, Nickel, in: Ullmann's Encycl. Ind. Chem., Wiley-VCH Verlag GmbH & Co. KGaA, 2000. doi:10.1002/14356007.a17_157.

[191] Ullmann's Encyclopedia, Cobalt and Cobalt Compounds, in: Ullmann's Encycl. Ind. Chem., Wiley-VCH Verlag GmbH & Co. KGaA, 2012: pp. 429–464. doi:10.1002/14356007.a07.

[192] C.D. Parker, APPLICATIONS – STATIONARY | Energy Storage Systems: Batteries, in: Encycl. Electrochem. Power Sources, Elsevier, 2009: pp. 53–64. doi:10.1016/B978-044452745-5.00382-8.

[193] A. Manthiram, Y. Fu, S.H. Chung, C. Zu, Y.S. Su, Rechargeable lithium-sulfur batteries, Chem. Rev. 114 (2014) 11751–11787. doi:10.1021/cr500062v.

[194] M. Wild, L. O'Neill, T. Zhang, R. Purkayastha, G. Minton, M. Marinescu, G.J. Offer, Lithium sulfur batteries, a mechanistic review, Energy Environ. Sci. 8 (2015) 3477–3494. doi:10.1039/C5EE01388G.

[195] M. Liu, X. Qin, Y.-B. He, B. Li, F. Kang, Recent innovative configurations in high-energy

lithium–sulfur batteries, J. Mater. Chem. A. 5 (2017) 5222–5234. doi:10.1039/C7TA00290D.

[196] M.R. Busche, P. Adelhelm, H. Sommer, H. Schneider, K. Leitner, J. Janek, Systematical electrochemical study on the parasitic shuttle-effect in lithium-sulfur-cells at different temperatures and different rates, J. Power Sources. 259 (2014) 289–299. doi:10.1016/j.jpowsour.2014.02.075.

[197] J. Kim, D.J. Lee, H.G. Jung, Y.K. Sun, J. Hassoun, B. Scrosati, An advanced lithium-sulfur battery, Adv. Funct. Mater. 23 (2013) 1076–1080. doi:10.1002/adfm.201200689.

[198] Q. Pang, J. Tang, H. Huang, X. Liang, C. Hart, K.C. Tam, L.F. Nazar, A Nitrogen and Sulfur Dual-Doped Carbon Derived from Polyrhodanine@Cellulose for Advanced Lithium-Sulfur Batteries, Adv. Mater. 27 (2015) 6021–6028. doi:10.1002/adma.201502467.

[199] Z.W. Seh, W. Li, J.J. Cha, G. Zheng, Y. Yang, M.T. McDowell, P.C. Hsu, Y. Cui, Sulphur-TiO_2 yolk-shell nanoarchitecture with internal void space for long-cycle lithium-sulphur batteries, Nat. Commun. 4 (2013) 1331. doi:10.1038/ncomms2327.

[200] Z. Yuan, H.J. Peng, T.Z. Hou, J.Q. Huang, C.M. Chen, D.W. Wang, X.B. Cheng, F. Wei, Q. Zhang, Powering Lithium-Sulfur Battery Performance by Propelling Polysulfide Redox at Sulfiphilic Hosts, Nano Lett. 16 (2016) 519–527. doi:10.1021/acs.nanolett.5b04166.

[201] J.Z. Wang, L. Lu, M. Choucair, J.A. Stride, X. Xu, H.K. Liu, Sulfur-graphene composite for rechargeable lithium batteries, J. Power Sources. 196 (2011) 7030–7034. doi:10.1016/j.jpowsour.2010.09.106.

[202] G.C. Li, G.R. Li, S.H. Ye, X.P. Gao, A Polyaniline-coated sulfur/carbon composite with an enhanced high-rate capability as a cathode material for lithium/sulfur batteries, Adv. Energy Mater. 2 (2012) 1238–1245. doi:10.1002/aenm.201200017.

[203] X. Liu, J.-Q. Huang, Q. Zhang, L. Mai, Nanostructured Metal Oxides and Sulfides for Lithium-Sulfur Batteries, Adv. Mater. 29 (2017) 1601759. doi:10.1002/adma.201601759.

[204] X. Rui, H. Tan, Q. Yan, Nanostructured metal sulfides for energy storage, Nanoscale. 6 (2014) 9889. doi:10.1039/C4NR03057E.

[205] Y. Mikhaylik, Electrolytes for lithium sulfur cells, US7354680B2, 2004.

[206] R.D. Rauh, A Lithium/Dissolved Sulfur Battery with an Organic Electrolyte, J. Electrochem. Soc. 126 (1979) 523. doi:10.1149/1.2129079.

[207] M. Barghamadi, A.S. Best, A.I. Bhatt, A.F. Hollenkamp, M. Musameh, R.J. Rees, T. Rüther, Lithium–sulfur batteries—the solution is in the electrolyte, but is the electrolyte a solution?, Energy Environ. Sci. 7 (2014) 3902–3920. doi:10.1039/C4EE02192D.

[208] M. Agostini, J. Hassoun, A lithium-ion sulfur battery using a polymer, polysulfide-added membrane, Sci. Rep. 5 (2015) 7591. doi:10.1038/srep07591.

[209] M. Rao, X. Geng, X. Li, S. Hu, W. Li, Lithium-sulfur cell with combining carbon nanofibers–sulfur cathode and gel polymer electrolyte, J. Power Sources. 212 (2012) 179–185. doi:10.1016/j.jpowsour.2012.03.111.

[210] S.S. Zhang, D.T. Tran, Z. Zhang, Poly(acrylic acid) gel as a polysulphide blocking layer for high-performance lithium/sulphur battery, J. Mater. Chem. A. 2 (2014) 18288–18292. doi:10.1039/C4TA04417G.

[211] Q. Wang, J. Jin, X. Wu, G. Ma, J. Yang, Z. Wen, A shuttle effect free lithium sulfur battery based on a hybrid electrolyte, Phys. Chem. Chem. Phys. 16 (2014) 21225–21229. doi:10.1039/C4CP03694H.

[212] S. Gu, X. Huang, Q. Wang, J. Jin, Q. Wang, Z. Wen, R. Qian, A hybrid electrolyte for long-life semi-solid-state lithium sulfur batteries, J. Mater. Chem. A. 5 (2017) 13971–13975. doi:10.1039/C7TA04017B.

[213] J. Hassoun, B. Scrosati, Moving to a solid-state configuration: A valid approach to making lithium-sulfur batteries viable for practical applications, Adv. Mater. 22 (2010) 5198–5201. doi:10.1002/adma.201002584.

[214] J. Hassoun, B. Scrosati, A High-Performance Polymer Tin Sulfur Lithium Ion Battery, Angew. Chemie Int. Ed. 49 (2010) 2371–2374. doi:10.1002/anie.200907324.

[215] T. Yamada, S. Ito, R. Omoda, T. Watanabe, Y. Aihara, M. Agostini, U. Ulissi, J. Hassoun, B. Scrosati, All Solid-State Lithium-Sulfur Battery Using a Glass-Type P_2S_5-Li_2S Electrolyte: Benefits on Anode Kinetics, J. Electrochem. Soc. 162 (2015) A646–A651. doi:10.1149/2.0441504jes.

[216] M. Nagao, A. Hayashi, M. Tatsumisago, Sulfur–carbon composite electrode for all-solid-state Li/S battery with Li_2S–P_2S_5 solid electrolyte, Electrochim. Acta. 56 (2011) 6055–6059. doi:10.1016/j.electacta.2011.04.084.

[217] X. Yao, N. Huang, F. Han, Q. Zhang, H. Wan, J.P. Mwizerwa, C. Wang, X. Xu, High-Performance All-Solid-State Lithium–Sulfur Batteries Enabled by Amorphous Sulfur-Coated Reduced Graphene Oxide Cathodes, Adv. Energy Mater. 7 (2017). doi:10.1002/aenm.201602923.

[218] M. Eom, S. Son, C. Park, S. Noh, W.T. Nichols, D. Shin, High performance all-solid-state lithium-sulfur battery using a Li_2S-VGCF nanocomposite, Electrochim. Acta. 230 (2017) 279–284. doi:10.1016/j.electacta.2017.01.155.

[219] F. Han, J. Yue, X. Fan, T. Gao, C. Luo, Z. Ma, L. Suo, C. Wang, High-performance all-solid-state lithium-sulfur battery enabled by a mixed-conductive Li_2S nanocomposite, Nano Lett. 16 (2016) 4521–4527. doi:10.1021/acs.nanolett.6b01754.

[220] M. Nagao, Y. Imade, H. Narisawa, R. Watanabe, T. Yokoi, T. Tatsumi, R. Kanno, Reaction mechanism of all-solid-state lithium-sulfur battery with two-dimensional mesoporous carbon electrodes, J. Power Sources. 243 (2013) 60–64. doi:10.1016/j.jpowsour.2013.05.037 Short communication.

[221] M. Nagao, Y. Imade, H. Narisawa, T. Kobayashi, R. Watanabe, T. Yokoi, T. Tatsumi, R. Kanno, All-solid-state Liesulfur batteries with mesoporous electrode and thio-LISICON solid electrolyte, J. Power Sources. 222 (2013) 237–242. doi:10.1016/jjpowsour.2012.08.041.

[222] X. Yao, D. Liu, C. Wang, P. Long, G. Peng, Y.S. Hu, H. Li, L. Chen, X. Xu, High-Energy All-Solid-State Lithium Batteries with Ultralong Cycle Life, Nano Lett. 16 (2016) 7148–7154. doi:10.1021/acs.nanolett.6b03448.

[223] T. Hakari, M. Nagao, A. Hayashi, M. Tatsumisago, All-solid-state lithium batteries with Li_3PS_4 glass as active material, J. Power Sources. 293 (2015) 721–725. doi:10.1016/j.jpowsour.2015.05.073.

[224] K.M. Abraham, A Polymer Electrolyte-Based Rechargeable Lithium/Oxygen Battery, J. Electrochem. Soc. 143 (1996) 1. doi:10.1149/1.1836378.

[225] A.C. Luntz, B.D. McCloskey, Nonaqueous Li-air batteries: A status report, Chem. Rev. 114 (2014) 11721–11750. doi:10.1021/cr500054y.

[226] O. Yamamoto, Introduction, in: Lithium Air Batter., Springer New York, 2014: pp. 1–21. doi:10.1007/978-1-4899-8062-5_1.

[227] B.D. McCloskey, C.M. Burke, J.E. Nichols, S.E. Renfrew, Mechanistic insights for the development of Li–O_2 battery materials: addressing Li_2O_2 conductivity limitations and electrolyte and cathode instabilities, Chem. Commun. 51 (2015) 12701–12715. doi:10.1039/C5CC04620C.

[228] B.D. McCloskey, D.S. Bethune, R.M. Shelby, G. Girishkumar, A.C. Luntz, Solvents critical role in nonaqueous Lithium-Oxygen battery electrochemistry, J. Phys. Chem. Lett. 2 (2011) 1161–1166. doi:10.1021/jz200352v.

[229] B.D. McCloskey, A. Speidel, R. Scheffler, D.C. Miller, V. Viswanathan, J.S. Hummelshøj, J.K. Nørskov, A.C. Luntz, Twin Problems of Interfacial Carbonate Formation in Nonaqueous Li–O 2 Batteries, J. Phys. Chem. Lett. 3 (2012) 997–1001. doi:10.1021/jz300243r.

[230] S.A. Freunberger, Y. Chen, Z. Peng, J.M. Griffin, L.J. Hardwick, F. Bardé, P. Novák, P.G. Bruce, Reactions in the rechargeable lithium-O_2 battery with alkyl carbonate electrolytes, J. Am. Chem. Soc. 133 (2011) 8040–8047. doi:10.1021/ja2021747.

[231] Y. Chen, S.A. Freunberger, Z. Peng, F. Bardé, P.G. Bruce, Li-O_2 battery with a dimethylformamide electrolyte, J. Am. Chem. Soc. 134 (2012) 7952–7957. doi:10.1021/ja302178w.

[232] D. Sharon, D. Hirshberg, M. Afri, A. Garsuch, A.A. Frimer, D. Aurbach, Lithium-oxygen electrochemistry in non-aqueous solutions, Isr. J. Chem. 55 (2015) 508–520. doi:10.1002/ijch.201400135.

[233] C. Wu, C. Liao, T. Li, Y. Shi, J. Luo, L. Li, J. Yang, A polymer lithium–oxygen battery based on semi-polymeric conducting ionomers as the polymer electrolyte, J. Mater. Chem. A. 4 (2016) 15189–15196. doi:10.1039/C6TA06082J.

[234] H. Kitaura, H. Zhou, All-solid-state lithium-oxygen battery with high safety in wide ambient temperature range, Sci. Rep. 5 (2015) 13271. doi:10.1038/srep13271.

[235] B. Kumar, J. Kumar, R. Leese, J.P. Fellner, S.J. Rodrigues, K.M. Abraham, A Solid-State, Rechargeable, Long Cycle Life Lithium–Air Battery, J. Electrochem. Soc. 157 (2010) A50. doi:10.1149/1.3256129.

[236] M. Balaish, A. Kraytsberg, Y. Ein-Eli, A critical review on lithium–air battery electrolytes, Phys. Chem. Chem. Phys. 16 (2014) 2801. doi:10.1039/c3cp54165g.

[237] B.D. McCloskey, D.S. Bethune, R.M. Shelby, T. Mori, R. Scheffler, A. Speidel, M. Sherwood, A.C. Luntz, Limitations in Rechargeability of Li-O_2 Batteries and Possible Origins, J. Phys. Chem. Lett. 3 (2012) 3043–3047. doi:10.1021/jz301359t.

[238] G.A. Elia, J. Hassoun, W.J. Kwak, Y.K. Sun, B. Scrosati, F. Mueller, D. Bresser, S. Passerini, P. Oberhumer, N. Tsiouvaras, J. Reiter, An advanced lithium-air battery exploiting an ionic liquid-based electrolyte, Nano Lett. 14 (2014) 6572–6577. doi:10.1021/nl5031985.

[239] J. Xie, Q. Dong, I. Madden, X. Yao, Q. Cheng, P. Dornath, W. Fan, D. Wang, Achieving Low Overpotential Li-O_2 Battery Operations by Li_2O_2 Decomposition through One-Electron Processes, Nano Lett. 15 (2015) 8371–8376. doi:10.1021/acs.nanolett.5b04097.

[240] K. Takechi, S. Higashi, F. Mizuno, H. Nishikoori, H. Iba, T. Shiga, Stability of Solvents against Superoxide Radical Species for the Electrolyte of Lithium-Air Battery, ECS Electrochem. Lett. 1 (2012) A27–A29. doi:10.1149/2.010201eel.

[241] Y. Li, Z. Zhang, D. Duan, Y. Sun, G. Wei, X. Hao, S. Liu, Y. Han, W. Meng, The correlation of the properties of pyrrolidinium-based ionic liquid electrolytes with the discharge–charge performances of rechargeable Li–O_2 batteries, J. Power Sources. 329 (2016) 207–215. doi:10.1016/j.jpowsour.2016.08.077.

[242] I. Ruggeri, C. Arbizzani, F. Soavi, A novel concept of Semi-solid, Li Redox Flow Air (O_2) Battery: A breakthrough towards high energy and power batteries, Electrochim. Acta. 206 (2016) 291–300. doi:10.1016/j.electacta.2016.04.139.

[243] S. Das, J. Højberg, K.B. Knudsen, R. Younesi, P. Johansson, P. Norby, T. Vegge, Instability of Ionic Liquid-Based Electrolytes in Li–O_2 Batteries, J. Phys. Chem. C. 119 (2015) 18084–18090. doi:10.1021/acs.jpcc.5b04950.

[244] T. Zhang, H. Zhou, From Li-O_2 to Li-Air batteries: Carbon nanotubes/ionic liquid gels with

a tricontinuous passage of electrons, ions, and oxygen, Angew. Chemie - Int. Ed. 51 (2012) 11062–11067. doi:10.1002/anie.201204983.

[245] T. Kuboki, T. Okuyama, T. Ohsaki, N. Takami, Lithium-air batteries using hydrophobic room temperature ionic liquid electrolyte, J. Power Sources. 146 (2005) 766–769. doi:10.1016/j.jpowsour.2005.03.082.

[246] M. Ara, T. Meng, G.-A. Nazri, S.O. Salley, K.Y. Simon Ng, Ternary Imidazolium-Pyrrolidinium-Based Ionic Liquid Electrolytes for Rechargeable Li-O_2 Batteries, J. Electrochem. Soc. 161 (2014) A1969–A1975. doi:10.1149/2.0031414jes.

[247] G.T. Kim, S.S. Jeong, M.Z. Xue, A. Balducci, M. Winter, S. Passerini, F. Alessandrini, G.B. Appetecchi, Development of ionic liquid-based lithium battery prototypes, J. Power Sources. 199 (2012) 239–246. doi:10.1016/j.jpowsour.2011.10.036.

[248] M. Agostini, U. Ulissi, D. Di Lecce, Y. Ahiara, S. Ito, J. Hassoun, A Lithium-Ion Battery based on an Ionic Liquid Electrolyte, Tin-Carbon Nanostructured Anode, and Li_2O-ZrO_2-Coated $Li[Ni_{0.8}Co_{0.15}Al_{0.05}]O_2$ Cathode, Energy Technol. 3 (2015) 632–637. doi:10.1002/ente.201402226.

[249] Q. Zhou, W.A. Henderson, G.B. Appetecchi, S. Passerini, Phase behavior and thermal properties of ternary ionic liquid lithium salt (IL-IL-LiX) electrolytes, J. Phys. Chem. C. 114 (2010) 6201–6204. doi:10.1021/jp911759d.

[250] H. Nakamoto, Y. Suzuki, T. Shiotsuki, F. Mizuno, S. Higashi, K. Takechi, T. Asaoka, H. Nishikoori, H. Iba, Ether-functionalized ionic liquid electrolytes for lithium-air batteries, J. Power Sources. 243 (2013) 19–23. doi:10.1016/j.jpowsour.2013.05.147 Short communication.

[251] Q. Li, R. Cao, J. Cho, G. Wu, Nanostructured carbon-based cathode catalysts for nonaqueous lithium–oxygen batteries, Phys. Chem. Chem. Phys. 16 (2014) 13568–13582. doi:10.1039/C4CP00225C.

[252] Z. Wen, C. Shen, Y. Lu, Air electrode for the lithium-air batteries: Materials and structure designs, Chempluschem. 80 (2015) 270–287. doi:10.1002/cplu.201402104.

[253] K. Song, D.A. Agyeman, J. Jung, M.R. Jo, J. Yang, Y.M. Kang, A Review of the design strategies for tailored cathode catalyst materials in rechargeable Li-O_2 batteries, Isr. J. Chem.

55 (2015) 458–471. doi:10.1002/ijch.201400089.

[254] H.-J. Shin, W.-J. Kwak, D. Aurbach, Y.-K. Sun, Large-Scale Li-O_2 Pouch Type Cells for Practical Evaluation and Applications, Adv. Funct. Mater. 27 (2017) 1605500. doi:10.1002/adfm.201605500.

[255] Y. Zhang, L. Wang, Z. Guo, Y. Xu, Y. Wang, H. Peng, High-Performance Lithium-Air Battery with a Coaxial-Fiber Architecture, Angew. Chemie Int. Ed. 55 (2016) 4487–4491. doi:10.1002/anie.201511832.

[256] R. Raccichini, A. Varzi, S. Passerini, B. Scrosati, The role of graphene for electrochemical energy storage, Nat. Mater. 14 (2015) 271–279. doi:10.1038/nmat4170.

[257] W. Zhou, H. Zhang, H. Nie, Y. Ma, Y. Zhang, H. Zhang, Hierarchical micron-sized mesoporous/macroporous graphene with well-tuned surface oxygen chemistry for high capacity and cycling stability Li-O_2 battery, ACS Appl. Mater. Interfaces. 7 (2015) 3389–3397. doi:10.1021/am508513m.

[258] Z. Zhang, J. Bao, C. He, Y. Chen, J. Wei, Z. Zhou, Hierarchical carbon-nitrogen architectures with both mesopores and macrochannels as excellent cathodes for rechargeable Li-O_2 batteries, Adv. Funct. Mater. 24 (2014) 6826–6833. doi:10.1002/adfm.201401581.

[259] Y. Li, X. Li, D. Geng, Y. Tang, R. Li, J.P. Dodelet, M. Lefèvre, X. Sun, Carbon black cathodes for lithium oxygen batteries: Influence of porosity and heteroatom-doping, Carbon N. Y. 64 (2013) 170–177. doi:10.1016/j.carbon.2013.07.049.

[260] J.K. Papp, J.D. Forster, C.M. Burke, H.W. Kim, A.C. Luntz, R.M. Shelby, J.J. Urban, B.D. McCloskey, Poly(vinylidene fluoride) (PVDF) Binder Degradation in Li-O_2 Batteries: A Consideration for the Characterization of Lithium Superoxide, J. Phys. Chem. Lett. 8 (2017) 1169–1174. doi:10.1021/acs.jpclett.7b00040.

[261] R. Black, S.H. Oh, J.H. Lee, T. Yim, B. Adams, L.F. Nazar, Screening for superoxide reactivity in Li-O_2 batteries: Effect on Li_2O_2/LiOH crystallization, J. Am. Chem. Soc. 134 (2012) 2902–2905. doi:10.1021/ja2111543.

[262] B.D. Mccloskey, A. Valery, A.C. Luntz, S.R. Gowda, G.M. Wallraff, J.M. Garcia, T. Mori, L.E. Krupp, Combining accurate O_2 and Li_2O_2 assays to separate discharge and charge

stability limitations in nonaqueous Li-O_2 Batteries, J. Phys. Chem. Lett. 4 (2013) 2989–2993. doi:10.1021/jz401659f.

[263] J. Hassoun, G. Derrien, S. Panero, B. Scrosati, A nanostructured Sn-C composite lithium battery electrode with unique stability and high electrochemical performance, Adv. Mater. 20 (2008) 3169–3175. doi:10.1002/adma.200702928.

[264] J. Hassoun, K.S. Lee, Y.K. Sun, B. Scrosati, An advanced lithium ion battery based on high performance electrode materials, J. Am. Chem. Soc. 133 (2011) 3139–3143. doi:10.1021/ja110522x.

[265] R. Hu, W. Sun, Y. Chen, M. Zeng, M. Zhu, Silicon/graphene based nanocomposite anode: large-scale production and stable high capacity for lithium ion batteries, J. Mater. Chem. A. 2 (2014) 9118–9125. doi:10.1039/C4TA01013B.

[266] A. Guerfi, M. Dontigny, P. Charest, M. Petitclerc, M. Lagacé, A. Vijh, K. Zaghib, Improved electrolytes for Li-ion batteries: Mixtures of ionic liquid and organic electrolyte with enhanced safety and electrochemical performance, J. Power Sources. 195 (2010) 845–852. doi:10.1016/j.jpowsour.2009.08.056.

[267] L. Lombardo, S. Brutti, M.A. Navarra, S. Panero, P. Reale, Mixtures of ionic liquid-Alkylcarbonates as electrolytes for safe lithium-ion batteries, J. Power Sources. 227 (2013) 8–14. doi:10.1016/j.jpowsour.2012.11.017.

[268] Q. Zhou, P.D. Boyle, L. Malpezzi, A. Mele, J.H. Shin, S. Passerini, W.A. Henderson, Phase behavior of ionic liquid-LiX mixtures: Pyrrolidinium cations and $TFSI^-$ anions - Linking structure to transport properties, Chem. Mater. 23 (2011) 4331–4337. doi:10.1021/cm201427k.

[269] A. E. Visser, N. J. Bridges, R. D.Rogers, Title, copyright, foreword, in: ACS Symp. Ser., 2012: pp. i–v. doi:10.1021/bk-2013-1135.fw001.

[270] N. DeVos, C. Maton, C. V. Stevens, Electrochemical Stability of Ionic Liquids: General Influences and Degradation Mechanisms, ChemElectroChem. 1 (2014) 1258–1270. doi:10.1002/celc.201402086.

[271] S. Brutti, J. Hassoun, B. Scrosati, C.Y. Lin, H. Wu, H.W. Hsieh, A high power Sn-C/C-

$LiFePO_4$ lithium ion battery, J. Power Sources. 217 (2012) 72–76. doi:10.1016/j.jpowsour.2012.05.102.

[272] G.A. Elia, D. Bresser, J. Reiter, P. Oberhumer, Y.K. Sun, B. Scrosati, S. Passerini, J. Hassoun, Interphase Evolution of a Lithium-Ion/Oxygen Battery, ACS Appl. Mater. Interfaces. 7 (2015) 22638–22643. doi:10.1021/acsami.5b07414.

[273] C. Schreiner, S. Zugmann, R. Hartl, H.J. Gores, Fractional walden rule for ionic liquids: Examples from recent measurements and a critique of the so-called ideal KCl line for the walden plot, J. Chem. Eng. Data. 55 (2010) 1784–1788. doi:10.1021/je900878j.

[274] J. Pires, L. Timperman, J. Jacquemin, A. Balducci, M. Anouti, Density, conductivity, viscosity, and excess properties of (pyrrolidinium nitrate-based Protic Ionic Liquid + propylene carbonate) binary mixture, J. Chem. Thermodyn. 59 (2013) 10–19. doi:10.1016/j.jct.2012.11.020.

[275] G.B. Appetecchi, M. Montanino, M. Carewska, M. Moreno, F. Alessandrini, S. Passerini, Chemical-physical properties of bis(perfluoroalkylsulfonyl)imide-based ionic liquids, Electrochim. Acta. 56 (2011) 1300–1307. doi:10.1016/j.electacta.2010.10.023.

[276] C.C. Nguyen, S.W. Song, Characterization of SEI layer formed on high performance Si-Cu anode in ionic liquid battery electrolyte, Electrochem. Commun. 12 (2010) 1593–1595. doi:10.1016/j.elecom.2010.09.003.

[277] A.M. Andersson, K. Edström, Chemical Composition and Morphology of the Elevated Temperature SEI on Graphite, J. Electrochem. Soc. 148 (2001) A1100. doi:10.1149/1.1397771.

[278] D. Aurbach, Review of selected electrode-solution interactions which determine the performance of Li and Li ion batteries, J. Power Sources. 89 (2000) 206–218. doi:10.1016/S0378-7753(00)00431-6.

[279] L. Grande, J. Von Zamory, S.L. Koch, J. Kalhoff, E. Paillard, S. Passerini, Homogeneous Lithium Electrodeposition with Pyrrolidinium-Based Ionic Liquid Electrolytes, ACS Appl. Mater. Interfaces. 7 (2015) 5950–5958. doi:10.1021/acsami.5b00209.

[280] H. Zheng, Q. Qu, L. Zhang, G. Liu, V.S. Battaglia, Hard carbon: a promising lithium-ion

battery anode for high temperature applications with ionic electrolyte, RSC Adv. 2 (2012) 4904. doi:10.1039/c2ra20536j.

[281] B.W. Zewde, G.A. Elia, S. Admassie, J. Zimmermann, M. Hagemann, C.S. Isfort, B. Scrosati, J. Hassoun, Polyethylene oxide electrolyte added by silane-functionalized TiO_2 filler for lithium battery, Solid State Ionics. 268 (2014) 174–178. doi:10.1016/j.ssi.2014.10.030.

[282] C. Masquelier, L. Croguennec, Polyanionic (phosphates, silicates, sulfates) frameworks as electrode materials for rechargeable Li (or Na) batteries, Chem. Rev. 113 (2013) 6552–6591. doi:10.1021/cr3001862.

[283] N. Böckenfeld, T. Placke, M. Winter, S. Passerini, A. Balducci, The influence of activated carbon on the performance of lithium iron phosphate based electrodes, Electrochim. Acta. 76 (2012) 130–136. doi:10.1016/j.electacta.2012.04.152.

[284] G.A. Elia, J. Wang, D. Bresser, J. Li, B. Scrosati, S. Passerini, J. Hassoun, A New, High Energy Sn–C/Li[$Li_{0.2}Ni_{0.4/3}Co_{0.4/3}Mn_{1.6/3}$]$O_2$ Lithium-Ion Battery, ACS Appl. Mater. Interfaces. 6 (2014) 12956–12961. doi:10.1021/am502884y.

[285] S.D. Beattie, T. Hatchard, A. Bonakdarpour, K.C. Hewitt, J.R. Dahn, Anomalous, High-Voltage Irreversible Capacity in Tin Electrodes for Lithium Batteries, J. Electrochem. Soc. 150 (2003) A701. doi:10.1149/1.1569477.

[286] B.A. Boukamp, A package for impedance/admittance data analysis, Solid State Ionics. 18–19 (1986) 136–140. doi:10.1016/0167-2738(86)90100-1.

[287] B.A. Boukamp, A Nonlinear Least Squares Fit procedure for analysis of immittance data of electrochemical systems, Solid State Ionics. 20 (1986) 31–44. doi:10.1016/0167-2738(86)90031-7.

[288] A. Lewandowski, A. Świderska-Mocek, Ionic liquids as electrolytes for Li-ion batteries-An overview of electrochemical studies, J. Power Sources. 194 (2009) 601–609. doi:10.1016/j.jpowsour.2009.06.089.

[289] M. Broussely, P. Biensan, F. Bonhomme, P. Blanchard, S. Herreyre, K. Nechev, R.J. Staniewicz, Main aging mechanisms in Li ion batteries, J. Power Sources. 146 (2005) 90–96. doi:10.1016/j.jpowsour.2005.03.172.

[290] C. V. Amanchukwu, J.R. Harding, Y. Shao-Horn, P.T. Hammond, Understanding the chemical stability of polymers for lithium-air batteries, Chem. Mater. 27 (2015) 550–561. doi:10.1021/cm5040003.

[291] J. Hassoun, H.G. Jung, D.J. Lee, J.B. Park, K. Amine, Y.K. Sun, B. Scrosati, A metal-free, lithium-ion oxygen battery: A step forward to safety in lithium-air batteries, Nano Lett. 12 (2012) 5775–5779. doi:10.1021/nl303087j.

[292] D. Aurbach, Review of selected electrode – solution interactions which determine the performance of Li and Li ion batteries, J. Power Sources. 89 (2000) 206–218. doi:http://dx.doi.org/10.1016/S0378-7753(00)00431-6.

[293] D. Aurbach, B. Markovsky, G. Salitra, E. Markevich, Y. Talyossef, M. Koltypin, L. Nazar, B. Ellis, D. Kovacheva, Review on electrode-electrolyte solution interactions, related to cathode materials for Li-ion batteries, J. Power Sources. 165 (2007) 491–499. doi:10.1016/j.jpowsour.2006.10.025.

[294] R. Younesi, M. Hahlin, K. Edström, Surface characterization of the carbon cathode and the lithium anode of Li-O_2 batteries using $LiClO_4$ or LiBOB salts, ACS Appl. Mater. Interfaces. 5 (2013) 1333–1341. doi:10.1021/am3026129.

[295] L. Grande, E. Paillard, G.T. Kim, S. Monaco, S. Passerini, Ionic liquid electrolytes for Li-air batteries: Lithium metal cycling, Int. J. Mol. Sci. 15 (2014) 8122–8137. doi:10.3390/ijms15058122.

[296] Z. Li, J. Huang, B. Yann Liaw, V. Metzler, J. Zhang, A review of lithium deposition in lithium-ion and lithium metal secondary batteries, J. Power Sources. 254 (2014) 168–182. doi:10.1016/j.jpowsour.2013.12.099.

[297] Y. Lu, Z. Tu, L.A. Archer, Stable lithium electrodeposition in liquid and nanoporous solid electrolytes, Nat. Mater. 13 (2014) 961–969. doi:10.1038/nmat4041.

[298] U.R. Farooqui, A.L. Ahmad, N.A. Hamid, Challenges and potential advantages of membranes in lithium air batteries: A review, Renew. Sustain. Energy Rev. 77 (2017) 1114–1129. doi:10.1016/j.rser.2016.11.220.

[299] D. Geng, N. Ding, T.S.A. Hor, S.W. Chien, Z. Liu, D. Wuu, X. Sun, Y. Zong, From Lithium-

Oxygen to Lithium-Air Batteries: Challenges and Opportunities, Adv. Energy Mater. 6 (2016) 1502164. doi:10.1002/aenm.201502164.

[300] H.G. Jung, J. Hassoun, J.B. Park, Y.K. Sun, B. Scrosati, An improved high-performance lithium-air battery, Nat. Chem. 4 (2012) 579–585. doi:10.1038/nchem.1376.

[301] Y. Hase, E. Ito, T. Shiga, F. Mizuno, H. Nishikoori, H. Iba, K. Takechi, Quantitation of Li_2O_2 stored in Li–O_2 batteries based on its reaction with an oxoammonium salt, Chem. Commun. 49 (2013) 8389. doi:10.1039/c3cc44723e.

[302] L. Trahey, C.S. Johnson, J.T. Vaughey, S.-H. Kang, L.J. Hardwick, S.A. Freunberger, P.G. Bruce, M.M. Thackeray, Activated Lithium-Metal-Oxides as Catalytic Electrodes for Li–O_2 Cells, Electrochem. Solid-State Lett. 14 (2011) A64. doi:10.1149/1.3555366.

[303] R.S. Assary, J. Lu, P. Du, X. Luo, X. Zhang, Y. Ren, L.A. Curtiss, K. Amine, The effect of oxygen crossover on the anode of a Li-O_2 battery using an ether-based solvent: Insights from experimental and computational studies, ChemSusChem. 6 (2013) 51–55. doi:10.1002/cssc.201200810.

[304] D. Aurbach, E. Zinigrad, Y. Cohen, H. Teller, A short review of failure mechanisms of lithium metal and lithiated graphite anodes in liquid electrolyte solutions, Solid State Ionics. 148 (2002) 405–416. doi:10.1016/S0167-2738(02)00080-2.

[305] C. Xia, R. Black, R. Fernandes, B. Adams, L.F. Nazar, The critical role of phase-transfer catalysis in aprotic sodium oxygen batteries, Nat. Chem. 7 (2015) 496–501. doi:10.1038/nchem.2260.

[306] N.B. Aetukuri, B.D. McCloskey, J.M. Garci??, L.E. Krupp, V. Viswanathan, A.C. Luntz, Solvating additives drive solution-mediated electrochemistry and enhance toroid growth in non-aqueous Li-O_2 batteries, Nat. Chem. 7 (2015) 50–56. doi:10.1038/nchem.2132.

[307] L. Johnson, C. Li, Z. Liu, Y. Chen, S.A. Freunberger, P.C. Ashok, B.B. Praveen, K. Dholakia, J.-M. Tarascon, P.G. Bruce, Erratum: The role of LiO_2 solubility in O_2 reduction in aprotic solvents and its consequences for Li–O_2 batteries, Nat. Chem. 7 (2014) 87–87. doi:10.1038/nchem.2138.

[308] W.-J. Kwak, H.-J. Shin, J. Reiter, N. Tsiouvaras, J. Hassoun, S. Passerini, B. Scrosati, Y.-K.

Sun, Understanding problems of lithiated anodes in lithium oxygen full-cells, J. Mater. Chem. A. 4 (2016) 10467–10471. doi:10.1039/C6TA03013K.

[309] G.Q. Zhang, J.P. Zheng, R. Liang, C. Zhang, B. Wang, M. Hendrickson, E.J. Plichta, Lithium–Air Batteries Using SWNT/CNF Buckypapers as Air Electrodes, J. Electrochem. Soc. 157 (2010) A953. doi:10.1149/1.3446852.

[310] Z. Ma, X. Yuan, L. Li, Z.-F. Ma, D.P. Wilkinson, L. Zhang, J. Zhang, A review of cathode materials and structures for rechargeable lithium–air batteries, Energy Environ. Sci. 8 (2015) 2144–2198. doi:10.1039/C5EE00838G.

[311] K.-N. Jung, J. Kim, Y. Yamauchi, M.-S. Park, J.-W. Lee, J.H. Kim, Rechargeable lithium–air batteries: a perspective on the development of oxygen electrodes, J. Mater. Chem. A. 4 (2016) 14050–14068. doi:10.1039/C6TA04510C.

[312] G.A. Elia, U. Ulissi, S. Jeong, S. Passerini, J. Hassoun, Exceptional long-life performance of lithium-ion batteries using ionic liquid-based electrolytes, Energy Environ. Sci. 9 (2016) 3210–3220. doi:10.1039/C6EE01295G.

[313] M. Marinaro, P. Balasubramanian, E. Gucciardi, S. Theil, L. Jörissen, M. Wohlfahrt-Mehrens, Importance of Reaction Kinetics and Oxygen Crossover in aprotic Li-O_2 Batteries Based on a Dimethyl Sulfoxide Electrolyte, ChemSusChem. 8 (2015) 3139–3145. doi:10.1002/cssc.201500600.

[314] L. Takacs, Self-sustaining reactions induced by ball milling, Prog. Mater. Sci. 47 (2002) 355–414. doi:10.1016/S0079-6425(01)00002-0.

[315] L. Takacs, Multiple combustion induced by ball milling, Appl. Phys. Lett. 69 (1996) 436–438. doi:10.1063/1.118086.

[316] D. Chaira, S.K. Karak, Fabrication of Nanostructured Materials by Mechanical Milling, in: Handb. Mech. Nanostructuring, Wiley-VCH Verlag GmbH & Co. KGaA, 2015: pp. 379–416. doi:10.1002/9783527674947.ch16.

[317] C. Xu, Y. Zeng, X. Rui, N. Xiao, J. Zhu, W. Zhang, J. Chen, W. Liu, H. Tan, H.H. Hng, Q. Yan, Controlled soft-template synthesis of ultrathin C@FeS nanosheets with high-Li-storage performance, ACS Nano. 6 (2012) 4713–4721. doi:10.1021/nn2045714.

[318] T.A. Yersak, C. Stoldt, S.-H. Lee, Electrochemical Evolution of an Iron Sulfide and Sulfur Based Cathode for All-Solid-State Li-Ion Batteries, J. Electrochem. Soc. 160 (2013) A1009–A1015. doi:10.1149/2.002308jes.

[319] T.A. Yersak, H.A. Macpherson, S.C. Kim, V.D. Le, C.S. Kang, S.B. Son, Y.H. Kim, J.E. Trevey, K.H. Oh, C. Stol dt, S.H. Lee, Solid state enabled reversible four electron storage, Adv. Energy Mater. 3 (2013) 120–127. doi:10.1002/aenm.201200267.

[320] E. Strauss, D. Golodnitsky, E. Peled, Study of phase changes during 500 full cycles of Li/composite polymer electrolyte/FeS_2 battery, Electrochim. Acta. 45 (2000) 1519–1525. doi:10.1016/S0013-4686(99)00368-0.

[321] J. Barker, E. Kendrick, The electrochemical insertion and safety properties of the low-cost Li-ion active material, Li_2FeS_2, J. Power Sources. 196 (2011) 6960–6963. doi:10.1016/j.jpowsour.2010.11.051.

[322] E. Kendrick, J. Barker, J. Bao, A. Świtek, The rate characteristics of lithium iron sulfide, J. Power Sources. 196 (2011) 6929–6933. doi:10.1016/j.jpowsour.2010.11.158.

[323] V. Pelé, F. Flamary, L. Bourgeois, B. Pecquenard, F. Le Cras, Perfect reversibility of the lithium insertion in FeS_2: The combined effects of all-solid-state and thin film cell configurations, Electrochem. Commun. 51 (2015) 81–84. doi:10.1016/j.elecom.2014.12.009.

[324] Y. Fujii, A. Miura, N.C. Rosero-Navarro, M. Higuchi, K. Tadanaga, $FePS_3$ electrodes in all-solid-state lithium secondary batteries using sulfide-based solid electrolytes, Electrochim. Acta. 241 (2017) 370–374. doi:10.1016/j.electacta.2017.04.089.

Chapter 7: Acknowledgements

This work has been carried out in Helmholtz Institute Ulm (HIU), founded in 2011 by Karlsruhe Institute of Technology (KIT) and part of the Helmholtz Association. This work has been financially supported by BMW AG and Samsung R&D Institute Japan.

My deepest gratitude goes to professor Stefano Passerini, who accepted me as Ph.D. student in his group, and guided me through my thesis work, allowing me to achieve remarkable results and grow from the professional point of view. I also would like to thank my close co-workers, particularly Dr. Alberto Varzi, who supported me toward the end of my thesis-related work, and Yanjiao Ma, whom I supervised during the first year of her Ph.D. work. Working with her also taught me a lot and helped me improve in several ways.

Special thanks to Samsung R&D Japan, particularly Dr. Yuichi Aihara and Dr. Seitaro Ito, who invited me in their institute and taught me very much about all-solid-state lithium sulfur batteries.

I also would like to thank professor Jusef Hassoun from University of Ferrara, who always supported me, both from the human and from the scientific point of view, particularly during the year prior to the official start of my Ph.D. career and through hard times, making most of my academic achievements possible. Dr. Giuseppe Antonio Elia was also an invaluable co-worker during my thesis and sharing lab activities with him was a great moment of learning. Dr. Rinaldo Raccichini, Dr. Daniele di Lecce, Dr. Ivana Hasa and Dr. Nelson Alexandre Galiote Silva were also invaluable co-workers, as productive, prolific discussions were the basis for improvement and learning.

Finally, I would like to mention and thank professor Bruno Scrosati, Dr. Priscilla Reale and Dr. Sergio Brutti, who motivated and taught me a lot during my early days as a bachelor and master student in Sapienza, Rome University.

"Family is a safe haven" …when braving the troubled waters of life
To the memory of my father, Ubaldo, and to my family, Ida and Riccardo